Tissue-engineered Human Cardiac Models for Quantitative Risk Assessment and Disease Modeling

by

Mark C. Daley

Brown University

A dissertation submitted in partial fulfillment of the requirements for the degree of Doctor of Philosophy in Biomedical Engineering

PROVIDENCE, RI

May 2025

This dissertation by Mark C. Daley is accepted in its present form by the Biomedical Engineering graduate program as satisfying the dissertation requirement for the degree of Doctor of Philosophy.

Date:_____ _____
Kareen L. K. Coulombe, PhD, Advisor

Recommend to the Graduate Council

Date:_____ _____
Anubhav Tripathi, PhD, Committee Chair

Date:_____ _____
Bum-Rak Choi, PhD, Reader

Date:_____ _____
Diane Hoffman-Kim, PhD, Reader

Date:_____ _____
Stephen Ferguson, PhD, External Reader

Approved by the Graduate Council

Date:_____ _____
Thomas Lewis, PhD, Dean of the Graduate School

Mark C. Daley

EDUCATION

Brown University, Ph.D. in Biomedical Engineering (GPA: 4.00/4.00) **Aug. 2020-May 2025**
Tufts University, M.S. in Biomedical Engineering (GPA: 3.96/4.00) **Aug. 2017-May 2020**
Bucknell University, B.S. in Biomedical Engineering (GPA: 4.00/4.00) **Aug. 2013-May 2017**

RESEARCH EXPERIENCE

Graduate Research Assistant, Brown University, Providence, RI **Aug. 2020-Present**
Supervised by Dr. Kareen Coulombe, School of Engineering, Biomedical Engineering

- **Tissue-engineered Human Cardiac Models for Quantitative Risk Assessment and Disease Modeling**
    - Advancing the collaborative Choi-Coulombe Lab *in vitro* cardiotoxicity platform by performing validation with pharmaceutical compounds, testing environmental toxicants, and developing methods for quantitative risk assessment.
    - Investigating co-therapies for cardiotoxicity arising from chemotherapy-induced toxicity.
    - Elucidating the triggers of atrial arrhythmias in Wolff-Parkinson-White Syndrome.

Graduate Research Assistant, Tufts University, Medford, MA **Aug. 2017-Aug. 2020**
Supervised by Dr. Lauren D. Black III, Department of Biomedical Engineering

- **Polarization of Cardiac Progenitor Cells Alters Microenvironment-Driven Vascular Differentiation**
    - Extended previous work on the effects of cECM developmental age on CPC differentiation to include interactions with membrane polarization.
- **Cardiac Extracellular Matrix Developmental Age and Cyclic Stretch Synergistically Improve Twitch Force in Engineered Cardiac Tissues**
    - Investigated *in vitro* effects of fetal and adult cardiac extracellular matrix and mechanical stretch on rat cardiomyocyte twitch mechanics within a custom bioreactor system.
    - Probed gene and protein expression related to cardiomyocyte maturation.

Summer Scholar, WFIRM, Winston-Salem, NC **May 2016-Aug. 2016**
Supervised by Dr. Sang Jin Lee and Dr. Young Min Ju, WFIRM

- ***In Vitro* Capture of Endothelial Progenitor Cells onto Dual-Antibody Conjugated Surfaces**
    - Prepared poly(ε-caprolactone)-collagen surfaces for testing of EPC capture.
    - Performed *in vitro* microfluidic studies to optimize antibody combinations for EPC capture.

Undergraduate Research Assistant, Bucknell University, Lewisburg, PA **Sep. 2014-Dec. 2016**
Supervised by Dr. James Baish, Department of Biomedical Engineering

- **Characterization of Particulate and Vapor Phase Nicotine in Electronic Cigarettes**
    - Designed and manufactured an Arduino-controlled device to control electronic cigarette samples.
    - Quantified nicotine bioavailability using gas chromatography-mass spectrometry.
    - Developed a pharmacokinetic model of dual-phase nicotine absorption in MATLAB.
    - Applied successfully for Bucknell University's Program for Undergraduate Research.

TEACHING EXPERIENCE

Adjunct Faculty, **Mechanics of Materials Lab**, Roger Williams University, Bristol, RI **2023-present**
Teach fundamentals of experimental and theoretical material mechanics including tension, shear, and bending as well as technical writing in a hands-on laboratory environment.

Graduate Instructor, Techniques in Regenerative Medicine, Brown University, Providence, RI **2023-present**
Design in-lab and take-home assignments to teach first-year undergraduates cell culture and related aseptic techniques as well as scientific literacy for understanding and performing tissue engineering and regenerative medicine research.

Teaching Assistant, Can We Build Organs?, Brown University, Providence, RI **2023**
Transformed undergraduate-level course material into a two-week-long, laboratory experience introducing high school students to the fundamentals of regenerative medicine research as a part of the Summer@Brown program.

Teaching Assistant, Biomaterials, Brown University, Providence, RI **2020-2022**
Provided support for online and in-person learning, graded, designed course assessments, and gave guest lectures.

Co-Instructor, Quantitative Physiology, Tufts University, Medford, MA **2019**
Designed and taught a multi-lecture pharmacokinetics module for a senior- and graduate-level course in physiology.

Teaching Assistant, Quantitative Physiology, Tufts University, Medford, MA **2018**
Contributed to student learning through in-lecture assistance and office hours.

Teaching Assistant, Fundamentals of Biomedical Engineering, Bucknell University, Lewisburg, PA **2017**
Participated in wet lab development and technical writing mentorship for first-year students.

Teaching Assistant, Fabrication and Experimental Design, Bucknell University, Lewisburg, PA **2016**
Provided in-class support for both cell culture and computer-aided design activities.

Student Grader, Bioinstrumentation I, Bucknell University, Lewisburg, PA **2016**
Marked assignments in a timely manner to enhance student learning.

PUBLICATIONS

1. **Daley, M.***, Moreau, M.*, *et al.* (2024) *In Vitro* to *In Vivo* Extrapolation from Three-Dimensional hiPSC-derived cardiac microtissues and physiologically based pharmacokinetic modeling to inform next-generation arrhythmia risk assessment. *Tox Sci.* kfae079 **Honorable Mention for Paper of the Year at the 2024 in Biological Modeling.**
2. Perreault, L., **Daley, M.**, *et al.* (2024) Characterization of Cardiac Fibroblast-Extracellular Matrix Crosstalk Across Developmental Ages Provides Insight into Age-related Changes in Cardiac Repair. *Front. Cell Dev. Biol.* 12: 1279832
3. Dwyer, K, Kant, R, Soepriatna, A, Roser, S, **Daley, M.**, *et al.* (2023). One Billion hiPSC-cardiomyocytes: Upscaling Engineered Cardiac Tissues to Create High Cell Density Therapies for Clinical Translation in Heart Regeneration. *Bioeng.* 10.5: 587

4. Soepriatna, A., Navarrete-Welton, A., Kim, T.Y., **Daley, M.**, *et al.* (2023). Action Potential Metrics and Automated Data Analysis Pipeline for Cardiotoxicity Testing Using Optically Mapped hiPSC-derived 3D Cardiac Microtissues. *PLoS One*. 18.2: e0280406
5. **Daley, M.,** *et al.* (2023) Beyond Pharmaceuticals: Fit-for-Purpose New Approach Methodologies for Environmental Carditoxicity Testing. *ALTEX*. 40.1: 103-116
6. Soepriatna, A., Kim, T.Y., **Daley, M.**, *et al.* (2021). Human Atrial Cardiac Microtissues for Chamber-Specific Arrhythmic Risk Assessment. *Cell. Mol. Bioeng.* 154.5: 441-457
7. **Daley, M.**, *et al.* (2020). The Effects of Membrane Potential and Extracellular Matrix Composition on Vascular Differentiation of Cardiac Progenitor Cells. *Biochem. Bioph. Res. Co.* 530.1:240-245
8. **Daley, M.**, Fenn, S., and Black, L. (2018). Applications of Cardiac Extracellular Matrix in Tissue Engineering and Regenerative Medicine. In Cardiac Extracellular Matrix (59-83). Springer, Cham.

CONFERENCE PRESENTATIONS

1. **Daley, M.** *et al.* Identification of cardioprotective strategies to prevent anthracycline-induced cardiotoxicity using an engineered human cardiac microtissue model. Poster at the 2024 BMES Annual Meeting (*Accepted)*
2. **Daley, M.** *et al.* Leveraging *In Vitro* 3D Human Cardiac Microtissues and Pharmacokinetic Modeling for Ventricular Pro-Modeling for Ventricular Pro-arrhythmic Risk Assessment. Oral presentation at the 2024 Society of Toxicology Annual Meeting. **Served as session chair.**
3. **Daley, M.,** *et al.* Quantification of Arrhythmia Risk from Chronic Chemical Exposure in Engineered Three-Dimensional Human Cardiac Microtissues. Oral Presentation at the 2023 Society of Toxicology Annual Meeting.
4. **Daley, M.***, Moreau, M.*, *et al.* (2022) Risk Assessment by Combined Three-Dimensional Human Cardiac Microtissues and Pharmacokinetic Modeling. Poster at the 2022 Society of Toxicology Annual Meeting. *Co-first author. **Top 10 Abstract in the Risk Assessment Specialty Section. Finalist for Best Trainee Abstract in the Biological Modeling Specialty Section.**
5. **Daley, M.**, Soepriatna, A., Kofron, C., Mende, U., Choi, B.R., Coulombe K. (2021). Three-Dimensional Human Cardiac Microtissues for *In Vitro* Risk Assessment of Arrhythmogenic Cardiotoxicity. Oral presentation at the 2021 Brown-Yale Cardiovascular Student Research Symposium.
6. **Daley, M.** and Black III, L. (2019). Depolarization of Cardiac Progenitor Cells Alters Microenvironment-Driven Vascular Differentiation. Oral presentation at the 2019 BMES Annual Meeting.
7. **Daley, M.**, Watson, M., Perreault, L., Bretherton, R., Stoppel, W., Black III, L. (2018). Cardiac ECM Developmental Age and Cyclic Stretch Synergistically Improve Twitch Force in Engineered Cardiac Tissues. Poster at the 2018 BMES Annual Meeting.
8. **Daley, M.,** Ju, Y.M., and Lee, S.J. (2016). *In Vitro* Capture of Endothelial Progenitor Cells onto Antibody Conjugated Poly(ε-Caprolactone)-Collagen Surfaces. Poster Presented at the annual WFIRM Summer Symposium.
9. **Daley, M.**, Baish, J., Dutcher, D., and Raymond, T. (2016). Characterization of Particulate and Vapor Phase Nicotine in Electronic Cigarettes. Poster at the 2016 BMES Annual Meeting.
10. **Daley, M.**, Baish, J., Dutcher, D., and Raymond, T. (2016). Characterization of Particulate and Vapor Phase Nicotine in Electronic Cigarettes. Poster at the 2016 Summer Biomechanics, Bioengineering and Biotransport Conference (SB^3C). **Third Prize in the 2016 SB^3C Undergraduate Student Paper Competition**

PATENTS

Coulombe, K., Choi, B. R., Soepriatna, A. H., Kim, T. Y., and **Daley, M. C.** *Atrial Cardiac Microtissues for Chamber Specific-Arrhythmogenic Toxicity Responses.* US Patent App. 17/675.895.

PROFESSIONAL DEVELOPMENT

Sheridan Center – Head Teaching Consultant, Brown University, Providence, RI **2024-present**
Co-organize and lead the Sheridan Center's Teaching Consultant Program to promote pedagogical development of graduate students and post-doctoral fellows at Brown through workshops, microteaching, and teaching observations.

Sheridan Center – Teaching Consultant Program, Brown University, Providence, RI **2023**
Led a semester-long, small-group workshop on reflective teaching to facilitate learning of evidence-based, inclusive teaching practices by graduate students and post-doctoral fellows.

Auburn Future Faculty Workshop, online via Auburn University **2022**
Completion of a three-part seminar to develop a competitive faculty application package.

Sheridan Center – Teaching Certificate I, Brown University, Providence, RI **2021**
Completion of the semester-long Teaching Seminar aimed at developing and refining teaching and assessment strategies.

RIHub Customer Discovery Course, Providence, RI **2021**
Completion of a combination seminar series and expert interviews focused on developing entrepreneurial skills and defining a target customer for commercialization of the Choi-Coulombe Lab cardiotoxicity platform.

Graduate Institute for Teaching, Tufts University, Medford, MA **2019**
Competitive program to enhance preparation in pedagogy via a series of seminars and workshops in teaching.

MENTORSHIP

Graduate Student Research Mentor, Brown University, Providence, RI **2021-present**
Supervised two master's students during the completion of their theses and seven undergraduate students through the Leadership Alliance's Summer Research Early Identification and Undergraduate Teaching and Research Awards Programs.

Graduate Student Research Mentor, Tufts University, Medford, MA **2017-2020**
Supervised the independent research projects of two undergraduate research assistants working in the Black Lab and their successful application to summer research programs.

TUBERS Program, Tufts University, Medford, MA **2017-2019**
Led lab activities to introduce high school students to tissue engineering research and mentor their independent summer research projects in the Black Lab.

SERVICE

Chair, BMEB Climate Committee, Brown University, Providence, RI **Aug. 2023-present**
Lead the Biomedical Engineering Board's Program Climate Committee as it coordinates institute-wide initiatives for improving faculty-student interactions and overall student experiences.

Faculty Meeting Observer, BMEB, Brown University, Providence, RI **May. 2023-present**
Act as the graduate student liaison for the Biomedical Engineering Board during faculty meetings to facilitate student-faculty coordination within the Institute for Biology, Engineering and Medicine.

Member, BMEB Climate Committee, Brown University, Providence, RI **Aug. 2022-Aug. 2023**
Plan initiatives such as the annual retreat and PhD recruitment to improve Institute cohesion.

Volunteer, Letters to a Pre-Scientist **Sep. 2018-2021**
Motivate interest and participation in STEM careers among underrepresented students.

Secretary, BEaChES, Tufts University, Medford, MA **Jun. 2019-Jun. 2020**
Manage event communication, website upkeep, and social media presence for the graduate Biomedical Engineering and Chemical Engineering Society (BEaChES) at Tufts.

Volunteer, Cambridge Science Festival, Cambridge, MA **Apr. 2019-Aug. 2020**
Engage members of the local community about current work in tissue engineering and biomaterials research.

Volunteer, Somerville High School Science Fair, Somerville, MA **Mar. 2019-Aug. 2020**
Provide constructive feedback to local science students regarding their independent projects.

Project Leader, ENABLE, Bucknell University, Lewisburg, PA **Jan. 2016-May 2017**
Organized a team responsible for the design and manufacture of 3D printed prosthetic hands and arms, providing two completed designs to members of the local community.

Junior Fellow, Residential Colleges Program, Bucknell University, Lewisburg, PA **Aug. 2014-May 2015**
Guided members of the Society and Technology Residential College through their first-year experience as a student mentor.

FELLOWSHIPS AND GRANTS

Brown Biomedical Innovations to Impact (BBII) Award, Brown University, Providence, RI **2020-present**
Supported the successful application for additional Phase 2 funding of the Coulombe Lab's BBII Award for work assessing cardiotoxicity in engineered tissues (renewed Winter 2022).

Wake Forest Institute for Regenerative Medicine Summer Scholar, WFIRM, Winston-Salem, NC **2016**
Funded research experience for undergraduates at WFIRM in tissue engineering and regenerative medicine.

Program for Undergraduate Research, Bucknell University, Lewisburg, PA **2015**
Grant-style application for summer research funding for undergraduate research.

PROJECT EXPERIENCE

Chronic Wound Care, Bucknell University, Lewisburg, PA **Aug. 2016-May 2017**
Worked with a small engineering team and clinicians at the Geisinger Health Center in Danville, PA to prototype an enhanced treatment for diabetic pressure ulcers.

AWARDS, HONORS, FELLOWSHIPS, AND SCHOLARSHIPS

Top 10 Abstract in the Risk Assessment Specialty Section, San Diego, CA **2022**
Prize for top abstracts related to risk assessment methods at SoT2022.

Finalist for Best Trainee Abstract in the Biological Modeling Specialty Section, San Diego, CA **2022**
Prize for top trainee abstracts related to biological methods at SoT2022.

Dean's Fellowship Recipient, Tufts University, Medford, MA **2017**
Awarded for being a top student of the incoming graduate cohort at Tufts University.

Summa Cum Laude, Bucknell University, Lewisburg, PA **2017**
Awarded to members of the graduating class with a cumulative GPA above 3.9.

The Bucknell Prize in Biomedical Engineering, Bucknell University, Lewisburg, PA **2017**
Awarded to the biomedical engineering student of the graduating class with the highest cumulative GPA.

The Maria Leonard Senior Book Award, Bucknell University, Lewisburg, PA **2017**
Awarded to the Alpha Lambda Delta member of the graduating class with the highest cumulative GPA.

The Oliver J. Decker Prize, Bucknell University, Lewisburg, PA **2017**
Awarded to the graduating member of the School of Engineering with the highest cumulative GPA.

The University Prize for Men, Bucknell University, Lewisburg, PA **2017**
Awarded to the male member of the graduating class with the highest cumulative GPA.

President's Award, Bucknell University, Lewisburg, PA **2014-17**
Awarded annually to individuals who maintain a perfect 4.0 GPA.

Third Prize in the 2016 SB^{3}C Undergraduate Student Paper Competition, National Harbor, MD **2016**
Prize for scientific merit in imaging, devices, human dynamics & injury, fluids & microfluidics, and heat transfer.

Tau Beta Pi, Bucknell University, Lewisburg, PA **2016-onward**
Inductees consist of the top members of their engineering class.

Professor George Morris Philips Prize in Mathematics, Bucknell University, Lewisburg, PA **2014**
Given to the top mathematics student of the first-year class.

Alpha Lambda Delta, Bucknell University, Lewisburg, PA **2014**
Inductees consist of the top members of their class at the end of the first year.

Dean's List, Bucknell University, Lewisburg, PA **2013-17**
Granted semesterly to individuals achieving a 3.5 GPA or above that semester.

Dean's Scholar, Bucknell University, Lewisburg, PA **2013**
Annual merit-based scholarship awarded to top members of the incoming class at Bucknell University.

Dedication and Acknowledgements

The 200+ pages of this dissertation would have been entirely impossible without the advice, support, and encouragement of countless people. First among them being the Coulombe Lab: Arvin, Alicia, Jeev, Kiera, Steph, and Zoe. Thank you all for being my daily support network both in and outside of the lab. To my mentees past and current, thank you for helping me figure it out with you. Without each of you to help me plan, complain, and celebrate, none of this would have been possible. I will be forever grateful to you all for making the lab feel like a home away from home. It was an honor to have you as a part of my scientific journey.

To my advisor Kareen, thank you for believing in me from the very beginning. You were the reason I chose to come to Brown and your support has exceeded even my wildest dreams. Thank you for coaching me into the scientist, mentor, and person that I am today. I hope to carry at least a fraction of your example forward.

To Bum-Rak, thank you for your infinite patience across countless hours and troubleshooting sessions. Your excitement for science is infectious and made even the longest days in the lab fulfilling. To my other committee members Diane Hoffman-Kim, Anhubav Tripathi, and Stephen Ferguson, thank you for generously giving me your time and advice. I am undoubtedly a better researcher because of your support. Thank you also to my collaborators who helped to fill in all the other gaps in my work. Thank you, Marjory, for welcoming me into the world of toxicology; Peter, for unparalleled computational support; and, Ulrike, for simultaneously sharp and supportive edits.

To Logan and Sara from the Sheridan Center, thank you for all that you do to build community at Brown. I know that my teaching would not be the same without you both and that my academic career would be nowhere near as well-rounded. To Toni-Marie Achilli, thank you for bringing me into your classroom and giving me space to develop my own teaching.

To friends old and new, thank you for being a reminder that there is a world away from the chaos that is graduate school. This would not have been possible without you pulling me away from the lab.

To my family, I could not ask for a better foundation from which to pursue a PhD. Mom, Dad, Heather, Brett, Rachel, Jim, and Liam, I know that you will always be an unwavering source of support. Thank you for your infinite love and patience. To Mae, I could not imagine being on this journey without you. Whether from hundreds of miles away or the next room over, you make every day better no matter what happens in the lab. I cannot wait to continue our journey together. Love you lots.

Table of Contents

List of Tables

List of Figures

Chapter 1 - Introduction

1.1. The need for improved preclinical models of cardiac tissue

Over recent decades, drug discovery has continued to become an increasingly resource-intensive, but less efficient process. Highlighting this reality is the fact that between 1980 and 2019, the number of investigational new drugs (INDs) approved by the United States Food and Drug Administration (FDA) has stayed approximately the same while the amount spent on pharmaceutical research increased from 10 billion dollars to over 80 billion dollars per year (inflation corrected) [1]. This amounts to an expected cost of one to two billion dollars per new drug with little indication that this trend will slow in the coming years [2]. A significant portion of these growing costs can be attributed to a disconnect between compounds that are identified in preclinical models and those that are ultimately safe and effective for use in human patients. Among compounds that pass preclinical assessment, only about 7% of them will reach and stay on the market for patient use [3, 4]. Since the majority of money used for drug development is spent on late-stage clinical trials [4, 5], addressing this preclinical-to-clinical gap presents a significant opportunity for mitigating inefficiencies in creating novel therapeutics [5].

Given the preeminence of cardiovascular disease as a cause of mortality and morbidity [6] and the broader challenges of drug development, it is unsurprising that a major contributor to the challenges facing preclinical drug assessment is the accurate prediction of cardiotoxicity. Of the 30% of compounds removed from the development pipeline due to safety concerns, approximately 15% of those are due to cardiac toxicities for both pre- and post-approval removals [3, 7, 8]. The picture is bleaker for cardiotoxicity associated with chemotherapies. Cancer survivors possess a 42% higher risk of developing cardiovascular disease compared to individuals who have not been treated for cancer [9]. Alarmingly, among patients with increasing rates of survival after their initial diagnosis, rates of mortality from cardiovascular disease have tended to increase [10]. While some of this increased risk can be explained by overlapping risk factors for cancer and cardiovascular disease [11], oncological treatment itself is a significant risk factor for

cardiovascular disease [12, 13]. As a result, early identification of cardiotoxicity, especially in second- and third-generation anti-cancer compounds, represents a significant barrier and major area of innovation in modern drug development [14].

From an efficacy perspective, investment in cardiovascular drug development has stagnated despite the growing toll of cardiovascular disease [15]. While this trend is multifactorial, the most significant contributor is the relatively high cost and long timescales of cardiovascular outcome trials and a reduced capacity for being able to rely on surrogate measurements of health outcomes (*e.g.* blood pressure) compared to other therapeutic areas like oncology. Among cardiovascular drugs that are discontinued in Phase 3 trials, about half are due to inadequate efficacy versus only about one-fourth due to safety [16]. Thus, significant improvements in the reliability of identifying effective compounds would have the possibility of substantially reducing the financial uncertainty of pursuing drugs for cardiovascular indications. Overall, this confluence of these challenges indicates a sustained need for improving preclinical cardiac models.

1.1.1. Current models of proarrhythmic cardiotoxicity

The primary focus of drug-related cardiac safety assessment is the detection of delays in ventricular repolarization [17]. Clinically, this appears as prolongation of the QT interval, the time between the initiation of the QRS complex and end of the T wave on an electrocardiogram [18, 19]. Increases in the QT interval greater than 10 milliseconds are considered clinically relevant and associated with a significant increase in the risk of potentially life-threatening ventricular fibrillation, or unsynchronized contractions in the lower chambers of the heart, that prevent effective blood flow throughout the body. At the cellular level, delayed ventricular repolarization is the result of prolongation of ventricular action potentials [17]. The predominant mechanism, which is also the primary mechanisms of regulatory concern, is inhibition of the rapidly activating delayed rectifier potassium channel (I_{Kr} or hERG channel), whose pore-forming α subunit is encoded by the human ether-a-go-go related gene (hERG) [20]. Inhibition of this channel delays

late-stage repolarization, extending the action potential, and can result in secondary action potentials known as early afterdepolarizations (EADs) that ultimately initiate ventricular fibrillation [21].

Delayed repolarization arose as a major regulatory concern after several rapid, high-profile withdrawals of three drugs (prenylamine, lidoflazine, and tordiline) within a three-year period due to their association with increased arrhythmia risk [22]. This led to the United State Food and Drug Administration's (FDA) adoption of the International Council for Harmonisation of Technical Requirements for Pharmaceuticals for Human Use (ICH) guideline S7B, which outlines required *in vivo* and *in vitro* models for detecting delayed ventricular repolarization and has become the standard for preclinical cardiotoxicity assessment [23].

Under the guidelines, *in vivo* assessment is performed using electrocardiogram in small rodent models to mimic the clinical gold standard. While able to reflect *in vivo* metabolism and pharmacokinetics, there are several significant challenges when mapping arrhythmias observed in animal models to humans [17, 24]. Namely, inter-species differences in electrophysiology can lead to substantially different responses, particularly the lack of hERG channel expression in rats and mice [25-28] in addition to fundamental differences in drug metabolism and transformation [29]. These biological challenges are in addition to practical limitations due to the high financial and labor costs associated with *in vivo* experiments and growing ethical concerns regarding the use of animals in toxicology [30]. As a result, the *in vivo* tests defined by S7B are complemented by the *in vitro* functional I_{Kr} assay, which screens changes in the activity of the I_{Kr} channel in immortalized cell lines. This assay is highly specific for proarrhythmic risk caused by hERG inhibition while simultaneously benefiting from high-throughput plate formats and automation. However, because this assay targets a single ion channel, it can fail to identify other potentially proarrhythmic effects as well as generate false positives due to an inability to measure interactions across multiple ion channels that may be compensatory [17]. For instance, sodium channel blockade is a known alternate mechanism for QT interval prolongation and also interferes with normal cardiac conduction [31].

Despite this, there is no standardized method for assessing sodium channel-related proarrhythmic cardiotoxicity. Ultimately, current approaches continue to have shortcomings in accurately predicting human arrhythmias holistically and accurately [32-34].

1.1.2. Current preclinical models of non-proarrhythmic cardiotoxicity

While the primary regulatory focus has been on proarrhythmic, and principally repolarization-related, cardiotoxicity, a range of additional mechanisms are known to cause non-arrhythmic toxicity [22]. Broadly, these additional mechanisms can be categorized as contractile (*e.g.* dysregulated calcium handling or damaged contractile proteins) as well as structural (*e.g.* cardiomyocyte viability, mitochondrial damage, oxidative stress, and DNA damage) cardiotoxicity [22, 35]. Non-cardiomyocyte toxicity also contributes significantly to cardiotoxicity [22, 36, 37], with effects on fibroblasts, smooth muscle cells, and endothelial cells indirectly influencing cardiomyocyte function. However, toxicity associated with these cell types is typically considered separately as either a part of vascular toxicity or general cytotoxicity outside of normal cardiac contraction.

Despite the impact of these mechanisms, non-proarrhythmic cardiotoxicity is less specifically regulated by the FDA than repolarization-related arrhythmias. Structural and contractile toxicity are broadly covered by ICH guideline S7A, which defines a core battery of endpoints for general safety pharmacology assessment *in vivo* [14, 38, 39]. Under this guideline, cardiovascular toxicity is broadly monitored via changes in blood pressure and heart rate along with secondary endpoints derived from the electrocardiographic monitoring required under guideline S7B, often with only single dose exposures. Optional follow ups measuring cardiovascular function (*e.g.* cardiac output and ventricular contractility) can also be used as warranted. Unfortunately, extrapolation to human risk from apical endpoints such as those found in guideline S7A often provide limited mechanistic insight [17]. Beyond these, drug developers will rely on miscellaneous models as deemed necessary by their preliminary toxicological

testing (*e.g.* primary cell and tissue culture). As a result, there is still significant room in the safety pharmacology sphere to define and refine human models of non-proarrhythmic cardiotoxicity.

1.1.3. Traditional preclinical models of cardiac disease

As with cardiotoxicity, there is a diverse range of underlying mechanisms and phenotypes responsible for cardiac disease. In contrast to the goal of cardiotoxicity models, which is to replicate the response of healthy tissue to toxicological stimuli, the goal of disease models is to faithfully recapitulate disease pathology prior to introducing therapeutic interventions which can include toxicant-driven pathology as well as pre-existing disease [40]. Most traditionally, these have been small (*e.g.* zebrafish, mice, and rats), medium (*e.g.* rabbits and guinea pigs), or large (*e.g.* pig and non-human primates) animal models with cardiac disease artificially induced through genetic, pharmacological, or surgical interventions [40]. The major advantage of this *in vivo* approach is its ability to capture multiple, interrelated mechanisms across physiological systems such as the vascular and immune systems. However, these and other models must strike a balance between recapitulating disease symptoms, underlying mechanisms, and responsiveness to therapeutic agents [41]. Thus, the specific *in vivo* models leveraged for a given disease are dictated by specific knowledge of its etiology as well as practical limitations for its induction such as time for disease progression and cost.

For example, long QT syndrome (LQTS) is a rare genetic condition that results in prolongation of cardiac action potentials and subsequently the QT interval, mirroring hERG-related cardiotoxicity [42, 43]. Across more than 50 years of research, the underlying, primarily monogenic mutations responsible for numerous variants of LQTS have been discovered and described [42]. As a result of this detailed understanding of specific causal mutations, small rodent models of each variant have been created for use in mechanistic and therapeutic studies [28, 44]. While these models are limited by the same inter-species differences in ion channel expression and electrophysiology as models of drug-induced arrhythmias, they provide a flexible tool for recapitulating complex *in vivo* pharmacokinetics and disease

mechanisms in a manner that is reflective of that observed in humans in the clinic. For instance, mouse models of LQTS have been used to show the efficacy of targeted gene therapy to normalize action potentials and QT intervals [45]. Ultimately, however, their success is predicated on the ability to specifically recapitulate a known mechanism *in vivo*. Other diseases, however, are not as successfully modeled in small rodent models [46]. In mouse models of Duchenne Muscular Dystrophy, in which the dystrophin protein has been genetically knocked out, mice possess only a mild form of cardiomyopathy while retaining a regular life expectancy compared to human patients who have a severe disease phenotype [47, 48]. Still others, like heart failure, are the manifestation of diverse array of interrelated mechanisms as well as environmental- and age-related mechanisms that require surgical or pharmacological intervention without the ability to rely on singular genetic mechanisms [49]. Thus, the outcomes predicted by these models can be more heavily dependent on the specific method of induction, reducing predictability.

Despite their utility, efforts to replace, reduce, and refine animal models increasingly promote the use of alternative *in vitro* systems to study cardiovascular disease [30]. A range of assays and culture formats from single cells, two-dimensional monolayers, and three-dimensional tissues have been used to mimic cardiovascular tissues *in vitro* depending on requirements [50, 51]. Traditionally, however, these have relied on genetically modified non-cardiovascular cells (*e.g.* HEK 293), primary animal cells (*e.g.* neonatal rat cardiomyocytes), and difficult-to-obtain or difficult-to-culture primary cells (*e.g.* cardiomyocytes, smooth muscle cells, and endothelial cells) [52, 53]. Human primary cardiac cells are among the most difficult-to-obtain and culture because they must be obtained from tissue samples. Cardiomyocytes represent an added challenge because they do not proliferate significantly *in vitro*. Thus, experiments are limited in scope with relatively fewer samples, test conditions, and endpoints, reducing the usefulness of a cell source that otherwise has the potential to overcome many of the species-specific limitations of animal models and cell sources.

1.2. hiPSC-CMs as models of cardiotoxicity

Human induced pluripotent stem cell-derived cardiomyocytes (hiPSC-CMs) are of particular interest for examining cardiotoxicity because they can be differentiated from proliferative hiPSCs, meaning that they serve as a continual source of human cardiomyocytes. This makes them substantially easier to obtain than primary isolates in addition to being significantly more representative of human cardiac physiology and able to model patient-specific toxicity [52, 53]. More recently, it has been shown that hiPSC-CMs can be induced to proliferate directly without affecting their functionality, further increasing their utility as a cell source for *in vitro* cardiotoxicity modeling [54, 55]. As with other cell-based models, hiPSC-CM-based approaches also benefit from flexible culture formats (*i.e.* monolayers, microtissues, engineered heart tissues, and microphysiological systems) that enable diverse functional readouts [56, 57], discussed in detail below. Unsurprisingly, researchers have begun turning towards hiPSC-CMs for developing predictive, human *in vitro* platforms for drug safety evaluation and development in order to complement existing regulatory requirements models with species-specific data [58-65].

The first regulatory submission to the FDA that included data derived from hiPSC-CMs was submitted in 2012, with a total of 29 applications that have included hiPSC-CM-derived data by 2019 [58]. A diverse range of therapeutic areas are represented with about one third being anticancer therapies and one fourth being antivirals. A slim majority (54%) were intended to detect proarrhythmic cardiotoxicity, suggesting this is still the primary mechanism of concern for drug developers, but that there is a substantial role for hiPSC-CMs to model non-proarrhythmic toxicities as well [22, 56]. Along with these early successes, there still remain several challenges that face the broad adoption of hiPSC-CM-based cardiotoxicity models with the primary hurdle being the well-known gap between the maturity of hiSPC-CMs and adult human cardiomyocytes in terms of electrophysiological, contractile, and metabolic (endogenous and xenobiotic) function [66-69]. Moreover, there is significant line-to-line variability that is known to alter susceptibility to cardiotoxicants [70-73]. These challenges have begun to be addressed

with the establishment of diverse cell libraries of hiPSCs [74] and the simultaneous differentiation and testing of mixed hiPSC cultures, called villages [75], that can capture this variability. Undoubtedly, however, as hiPSC-CMs are increasingly adopted as preclinical models and experimental techniques are improved, these limitations may be overcome.

1.2.1. hiPSC-CMs as models of proarrhythmic cardiotoxicity

Given the FDA's regulatory focus on proarrhythmic cardiotoxicity, there has been significant effort to develop hiPSC-CM-based approaches for identifying arrhythmogenic drug exposures with a specific focus on endpoints that measure action potential duration as an *in vitro* surrogate for QT interval [35, 56]. Methodologically, these fall into two categories: transmembrane and extracellular recordings [56]. Transmembrane recording can be performed either via intracellular electrodes (*i.e.* patch-clamping) or with voltage-sensitive dyes that enable detection of changes in membrane potential via alterations in fluorescence intensity. High-temporal resolution transmembrane recordings offer direct insight into action potential shape, with changes reflecting the integration of effects on multiple, integrated ion currents [22, 51, 56, 76]. Thus, prolongation of *in vitro* action potentials is used to predict QT prolongation *in vitro* for the detection of repolarization-related proarrhythmic toxicity [62, 77]. Image-based methods are more readily amenable to both two- and three-dimensional systems, while intracellular electrodes can typically only be used with two-dimensional monolayers, which limits the maturity of hiPSC-CMs examined in these systems. However, progress is being made in applying patch clamping to three-dimensional culture systems [78]. In contrast, extracellular recordings are typically performed with microelectrode arrays (MEAs) embedded in the bottom of 96- or 384-well plates to record electric field potentials [79]. The major advantage of this approach is the ability to measure changes in field potential from the same set of cells across time because MEAs acquire a continuous extracellular signal and do not require piercing individual cells or the use of potentially cytotoxic dyes. However, this advantage is partially offset by the fact that field potentials represent the summation of all cellular membrane

potentials within a small area or "field" surrounding an electrode [79, 80]. While there are substantial data suggesting that metrics like field potential duration is correlated with action potential duration [81], the lack of a one-to-one mapping of the features of field potentials to action potentials confound the interpretation of the effects on multiple ion channels. Both approaches also offer an ability to measure additional endpoints (*e.g.* conduction velocity) that reflect non-repolarization-related arrhythmia risks (*e.g.* sodium channel blockade).

1.2.2. hiPSC-CMs as models of contractile cardiotoxicity

As with proarrhythmic cardiotoxicity, hiPSC-CMs enable a more human-relevant foundation from which to measure drug-induced changes in contractility and electromechanical coupling [22, 46, 56]. This is particularly relevant for drugs and chemicals that directly impact normal force generation in cardiomyocytes. For instance, tyrosine kinase inhibitors, a diverse class of chemotherapeutics, are known to cause reduced left ventricular ejection fraction and heart failure via the loss of cardiomyocyte contraction [82-84]. Serving as an *in vitro* proxy for cardiac force generation and ejection fraction, hiPSC-CM contractility can be measured either indirectly or directly using a variety of techniques [22, 56]. Indirect contractility endpoints include impedance-based measurements and optical motion tracking. Impedance measurements are based on the incorporation of small film electrodes placed underneath two-dimensional monolayers of hiPSC-CMs. Alternating currents in the milliampere range allow for precise and frequent measurements of the electrical impedance using Ohm's Law [85], which changes as beating cardiomyocytes change shape during regular contractions and enables detection of both beat rate and amplitude across time. Because baseline impedance also increases with cell adherence, it can simultaneously be used as a measure of cell viability in addition to contraction [86, 87]. Like MEAs for field potential measurements, it is only suitable for two-dimensional cell culture. Optical motion tracking is more flexible across culture formats and can be used with both two-dimensional monolayers and three-dimensional engineered cardiac tissues [88-90]. Motion is recorded as a surrogate for contraction using

simple brightfield or phase contrast videos and contraction signals are reconstructed by quantifying changes in pixel intensity, edge displacement, or post deflection. When using larger tissues grown on polymers with known stiffnesses, it is possible to estimate force generation as well [63, 91]. Fluorescence-based calcium imaging utilizing genetically encoded calcium sensors or calcium-sensitive dyes are also used as a surrogate contraction endpoint that give additional insight into excitation-contraction coupling. Since calcium release is voltage-sensitive, some groups leverage calcium as an *in vitro* surrogate of QT interval [61, 92, 93], although there is some evidence that it can be less sensitive to inhibition of certain ion channels [94]. Similarly, because of the close relationship between calcium and cardiomyocyte contraction [95], it also is used as a proxy for cardiomyocyte contractility [96], and may ultimately better serve as its own independent metric rather than as a proxy for either mode of toxicity. Lastly, direct force measurements are most typically taken using engineered tissues, although they can be performed using single-cell traction force microscopy and other high-sensitivity instruments [57, 97]. For three-dimensional culture formats, tissues are designed to permit the use of high-sensitivity force transducers [98-100]. While typically less high throughput than their indirect counterparts, direct force measurements provide better mechanistic insight into the underlying cardiac physiology [101].

1.2.3. hiPSC-CMs as models of structural Cardiotoxicity

Techniques for measuring structural cardiotoxicity in hiPSC-CM-based models span the broadest array of endpoints due to the diversity of cell viability measurements compared to more cardiac-specific functional assays. The principal assays are standard fluorescent or colorimetric methods for directly detecting cell viability (*e.g.* MTT or ATP assays). Similarly, techniques quantifying cell death (*e.g.* LIVE/DEAD staining) or apoptosis (*e.g.* caspase activity assays) can be used as a complement to cellular viability. Alternatively, release of cardiac-specific injury markers, like troponin, can measure overall cell injury in a manner reflective of existing clinical biomarkers for detecting cardiac injury [102, 103]. The major advantage of these assays is that they are universally applicable and generally agnostic to the

upstream mechanism that is resulting in cardiotoxicity and can be applied broadly [104]. When used with non-cardiomyocytes derived from hiPSCs, for instance, they can be leveraged to examine human-specific cardiovascular toxicity [22]. However, they do not provide insight into the trigger of cell death. More specific mitochondrial stress assays (*e.g.* membrane potential and reactive oxygen species (ROS) generation) or DNA damage assays can provide additional causal ties to a chemical's mechanism of toxicity.

1.3. hiPSC-CMs as disease models

1.3.1. Genetic cardiac disease modeling with hiPSC-CMs

As with animal models of cardiac disease, hereditary genetic disorders, especially monogenic conditions, are comparatively easier to model with hiPSC-CMs than those with complex, multi-cause etiologies [66]. Derivation of hiPSC-CMs from donors with a given disease is often sufficient to recapitulate disease phenotypes *in vitro.* Alternatively, genetic engineering can be leveraged to introduce mutations associated with given disorders into otherwise healthy hiPSC lines or to reverse the mutation in a donor line to create an isogenic system with which to study the effects of a specific mutation.

As a result, high-penetrance cardiac disorders have been the most intensely studied using hiPSC-CM-based model systems [105-107]. An array of cell lines has been produced that are capable of recapitulating inherited arrhythmias such as LQTS [108]; catecholaminergic polymorphic ventricular tachycardia [106]; cardiomyopathies like dilated [106, 109], hypertrophic [110], and arrhythmogenic right ventricular cardiomyopathy [111]; and metabolic disorders including Barth syndrome [112, 113] and Pompe disease [114]. In addition to providing human-specific models of cardiac disease for known mutations, hiPSC-CMs have been leveraged to validate the effects of novel mutations. For example, the introduction of a novel mutation in the *ALPK3* gene associated with inherited pediatric cardiomyopathy into hiPSC-CMs enabled the confirmation that the specific biallelic mutation was responsible for the phenotype observed *in vivo* [115, 116]. Similarly, genetically edited isogenic hiPSC-CMs were able to confirm that varied clinical

severity of familial dilated cardiomyopathy in a large family could be explained by the convergence of two separate mutations in the *TPM1* and *VCL* genes [106, 109]. Even without prior screening studies to indicate a specific genetic mechanism, the use of patient-derived hiPSC-CMs can capture genetic predispositions to environmental disease triggers [117, 118]. For instance, hiPSC-CMs derived from diabetic patients with different disease severities demonstrated similar susceptibility to dysfunction *in vitro* with cells from the patient with the more severe phenotype being more resistant to pharmacological intervention [117, 119]. Undoubtedly, there is still untapped potential for leveraging hiPSC-CMs to gain additional insight into these and understudied genetic cardiac disorders.

1.3.2. Non-genetic cardiac disease modeling with hiPSC-CMs

Unlike diseases with a causal genetic component, non-genetic cardiac diseases are the confluence of multiple cardiovascular risk factors such as age, environmental exposures, and lifestyle (*e.g.* diet and exercise) superimposed onto complex genetic backgrounds [120, 121]. Without the ability to directly engineer the molecular mechanism of a disease into an hiPSC line, researchers are reliant on inducing disease phenotypes via other means. Among the most prominent examples of this approach are models of ischemic heart disease [122-125]. Clinically, ischemic heart disease occurs due to reduced blood flow and a subsequent imbalance between oxygen supply and demand [126], which can be replicated by exposing hiPSC-CMs to hypoxic conditions [122-125]. *In vitro* models of ischemia and ischemia-reperfusion injuries have successfully recapitulated structural [123-125], functional [122, 125], transcriptomic [122, 124] , and proteomic [124] effects of acute hypoxic injury in line with known *in vivo* effects. These models have also been extended to demonstrate the viability of *in vitro* ischemia models as drug discovery tools that can overcome the limitations of animal models in predicting therapeutic efficacy. Specifically, cardiac organoids exposed to hypoxic conditions have shown increased sensitivity to doxorubicin-induced cardiotoxicity [122] while metabolically matured hiPSC-CMs co-exposed to hypoxia and a known necroptosis inhibitor (necrostatin-1) were better protected from hypoxic injury than

untreated controls, mimicking its known cardioprotective effect [123]. Other stress stimuli have also been used to generate disease phenotypes *in vitro*, including chronic adrenergic stimulation for cardiac hypertrophy [127] and chronic intermittent tachypacing for arrhythmia formation [128].

Metabolic disorders have also begun to be modeled using hiPSC-CMs with Type 2 diabetes being a common example [119, 129-131] due to its correlation with cardiovascular disease generally [132]. Defined by abnormal glucose metabolism due to impaired insulin release and acquired insulin resistance [133], supplementation of cell culture media can be used to mirror a diabetic environment *in vitro [129, 130]*. For instance, culturing hiPSC-CMs in media containing high concentrations of palmitate has been shown to induce insulin resistance as well as contractile dysfunction associated with diabetic cardiomyopathy [131]. The addition of high glucose concentrations, in addition to endothelin-1 and cortisol, into the culture medium of hiPSC-CMs similarly increased lipid accumulation, oxidative stress, brain natriuretic peptide release, and calcium dysregulation [119]. The removal of media components has also been shown to be an effective approach for modeling cardiac disease using hiPSC-CMs. Ten-day-long culture of hiSPC-CMs in media without glucose has been found to generate hiPSC-CMs with a phenotype that mimics ischemic heart disease, with hiPSC-CMs possessing prolonged action potentials and dysregulated calcium handling [134]. Ultimately, a better understanding of the pathogenic cues that contribute to cardiac diseases will serve to advance the ability of hiPSC-CMs to model complex, non-genetic disorders *in vitro* and assist in the development of next-generation therapeutics for their treatment.

1.4. Project objectives and specific aims

Given the vital role of preclinical models for studying cardiac toxicity and disease, there remains a critical need to understand their underlying causes as well as to develop methods with which to prevent and treat them. I hypothesized that risk from chemical exposures and pathophysiology can be identified by predictive *in vitro* models of cardiac physiology leveraging hiPSC-CMs as a source of donor- and

chamber-specific cardiomyocytes. I employed a multipronged approach across a range of contexts of use including both cardiotoxicity assessment and disease modeling split across three Specific Aims. Toward that end, the following is a description of our progress towards the development and application of fit-for-purpose hiPSC-CM-based *in vitro* models for (1) performing human specific risk assessment for acute proarrhythmic cardiotoxicity; (2) the prevention of chronic, anthracycline-induced cardiotoxicity; and (3) the development of a novel *in vitro* model of Wolff-Parkinson-White (WPW) syndrome.

1.4.1. Specific Aim 1: Enhance the assessment of acute, proarrhythmic ventricular cardiotoxicity in response to pharmaceutical chemicals.

In Aim 1, we hypothesized that the *in vivo* risks associated with known proarrhythmic compounds could be recapitulated by hiPSC-CMs cultured in physiologically relevant, three-dimensional microtissues. We measured concentration-responses for four representative test compounds all known to inhibit the same ion channel (hERG) but that possess a range of proarrhythmic risk profiles *in vivo* (quinidine, cisapride, ranolazine, and verapamil). Leveraging this rich data set and computational modeling, we developed a robust method for quantifying physiologically relevant concentrations (*i.e.* point-of-departure) that cause physiologically relevant changes in action potentials. We subsequently used these estimates in combination with physiologically based pharmacokinetic modeling to perform *in vitro* to *in vivo* extrapolation, directly predicting *in vivo* risk. We found good agreement between our *in vitro* predictions and the known proarrhythmic profiles of these compounds, providing a methodological foundation for using this platform to mitigate proarrhythmic risk during drug development.

1.4.2. Specific Aim 2: Evaluate therapeutic approaches for the prevention of chemotherapy-induced cardiotoxicity from long-term drug exposures.

In Aim 2, we hypothesized that, in addition to predicting chronic anthracycline-induced cardiotoxicity, that hiPSC-CM-based models would enable the prediction of potentially protective therapies for its prevention. We demonstrated that both hiPSC-CMs cultured in both two and three dimensions responded in time- and concentration-dependent manners to exposure to the prototypical anthracycline,

doxorubicin, reducing hiPSC-CM viability and function *in vitro*. Building upon our findings, we investigated the effects of cotreatment with both existing heart failure therapies and novel interventions to prevent cardiotoxicity. The long-term goal of this work is to develop toxicity-mitigating co-therapies to enhance the health and long-term quality of life of cancer survivors.

1.4.3. Specific Aim 3: Develop an *in vitro* model of triggered atrial arrhythmias in Wolff-Parkinson-White Syndrome.

In Aim 3, we hypothesized that hiPSC-CM-based engineered cardiac tissues generated from hiPSC-CMs derived from a donor with Wolff-Parkinson-White (WPW) Syndrome would be able to recapitulate relevant disease etiology and electrophysiology *in vitro* to investigate the effects of physiological stressors on the initiation of arrhythmias associated with WPW syndrome. Toward this end, we successfully generated a novel WPW hiPSC line and were able to successfully differentiate both ventricular and atrial cardiomyocytes. We further observed phenotypic and electrophysiological shifts in atrial cardiomyocytes derived from WPW hiPSCs that suggest potentially proarrhythmic changes compared to control cell lines. This works provides a foundational model with which to continue to explore the mechanisms that drive the initiation of arrhythmias in WPW patients.

1.5. References

1. CBO, *Research and Development in the Pharmaceutical Industry*. 2021.
2. May, E., et al., *Unleash AI's potential Measuring the return from pharmaceutical innovation*. 2023, Deloitte.
3. Kola, I. and J. Landis, *Can the pharmaceutical industry reduce attrition rates?* Nature reviews Drug discovery, 2004. **3**(8): p. 711-716.
4. DiMasi, J.A., H.G. Grabowski, and R.W. Hansen, *Innovation in the pharmaceutical industry: new estimates of R&D costs.* Journal of health economics, 2016. **47**: p. 20-33.

5. Fermini, B., S.T. Coyne, and K.P. Coyne, *Clinical trials in a dish: a perspective on the coming revolution in drug development.* SLAS DISCOVERY: Advancing Life Sciences R&D, 2018. **23**(8): p. 765-776.

6. Martin, S.S., et al., *2024 heart disease and stroke statistics: a report of US and global data from the American Heart Association.* Circulation, 2024. **149**(8): p. e347-e913.

7. Laverty, H., et al., *How can we improve our understanding of cardiovascular safety liabilities to develop safer medicines?* British journal of pharmacology, 2011. **163**(4): p. 675-693.

8. Onakpoya, I.J., C.J. Heneghan, and J.K. Aronson, *Post-marketing withdrawal of 462 medicinal products because of adverse drug reactions: a systematic review of the world literature.* BMC medicine, 2016. **14**(1): p. 1-11.

9. Florido, R., et al., *Cardiovascular disease risk among cancer survivors: the atherosclerosis risk in communities (ARIC) study.* Journal of the American College of Cardiology, 2022. **80**(1): p. 22-32.

10. Sturgeon, K.M., et al., *A population-based study of cardiovascular disease mortality risk in US cancer patients.* European heart journal, 2019. **40**(48): p. 3889-3897.

11. Ferdinandy, P., et al., *Definition of hidden drug cardiotoxicity: paradigm change in cardiac safety testing and its clinical implications.* European heart journal, 2019. **40**(22): p. 1771-1777.

12. Lau, E.S., et al., *Cardiovascular risk factors are associated with future cancer.* Cardio Oncology, 2021. **3**(1): p. 48-58.

13. Wilcox, N.S., et al., *Cardiovascular disease and cancer: shared risk factors and mechanisms.* Nature Reviews Cardiology, 2024. **21**(9): p. 617-631.

14. Hamdam, J., et al., *Safety pharmacology—Current and emerging concepts.* Toxicology and applied pharmacology, 2013. **273**(2): p. 229-241.

15. Fordyce, C.B., et al., *Cardiovascular drug development: is it dead or just hibernating?* Journal of the American College of Cardiology, 2015. **65**(15): p. 1567-1582.

16. Hwang, T.J., et al., *Temporal trends and factors associated with cardiovascular drug development, 1990 to 2012.* JACC: Basic to Translational Science, 2016. **1**(5): p. 301-308.

17. Gintant, G., P.T. Sager, and N. Stockbridge, *Evolution of strategies to improve preclinical cardiac safety testing.* Nature Reviews Drug Discovery, 2016. **15**(7): p. 457.

18. Darpo, B., *The thorough QT/QTc study 4 years after the implementation of the ICH E14 guidance.* British journal of pharmacology, 2010. **159**(1): p. 49-57.

19. ICH, *The clinical evaluation of QT/QTc interval prolongation and proarrhythmic potential for non-antiarrhythmic drugs E14*. 2006.

20. Priest, B., I.M. Bell, and M. Garcia, *Role of hERG potassium channel assays in drug development.* Channels, 2008. **2**(2): p. 87-93.

21. Qu, Z., et al., *Early afterdepolarizations in cardiac myocytes: beyond reduced repolarization reserve.* Cardiovascular research, 2013. **99**(1): p. 6-15.

22. Magdy, T., et al., *Human induced pluripotent stem cell (hiPSC)-derived cells to assess drug cardiotoxicity: opportunities and problems.* Annual review of pharmacology and toxicology, 2018. **58**: p. 83-103.

23. ICH, *The non-clinical evaluation of the potential for delayed ventricular repolarization (Qt Interval Prolongation) by human pharmaceuticals*. 2005.

24. Mercola, M., A. Colas, and E. Willems, *Induced pluripotent stem cells in cardiovascular drug discovery.* Circulation research, 2013. **112**(3): p. 534-548.

25. Nerbonne, J.M., et al., *Genetic manipulation of cardiac K+ channel function in mice: what have we learned, and where do we go from here?* Circulation research, 2001. **89**(11): p. 944-956.

26. Sallam, K., et al., *Finding the rhythm of sudden cardiac death: new opportunities using induced pluripotent stem cell–derived cardiomyocytes.* Circulation research, 2015. **116**(12): p. 1989-2004.

27. O'Hara, T. and Y. Rudy, *Quantitative comparison of cardiac ventricular myocyte electrophysiology and response to drugs in human and nonhuman species.* American Journal of Physiology-Heart and Circulatory Physiology, 2012. **302**(5): p. H1023-H1030.

28. Baczkó, I., et al., *Transgenic rabbit models in proarrhythmia research.* Frontiers in Pharmacology, 2020. **11**: p. 853.

29. Baillie, T.A. and A.E. Rettie, *Role of biotransformation in drug-induced toxicity: influence of intra- and inter-species differences in drug metabolism.* Drug metabolism and pharmacokinetics, 2011. **26**(1): p. 15-29.

30. Törnqvist, E., et al., *Strategic focus on 3R principles reveals major reductions in the use of animals in pharmaceutical toxicity testing.* PloS one, 2014. **9**(7): p. e101638.

31. Chaudhary, K.W., et al., *An overview of drug-induced sodium channel blockade and changes in cardiac conduction: Implications for drug safety.* Clinical and Translational Science, 2024. **17**(12): p. e70098.

32. Olson, H., et al., *Concordance of the toxicity of pharmaceuticals in humans and in animals.* Regulatory Toxicology and Pharmacology, 2000. **32**(1): p. 56-67.

33. Oren, O., et al., *Cardiovascular safety assessment in cancer drug development.* Journal of the American Heart Association, 2021. **10**(24): p. e024033.

34. Gintant, G., *An evaluation of hERG current assay performance: translating preclinical safety studies to clinical QT prolongation.* Pharmacology & therapeutics, 2011. **129**(2): p. 109-119.

35. Daley, M.C., et al., *Beyond pharmaceuticals: Fit-for-purpose new approach methodologies for environmental cardiotoxicity testing.* ALTEX-Alternatives to animal experimentation, 2023. **40**(1): p. 103-116.

36. Appels, Y., et al., *Cardiotoxicity Beyond Cardiomyocytes—Focus on the Role of Cardiac Fibroblasts and Endothelial Cells.* Heart, Lung and Circulation, 2025.

37. Mamoshina, P., B. Rodriguez, and A. Bueno-Orovio, *Toward a broader view of mechanisms of drug cardiotoxicity.* Cell Reports Medicine, 2021. **2**(3).

38. ICH, *Safety pharmacology studies for human pharmaceuticals S7A*. 2001. p. 36791-36792.

39. Porsolt, R.D., S. Picard, and P. Lacroix, *International safety pharmacology guidelines (ICH S7A and S7B): where do we go from here?* 2005, Wiley Online Library. p. 83-89.

40. van Doorn, E.C., et al., *Preclinical models of cardiac disease: a comprehensive overview for clinical scientists.* Cardiovascular Engineering and Technology, 2024. **15**(2): p. 232-249.

41. McGonigle, P. and B. Ruggeri, *Animal models of human disease: challenges in enabling translation.* Biochemical pharmacology, 2014. **87**(1): p. 162-171.

42. Schwartz, P.J., *1970–2020: 50 years of research on the long QT syndrome—from almost zero knowledge to precision medicine.* European Heart Journal, 2021. **42**(11): p. 1063-1072.

43. Krahn, A.D., et al., *Congenital long QT syndrome.* Clinical Electrophysiology, 2022. **8**(5): p. 687-706.

44. Salama, G. and B. London, *Mouse models of long QT syndrome.* The Journal of physiology, 2007. **578**(1): p. 43-53.

45. Brunner, M., et al., *In vivo gene transfer of Kv1. 5 normalizes action potential duration and shortens QT interval in mice with long QT phenotype.* American Journal of Physiology-Heart and Circulatory Physiology, 2003. **285**(1): p. H194-H203.

46. Milani-Nejad, N. and P.M. Janssen, *Small and large animal models in cardiac contraction research: advantages and disadvantages.* Pharmacology & therapeutics, 2014. **141**(3): p. 235-249.

47. Bulfield, G., et al., *X chromosome-linked muscular dystrophy (mdx) in the mouse.* Proceedings of the National Academy of Sciences, 1984. **81**(4): p. 1189-1192.

48. Delfín, D.A., et al., *Cardiomyopathy in the dystrophin/utrophin-deficient mouse model of severe muscular dystrophy is characterized by dysregulation of matrix metalloproteinases.* Neuromuscular Disorders, 2012. **22**(11): p. 1006-1014.

49. Halapas, A., et al., *In vivo models for heart failure research.* in vivo, 2008. **22**(6): p. 767-780.

50. Truskey, G.A., *Human microphysiological systems and organoids as in vitro models for toxicological studies.* Frontiers in public health, 2018. **6**: p. 185.

51. Zuppinger, C., *3D cardiac cell culture: a critical review of current technologies and applications.* Frontiers in cardiovascular medicine, 2019. **6**: p. 87.

52. Lippi, M., et al., *Human cell modeling for cardiovascular diseases.* International Journal of Molecular Sciences, 2020. **21**(17): p. 6388.

53. Parrotta, E.I., et al., *Stem cells: the game changers of human cardiac disease modelling and regenerative medicine.* International journal of molecular sciences, 2019. **20**(22): p. 5760.

54. Buikema, J.W., et al., *Wnt activation and reduced cell-cell contact synergistically induce massive expansion of functional human iPSC-derived cardiomyocytes.* Cell stem cell, 2020. **27**(1): p. 50-63. e5.

55. Maas, R.G., et al., *Massive expansion and cryopreservation of functional human induced pluripotent stem cell-derived cardiomyocytes.* STAR protocols, 2021. **2**(1): p. 100334.

56. Gintant, G., et al., *Use of Human Induced Pluripotent Stem Cell–Derived Cardiomyocytes in Preclinical Cancer Drug Cardiotoxicity Testing: A Scientific Statement From the American Heart Association.* Circulation research, 2019. **125**(10): p. e75-e92.

57. Pesl, M., et al., *Phenotypic assays for analyses of pluripotent stem cell–derived cardiomyocytes.* Journal of Molecular Recognition, 2017. **30**(6): p. e2602.

58. Yang, X., et al., *Use of human iPSC-CMs in nonclinical regulatory studies for cardiac safety assessment.* Toxicological Sciences, 2022. **190**(2): p. 117-126.

59. Blinova, K., et al., *International multisite study of human-induced pluripotent stem cell-derived cardiomyocytes for drug proarrhythmic potential assessment.* Cell reports, 2018. **24**(13): p. 3582-3592.

60. Grimm, F.A., et al., *High-content assay multiplexing for toxicity screening in induced pluripotent stem cell-derived cardiomyocytes and hepatocytes.* Assay and drug development technologies, 2015. **13**(9): p. 529-546.

61. Pfeiffer-Kaushik, E.R., et al., *Electrophysiological characterization of drug response in hSC-derived cardiomyocytes using voltage-sensitive optical platforms.* Journal of pharmacological and toxicological methods, 2019. **99**: p. 106612.

62. Kofron, C., et al., *A Predictive in Vitro Risk Assessment Platform for Pro-Arrhythmic Toxicity Using Human 3D Cardiac Microtissues.* Scientific Reports, 2021. **11**: p. 1-16.

63. Feric, N.T., et al., *Engineered cardiac tissues generated in the Biowire II: a platform for human-based drug discovery.* Toxicological Sciences, 2019. **172**(1): p. 89-97.

64. Pointon, A., et al., *From the cover: high-throughput imaging of cardiac microtissues for the assessment of cardiac contraction during drug discovery.* Toxicological Sciences, 2017. **155**(2): p. 444-457.

65. Archer, C.R., et al., *Characterization and validation of a human 3D cardiac microtissue for the assessment of changes in cardiac pathology.* Scientific reports, 2018. **8**(1): p. 1-15.

66. Zhao, Y., et al., *Towards chamber specific heart-on-a-chip for drug testing applications.* Advanced Drug Delivery Reviews, 2020. **165-166**: p. 60-76.

67. Robertson, C., D.D. Tran, and S.C. George, *Concise review: maturation phases of human pluripotent stem cell-derived cardiomyocytes.* Stem cells, 2013. **31**(5): p. 829-837.

68. Denning, C., et al., *Cardiomyocytes from human pluripotent stem cells: From laboratory curiosity to industrial biomedical platform.* Biochimica et Biophysica Acta (BBA)-Molecular Cell Research, 2016. **1863**(7): p. 1728-1748.

69. Scuderi, G.J. and J. Butcher, *Naturally engineered maturation of cardiomyocytes.* Frontiers in cell and developmental biology, 2017. **5**: p. 50.

70. Burnett, S.D., et al., *Population-based toxicity screening in human induced pluripotent stem cell-derived cardiomyocytes.* Toxicology and applied pharmacology, 2019. **381**: p. 114711.

71. Burnett, S.D., et al., *Cardiotoxicity Hazard and Risk Characterization of ToxCast Chemicals Using Human Induced Pluripotent Stem Cell-Derived Cardiomyocytes from Multiple Donors.* Chemical Research in Toxicology, 2021. **34**(9): p. 2110-2124.

72. Blanchette, A.D., et al., *A tiered approach to population-based in vitro testing for cardiotoxicity: Balancing estimates of potency and variability.* Journal of Pharmacological and Toxicological Methods, 2022: p. 107154.

73. Burridge, P.W., et al., *Human induced pluripotent stem cell–derived cardiomyocytes recapitulate the predilection of breast cancer patients to doxorubicin-induced cardiotoxicity.* Nature medicine, 2016. **22**(5): p. 547.

74. Schaniel, C., et al., *A library of induced pluripotent stem cells from clinically well-characterized, diverse healthy human individuals.* Stem Cell Reports, 2021. **16**(12): p. 3036-3049.

75. Neavin, D.R., et al., *A village in a dish model system for population-scale hiPSC studies.* Nature Communications, 2023. **14**(1): p. 3240.

76. Frommeyer, G. and L. Eckardt, *Drug-induced proarrhythmia: risk factors and electrophysiological mechanisms.* Nature Reviews Cardiology, 2016. **13**(1): p. 36-47.

77. da Rocha, A.M., et al., *Detection of Drug-Induced Torsades de Pointes Arrhythmia Mechanisms Using hiPSC-CM Syncytial Monolayers in a High-Throughput Screening Voltage Sensitive Dye Assay.* Toxicological Sciences, 2020. **173**(2): p. 402-415.

78. Chubinskiy-Nadezhdin, V.I., et al., *Single ion channel recording in 3D culture of stem cells using patch-clamp technique.* Biochemical and biophysical research communications, 2022. **619**: p. 22-26.

79. Kussauer, S., R. David, and H. Lemcke, *hiPSCs derived cardiac cells for drug and toxicity screening and disease modeling: what micro-electrode-array analyses can tell us.* Cells, 2019. **8**(11): p. 1331.

80. Buzsáki, G., C.A. Anastassiou, and C. Koch, *The origin of extracellular fields and currents—EEG, ECoG, LFP and spikes.* Nature reviews neuroscience, 2012. **13**(6): p. 407-420.

81. Halbach, M., et al., *Estimation of action potential changes from field potential recordings in multicellular mouse cardiac myocyte cultures.* Cellular Physiology and Biochemistry, 2003. **13**(5): p. 271-284.

82. Wan, Z., et al., *Bridging the Gap Between hiPSC-CMs Cardiotoxicity Assessment and Clinical LVEF Decline Risk: A Case Study of 21 Tyrosine Kinase Inhibitors.* Pharmaceuticals, 2025. **18**(4): p. 450.

83. Yang, B. and T. Papoian, *Preclinical approaches to assess potential kinase inhibitor-induced cardiac toxicity: Past, present and future.* Journal of Applied Toxicology, 2018. **38**(6): p. 790-800.

84. Lamore, S.D., et al., *Cardiovascular toxicity induced by kinase inhibitors: mechanisms and preclinical approaches.* Chemical Research in Toxicology, 2019. **33**(1): p. 125-136.

85. Peters, M.F., et al., *Human stem cell-derived cardiomyocytes in cellular impedance assays: bringing cardiotoxicity screening to the front line.* Cardiovascular Toxicology, 2015. **15**: p. 127-139.

86. Koci, B., et al., *An impedance-based approach using human iPSC-derived cardiomyocytes significantly improves in vitro prediction of in vivo cardiotox liabilities.* Toxicology and applied pharmacology, 2017. **329**: p. 121-127.

87. Ke, N., et al., *The xCELLigence System for Real-Time and Label-Free Monitoring of Cell Viability*, in *Mammalian Cell Viability: Methods and Protocols*, M.J. Stoddart, Editor. 2011, Humana Press: Totowa, NJ. p. 33-43.

88. Sala, L., et al., *MUSCLEMOTION: a versatile open software tool to quantify cardiomyocyte and cardiac muscle contraction in vitro and in vivo.* Circulation research, 2018. **122**(3): p. e5-e16.

89. Kobeissi, H., et al., *MicroBundleCompute: Automated segmentation, tracking, and analysis of subdomain deformation in cardiac microbundles.* arXiv preprint arXiv:2308.04610, 2023.

90. Van Meer, B.J., et al., *Simultaneous measurement of excitation-contraction coupling parameters identifies mechanisms underlying contractile responses of hiPSC-derived cardiomyocytes.* Nature Communications, 2019. **10**(1): p. 4325.

91. Agarwal, A., et al., *Microfluidic heart on a chip for higher throughput pharmacological studies.* Lab on a Chip, 2013. **13**(18): p. 3599-3608.

92. Cerignoli, F., et al., *High throughput measurement of Ca2+ dynamics for drug risk assessment in human stem cell-derived cardiomyocytes by kinetic image cytometry.* Journal of pharmacological and toxicological methods, 2012. **66**(3): p. 246-256.

93. Blanchette, A.D., et al., *Thorough QT/QTc in a dish: an in vitro human model that accurately predicts clinical concentration-QTc relationships.* Clinical Pharmacology & Therapeutics, 2019. **105**(5): p. 1175-1186.

94. Dempsey, G.T., et al., *Cardiotoxicity screening with simultaneous optogenetic pacing, voltage imaging and calcium imaging.* Journal of pharmacological and toxicological methods, 2016. **81**: p. 240-250.

95. Bers, D.M., *Cardiac excitation–contraction coupling.* Nature, 2002. **415**(6868): p. 198-205.

96. Hayakawa, T., et al., *Image-based evaluation of contraction–relaxation kinetics of human-induced pluripotent stem cell-derived cardiomyocytes: Correlation and complementarity with extracellular electrophysiology.* Journal of molecular and cellular cardiology, 2014. **77**: p. 178-191.

97. Wheelwright, M., et al., *Investigation of human iPSC-derived cardiac myocyte functional maturation by single cell traction force microscopy.* PLoS One, 2018. **13**(4): p. e0194909.

98. Sasaki, D., et al., *Contractile force measurement of human induced pluripotent stem cell-derived cardiac cell sheet-tissue.* PloS one, 2018. **13**(5): p. e0198026.

99. Zhang, D., et al., *Tissue-engineered cardiac patch for advanced functional maturation of human ESC-derived cardiomyocytes.* Biomaterials, 2013. **34**(23): p. 5813-5820.

100. Minor, A.J. and K.L. Coulombe, *Stimulating Calcium Handling in hiPSC-Derived Engineered Cardiac Tissues Enhances Force Production.* Stem Cells Translational Medicine, 2022. **11**(1): p. 97-106.

101. Meyer, T., M. Tiburcy, and W.-H. Zimmermann, *Cardiac macrotissues-on-a-plate models for phenotypic drug screens.* Advanced Drug Delivery Reviews, 2019. **140**: p. 93-100.

102. Adamcová, M., et al., *In vitro and in vivo examination of cardiac troponins as biochemical markers of drug-induced cardiotoxicity.* Toxicology, 2007. **237**(1-3): p. 218-228.

103. Cardinale, D., et al., *Using biomarkers to predict and to prevent cardiotoxicity of cancer therapy.* Expert review of molecular diagnostics, 2017. **17**(3): p. 245-256.

104. Moffat, J.G., et al., *Opportunities and challenges in phenotypic drug discovery: an industry perspective.* Nature reviews Drug discovery, 2017. **16**(8): p. 531-543.

105. Chen, I.Y., E. Matsa, and J.C. Wu, *Induced pluripotent stem cells: at the heart of cardiovascular precision medicine.* Nature Reviews Cardiology, 2016. **13**(6): p. 333.

106. Brink, L., et al., *Inherited cardiac diseases, pluripotent stem cells, and genome editing combined—the past, present, and future.* Stem Cells, 2020. **38**(2): p. 174-186.

107. Giacomelli, E., C. Mummery, and M. Bellin, *Human heart disease: lessons from human pluripotent stem cell-derived cardiomyocytes.* Cellular and Molecular Life Sciences, 2017. **74**: p. 3711-3739.

108. Moretti, A., et al., *Patient-specific induced pluripotent stem-cell models for long-QT syndrome.* New England Journal of Medicine, 2010. **363**(15): p. 1397-1409.

109. Deacon, D.C., et al., *Combinatorial interactions of genetic variants in human cardiomyopathy.* Nature biomedical engineering, 2019. **3**(2): p. 147-157.

110. Han, L., et al., *Study familial hypertrophic cardiomyopathy using patient-specific induced pluripotent stem cells.* Cardiovascular research, 2014. **104**(2): p. 258-269.

111. Caspi, O., et al., *Modeling of arrhythmogenic right ventricular cardiomyopathy with human induced pluripotent stem cells.* Circulation: Cardiovascular Genetics, 2013. **6**(6): p. 557-568.

112. Wang, G., et al., *Modeling the mitochondrial cardiomyopathy of Barth syndrome with induced pluripotent stem cell and heart-on-chip technologies.* Nature medicine, 2014. **20**(6): p. 616-623.

113. Dudek, J., et al., *Cardiolipin deficiency affects respiratory chain function and organization in an induced pluripotent stem cell model of Barth syndrome.* Stem cell research, 2013. **11**(2): p. 806-819.

114. Huang, H.-P., et al., *Human Pompe disease-induced pluripotent stem cells for pathogenesis modeling, drug testing and disease marker identification.* Human molecular genetics, 2011. **20**(24): p. 4851-4864.

115. Almomani, R., et al., *Biallelic truncating mutations in ALPK3 cause severe pediatric cardiomyopathy.* Journal of the American College of Cardiology, 2016. **67**(5): p. 515-525.

116. Phelan, D.G., et al., *ALPK3-deficient cardiomyocytes generated from patient-derived induced pluripotent stem cells and mutant human embryonic stem cells display abnormal calcium handling and establish that ALPK3 deficiency underlies familial cardiomyopathy.* European heart journal, 2016. **37**(33): p. 2586-2590.

117. Bellin, M. and C.L. Mummery, *Inherited heart disease–what can we expect from the second decade of human i PS cell research?* FEBS letters, 2016. **590**(15): p. 2482-2493.

118. Cambien, F.o. and L. Tiret, *Genetics of cardiovascular diseases: from single mutations to the whole genome.* Circulation, 2007. **116**(15): p. 1714-1724.

119. Drawnel, F.M., et al., *Disease modeling and phenotypic drug screening for diabetic cardiomyopathy using human induced pluripotent stem cells.* Cell reports, 2014. **9**(3): p. 810-820.

120. Kartiosuo, N., et al., *Cardiovascular risk factors in childhood and adulthood and cardiovascular disease in middle age.* JAMA Network Open, 2024. **7**(6): p. e2418148-e2418148.

121. López-Bueno, R., et al., *Global prevalence of cardiovascular risk factors based on the Life's Essential 8 score: an overview of systematic reviews and meta-analysis.* Cardiovascular Research, 2024. **120**(1): p. 13-33.

122. Richards, D.J., et al., *Human cardiac organoids for the modelling of myocardial infarction and drug cardiotoxicity.* Nature Biomedical Engineering, 2020. **4**(4): p. 446-462.

123. Peters, M.C., et al., *Metabolic maturation increases susceptibility to hypoxia-induced damage in human iPSC-derived cardiomyocytes.* Stem cells translational medicine, 2022. **11**(10): p. 1040-1051.

124. Sebastião, M.J., et al., *Bioreactor-based 3D human myocardial ischemia/reperfusion in vitro model: a novel tool to unveil key paracrine factors upon acute myocardial infarction.* Translational Research, 2020. **215**: p. 57-74.

125. Häkli, M., et al., *Human induced pluripotent stem cell-based platform for modeling cardiac ischemia.* Scientific reports, 2021. **11**(1): p. 4153.

126. Jensen, R.V., M.V. Hjortbak, and H.E. Bøtker. *Ischemic heart disease: an update*. in *Seminars in nuclear medicine*. 2020. Elsevier.

127. Tiburcy, M., et al., *Defined engineered human myocardium with advanced maturation for applications in heart failure modeling and repair.* Circulation, 2017. **135**(19): p. 1832-1847.

128. Lemme, M., et al., *Chronic intermittent tachypacing by an optogenetic approach induces arrhythmia vulnerability in human engineered heart tissue.* Cardiovascular research, 2020. **116**(8): p. 1487-1499.

129. Granéli, C., et al., *Diabetic cardiomyopathy modelling using induced pluripotent stem cell derived cardiomyocytes: recent advances and emerging models.* Stem cell reviews and reports, 2019. **15**: p. 13-22.

130. Geraets, I.M., et al., *Human embryonic stem cell-derived cardiomyocytes as an in vitro model to study cardiac insulin resistance.* Biochimica et Biophysica Acta (BBA)-Molecular Basis of Disease, 2018. **1864**(5): p. 1960-1967.

131. Liu, Y., et al., *Palmitate-induced vacuolar-type H+-ATPase inhibition feeds forward into insulin resistance and contractile dysfunction.* Diabetes, 2017. **66**(6): p. 1521-1534.

132. Wang, J., et al., *Causes and characteristics of diabetic cardiomyopathy.* The Review of Diabetic Studies, 2006. **3**(3): p. 108.

133. Galicia-Garcia, U., et al., *Pathophysiology of type 2 diabetes mellitus.* International journal of molecular sciences, 2020. **21**(17): p. 6275.

134. Davis, J., et al., *In vitro model of ischemic heart failure using human induced pluripotent stem cell–derived cardiomyocytes.* JCI insight, 2021. **6**(10): p. e134368.

Chapter 2 - *In vitro* to *in vivo* extrapolation from 3D hiPSC-derived cardiac microtissues and physiologically based pharmacokinetic modeling to inform next-generation arrhythmia risk assessment

Reproduced with permission from Daley, M.C., Moreau, M. *et al "*In vitro to in vivo extrapolation from 3D hiPSC-derived cardiac microtissues and physiologically based pharmacokinetic modeling to inform next-generation arrhythmia risk assessment", *Toxicological Sciences*, Volume 201, Issue 1, September 2024, Pages 145–157, https://doi.org/10.1093/toxsci/kfae079

2.1. Abstract

Proarrhythmic cardiotoxicity remains a substantial barrier to drug development as well as a major global health challenge. *In vitro* human pluripotent stem cell-based new approach methodologies have been increasingly proposed and employed as alternatives to existing *in vitro* and *in vivo* models that do not accurately recapitulate human cardiac electrophysiology or cardiotoxicity risk. In this study, we expanded the capacity of our previously established three-dimensional human cardiac microtissue model to perform quantitative risk assessment by combining it with a physiologically based pharmacokinetic model, allowing a direct comparison of potentially harmful concentrations predicted *in vitro* to *in vivo* therapeutic levels. This approach enabled the measurement of concentration responses and margins of exposure for two physiologically relevant metrics of proarrhythmic risk (*i.e.*, action potential duration and triangulation assessed by optical mapping) across concentrations spanning three orders of magnitude. The combination of both metrics enabled accurate proarrhythmic risk assessment of four compounds with a range of known proarrhythmic risk profiles (*i.e.,* quinidine, cisapride, ranolazine, and verapamil) and demonstrated relative potency profiles according to close agreement with their known clinical effects. Action potential triangulation was found to be a more sensitive metric for predicting proarrhythmic risk

associated with the primary mechanism of concern for pharmaceutical-induced fatal ventricular arrhythmias, delayed cardiac repolarization due to inhibition of the rapid delayed rectifier potassium channel, or hERG channel. This study advances human induced pluripotent stem cell-based three-dimensional cardiac tissue models as new approach methodologies that enable *in vitro* proarrhythmic risk assessment with high precision of quantitative metrics for understanding clinically relevant cardiotoxicity.

2.2. Introduction

Both pharmaceutical- and pollutant-induced cardiotoxicity remain significant contributors to the prevalence and severity of cardiovascular disease worldwide. Cardiotoxicity is responsible for approximately 14% of safety-related post-market withdrawals of pharmaceuticals and has been associated with nearly 2,000 marketed drugs [1, 2]. Similarly, between 7 and 23% of cardiovascular disease has been attributed to environmental factors even as the cardiotoxicity of thousands of environmental chemicals remains underexamined [3, 4].

Traditionally, cardiotoxicity assessment has depended heavily on *in vivo* animal tests including acute and chronic studies that assess functional (arterial blood pressure, heart rate, electrophysiology, and cardiac contractility) and structural (morphologic, hematologic, and biochemical endpoints) liabilities [5]. Animal-based tests are costly, time-consuming, and may not accurately predict human cardiotoxicity due to inter-species physiological differences, particularly those related to cardiac electrophysiology such as ion channel expression [6-9]. Moreover, the large doses used in animal experiments and differences in pharmacokinetic parameters lead to tissue-level concentrations that are often not reflective of human therapeutic concentrations. These limitations, paired with growing ethical pressure to implement the 3Rs in toxicology, have increasingly led regulatory agencies to promote alternatives to animal models, especially for detecting cardiac arrhythmias, which remain among the primary manifestations of cardiotoxicity [2, 10-14].

Current United States Food and Drug Administration (FDA) guidelines for proarrhythmia testing complement traditional *in vivo* proarrhythmia assessment with additional *in vitro* testing via the functional I_{Kr}, or hERG, assay [15, 16]. This test examines a compound's ability to bind to or inhibit the rapid delayed rectifier potassium channel, which is primarily responsible for the late-stage repolarization of cardiomyocytes [17]. Inhibition of this channel leads to both action potential and QT interval prolongation as well as potentially life-threating ventricular arrhythmias [16]. The functional I_{Kr} assay is effective at identifying targeted channel blockade but does not account for multiple ion channels and their summative role in causing QT prolongation. Additionally, drug binding to the I_{Kr} channel is dependent on channel state (*i.e.*, opened, closed, or inactivated) and simple voltage clamp protocols may overestimate I_{Kr} block and QT prolongation [18-20]. In fact, when predicting proarrhythmic effects due to I_{kr} current inhibition, the I_{Kr} assay alone is only about 70-80% accurate [21].

Stem cell-based models have emerged as the next phase of new approach methodologies (NAMs) for *in vitro* cardiotoxicity assays [2, 16, 22-24]. These models typically utilize human induced pluripotent stem cell-derived cardiomyocytes (hiPSC-CMs) to holistically recapitulate human cardiac physiology *in vitro* through an array of cell culture systems (such as monolayers, spheroids or microtissues, engineered tissues, and microphysiological systems) to investigate diverse modes of cardiotoxicity. hiPSC-CM-based cardiotoxicity data are increasingly included in regulatory applications to the FDA for both proarrhythmic and non-proarrhythmic safety assessment [25]. An ongoing challenge has been to quantitatively compare bioactivity levels seen *in vitro* to real-world exposures. *In vitro* to *in vivo* extrapolation (IVIVE) is an approach that uses pharmacokinetic modeling to estimate human exposures which give rise to concentrations equivalent to the active concentrations measured *in vitro* [26]. Combining advanced *in vitro* models and generalized pharmacokinetic models offers significant promises in bridging the gap between *in vitro* and *in vivo* risk assessment.

The objective of this study was to utilize *in vitro* three-dimensional human cardiac microtissues and pharmacokinetic modeling to predict pharmaceutical-induced arrhythmias and advance next generation proarrhythmic risk assessment via IVIVE. Microtissues formed from hiPSC-CMs, which we previously demonstrated to have reproducible action potentials and physiological proarrhythmic drug responses [27, 28], were used to measure action potential responses to four test compounds (cisapride, ranolazine, quinidine, and verapamil) that inhibit I_{Kr} but span a range of proarrhythmic risks. *In vivo* safety was assessed via margins of exposure (MOEs) to compare *in vitro* and *in vivo* concentrations in the heart, as opposed to plasma, to specifically predict cardiotoxicity. Our data support the idea that combining human-relevant, whole action potential measurements in three-dimensional cardiac microtissues with flexible physiologically based pharmacokinetic (PBPK) modeling enables accurate proarrhythmia risk assessment.

2.3. Materials and methods

2.3.1. Overview of approach

We performed risk assessment by calculating a margin of exposure (MOE) that compared concentrations that caused proarrhythmic effects *in vitro* to human-relevant exposures. *In vitro* PODs were derived from the concentration responses of action potentials acquired via optical mapping three-dimensional human cardiac microtissues, which served as estimates of the effects at equivalent concentrations in the heart *in vivo*. A validated, generalized PBPK model simulating the absorption, distribution, metabolism, and excretion of each compound within the human body enabled the prediction of a human equivalent dose (HED) that results in a heart concentration equal to the *in vitro* POD and subsequent calculation of the MOE via comparison to known therapeutic doses.

2.3.2. Compound selection

Four test compounds were chosen that inhibit ventricular repolarization via the rapid delayed rectifier potassium (I_{Kr}) channel but represent a range of proarrhythmic capacity due to effects on other ion channels as identified by the Comprehensive *in vitro* Proarrhythmia Assay (CiPA) Project [29] (**Table 2.1**). From high to low risk of pharmaceutical-induced arrhythmia these were quinidine, cisapride, ranolazine,

and verapamil. Quinidine, an anti-arrhythmic compound, inhibits sodium channels as its primary mechanism of action but also causes QT prolongation due to off-target I_{Kr} blockade which can greatly increase the risk of ventricular fibrillation [30, 31]. Cisapride, a pro-gastrokinetic compound used for the treatment of nocturnal heartburn, also causes off-target inhibition the I_{Kr} current, resulting in QT prolongation and intermediate risk of ventricular arrhythmia [32]. Ranolazine is used for the treatment of stable angina due to its inhibition of the late sodium current, which reduces its proarrhythmic risk by counteracting the effects of its own I_{Kr} inhibition [16, 33]. Lastly, verapamil is a non-dihydropyridine L-type calcium channel blocker used for the treatment of angina [16, 34]. It possesses a low arrhythmic risk because inhibition of calcium channels in the heart causes action potential shortening that overrides the effects of delayed repolarization by I_{Kr} blockade.

Table 2.1. Chemical properties of selected proarrhythmic compounds.

	Quinidine	Cisapride	Ranolazine	Verapamil
CAS Number	56-54-2	81098-60-4	95635-55-5	52-52-9
Chemical Formula	$C_{2\text{-}}H_{24}N_2O_2$	$C_{23}H_{29}ClFN_3O_4$	$C_{20}H_{33}N_3O_4$	$C_{27}H_{38}N_2O_4$
Molecular Weight (g/mol)	324.42	465.95	427.54	454.61
LogP	3.44	3.3	2.07	3.79
Solubility (mg/mL)	0.14	0.00271	1	0.00394
CiPA Risk Category	High	Intermediate	Low to No	Low to No
Primary Current Affected	Early I_{Na}	I_{Kr}	Late I_{Na}	$I_{Ca\text{-}L}$

2.3.3. hiPSC culture and cardiomyocyte differentiation

Ventricular cardiomyocytes were differentiated from GCaMP6f-expressing human induced pluripotent stem cells (hiPSCs; WTC human male iPSCs, Gladstone Institutes) similarly to previous methods [35] (**Figure 2.1A**). hiPSCs were cultured on 100 mm-diameter tissue culture dishes (Fisher Scientific) coated with 5 μg/mL vitronectin (Thermo Fisher Scientific) and fed daily with Essential 8

medium (Thermo Fisher Scientific) for 4-5 days. Once 80% confluent, hiPSCs were singularized with versene (0.5 M EDTA, 1.1 mM D-glucose; MilliporeSigma) for 4-6 minutes before being seeded onto 12-well plates coated with Geltrex™ (Life Technologies) in Essential 8 medium containing 5 μM ROCK-inhibitor (Y-27632 dihydrochloride, Tocris). When hiPSCs again reached 80% confluence, they were treated with 3.5-4.8μM of a GSK3-inhibitor (CHIR99021, Tocris) for 24 ± 1 hours in cardiac differentiation media with 3 components (CDM3) consisting of a RPMI 1640 basal media (Gibco) supplemented with 213 ug/mL L-ascorbic acid (Sigma) and 500 μg/mL human serum albumin (ScienCell) [36]. Next, hiPSCs were exposed to regular CDM3 until 72 ± 2 hours after the start of differentiation when they were treated with 5 μM IWP2 (Tocris), a small molecule Wnt inhibitor in a 1:1 mixture of fresh and spent CDM3 for 2 days. Beginning on day 5, hiPSCs were fed with regular CDM3 every other day until beating began between days 8 and 10 at which point cells were fed with RPMI 1640 with B27 supplement (Life Technologies) (RPMI/B27). Between days 13-15, hiPSC-derived cardiomyocytes (hiPSC-CMs) were passaged with 0.25% trypsin (Life Technologies) in versene and replated onto another Geltrex™-coated 12-well plate (~0.5M cells/cm^2) in RPMI/B27 supplemented with 10% fetal bovine serum (Life Technologies), 1% penicillin-streptomycin (Sigma), and 5 μM ROCK-inhibitor for 24 hours. hiPSC-CMs were allowed to recover for at least 48 hours in unsupplemented RPMI/B27 before four days of metabolic selection in lactate media comprised of 4 mM sodium L-lactate (Sigma) in glucose- and sodium pyruvate-free DMEM (Gibco) with media exchanges every other day. After metabolic selection, hiPSC-CMs were maintained in RPMI/B27 until incorporation into three-dimensional cardiac microtissues.

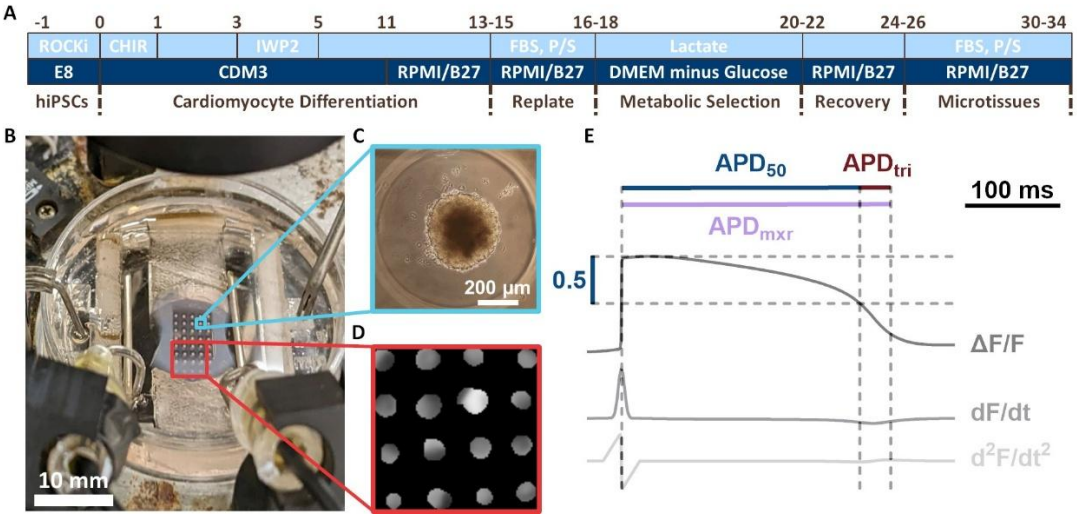

Figure 2.1. Cardiomyocyte differentiation, microtissue generation, and metrics of proarrhythmic risk. (A) human induced pluripotent stem cell-derived cardiomyocytes (hiPSC-CMs) are differentiated using a small-molecule modulation of the Wnt signaling pathway followed by lactate-based metabolic selection and microtissue formation. (B-C) hiPSC-CMs are combined with 5% primary human cardiac fibroblasts in agarose molds with 35-microwells to allow for self-assembly of cardiac microtissues over one week of culture prior to (D) optical mapping. (E) Action potentials are recorded via optical mapping of voltage sensitive dye signals before extraction of key action potential metrics.

2.3.4. Cardiac fibroblast culture and storage

Primary human cardiac fibroblasts (hCFs; Cell Applications) were cultured in DMEM/F12 (Gibco) supplemented with 10% fetal bovine serum, 1% penicillin-streptomycin, and 4 ng/mL basic fibroblast growth factor (Reprocell) with media changes every other day. When hCFs were 80-90% confluent, they were passaged using 0.05% trypsin in versene at a density of 5,000-10,000 cells/cm^2. hCFs were frozen in cell media with 10% dimethyl sulfoxide (DMSO; Thermo Fisher Scientific) and kept overnight in -80 °C before being transferred to liquid nitrogen.

2.3.5. Cardiac microtissue preparation

Agarose microtissue molds were created by pipetting sterile 2% (wt/vol) agarose (Invitrogen) in 1x phosphate buffered saline into sterile 35-microwell negative molds with hemispherical bottoms (Microtissues, Inc). Once cooled, the agarose molds were removed and placed in RPMI/B27 media with 1% penicillin-streptomycin for at least one hour at 37 °C prior to use. Metabolically selected hiPSC-CMs were dissociated and singularized with 0.25% trypsin in versene before being combined with 5% hCFs (P4-P6) prepared directly from thaw. A total of 350,000 cells/mold (10,000 cells/microtissue) were pipetted

into the center of each mold in 100 µL of RPMI/B27 supplemented with 10% fetal bovine serum, 1% penicillin-streptomycin, and 5 µM ROCK-inhibitor (Y-27632 dihydrochloride, Tocris). Cells were allowed to settle via gravity for 30 minutes at 37 °C prior to being covered in media, enabling the self-assembly of spheroidal microtissues. Cardiac microtissues were placed under electrical field stimulation with a 1 Hz, 10 V, 4 ms duration bipolar pulse train (C-Pace EP, IonOptix) and kept under these conditions for the remainder of culture. After 24 hours, cell culture media was changed to media without ROCK-inhibitor and refreshed every other day thereafter. Significant compaction occurred over the first three days of culture with microtissues reaching a final diameter of approximately 350-400 µm (**Figure 2.1B-C**) during which time the cardiac microtissues would begin to beat synchronously under 1 Hz pacing. After 6-8 days, microtissues were ready for downstream use.

2.3.6. Optical mapping of cardiac action potentials and drug treatment

Optical mapping (**Figure 2.1D**) was performed as previously described elsewhere [28]. Briefly, cardiac microtissues were transferred to a 35-mm diameter tissue culture dish on a temperature-controlled chamber containing a solution of (in mM) 140 NaCl, 4.0 KCl, 1.0 $MgCl_2$, 1.25 $CaCL_2$, 0.33 NaH_2PO_4, 5.0 HEPES, 5.0 sodium pyruvate, and 7.5 glucose. Additional solution was gently perfused through the chamber. Microtissues were stained with a 5 µM solution of a voltage-sensitive dye (di-4-ANEPPS; Invitrogen) for 2-3 minutes before washing to remove excess to enable recording of action potential (AP) traces of individual microtissues. A CMOS camera (Ultima-L, Scimedia, Japan) was used to record fluorescent images at 1,000-2,000 frames per second under 0.5 Hz pacing. AP traces were reconstructed from fluorescence intensity data and semi-automated analysis using in-house software enabled measurement of action potential duration (APD) at the maximum rate of repolarization (APD_{mxr}) and APD triangulation (APD_{tri}), which is defined as APD_{mxr} minus APD at 50% repolarization (APD_{50}) (**Figure 2.1E**) [28].

Multiple baseline recordings were acquired prior to drug treatment to ensure a stable baseline prior to drug screening. Stock solutions of cisapride, ranolazine, quinidine, and verapamil were prepared in DMSO and diluted in optical mapping solution to the desired concentrations. Solutions were supplemented with additional DMSO to achieve a final DMSO concentration of 0.1%, as needed. Drug-containing solution was perfused at a rate of 3 mL/min for 5 minutes using a programmable syringe pump (World Precision Instruments) followed by an additional 10-minute equilibration time to allow for drug diffusion into the cardiac microtissues. AP responses were recorded after exposure to six sequentially increasing concentrations on a half-log scale covering three orders of magnitude. For each compound, cardiotoxicity data was collected for three separate molds from two or three cardiac differentiations. APD_{mxr} and APD_{tri} data were normalized by dividing data by individual baseline measurements for each microtissue to enable comparison across molds and batches. Only microtissues with at least one successfully stimulated AP for all doses were included in subsequent POD analysis (**Supplemental Figure A.1**).

2.3.7. Point of departure estimation

Points of departure (PODs) were estimated using sequential spline and sigmoid regression on resampled concentration response data for APD_{mxr} and APD_{tri} (**Figure 2.2**). Concentration responses were constructed from normalized data with log-transformed concentrations. The untreated control was incorporated as a concentration one-half log below the lowest tested concentration in order to better model baseline responses on a log scale (**Figure 2.2A**). Resampled data sets (B = 10,000 repeats) were generated via bootstrapping by randomly selecting microtissues with replacement (n = 51-95 microtissues) and weighting the resulting bootstrapped data by mold (**Figure 2.2B**). This computationally simulates the distribution of possible concentration responses represented by the experimental data without additional assumptions regarding the distribution of data while maintaining the paired nature of the response data and accounting for relative differences in the number of

microtissues recorded in each mold. For each resampled data set, a cubic spline was first applied to interpolate between the experimental data (**Figure 2.2C**) before a four-parameter logistic curve was subsequently fit (**Figure 2.2D, Equation 2.1**).

$$y_{modeled} = (t - b)/(1 + 10^{(c_o - c)*h}) + b \quad \textbf{(Equation 2.1)}$$

$y_{modeled}$ is the predicted response (normalized APD_{mxr} or APD_{tri}) at a given log-transformed concentration (c) where b is the baseline response, t is the maximum response, h is the hill coefficient describing the steepness of the curve, and c_o is the log-transformed concentration that gives a half-maximal effect. Boundary conditions were set such that modelled logistic curves were physiologically plausible. The lower asymptote was limited to be above 0, the upper asymptote was bound between 0 and five times the maximum interpolated response, and the log-transformed half-maximal concentration, c_o, was restricted above the minimum tested concentration. The magnitude of the hill coefficient was sign-limited based on the direction of the concentration response (*i.e.*, for an increasing response, h was greater than 0).

This two-step approach, with an initial interpolation step, and the applied boundary conditions are required because our assessment focuses on concentration ranges below response saturation. Focusing on this concentration range avoided the generation of early after depolarization (EADs) which significantly increase beat-to-beat variability. By first fitting a cubic spline, the fitted sigmoidal curves are prevented from modeling a pre-mature asymptote within the tested concentration range. Finally, PODs for each simulated response were calculated as the concentration at which the sigmoidal curve exceeded a 5% deviation from the baseline response to reflect clinically significant changes (**Figure 2.2D**) which were combined to estimate the distribution of mean PODs (**Figure 2.2E**). The 5^{th} and 95^{th} percentiles of this distribution represent the boundaries of the two-tailed 90% confidence interval for the estimated mean POD. All POD analysis was performed using Python version 3.9.7. Both the analysis code and data are available via the Dryad Digital Repository [37].

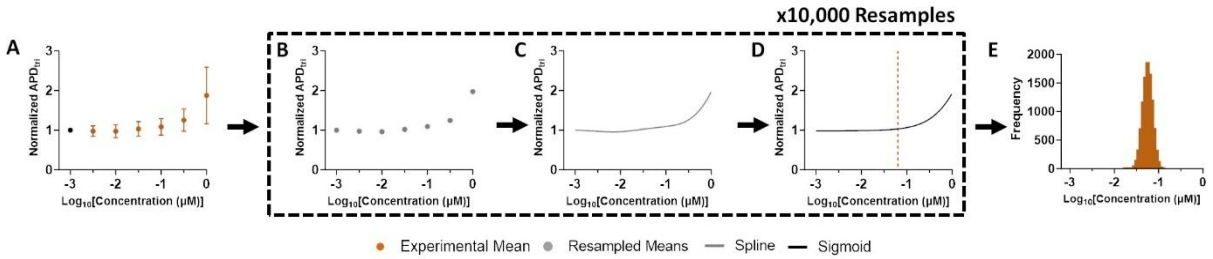

Figure 2.2. Point of Departure (POD) Estimation. (A) Normalized concentration response data are used to estimate point of departure (POD) across molds and differentiation batches (given example is cisapride APD_{tri}). Vehicle controls are treated as having a concentration one-half lower than the lowest tested concentration on a log-scale (left-most point, black). (B) Simulated data sets are generated by randomly selecting microtissues with replacement to generate bootstrapped samples of an equivalent size. (C) The data are weighted by mold, averaged, and a cubic spline is fit to the resampled data prior to (D) fitting a sigmoidal curve. This sequential curve fitting ensures the fit sigmoid does not approach an asymptote without a saturated concentration response. The POD is estimated as the concentration where the fit sigmoid is 5% greater than the baseline response (dashed orange line, equivalent to an ~10-20 ms change in APD_{mxr}). (E) This process is repeated 10,000 times to determine the confidence interval of the POD represented by the experimental data.

2.3.8. *In vitro* kinetics and point of departure adjustments

To account for small molecule-binding to tissue culture plastic and agarose during optical mapping, compound concentrations were measured before and after perfusion through the optical mapping setup as described above but without microtissues, only empty agarose molds. This process was repeated for two concentrations per compound with new syringes, tubing, culture dishes, and agarose molds for each compound. Samples were frozen at -80 °C until analysis by high-performance liquid chromatography tandem mass spectrometry to measure the relative free concentration of drug compared to the original solution prior to perfusion (Alera Labs, LLC). Prior to MOE calculation, PODs were adjusted proportionally by the percentage of each compound that was found to bind *in vitro*.

2.3.9. Physiologically based pharmacokinetic model development and structure

2.3.9.1. Model development and structure

The generic PBPK model for the four compounds had six compartments, including liver, brain, heart, blood, slowly perfused tissues, and rapidly perfused tissues (**Supplemental Figure A.2**). The model simulated exposure by oral, inhalation, or intravenous dosing and incorporated metabolism in liver and urinary excretion. The PBPK model assumed flow-limited tissue uptake for all compartments, meaning that the tissue and blood concentrations reach an equilibrium as the blood passes through the tissue and

that the blood flow to the tissues is the limiting process. The permeability area coefficient was therefore set to 100 by default, forcing this flow-limited behavior. Binding to plasma protein was not considered, assuming that it would not impact the kinetics. Modeling was performed using Berkeley Madonna version 10.5.1.

2.3.9.2. Physiological parameters

All physiological parameters used in the current model are summarized in **Supplemental Table A.1**. Cardiac output, tissue volume, and tissue plasma flow [38] as well as glomerular filtration rate [39] are from the literature. Body weight was set to 81.2 kg when not specified in the *in vivo* studies from the literature used to calibrate and validate the model.

2.3.9.3. Chemical-specific parameters

All chemical-specific parameters used in the current model are summarized in **Supplemental Table A.2.**

2.3.9.4. Liver metabolism

Liver metabolism was described using a first-order metabolism rate for all of the compounds. Elimination rates for humans were derived from the literature (**Supplemental Table A.2**). Metabolism data found in the literature were based on human or *in vitro* data. In the case of human data, the total clearance was usually reported. We assumed the total clearance to be the sum of the renal and hepatic clearance. The renal clearance was calculated as the glomerular filtration rate times the unbound fraction. The intrinsic clearance observed *in vivo* (CL_{int}) was calculated using a previously described well-stirred liver physiological model [40] (**Equation 2.2**).

$$CL_{int} = CL_h/[f_u(1 - CL_h/QL)] \quad \textbf{(Equation 2.2)}$$

CL_h is the hepatic clearance, f_u is the fraction unbound in plasma, and QL is the hepatic blood flow. Assuming unrestrictive clearance (f_u = 1) better fit the *in vivo* data.

The intrinsic *in vitro* clearances (µmol/min/10^6 hepatocytes) were extrapolated into *in vivo* intrinsic clearances (L/h). The *in vitro* CL_{int} data measured with hepatocytes from adult humans were scaled up to the corresponding *in vivo* enzyme CL_{int} in human using the appropriate scaling factors [41] (**Equation 2.3**).

$$CL_{int} = CL_{iv} * HPGL * LW \quad \textbf{(Equation 2.3)}$$

CL_{iv} is the *in vitro* CL_{int}, HPGL is hepatocellularity per gram liver (number of hepatocytes/g liver), and LW is the liver weight.

2.3.9.5. Tissue partitioning

Tissue-blood partition coefficients are defined as the ratio of the equilibrium concentration of a test chemical between a specific tissue and blood. Partition coefficients are important determinants of the disposition of chemicals in different tissues. Tissue-blood partition coefficients were estimated using a previously published algorithm [42]. The inputs to the algorithm were the octanol-water partition coefficient (K_{ow}), the fraction unbound in blood (f_{ub}), and the dissociation constant (pKa). *In vivo* partition coefficients were used when available in the literature.

2.3.9.6. Absorption-related parameters

Parameters describing the absorption of the compounds to the systemic circulation are summarized in **Supplemental Table A.2**. Oral exposure is modeled using an absorption from the gut lumen to the liver. The blood flow from the GI enters the liver via the portal vein. The rate constants for oral uptake were adjusted to provide enough delay in absorption to match the maximum concentration reported in the *in vivo* studies. Inhalation was described as a direct absorption to the systemic circulation.

2.3.9.7. Pharmacokinetic model performance

The degree of similarity of model simulations to experimental data can determine the level of confidence associated with a PBPK model. The performance of the model was evaluated using *in vivo* pharmacokinetic studies in humans. The visual fitting method was used to objectively determine the model's goodness-of-fit [43]. In all the data sets used for model development, the mean values of the observed concentrations were reported instead of individual data points. Therefore, the accuracy of

model predictions was graphically assessed by superimposing the predicted and observed mean plasma concentration-time profiles. Predictions of maximal concentration ($C_{max,plasma}$) that were within a factor of two of the experimental data were considered adequate as proposed by the World Health Organization [44]. Monte Carlo (MC) analysis was also conducted to investigate the population variability. Only the sensitive parameters from the sensitivity analysis were varied. Partition coefficients, body weight, cardiac output, ventilation rate, and metabolic constants were simulated as log-normally distributed. Blood flows and tissue volumes were simulated as normally distributed. The coefficients of variation (CV) for cardiac output and partition coefficients were 20% and 30%, the CV of body weight was 22%, and the CVs for the heart and blood volumes were 14% and 11%, respectively. CVs of 16% and 15% were used for the blood flow to the liver and the blood flow to the slowly perfused tissues, respectively [45], while a CV of 30% was assumed for the remaining model parameters. The distributions were truncated at two standard deviations to ensure physiological plausibility [46]. The PBPK model was run 1,000 times (the maximum number of iterations in a batch run in Berkeley Madonna) and the median (50^{th} percentile) as well as the 5^{th} and 95^{th} percentile blood concentrations were used for subsequent IVIVE.

2.3.10. *In vitro* to *in vivo* extrapolation

PODs from three-dimensional human cardiac microtissues were used to derive HEDs via reverse dosimetry with our generalized PBPK model and calculate the distribution of MOEs for each compound (**Figure 2.3**). 5^{th}, 50^{th}, and 95^{th} percentile maximal heart tissue concentrations ($C_{max,heart}$) were first derived at a standard dose of 1 mg/kg using Monte Carlo simulation (described above). Corresponding HEDs were calculated by dividing each *in vitro* POD by the corresponding 1 mg/kg $C_{max,heart}$ and multiplying the result by assumed body mass (81.2 kg) to obtain the dose (in mg) that would result in a $C_{max,heart}$ equivalent to the *in vitro* POD. MOEs were calculated by taking the ratio of HED to human therapeutic level (HTL) (*i.e.* typical clinical dose) for low, middle, or high doses (**Table 2.2**).

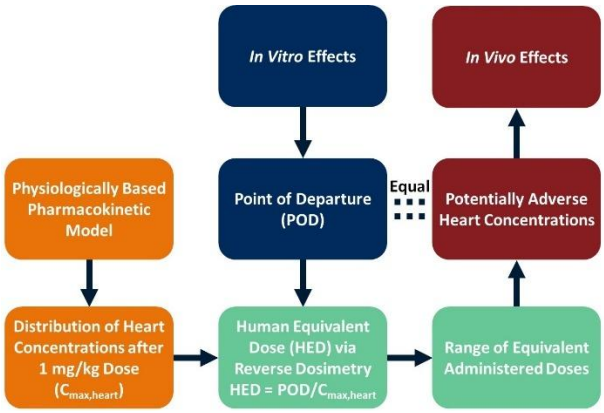

Figure 2.3. *In vitro* to *in vivo* extrapolation. Physiological parameters as well as parameters describing the absorption, distribution, metabolism, and elimination of the chemical through the system were used to develop a physiologically based pharmacokinetic model that can be used to predict the population distribution of tissue concentration from any given daily dose. Reverse dosimetry predicts administered doses equivalent to an *in vitro* active concentration (*i.e.*, point of departure), which can be compared to *in vivo* doses. Figure adapted from [47].

Table 2.2. Margin of exposure (MOE) calculations in the human population. Non-adjusted point of departure (POD), *In vitro* binding-adjusted (POD), predicted maximal heart concentration (C_{max}) for a 1 mg/kg dose, human equivalent dose (HED), and human therapeutic level (HTL) for the four test compounds were used to determine estimate margins of exposure (MOEs) after a bolus oral dose of each drug. Values for POD and heart C_{max} are expressed as mean values with 5th and 95th percentiles. HTLs are expressed as mean and range. HEDs are expressed as the mean estimate with the range of values calculated from 5th percentile POD and 95th percentile heart C_{max} (lower bound) or 95th percentile POD and 5th percentile heart C_{max} (upper bound). MOEs were similarly expressed as mean and range with boundaries calculated using low HED and high HTL (lower bound) or high HED and low HTL (upper bound). Body mass was assumed to be 81.2 kg.

Compound	Metric	POD (μM)	Adjusted POD (μM)	Heart C_{max} 1 mg/kg dose (μM)	HED (mg)	HTL (mg)	MOE
Quinidine	APDmxr	8.26 (7.63, 8.90)	7.86 (7.25, 8.47)	5.63 (3.56, 8.91)	113 (66, 193)	212.5 (100-325)	0.53 (0.20, 1.93)
	APDtri	2.70 (2.40, 3.06)	2.56 (2.29, 2.91)		37 (21, 66)		0.17 (0.06, 0.66)
Cisapride	APDmxr	0.24 (0.20, 0.28)	0.21 (0.18, 0.25)	2.36 (1.40, 3.85)	7.2 (3.8, 14.5)	12.5 (5-20)	0.58 (0.19, 2.90)
	APDtri	0.058 (0.037, 0.084)	0.051 (0.033, 0.075)		1.75 (0.70, 4.35)		0.14 (0.03, 0.87)
Ranolazine	APDmxr	17.1 (16.0, 18.2)	16.1 (15.1, 17.1)	0.40 (0.22, 0.72)	3268 (1703, 6312)	687.5 (375-1000)	4.75 (1.70, 16.8)
	APDtri	3.16 (1.94, 4.81)	2.97 (1.83, 4.53)		603 (206, 1672)		0.88 (0.21, 4.46)
Verapamil	APDmxr	0.39 (0.24, 0.50)	0.32 (0.20, 0.41)	0.315 (0.166, 0.559)	82 (29, 201)	200 (40-360)	0.41 (0.08, 5.01)
	APDtri	3.12 (2.41, 3.89)	2.55 (1.97, 3.19)		657 (286, 1560)		3.29 (0.79, 39.0)

2.3.11. Data visualization and reporting

Data was visualized using GraphPad Prism version 10.0.2 (GraphPad Software) or Python version 3.9.7 (Python Software Foundation). Concentration response data was displayed as mean ± standard deviation whereas PODs were shown as kernel density estimates of probability density. MOEs are displayed as the range of predicted values. Tabulated pharmacokinetic and risk assessment metrics were displayed as median values with associated 5th and 95th percentiles.

2.4. Results

2.4.1. Electrophysiological concentration responses and point of departure estimates

Four test compounds known to inhibit ventricular repolarization, but with a range of proarrhythmic risks due to compensatory effects on other ion channels, were selected for analysis. In order from high to low risk these were quinidine, cisapride, ranolazine, and verapamil [29]. The electrophysiological responses of individual cardiac microtissues were measured after sequential exposure to increasing concentrations of each compound or a time-matched exposure to vehicle (0.1% DMSO). Action potentials were recorded via optical mapping with a voltage-sensitive dye (Di-4-ANEPPS) and APD_{mxr} and APD_{tri}, the AP metrics most sensitive to altered late-stage repolarization, were quantified (**Figure 2.4, Supplemental Figure A.3**). Only data from microtissues with at least one successfully stimulated AP at all tested concentrations (51-97%) were included in subsequent POD analysis (Supplemental Figure A.1). Microtissues treated with cisapride, ranolazine, and quinidine showed visibly prolonged action potentials while verapamil-treated microtissues had shortened action potentials (**Figure 2.4A-D**). At the maximum tested concentrations, quantified changes in normalized APD_{mxr} (quinidine: 1.49 ± 0.27; cisapride: 1.21 ± 0.16; ranolazine: 1.19 ± 0.17; verapamil: 0.45 ± 0.08) (**Figure 2.4E-H**) and APD_{tri} (quinidine: 3.68 ± 0.97; cisapride: 1.88 ± 0.78; ranolazine: 2.31 ± 0.86; verapamil: 0.67 ± 0.20) (**Figure 2.4I-L**) were reflective of the qualitative observations made with the action potential traces of individual microtissues.

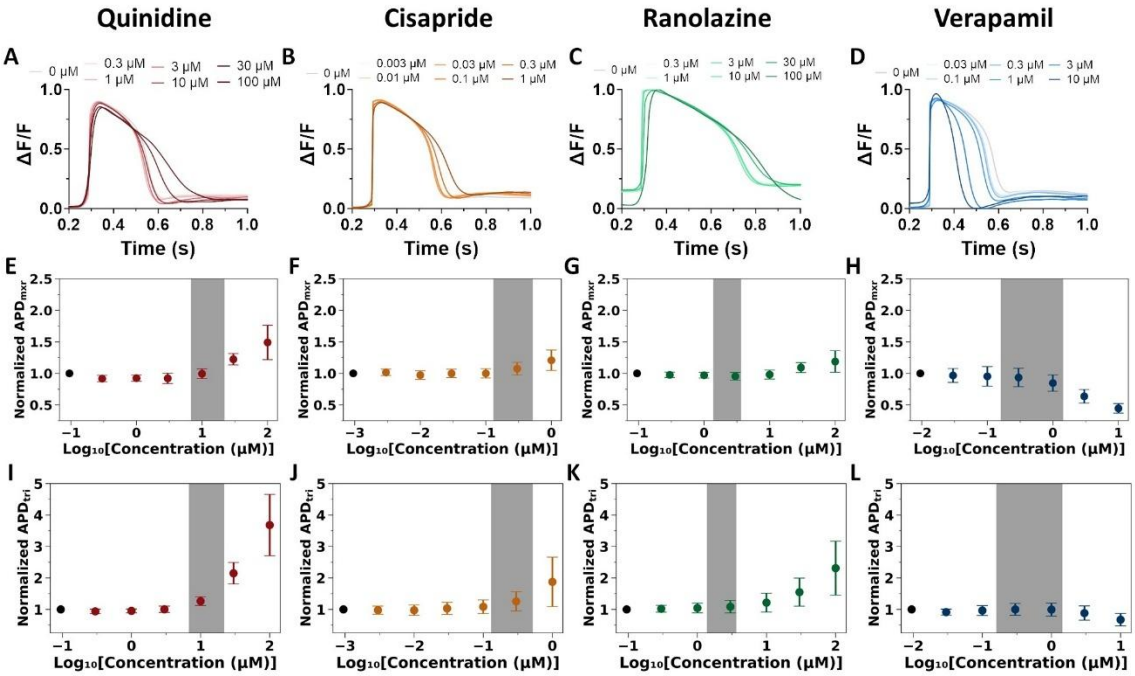

Figure 2.4. Action potential concentration responses of engineered human cardiac microtissues. (A-D) Representative action potential traces of microtissues exposed to (A) quinidine, (B) cisapride, (C) ranolazine, and (D) verapamil for 15 minutes at indicated concentrations. Darker colors indicate higher concentrations. (E-H) Normalized concentration responses of action potential duration to maximum rate of repolarization (APD_{mxr}) and (I-L) action potential triangulation (APD_{tri}) from all microtissues. The left-most point (black) indicates the pre-treatment control with a normalized value of one and standard deviation of zero placed one-half lower than the lowest tested concentration on the log scale where it was used for point of departure (POD) calculation. The gray shaded regions indicate therapeutic range of maximum heart concentration predicted by pharmacokinetic modeling. Data are presented as mean ± standard deviation for n = 51-95 microtissues across 3 molds and 2-3 differentiations per compound.

Normalized concentration responses were next leveraged to estimate PODs for subsequent risk assessment (**Figure 2.5, Table 2.2**). PODs (mean ± standard error) derived from APD_{tri} responses for APD-prolonging compounds (quinidine: 2.7 ± 0.2 μM; cisapride: 0.058 ± 0.015 μM; ranolazine: 3.2 ± 0.9 μM) were lower than those derived from APD_{mxr} (quinidine: 8.3 ± 0.4 μM; cisapride: 0.23 ± 0.02 μM; ranolazine: 17.0 ± 0.7 μM). Conversely for the APD-shortening compound verapamil, the mean POD derived from APD_{mxr} (verapamil: 0.39 ± 0.08 μM) was lower than of APD_{tri} (verapamil: 3.1 ± 0.5 μM). Prior to risk assessment, PODs were adjusted proportionally by the mean percentage of free compound remaining after *in vitro* binding in the microtissue-free optical mapping setup (quinidine: 95.1 ± 5.3%; cisapride: 88.8 ± 12.7%; ranolazine: 94.2 ± 6.1%; verapamil: 81.9 ± 10.8%) (**Table 2.2, Supplemental Figure A.4**). Comparison of model-predicted and previously reported plasma concentrations supports that measured

in vitro PODs occur at clinically relevant concentrations that cause QT prolongation in humans for QT-prolonging compounds (**Supplemental Table A.4-Supplemental Table** A.5).

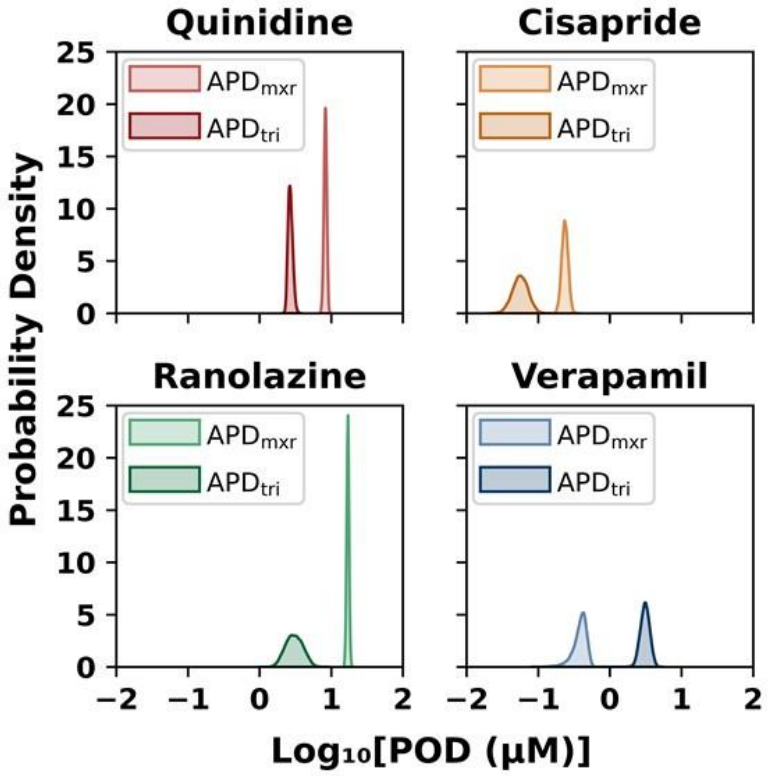

Figure 2.5. Point of Departure Estimation. Points of departure (PODs) were estimated from resampled normalized concentration-response data. PODs were calculated from each of 10,000 data sets generated via bootstrapping and the 90% confidence intervals were calculated from the 5th and 95th quantiles. Data are displayed as a kernel density estimation. Light and dark colors represent POD estimates from APD_{mxr} and APD_{tri} concentration responses, respectively.

2.4.2. Human PBPK model

2.4.2.1. Model verification

Quinidine was calibrated with the *in vivo* pharmacokinetic data from Laganière et al. (1996) (plasma concentration between 0-24 h post exposure). No other datasets were used for quinidine, but it is important to note that the structure of the model used was the same for all four drugs. The only parameters changing were the partition coefficients and clearance. For cisapride, model performance was first evaluated using *in vivo* pharmacokinetic data (plasma concentrations between 0-6 h post exposure) from Rowbotham et al. (1991). Validation was performed using *in vivo* pharmacokinetics from Desta et al. (2001). Ranolazine model performance was initially evaluated using *in vivo* pharmacokinetic data (plasma

concentrations between 0-24 h post exposure) from Tan et al. (2013) at 3 different doses followed by a validation using the *in vivo* dataset from Yoo et al. (2021). Lastly, verapamil model performance was evaluated using *in vivo* data (plasma concentrations between 0-6 h post exposure) from Dominic et al. (1981) followed by a validation using three other *in vivo* sets of pharmacokinetic data from Mooy et al. (1985) (after intravenous and oral exposure) and John et al (1992). A complete list of *in vivo* data sets is provided in **Supplemental Table A.3**.

All model-predicted mean plasma concentration time courses were in good agreement with experimental observations across all data sets (**Supplemental Figure A.5-A.9**). Predicted mean maximal concentrations ($C_{max,plasma}$) were within a factor of two of the observed values. For all the chemicals, the concentration time-profile was in good agreement with the *in vivo* data. The pharmacokinetic clearance behavior of cisapride [48], one set of ranolazine data [49], and one set of verapamil data (Mooy et al. 1985) was not captured by model predictions, but was adequate in predicting the concentration time-profile.

2.4.2.2. Sensitivity analysis and uncertainty

Sensitivity analysis was used to evaluate the impact of model parameters on the concentration of each chemical in the heart (**Supplemental Figure A.10**). For ranolazine, cisapride, quinidine and verapamil, the most influential parameters to the heart internal exposure were the heart blood flow and volume, the blood-heart partition coefficient, the intrinsic clearance, the body weight, and the cardiac output.

The uncertainty of a model reflects the level of confidence in model predictions. This uncertainty usually arises from limitations in available knowledge in some input parameters that affect the model predictions. The uncertainty was qualitatively defined based on the origin and confidence in each parameter that were sensitive in the model. Most of our model parameters are reported to have medium or low uncertainty. All parameters that are either directly measured or based on data from the literature (body weight, cardiac output, tissue volumes or blood flows) can be considered to have low uncertainty.

All parameters related to metabolism in the liver have medium to high sensitivity and are considered to have medium uncertainty. Partition coefficients were mainly predicted by QSAR modeling and are therefore considered with medium uncertainty.

2.4.3. Margins of exposure reflect relative proarrhythmic risk

The proarrhythmic risk of each compound was determined by calculating an MOE relating HTLs to HEDs predicted to cause a maximal heart concentration equivalent to the *in vitro* POD (**Figure 2.6, Table 2.2**). Mean MOEs were calculated using central estimates for *in vitro* PODs, maximal heart concentration, and HTL for each compound. Population-level variability was captured by calculating the lower (low POD and HED estimates for the highest therapeutic dose) and upper (high POD and HED estimates for the lowest therapeutic dose) extremes.

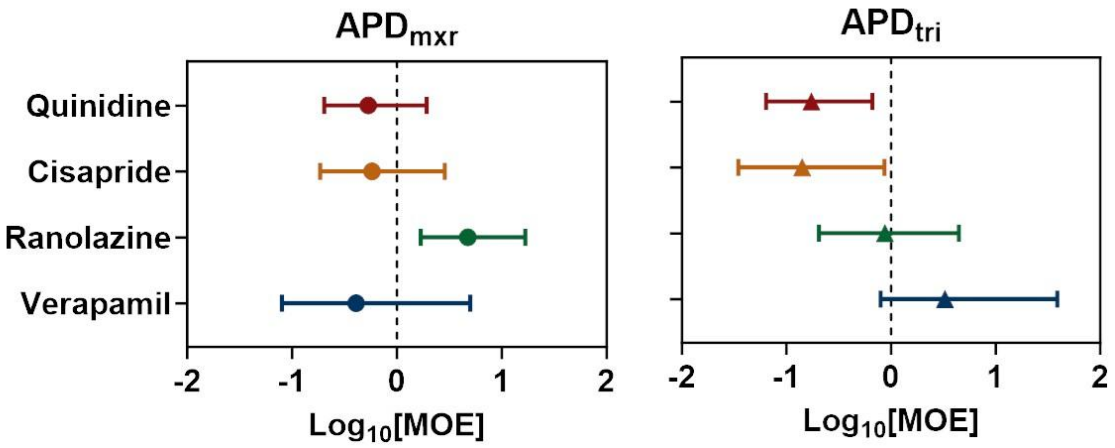

Figure 2.6. Proarrhythmic risk assessment via *in vitro* to *in vivo* extrapolation. Margins of exposure (MOEs) were calculated for each compound using both (left) APD_{mxr} and (right) APD_{tri} data. Points of departure (PODs) were adjusted for *in vitro* binding and converted to a human equivalent dose (HED) using a physiologically based pharmacokinetic model. Mean MOEs (points) were calculated using central estimates of POD and HED at the average therapeutic dose. Lower and upper estimates (error bars) were calculated using worst-case (low POD and HED estimates for the highest therapeutic dose) and best-case (high POD and HED estimates for the lowest therapeutic dose) scenarios, respectively. A $Log_{10}MOE$ equal to zero occurs when the HED and therapeutic dose are equivalent, marking the transition from higher to lower risk (dashed vertical line).

Quinidine and cisapride possessed the highest predicted proarrhythmic risk of the four test compounds. Both compounds prolonged action potentials and had mean MOEs less than one for both APD_{mxr} and APD_{tri} (**Figure 2.6**). Moreover, the entire range of MOEs estimated from APD_{tri} data was below

one, suggesting that inhibition of I_{Kr} occurs at concentrations less than the concentration caused by a therapeutic dose. These results align with the known proarrhythmic risks of quinidine, which has a black box warning and was classified as high risk by the CiPA initiative, and cisapride, which was removed from the market after reports of QT prolongation despite a CiPA classification as an intermediate risk compound [32, 50] (**Table 2.1**). Results from our experiments with ranolazine show a moderate predicted proarrhythmic risk. While MOEs calculated using APD_{mxr} data were greater than one, suggesting a reasonably safe therapeutic index, the mean APD_{tri} MOE was slightly below one, suggesting that there is increased risk for delayed repolarization due to inhibited I_{Kr}, which aligns with known QT prolongation at high doses of ranolazine in patients [50, 51]. Thus, our platform predicts a low risk based on APD_{mxr} in agreement with the CiPA categorization (**Table 2.1**) and higher risk based on APD_{tri}, which is consistent with current clinical knowledge and not specifically identified in *in vitro* hiPSC-CM-based NAMs that rely on APD alone. Our MOE results for the two metrics further suggest that compound risk will vary dependent on dose and an individual's susceptibility to drug-induced arrhythmias, as is included on the label of ranolazine [50]. Finally, verapamil had the lowest predicted MOE based on APD_{mxr} data and caused APD shortening, an effect that is not associated with repolarization-related arrhythmias via I_{Kr} block and likely is indicative of its therapeutic inhibition of L-type calcium channels and shorten the plateau phase of the action potential. Verapamil's MOE calculated from APD_{tri} data, the metric more directly associated with late-stage cardiac repolarization and inhibition of I_{Kr}, was the highest of the four test compounds, indicating the lowest fatal arrhythmia risk as expected. In sum, evaluation of these four compounds in our three-dimensional hiPSC-CM-based microtissue platform demonstrates close alignment with established proarrhythmic profiles of each compound based on known inhibition of I_{Kr}, which is the most concerning mechanism of fatal drug-induced arrhythmias for regulatory bodies, prescribing clinicians, and patients.

2.5. Discussion

Increasingly, there is both the need and desire for *in vitro* models that predict human proarrhythmic risk while simultaneously reducing reliance on animal testing [10-12]. We addressed this challenge by performing quantitative risk assessment for four compounds with known proarrhythmic risk profiles by combining our existing *in vitro* three-dimensional human ventricular cardiac microtissue model capable of quantifying concentration-dependent changes in excitability and seven other metrics reflective of human cardiomyocyte electrophysiology [27, 28] with *in silico* PBPK modeling. Action potentials recorded using a voltage-sensitive dye allowed for the measurement of two endpoints reflective of repolarization-related proarrhythmic risk in the same microtissue across multiple concentrations. This enabled robust quantification of *in vitro* PODs and the ability to perform IVIVE using reverse dosimetry to compare potentially adverse concentrations identified *in vitro* to clinical *in vivo* exposures. We found good agreement between our IVIVE predictions and the known cardiotoxicity risk of the four test compounds, supporting the potential of combining an hiPSC-CM-based *in vitro* cardiotoxicity platform and IVIVE as an alternative to conventional animal-dependent cardiotoxicity risk assessment.

Critical to the ability of an *in vitro* model to accurately predict *in vivo* responses is a direct link between the *in vitro* endpoint and *in vivo* outcome [24, 52, 53]. The two metrics utilized in this study, APD_{mxr} and APD_{tri} (**Figure 2.1D**), are specific measures of the predominant cellular mechanism responsible for delayed ventricular repolarization that causes the most concerning drug-induced fatal ventricular arrhythmias *in vivo* [17, 21]. In contrast, many cardiotoxicity platforms, including those using hiPSC-derived cardiomyocytes, rely on indirect measures of proarrhythmic cardiotoxicity downstream of the cardiac action potential, such as spontaneous beat rate, calcium transient kinetics, or contraction force [54]. The use of endpoints that are pre-clinical correlates for QT prolongation and proarrhythmic risk, like those in this study, eases interpretation of *in vitro* PODs and paves the way for improved predictive capacity in human studies. This is supported by the close agreement between the plasma concentrations at POD

predicted by the PBPK model and human *in vivo* plasma concentrations that result in clinically relevant changes in QT interval (**Supplemental Table A.5**).

Another advantage of the current study is the ability to record action potentials from an array of microtissues tracked individually across multiple concentrations. Variation of terminally differentiated cells from hiPSCs is known to require inclusion of multiple batches, normalization to internal experimental controls, along with an understanding of the strengths and limitations of hiPSCs in recapitulating human-relevant physiology. By following individual microtissue concentration responses, we could address these hurdles and account for multiple levels of biological variability (*i.e.,* batch, mold, microtissue) in our system. Moreover, most other studies performing *in vitro* proarrhythmic risk assessment rely on comparisons to drug plasma concentrations rather than the tissue-level concentrations utilized in this study, potentially reducing predictive capacity [55-57]. The quantitative IVIVE performed in this study accounts for both *in vitro* and *in vivo* drug kinetics. PODs were adjusted (4.9%-18.1%) for binding to plastics, serum proteins, and other components, as well as evaporation via direct measurement of the relative fraction of unbound drug, reducing our approach's reliance on nominal (*i.e.,* administered) concentration, which can limit the accuracy of IVIVE [58-60] (**Supplemental Figure A.4**). Adjusted PODs were converted to the oral dose that would result in the equivalent heart concentration *in vivo* via reverse dosimetry with a generalized PBPK model to account for absorption, distribution, metabolism, and elimination that are not otherwise present *in vitro*, improving the accuracy of risk assessment. These kinetic considerations are in addition to the fact that the potentially adverse concentrations measured in this study were derived from modeled concentration responses rather than traditional statistical identification of adverse concentrations such as a no-observed-effect-level (NOEL) or low-observed-effect-level (LOEL), which are known to be limited by study design [61, 62].

The resulting MOEs distinguished the relative proarrhythmic risk associated with the four test compounds between those with higher (quinidine, cisapride) and lower (ranolazine, verapamil) clinical

risk. Our data provide more mechanistic insights about how I_{Kr} block influences the overall compound risk profile (**Figure 6**) compared to other published *in vitro* risk assessment models using hiPSC-CMs [55, 56, 63].The MOEs calculated using APD_{tri} data predicted higher risk than those predicted using APD_{mxr} for quinidine, cisapride, and ranolazine, which are known to cause APD prolongation due to I_{Kr} inhibition (**Figure 2.5, Figure 2.6, and Table 2.1**). Conversely, relative risk decreased when assessing APD_{tri} for verapamil despite its known inhibition of I_{Kr}, which can likely be explained by the effects of verapamil to shorten APD and counteract its effects on I_{Kr}. Moreover, the shifts in MOE between the two metrics were larger for the lower risk compounds ranolazine and verapamil, where APD_{tri} more precisely stratified risk, which we attribute to compensatory ion currents in matured three-dimensional microtissue because APD_{mxr} reflects the sum of many ion fluxes whereas APD_{tri} is specific to the repolarization phase of the action potential, particularly I_{Kr} [27, 64, 65]. These differences suggest that metrics from each phase of the action potential like the one used in this study can provide nuanced insight into mechanism-specific arrhythmia risks and that APD_{tri} is a more sensitive metric for predicting fatal proarrhythmic risk due to delayed ventricular repolarization. Thus, our human cardiac microtissue platform is fit for studies where information regarding the mechanism of arrhythmia risk is a desired outcome.

An ideal *in vitro* risk assessment model would be able to perform quantitative IVIVE and cardiotoxic risk assessment based on *in vitro* data alone. While our results suggest that such a “clinical trial in a dish” is possible, there are several remaining hurdles, particularly when applying these methods to novel chemical compounds and drugs. From a pharmacokinetic perspective, *in vitro*-only IVIVE is particularly challenging when pre-existing *in vivo* data are lacking for model validation. While *in vivo* pharmacokinetic data are readily available for marketed and previously marketed drugs such as those used in this study, this is not the case for many chemicals or investigational new drugs. As risk assessment continues to shift from animal testing to NAMs based on *in vitro* and *in silico* approaches, alternative strategies will be needed to integrate and use non-animal data. Guidelines like the Guidance Document on the

Characterization, Validation, and Reporting of Physiologically Based Kinetic (PBK) Models for Regulatory Purposes from the Organisation for Economic Co-operation and Development are beginning to address the need for parameterizing and validating PBPK models when *in vivo* data are limited or not available, especially for use in risk assessment by following a specific workflow to ensure the validity and applicability according to its context of use [66]. Tools such as these will be essential in refining PBPK model conceptualization and evaluation as risk assessment continues to move toward an *in vitro* focus. Moreover, as data accumulates for a greater number of drugs and compounds across a wider range of chemical classes, it may be possible to predict both qualitative and quantitative clearance using quantitative structure-activity relationship (QSAR) approaches over a broader domain of applicability [41, 67]. In this way, compounds with similar properties can be grouped and data for similar compounds can be used to fill gaps in the knowledge of a particular compound. Additionally, *in vitro* assessment using multi-organ, microphysiological systems could offer an empirical approach to estimating the pharmacokinetic profiles of novel compounds for later *in silico* evaluation [68-70]. Already, *in vitro* microtissue models similar to those used in this study have been incorporated into such multi-organ platforms to predict the cardiotoxicity of liver metabolites on several tissues simultaneously [71, 72].

Beyond acting solely as *in vivo* replacements, NAMs, particularly those utilizing hiPSC-derived cells, could expand the types of evaluation that can be performed by offering greater flexibility for examining cardiotoxicity risk in the contexts of underlying disease (*i.e.*, hidden cardiotoxicity) [73], genetic susceptibility [74-76], population variability [63, 77], and complex exposures [78, 79] than their *in vivo* counterparts. Overall, this study advances the capability of three-dimensional hiPSC-derived cardiac microtissues to quantitatively predict *in vivo* risk by combining human-focused, physiologically relevant *in vitro* and *in silico* models without a reliance on animal testing and aids in the development of cardiac risk assessment for pharmaceuticals and non-pharmaceuticals alike.

2.6. Funding

This work was supported by funding from the National Institutes of Health National Institute of Environmental Health Sciences (U01 ES028184 to UM, BRC, PM, KLKC) and a Brown University Biomedical Innovation to Impact Award (to UM, BRC, and KLKC).

2.7. Acknowledgements

We thankfully acknowledge Dr. Andy Nong for his input on the content of this manuscript, Dr. Arvin Soepriatna for his technical assistance, and Alera Labs, LLC for their analytical support.

2.8. Supplemental Data and Data Availability

Supplemental data are available in **Appendix A – Supplemental Material for Chapter 2**. Data and code related to POD calculations is available via the Dryad Digital Repository at doi:10.5061/dryad.sqv9s4nbn.

2.9. References

1. Onakpoya, I.J., C.J. Heneghan, and J.K. Aronson, *Post-marketing withdrawal of 462 medicinal products because of adverse drug reactions: a systematic review of the world literature.* BMC medicine, 2016. **14**(1): p. 1-11.
2. Magdy, T., et al., *Human induced pluripotent stem cell (hiPSC)-derived cells to assess drug cardiotoxicity: opportunities and problems.* Annual review of pharmacology and toxicology, 2018. **58**: p. 83-103.
3. Prüss-Ustün, A. and C.F. Corvalán, *Preventing disease through healthy environments: towards an estimate of the environmental burden of disease*. 2006: World Health Organization.
4. Judson, R., et al., *The toxicity data landscape for environmental chemicals.* Environmental health perspectives, 2009. **117**(5): p. 685-695.
5. Pang, L., et al., *Workshop report: FDA workshop on improving cardiotoxicity assessment with human-relevant platforms.* Circulation research, 2019. **125**(9): p. 855-867.

6. Nerbonne, J.M., et al., *Genetic manipulation of cardiac K+ channel function in mice: what have we learned, and where do we go from here?* Circulation research, 2001. **89**(11): p. 944-956.

7. Mercola, M., A. Colas, and E. Willems, *Induced pluripotent stem cells in cardiovascular drug discovery.* Circulation research, 2013. **112**(3): p. 534-548.

8. Sallam, K., et al., *Finding the rhythm of sudden cardiac death: new opportunities using induced pluripotent stem cell–derived cardiomyocytes.* Circulation research, 2015. **116**(12): p. 1989-2004.

9. Olson, H., et al., *Concordance of the toxicity of pharmaceuticals in humans and in animals.* Regulatory Toxicology and Pharmacology, 2000. **32**(1): p. 56-67.

10. Fischer, I., C. Milton, and H. Wallace, *Toxicity testing is evolving!* Toxicology Research, 2020. **9**(2): p. 67-80.

11. Adashi, E.Y., D.P. O'Mahony, and I.G. Cohen, *The FDA Modernization Act 2.0: Drug Testing in Animals is Rendered Optional.* The American Journal of Medicine, 2023.

12. Ahmed, S.M., R.V. Shivnaraine, and J.C. Wu, *FDA modernization act 2.0 paves the way to computational biology and clinical trials in a dish.* Circulation, 2023. **148**(4): p. 309-311.

13. Lind, L., et al., *Key characteristics of cardiovascular toxicants.* Environmental health perspectives, 2021. **129**(9): p. 095001.

14. Cosselman, K.E., A. Navas-Acien, and J.D. Kaufman, *Environmental factors in cardiovascular disease.* Nature Reviews Cardiology, 2015. **12**(11): p. 627-642.

15. ICH, *The non-clinical evaluation of the potential for delayed ventricular repolarization (Qt Interval Prolongation) by human pharmaceuticals*. 2005.

16. Gintant, G., P.T. Sager, and N. Stockbridge, *Evolution of strategies to improve preclinical cardiac safety testing.* Nature Reviews Drug Discovery, 2016. **15**(7): p. 457.

17. Priest, B., I.M. Bell, and M. Garcia, *Role of hERG potassium channel assays in drug development.* Channels, 2008. **2**(2): p. 87-93.

18. Yao, J.-A., et al., *Estimation of potency of HERG channel blockers: impact of voltage protocol and temperature.* Journal of pharmacological and toxicological methods, 2005. **52**(1): p. 146-153.

19. Milnes, J.T., et al., *Investigating dynamic protocol-dependence of hERG potassium channel inhibition at 37 C: Cisapride versus dofetilide.* Journal of pharmacological and toxicological methods, 2010. **61**(2): p. 178-191.

20. Gomis-Tena, J., et al., *When does the IC50 accurately assess the blocking potency of a drug?* Journal of chemical information and modeling, 2020. **60**(3): p. 1779-1790.

21. Gintant, G., *An evaluation of hERG current assay performance: translating preclinical safety studies to clinical QT prolongation.* Pharmacology & therapeutics, 2011. **129**(2): p. 109-119.

22. Burnett, S.D., et al., *Human induced pluripotent stem cell (iPSC)-derived cardiomyocytes as an in vitro model in toxicology: strengths and weaknesses for hazard identification and risk characterization.* Expert Opinion on Drug Metabolism & Toxicology, 2021: p. 1-16.

23. Gintant, G., et al., *Use of Human Induced Pluripotent Stem Cell–Derived Cardiomyocytes in Preclinical Cancer Drug Cardiotoxicity Testing: A Scientific Statement From the American Heart Association.* Circulation research, 2019. **125**(10): p. e75-e92.

24. Daley, M.C., et al., *Beyond pharmaceuticals: Fit-for-purpose new approach methodologies for environmental cardiotoxicity testing.* ALTEX-Alternatives to animal experimentation, 2023. **40**(1): p. 103-116.

25. Yang, X., et al., *Use of human iPSC-CMs in nonclinical regulatory studies for cardiac safety assessment.* Toxicological Sciences, 2022. **190**(2): p. 117-126.

26. Wetmore, B.A., et al., *Integration of dosimetry, exposure, and high-throughput screening data in chemical toxicity assessment.* Toxicological Sciences, 2012. **125**(1): p. 157-174.

27. Kofron, C., et al., *A Predictive in Vitro Risk Assessment Platform for Pro-Arrhythmic Toxicity Using Human 3D Cardiac Microtissues.* Scientific Reports, 2021. **11**: p. 1-16.

28. Soepriatna, A.H., et al., *Action potential metrics and automated data analysis pipeline for cardiotoxicity testing using optically mapped hiPSC-derived 3D cardiac microtissues.* Plos one, 2023. **18**(2): p. e0280406.

29. Colatsky, T., et al., *The comprehensive in vitro proarrhythmia assay (CiPA) initiative—update on progress.* Journal of pharmacological and toxicological methods, 2016. **81**: p. 15-20.

30. Yang, F., et al., *Quinidine revisited.* The American journal of medicine, 2009. **122**(4): p. 317-321.

31. Serdoz, L.V., et al., *Quinidine—A legacy within the modern era of antiarrhythmic therapy.* Pharmacological Research, 2019. **144**: p. 257-263.

32. Wysowski, D.K., et al., *Postmarketing reports of QT prolongation and ventricular arrhythmia in association with cisapride and Food and Drug Administration regulatory actions.* The American journal of gastroenterology, 2001. **96**(6): p. 1698-1703.

33. Wu, L., et al., *Reduction of repolarization reserve unmasks the proarrhythmic role of endogenous late Na+ current in the heart.* American Journal of Physiology-Heart and Circulatory Physiology, 2009. **297**(3): p. H1048-H1057.

34. Zhang, S., et al., *Mechanism of block and identification of the verapamil binding domain to HERG potassium channels.* Circulation Research, 1999. **84**(9): p. 989-998.

35. Burridge, P.W., A. Holmström, and J.C. Wu, *Chemically defined culture and cardiomyocyte differentiation of human pluripotent stem cells.* Current Protocols in Human Genetics, 2015. **87**(1): p. 21.3. 1-21.3. 15.

36. Burridge, P.W., et al., *Chemically defined and small molecule-based generation of human cardiomyocytes.* Nat. Methods, 2014. **11**.

37. Daley, M.C., et al., *Concentration-Response and Point of Departure Derivation for In Vitro to In Vivo Extrapolation from Three-Dimensional hiPSC-derived Cardiac Microtissues*. 2024.

38. Brown, R.P., et al., *Physiological parameter values for physiologically based pharmacokinetic models.* Toxicology and industrial health, 1997. **13**(4): p. 407-484.

39. Lin, J.H., *Applications and limitations of interspecies scaling and in vitro extrapolation in pharmacokinetics.* Drug metabolism and disposition, 1998. **26**(12): p. 1202-1212.

40. Zanelli, U., et al., *Comparison of cryopreserved HepaRG cells with cryopreserved human hepatocytes for prediction of clearance for 26 drugs.* Drug Metabolism and Disposition, 2012. **40**(1): p. 104-110.

41. Yoon, M., et al., *Quantitative in vitro to in vivo extrapolation of cell-based toxicity assay results.* Critical reviews in toxicology, 2012. **42**(8): p. 633-652.

42. Poulin, P. and F.-P. Theil, *Prediction of pharmacokinetics prior to in vivo studies. II. Generic physiologically based pharmacokinetic models of drug disposition.* Journal of pharmaceutical sciences, 2002. **91**(5): p. 1358-1370.

43. EPA, *Approaches For the Application of Physiologically Based Pharmacokinetic (PBPK) Models and Supporting Data In Risk Assessment (Final Report)*. 2006, U.S. Environmental Protection Agency: Washington, DC.

44. International Programme on Chemical Safety and Inter-Organization Programme for the Sound Management of Chemicals, *Characterization and application of physiologically based phamacokinetic models in risk assessment*. 2010, World Health Organization: Geneva.

45. Price, P.S., et al., *Modeling interindividual variation in physiological factors used in PBPK models of humans.* Critical reviews in toxicology, 2003. **33**(5): p. 469-503.

46. Clewell, R.A. and H.J. Clewell III, *Development and specification of physiologically based pharmacokinetic models for use in risk assessment.* Regulatory Toxicology and Pharmacology, 2008. **50**(1): p. 129-143.

47. Bell, S.M., et al., *In vitro to in vivo extrapolation for high throughput prioritization and decision making.* Toxicology In Vitro, 2018. **47**: p. 213-227.

48. Desta, Z., et al., *Stereoselective pharmacokinetics of cisapride in healthy volunteers and the effect of repeated administration of grapefruit juice.* British journal of clinical pharmacology, 2001. **52**(4): p. 399-407.

49. Yoo, H., et al., *Pharmacokinetics and Safety of Extended-release Ranolazine in Korean and White Healthy Subjects.* Clinical Therapeutics, 2021. **43**(3): p. 526-534. e4.

50. NLM, *DailyMed*. 2005, U.S. National Library of Medicine: Bethesda, MD.

51. Tzeis, S. and G. Andrikopoulos, *Antiarrhythmic properties of ranolazine–from bench to bedside.* Expert opinion on investigational drugs, 2012. **21**(11): p. 1733-1741.

52. Vincent, F., et al., *Developing predictive assays: the phenotypic screening "rule of 3".* Science translational medicine, 2015. **7**(293): p. 293ps15-293ps15.

53. Moffat, J.G., et al., *Opportunities and challenges in phenotypic drug discovery: an industry perspective.* Nature reviews Drug discovery, 2017. **16**(8): p. 531-543.

54. Gintant, G., et al., *Repolarization studies using human stem cell-derived cardiomyocytes: Validation studies and best practice recommendations.* Regulatory toxicology and pharmacology, 2020. **117**: p. 104756.

55. Guo, L., et al., *Refining the human iPSC-cardiomyocyte arrhythmic risk assessment model.* toxicological sciences, 2013. **136**(2): p. 581-594.

56. Ando, H., et al., *A new paradigm for drug-induced torsadogenic risk assessment using human iPS cell-derived cardiomyocytes.* Journal of Pharmacological and Toxicological Methods, 2017. **84**: p. 111-127.

57. Blanchette, A.D., et al., *A bayesian method for population-wide cardiotoxicity hazard and risk characterization using an in vitro human model.* Toxicological Sciences, 2020. **178**(2): p. 391-403.

58. Kramer, N.I., et al., *Quantifying processes determining the free concentration of phenanthrene in basal cytotoxicity assays.* Chemical research in toxicology, 2012. **25**(2): p. 436-445.

59. Gülden, M. and H. Seibert, *Influence of protein binding and lipophilicity on the distribution of chemical compounds in in vitro systems.* Toxicology in vitro, 1997. **11**(5): p. 479-483.

60. Groothuis, F.A., et al., *Dose metric considerations in in vitro assays to improve quantitative in vitro–in vivo dose extrapolations.* Toxicology, 2015. **332**: p. 30-40.

61. Sand, S., K. Victorin, and A.F. Filipsson, *The current state of knowledge on the use of the benchmark dose concept in risk assessment.* Journal of Applied Toxicology: An International Journal, 2008. **28**(4): p. 405-421.

62. Jensen, S.M., F.M. Kluxen, and C. Ritz, *A review of recent advances in benchmark dose methodology.* Risk Analysis, 2019. **39**(10): p. 2295-2315.

63. Burnett, S.D., et al., *Cardiotoxicity Hazard and Risk Characterization of ToxCast Chemicals Using Human Induced Pluripotent Stem Cell-Derived Cardiomyocytes from Multiple Donors.* Chemical Research in Toxicology, 2021. **34**(9): p. 2110-2124.

64. Guerard, N., et al., *Selective block of IKs plays a significant role in MAP triangulation induced by IKr block in isolated rabbit heart.* Journal of pharmacological and toxicological methods, 2008. **58**(1): p. 32-40.

65. Ziupa, D., et al., *Pronounced effects of HERG-blockers E-4031 and erythromycin on APD, spatial APD dispersion and triangulation in transgenic long-QT type 1 rabbits.* PLoS One, 2014. **9**(9): p. e107210.

66. OECD, *Guidance document on the characterisation, validation and reporting of Physiologically Based Kinetic (PBK) models for regulatory purposes*, in *OECD Series on Testing and Assessment*. 2021.

67. Pradeep, P., et al., *Using chemical structure information to develop predictive models for in vitro toxicokinetic parameters to inform high-throughput risk-assessment.* Computational Toxicology, 2020. **16**: p. 100136.

68. Truskey, G.A., *Human microphysiological systems and organoids as in vitro models for toxicological studies.* Frontiers in public health, 2018. **6**: p. 185.

69. Abaci, H.E. and M.L. Shuler, *Human-on-a-chip design strategies and principles for physiologically based pharmacokinetics/pharmacodynamics modeling.* Integrative Biology, 2015. **7**(4): p. 383-391.

70. Low, L. and D. Tagle, *Tissue chips–innovative tools for drug development and disease modeling.* Lab on a Chip, 2017. **17**(18): p. 3026-3036.

71. Skardal, A., et al., *Multi-tissue interactions in an integrated three-tissue organ-on-a-chip platform.* Scientific reports, 2017. **7**(1): p. 1-16.

72. Skardal, A., et al., *Drug compound screening in single and integrated multi-organoid body-on-a-chip systems.* Biofabrication, 2020. **12**(2): p. 025017.

73. Ferdinandy, P., et al., *Definition of hidden drug cardiotoxicity: paradigm change in cardiac safety testing and its clinical implications.* European heart journal, 2019. **40**(22): p. 1771-1777.

74. Burridge, P.W., et al., *Human induced pluripotent stem cell–derived cardiomyocytes recapitulate the predilection of breast cancer patients to doxorubicin-induced cardiotoxicity.* Nature medicine, 2016. **22**(5): p. 547.

75. Stillitano, F., et al., *Modeling susceptibility to drug-induced long QT with a panel of subject-specific induced pluripotent stem cells.* Elife, 2017. **6**: p. e19406.

76. Shinozawa, T., et al., *Recapitulation of clinical individual susceptibility to drug-induced QT prolongation in healthy subjects using iPSC-derived cardiomyocytes.* Stem Cell Reports, 2017. **8**(2): p. 226-234.

77. Burnett, S.D., et al., *Population-based toxicity screening in human induced pluripotent stem cell-derived cardiomyocytes.* Toxicology and applied pharmacology, 2019. **381**: p. 114711.

78. Grimm, F.A., et al., *High-content assay multiplexing for toxicity screening in induced pluripotent stem cell-derived cardiomyocytes and hepatocytes.* Assay and drug development technologies, 2015. **13**(9): p. 529-546.

79. Hsieh, N.-H., et al., *Risk characterization and probabilistic concentration–response modeling of complex environmental mixtures using new approach methodologies (NAMs) data from organotypic in vitro human stem cell assays.* Environmental Health Perspectives, 2021. **129**(1): p. 017004.

Chapter 3 - Computationally informed point of departure evaluation for proarrhythmic cardiotoxicity assessment using 3D engineered cardiac microtissues from human iPSC-derived cardiomyocytes

Reproduced with permission from Daley, M.C., Bronk, P. *et al "*Computationally informed point of departure evaluation for proarrhythmic cardiotoxicity assessment using 3D engineered cardiac microtissues from human iPSC-derived cardiomyocytes" Submitted for publication in *Toxicological Sciences*.

3.1. Abstract

Human induced pluripotent stem cell-derived cardiomyocytes (hiPSC-CMs) are a promising new approach for *in vitro* proarrhythmic cardiotoxicity assessment. However, variation due to differentiation batch, individual sample variation, and non-linear responses to test drugs complicate prediction of proarrhythmic drug concentrations. This study combines a computational human action potential (AP) model of hERG channel block with experimental data from three-dimensional hiPSC-CM engineered microtissues to optimize point of departure (POD) estimation of drug-induced prolongation of AP duration (APD). Computer simulations predicted that APD prolongation from hERG block follows a logistic curve and that >81% hERG block induced early afterdepolarizations (EADs) which significantly shifted the APD response curve. Curve fitting of APD response by logistic, bilinear breakpoint, and maximal curvature was more accurate prior to EAD onset. Goodness-of-fit testing indicated that logistic regression with ≥6 test concentrations was sufficient to accurately estimate PODs. Power analysis, based on experimental variations between batches (n=14), molds (n=57), and microtissues (n=1701) predicted that PODs from 2~3 batches with 10 microtissues per mold using a 5% threshold for APD prolongation detected

proarrhythmic cardiotoxicity with a negligible false positive rate. We then applied this POD analysis to hiPSC-CM microtissue data after treatment with well characterized drugs (*i.e.*, cisapride, ranolazine, quinidine, and verapamil). Using bootstrapping, we estimated PODs and confidence intervals that matched concentrations known to cause proarrhythmic effects in patients. This study identified a robust method for calculating PODs for proarrhythmic cardiotoxicity risk *in vitro* and developed a framework for experimental design in this and other *in vitro* platforms (**Figure 3.1**).

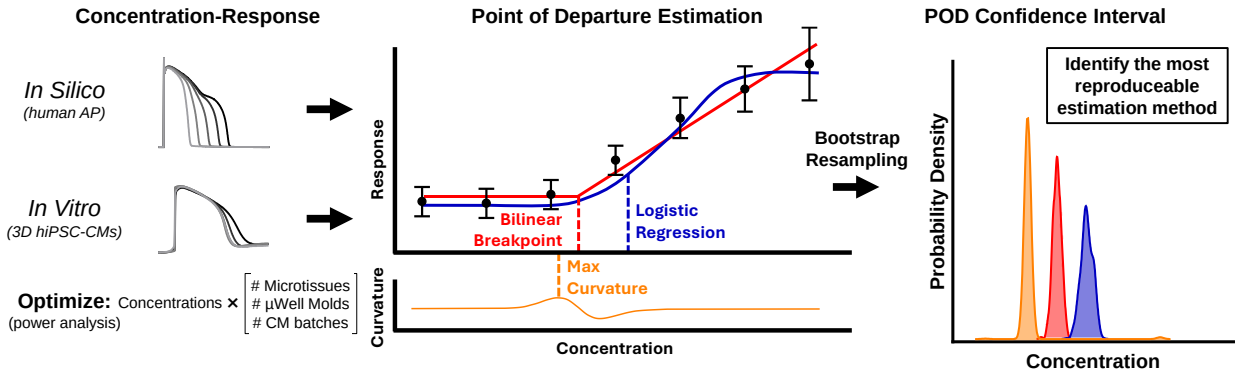

Figure 3.1. Graphical Abstract. Optimization of point of departure estimation in hiPSC-CM Microtissues

3.2. Introduction

Pharmaceutical-induced proarrhythmic cardiotoxicity remains a major health concern, regulatory focus, and obstacle to efficient drug development. Conventional pre-clinical screening has relied on reductionist *in vitro* assays lacking the complexity of human action potential changes under drug exposure [1, 2]. Therefore, pipeline compounds may be unnecessarily removed, or unsafe compounds may progress to clinical studies. Consequently, focus has turned to new approach methodologies (NAMs) using human induced pluripotent stem cell-derived cardiomyocytes (hiPSC-CMs) [2-7]. However, validating the relevance of *in vitro* endpoint metrics from hiPSC-CM systems to human safety requires improved understanding of how experimental design and analysis influence risk assessment.

Human drug-induced proarrhythmic risk is assessed by QTc prolongation >10 ms at the upper bound of the 95% one-sided confidence interval [8-11]. This QTc prolongation is typically associated with I_{Kr} (hERG channel) inhibition, which delays late-stage cardiac action potential (AP) repolarization. Pre-clinical

arrhythmia risk assessment focuses on hERG channel blockade since it initiates severe and even fatal ventricular arrhythmias. The challenge for emerging hiPSC-CM-based systems is to define platform- and endpoint metric-specific perturbations that accurately predict adverse effects, i.e. increased QTc interval. Furthermore, experiments and analyses must address inherent hiPSC-CM preparation variability: culture conditions (e.g., 2D monolayers vs. 3D tissues, culture growth medium, duration of culture, etc.), and output metrics (e.g., optically mapped AP duration (APD) or Ca^{2+} transient duration, microelectrode array field potential duration, spontaneous beating rate, contractility, and others). The stem cell biology field generally agrees that *in vitro* toxicity assessment experiments require multiple differentiation batches; however, data and statistical analyses (power calculations) are not available to determine batch number or within batch sample size. Further, this guidance may depend on the hiPSC-CM platform reproducibility, endpoint metric, and/or the point of departure (POD) calculation accuracy.

Traditionally, chemical toxicological risk has been quantified for a single metric by estimating the POD at a discrete no observed adverse effect level (NOAEL) or low observed adverse effect level (LOAEL), defined as the highest tested exposure without and the lowest exposure with a statistically significant response compared to control, respectively [12]. The accuracy of PODs derived from NOAELs or LOAELs depends on sample number and test concentrations. Alternatively, the mathematical modeling-based benchmark dose (BMD) approach has recently become the preferred technique [12-14]. A BMD is a concentration producing a predetermined change in the response of a known adverse effect endpoint. Thus, physiology must define a meaningful change in response (*e.g.*, APD increase >10 ms (~5%) increases risk for ventricular arrhythmia) and we must design the experiment considering test concentration number and sample number per condition based on confidence interval and statistical power calculations. Robustness of fit and reproducibility guide the selection of the mathematical model used to fit the concentration-response data and quantify (or estimate) the POD or BMD. Understanding the key

parameters for accurate estimation of BDM becomes more critical with increasing complexity and variability, i.e. using hiPSC-CMs for *in vitro* cardiotoxicity assessment.

This study aimed to determine the optimal method for BMD analysis through *in silico* modeling of human arrhythmogenic cardiotoxicity to assess curve fitting accuracy, and then evaluate with empirical data from our previous *in vitro* human cardiac microtissue model [15]. We used computer simulation of human ventricular action potentials [16] while increasing I_{Kr} inhibition to generate concentration response curves for BMD analysis (*i.e.,* logistic regression, bilinear breakpoint, and maximal curvature). The simulated data informed experimental design requirements and data analysis (*i.e.,* minimum test concentrations, minimum microtissues per group, curve fitting to estimate POD, and confidence interval estimation using bootstrapping). We utilized 3D hiPSC-derived cardiac microtissues [15] to assess the robustness of the *in silico* results using data from four drugs (cisapride, ranolazine, quinidine, and verapamil) used by the Comprehensive in Vitro Proarrhythmia Assay (CiPA) Initiative [17-19]. We present a framework to advance POD estimation from complex biological NAMs, including hiPSC-CM-based platforms for *in vitro* proarrhythmic assessment, and discuss how our findings may guide experiment design and analysis using other AP metrics (*e.g.,* stimulation delay, rise time, APD_{30}), cardiac currents (*e.g.*, I_{Na} and I_{Ca}), or functional endpoints (e.g., contraction).

3.3. Materials and methods

3.3.1. In silico modeling of human action potential in response to hERG Blockade

We primarily used the human ventricular myocyte action potential (AP) computer model of Tomek et al. [16] (referred to as ToRORd in Figures) which is a modification of the O'Hara Rudy human AP model [20] (referred to as ORd in Figures). For comparison, results from the ORd model are presented in Supplemental Figure B.2.

We modeled hERG drug binding using **Equation 3.1**.

$$Block\ Ratio\ = \frac{1}{1 + \left(\frac{IC50}{C}\right)^{h}}$$ **(Equation 3.1)**

IC_{50} is a half maximum inhibitory concentration, c is the concentration of a drug, and h is a Hill coefficient. In this study, the drug concentration was varied from 1 nM to 1 mM with an IC_{50} of 1 µM and Hill coefficient, h = 1. hERG conductance of 0.04173 mS/mF (epicardial myocyte default value from [16]) was used for healthy/control condition and multiplied by (1 - Block ratio) to simulate the effect of blocking hERG in the AP model.

To study whether and how the presence of early afterdepolarizations (EADs) influenced POD estimation, we varied the conductance of I_{Ks} (g_{Ks}) from 0.5 times to 10 times the base g_{Ks} value of 0.0011 mS/mF since high I_{Ks} compensates for low I_{Kr}. The results were confirmed in simulations of 200 cells with Gaussian distributions of six conductance parameters (g_{Na}/g_{NaL}, g_{Ito}, p_{Ca}, g_{Kr}, g_{Ks}, and g_{K1}). The original parameter, referenced in [16] was set as the mean value of the distribution with the width set from a standard deviation equal to 20% of the original parameter values as previously described The simulations to investigate the effect of blocking hERG channels were carried out for 150 beats at a cycle length of 2000 ms with double precision on a Nvidia Tesla K40 multicore graphic processing unit using the CUDA toolkit (https://developer.nvidia.com/cuda-zone). Data visualization was performed using Python packages (python version 3.11, matplotlib v3.9, scipy v1.14, and seaborn v0.13).

3.3.2. Point of departure estimation

3.3.2.1. Concentration-response regression methods and benchmark dose definitions

Action potential durations (APDs) from simulation data were measured by subtracting depolarization time from repolarization time (90% recovery, APD_{90}) using custom python scripts as described in [21]. Three different definitions of BMD curve fitting approaches were tested for calculating a POD using simulated APD_{90} and APD_{tri} (APD_{90} – APD_{50}) data with log-transformed concentrations. These included 1) the point of maximal curvature where the drug response has the highest rate of change, 2) logistic function and a 5% increase relative to baseline, and 3) the breakpoint derived from a two or three-

segment piecewise linear regression (bilinear and trilinear regression) that separates the baseline with little drug effect versus APD prolongation region.

Maximal curvature: The curvatures of APD versus drug concentration were measured using a 3-point Menger curvature estimation in Python (v3.11) based on the R package by Kim T. To and Lyle Burgoon [https://rdrr.io/github/k-t-to/gravee/: Good Risk Assessment Values for Environmental Exposures]. Since this method fits a circle to 3 points and the curvature is defined by 1/R (R = radius of circle), it is highly sensitive to the unit of the x axis. To ensure the overall fitting increases monotonically with concentration, the x axis unit was altered to be $\Delta x > \max(\Delta y)$. After curvature calculation, POD was chosen as the concentration with the maximal curvature.

Logistic regression: The computer modeling demonstrated that APD versus hERG block behaves logistically until the concentrations when EADs occur. The concentration-response curves were fitted to a logistic function defined by **Equation 3.2.**

$$y = \frac{L}{1+e^{-k(x-x_0)}} + b \qquad \textbf{(Equation 3.2)}$$

Here, y is APD, x is log scale of drug concentration, x_0 is a half concentration of overall APD change, L is the overall APD change, k is steepness of the curve, and b is the baseline APD. The scipy.optimize.curve_fit package was used with appropriate boundary conditions and max_iteration=5000.

Bilinear regression and its acceleration using the softplus function: The concentration-response curves were fitted to piecewise linear functions using the Python pwlf package (https://pypi.org/project/pwlf/). Typically, bilinear regression was sufficient with the POD estimated at the breakpoint separating the two segments. The algorithm of piecewise linear regression requires significant computing time to search possible breakpoints and best segment combinations. In the case of APD versus hERG block where APD prolongation is largest around IC_{50}, the curve can be fitted to the softplus function that is a smoothed

version of the rectifier or ramp function where the output increases linearly when x >0 and is frequently used in machine learning as an activation function. We used a modified softplus function (**Equation 3.3**) where L is for the overall change (ΔAPD) and k determines smoothness around x_0, as well as used curve_fit package for fitting as described in the logistic regression.

$$y = \log\left(1 + e^{k(x-x_0)}\right) + b \qquad \textbf{(Equation 3.3)}$$

Interpolation of downsampled data: Experimentally, the number of test concentrations are limited to 6~10 concentrations. Downsampled data was interpolated with a cubic spline to have the same number as original data and the interpolated data used for maximal curvature, logistic regression, bilinear regression, or softplus regression.

Conversion of POD to exponential form: POD values were initially calculated as log[concentration] and then converted to concentration (exponential form). When a population of POD values were calculated, the statistics were performed on the log[concentration] values and then the mean was converted to concentration.

3.3.3. Bootstrapping and estimation of point of departure confidence intervals

Confidence intervals of PODs were estimated using bootstrapping of concentration-response curves, which does not require an assumption of normal distribution of data. Two bootstrapping methods were tested: bootstrapping the concentration-response curves from individual microtissues and bootstrapping each concentration from pooled data.

The individual microtissue bootstrap (**Supplemental Figure B.1A**) randomly selects the complete AP metric data (APD_{mxr} or APD_{tri}) from each microtissue and then calculates a mean concentration response curve from the randomly chosen microtissues. For logistic regression and maximal curvature methods, a cubic spline is fit to this mean response curve and then the fit data are used to apply the respective POD calculation method. The bilinear regression is fit to the concentration data directly. This process was

repeated 5000 times and the POD distributions were created from the resampled data set (N=5000 repeats). The 5th and 95th percentiles of this distribution represent the boundaries of the two-tailed 90% confidence interval for the estimated mean POD.

In the case of the pooled bootstrapping (**Supplemental Figure B.1B**), the AP metric data are pooled for each compound concentration and from these pools, a concentration response curve is created from random selection of microtissue data (each curve represents different microtissues at each concentration) and then the mean concentration response is fit as in the individual bootstrapping.

3.3.4. Empirical measurement of in vitro action potentials

The empirical data used in this study to complement work performed *in silico* was from a previously published study that used four well-characterized test compounds (i.e., cisapride, ranolazine, quinidine, and verapamil) that inhibit the hERG channel but have different proarrhythmic risks [17]. The data are publicly available via the Dryad Digital Repository [17]. The following is a very brief description of how these data were generated with a focus on its direct relevance to the present study in terms of both microtissue generation (**Section 3.3.4.1.**) and AP recording (**Section 3.3.4.2.**). A full description of experimental details is available in the referenced study.

3.3.4.1. Human cardiac microtissues generation

Ventricular hiPSC-CMs were differentiated from GCaMP6f-expressing hiPSCs (WTC11 human male, Gladstone Institutes) following established protocols leveraging bi-phasic Wnt activation and inhibition [17, 22]. After differentiation, hiPSC-CMs were metabolically purified using DMEM minus glucose (Gibco) supplemented with 4 mM sodium lactate (Sigma). Purified hiPSC-CMs were combined with 5% primary human cardiac fibroblasts (hCFs; Cell Applications) into 35-microwell agarose molds with hemispherical bottoms (3D Petri Dish®, Microtissues, Inc) to allow for self-assembly. The microtissues were subsequently cultured for 6-8 days under electrical field stimulation with a 1 Hz, 10 V, 4 ms duration bipolar pulse train (C-Pace EP, IonOptix) with media changes after the first 24 hours and every 2-3 days until use.

3.3.4.2. Optical mapping of cardiac action potentials

Microtissue action potentials were recorded using the voltage-sensitive dye di-4-ANEPPS (Invitrogen) (**Figure 2.1**). AP traces were subsequently reconstructed from fluorescence intensity data and semi-automated analysis using in-house software to enable the measurement of AP duration and its triangulation as previously described [21, 23] (**Figure 2.1D**). Fluorescence recordings of AP from microtissues often exhibit baseline drift, which can interfere with the detection of repolarization times. Thus, microtissue APDs were measured using the maximum rate of repolarization (APD_{mxr}) defined by the maximum second derivative as described in [21] instead of APD_{90} as in the case for simulated data (Section 3.2.1). Measurements were obtained at baseline with vehicle (DMSO) and after exposure to six sequentially increasing concentrations covering three orders of magnitude with half-log spacing. For each compound, data were collected for three separate agarose molds (up to 35 microtissues each) from two to three independent cardiac differentiations. Additional baseline data was collected for analysis of sources of biological and technical variation described in the next section that does not appear in the previously published study.

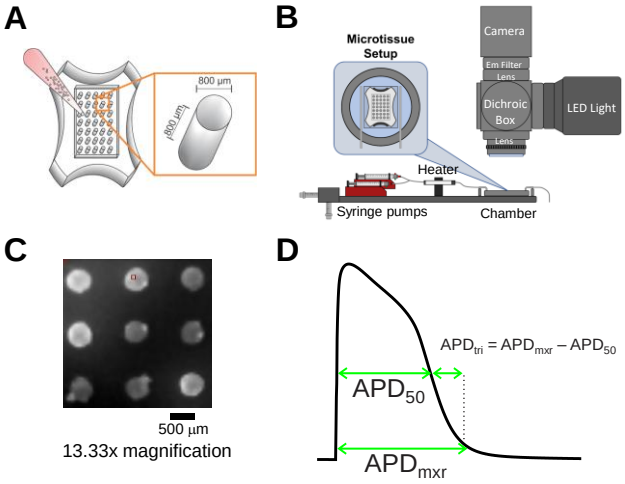

Figure 3.2. Microtissue Optical Mapping Platform. (A) Drawing of microtissue mold with 35 wells. Each well contains 1 microtissue. Inset shows the dimensions of 1 well. **(B)** Cartoon of the optical mapping setup. Solutions are perfused via syringe pumps through an inline heater into a temperature-controlled chamber and evacuated by vacuum suction. Inset shows orientation of the mold in the chamber with stimulating electrodes (left and right sides). **(C)** Sample image of 9 microtissues from the camera setup showing baseline Di-4-ANEPPS fluorescence. **(D)** Illustration of an action potential (AP) trace and the definitions of APD at maximum repolarization (APD_{mxr}) and APD triangulation (APD_{tri}) measured from microtissue imaging data.

3.3.4.3. Power analysis using Monte Carlo simulation of empirical microtissue data

Standard deviations between batches, molds, microtissues, beats within the same scan and repeated measures were calculated from the baseline data of 14 CM batches, 57 agarose molds, and 1701 individual microtissues in addition to variability after treatment with cisapride for a subset of the data for which it was available (**Supplemental Table B.2**). The batch standard deviation represents the standard deviation of all batch APD_{mxr} values calculated from the mean mold APD_{mxr} values for each batch. The mold standard deviation represents the mean of standard deviations calculated from the microtissue APD_{mxr} values for each mold. Microtissue standard deviations within each mold were calculated and then the mean of those standard deviations represents the microtissue-to-microtissue standard deviation. Each microtissue recording included four APs, termed 'beats'. The standard deviation of the APD_{mxr} values for each microtissue was calculated, and the mean of these standard deviations represents the beat-to-beat variation. The microtissue recordings were repeated multiple times (~3 times) to obtain variations between scans from the same microtissues (repeated measure standard deviation).

To determine sample size requirements for detecting physiologically relevant (5-10%) shifts in APD as well as the risk of incorrectly identifying statistically significant shifts in untreated microtissues (0%), the Monte Carlo method was used to simulate two sets of microtissues data. For each level of variance modelled, excluding the batch-level, the simulation-specific standard deviation was defined by randomly selecting values from a Gaussian distribution defined by the mean standard deviation and standard deviation of standard deviations at the mold, microtissue, and beat level based on the number of simulated batches, molds, and microtissues. For batch-level variance, the standard deviation was constant as a standard deviation of standard deviations could not be calculated.

Next, random selection from Gaussian distributions with means of zero and the selected standard deviations were used to select the batch-, mold-, microtissue-, and beat-level shifts from the overall mean APD for every simulated beat. This process was repeated for mold- and microtissue-level variation that

resulted from recording-to-recording variability. Drug responses were simulated at the batch-level with the mean batch response set to either 0%, 5%, or 10% of the overall mean APD at baseline with variance scaled from the cisapride response data. The net sum of these values for each beat resulted in the final simulated data.

For each combination of sample size for batch, mold, and microtissue, the false positive rate (type I error rate) was determined by simulating 200 data sets with a mean drug effect of 0% (0 ms) and performing either an ANOVA or repeated measures ANOVA (ANOVARM) based on independent or paired analysis, as appropriate. It should be noted that in the case of two experimental groups, an ANOVA is mathematically equivalent to a t-test. Since there was no simulated drug effect, a p-value of less than 0.05 was taken to be a false positive caused by either biological or technical variation. A similar approach was used to estimate the rate of false negatives (type II error rate), but the drug effect was set to either 5% (19.5 ms) or 10% (39 ms). In this instance a p-value greater than 0.05 would be considered a false negative since there was a preset drug response.

3.4. Results

3.4.1. In silico modeling and POD estimation

3.4.1.1. Simulated concentration-dependent action potential responses to hERG blockade

BMD analysis requires selecting a proper model to fit the concentration-response data and interpretation of risks accordingly. One of the major conditions underlying drug-induced arrhythmia is acquired long QT syndrome, caused by inhibition of hERG channels, which pass a major repolarizing current. Inhibition of hERG channels by chemicals can delay repolarization, resulting in prolonged APD or early afterdepolarizations (EADs, additional depolarizations before full repolarization of cardiac action potentials) (**Figure 3.3A**). As a result, the APD response to hERG inhibition is non-linear, making it difficult to choose proper models for BMD analysis.

We first investigated the dynamics of APD prolongation as a function of hERG block using computer simulation of human cardiomyocyte APs. hERG current was varied from 100 to 0% of the initial value of

hERG conductance, g_{Kr}. To study how the presence of EADs alters APD dynamics and curve fitting, I_{Ks} channel conductance (g_{Ks}) was also varied in the model from 50% to 1000% of the initial value to provide conditions that either trigger EADs (1x g_{Ks}) or prevent EADs (10x g_{Ks}) at high hERG block ratios. **Figure 3.3A-B** show sample AP traces from the human AP simulation under conditions with EADs (panel A, green/orange traces) or no EADs (panel B) respectively at different percentages of hERG block. For the ToRORd model, APD prolongation is linear ($R^2 > 0.95$) to ~ 68% hERG block with EADs and ~ 80% block without EADs (**Figure 3.3C-D**). Therefore, in the presence of EADs, APD dependency of hERG block deviates from a linear relationship at a lower percentage block than without EADs.

We then investigated the relationship between APD and drug concentration. When the Hill equation was used to model hERG inhibition (IC_{50} = 1 μM), APD prolongation follows a sigmoidal relationship but is shifted relative to the drug binding relationship (**Figure 3.3E, right panel**, dashed black line), and this shift (red arrow) persists whether the data are plotted as raw APD, ΔAPD, normalized APD (not shown), or normalized ΔAPD. This is mainly because APD prolongation is no longer linear to hERG block at higher concentrations where APDs prolong more rapidly as shown in panels C and D. At the IC_{50} for drug block, the model predicts an ~40% increase in APD in the presence of EADs and an ~33% increase without EADs. The normalized ΔAPD plot (**Figure 3.3E, right panel**) shows that the presence of EADs causes further deviation from the shape of a typical logistic function. The ORd human AP model [20] also exhibits a similar relation between IC_{50} and change in APD (**Supplemental Figure B.2**), highlighting difficulties in simulating concentration-response relationships.

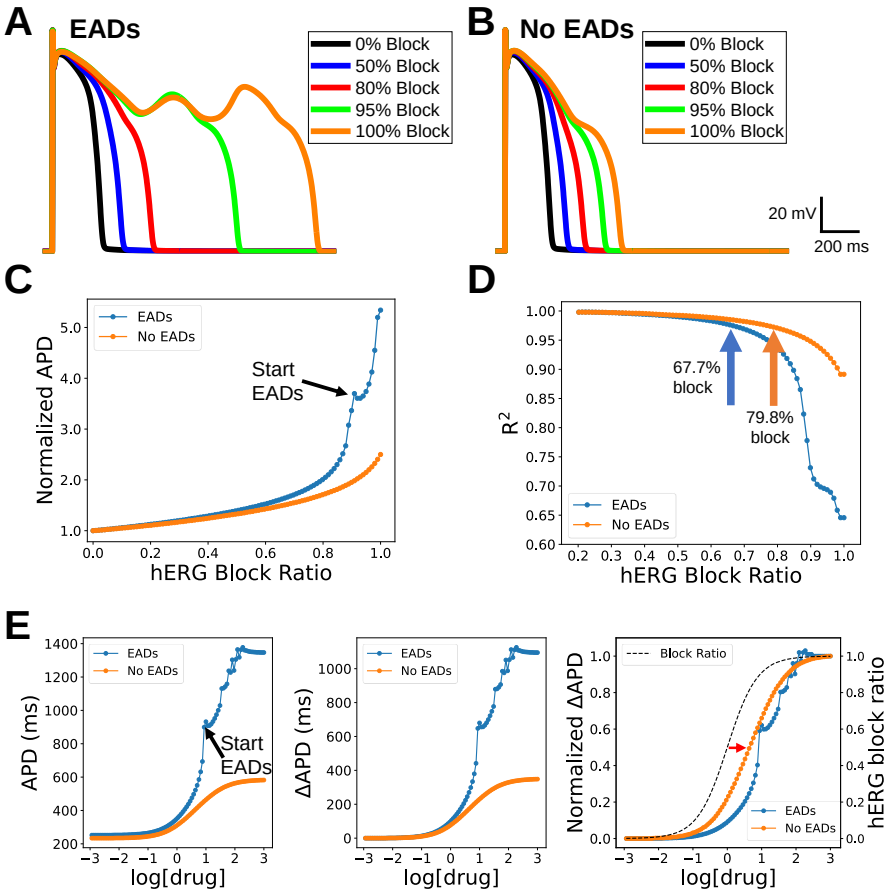

Figure 3.3. APD prolongation due to hERG block only is linear to ~67 - 80% block. (A) Sample simulation traces from the Tomek et al. [16] human action potential model at different percentages of hERG block with gKs=0.0011 mS/µF (1x) that allowed early after depolarizations (EADs) with 90 – 100% block of hERG. Note EADs at 95% and 100% hERG block. **(B)** Sample simulation traces as in (A) with no EADs (gKs=0.011 mS/µF, 10x). **(C)** Plot of normalized APD versus hERG block ratio showing non-linear behavior of APD above 50% hERG block. **(D)** Plot of R^2 versus hERG block ratio. R^2 drops below 0.95 after 67.7% (EADs) or 79.8% (No EADs) block. **(E)** Plots of raw APD (left panel) and ΔAPD (center panel) versus log drug concentration (IC_{50} of 1 µM), and normalized ΔAPD values (left y-axis), hERG block ratio (right y-axis, black dashed line) versus log drug concentration (right panel) all under conditions of no EADs (orange) or EADs (blue). Note the rightward shift in the dependency of normalized ΔAPD on log[drug] (red arrow) compared to the block ratio dependency (black dashed line). ΔAPD (%) at 1 µM concentration (IC_{50}) is 39.7 % for the EAD condition and 32.9 % for the no EAD condition.

3.4.1.2. Difficulties of curve fitting and POD estimation due to the presence of EADs

We tested three different methods for calculating POD from the human AP simulation data: (1) point of 5% increase of a logistic regression over the baseline, (2) bilinear breakpoint from a two-segment piecewise linear regression, and (3) point of maximal curvature by the Menger calculation. **Figure 3.4A-C** show the APD response to concentration data and curve fits for simulations with and without EADs (blue and red lines, respectively). The presence of EADs had minimal influence on the POD values (0.107 µM

versus 0.096 μM, 11.5%) obtained from the logistic regression analysis compared to no EADs; whereas the maximal curvature and bilinear methods generated PODs that were more than 4-fold higher with EADs compared to the no EAD condition (maximal curvature: 6.6 μM (EADs), 0.81 μM (No EADs); bilinear: 0.59 μM (EADs), 0.14 μM (No EADs). For the no EAD condition, the bilinear method gave a POD closer to the logistic regression, but the maximal curvature POD was still shifted to a higher drug concentration. These POD differences appeared because bilinear regression and maximal curvature analysis are greatly affected by the rapid increase of APD at higher drug concentrations while the POD estimation using logistic regression with 5% above the baseline is less affected by the rapid increase of APD and presence of EADs at higher drug concentrations.

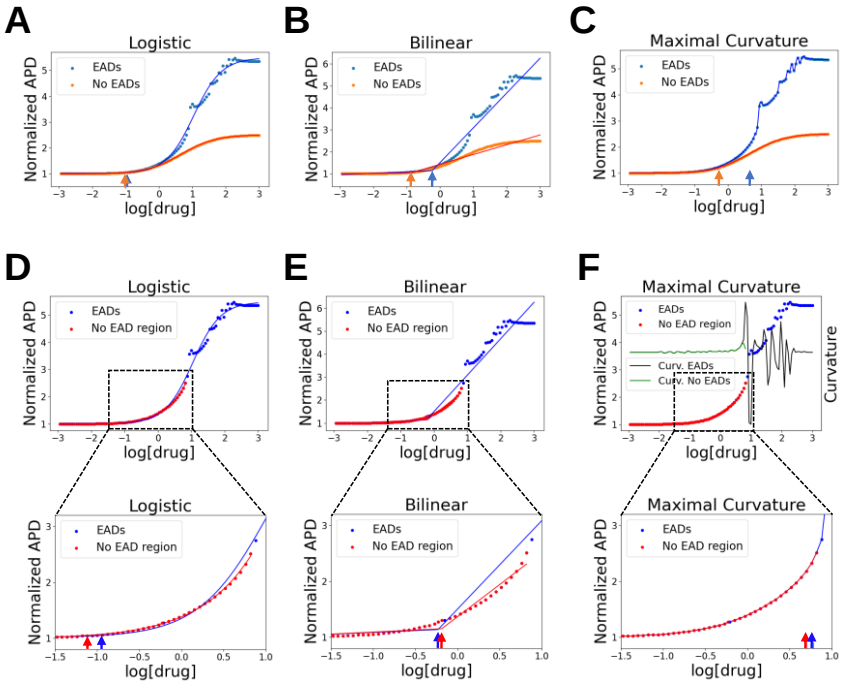

Figure 3.4. Benchmark logistic regression calculation of POD from *in silico* APD data is the most invariant method over a range of AP conditions. (A-C) Comparison of POD values between EAD condition vs. no EAD condition by enhanced g_{Ks}. Plots show normalized APD_{90} for full data sets from human AP computer simulations with (blue) and without EADs (red). Dark blue and orange lines indicate curve fit results from EAD and no EAD conditions respectively. Blue and orange arrows on graph indicate estimated POD values on graph. Logistic regression, with EADs: POD=0.11 μM, % hERG block at POD=10. Logistic Regression, EAD region removed**:** POD=0.096 μM, % hERG block at POD=9. Bilinear, EADs**:** POD=0.59 μM, % hERG block at POD=37. Bilinear, EAD region removed**:** POD=0.13 μM, % hERG block at POD=12. Maximal Curvature, EADs**:** POD=6.6 μM, % hERG block at POD=87. Maximal Curvature, EAD region removed**:** POD=0.81 μM, % hERG block at POD=45. **(D – F)** comparison of POD values between full range (x range from -3 to 3) vs. reduced range (x range from -3 to 1) where EADs are absent. Expanded plots show details of curve fitting and that removing the EAD region improves fitting. Logistic regression, EADs: POD=0.11 μM, % hERG

block at POD=10; Logistic Regression, EAD region removed: POD=0.077 μM, % hERG block at POD=7. Bilinear, EADs: POD=0.59 μM, % hERG block at POD=37; Bilinear, EAD region removed: POD=0.65 μM, % hERG block at POD=39. Maximal Curvature, EADs: POD=6.6 μM, % hERG block at POD=87; Maximal Curvature, EAD region removed: POD=5.7 μM, % hERG block at POD=85. **(F)** Note the oscillations in the curvature measurements (black line, top panel) due to the abrupt APD increases in beat-to-beat EAD genesis.

Since a sudden increase of APDs and the presence of EADs at higher concentrations alters overall curve fitting and POD estimation, removing that portion of the data should reduce fitting residuals for better POD estimation. **Figure 3.4D** shows a plot of the full range of APD data with EADs overlaid on the same dataset with the EAD region not included for curve fitting. The expanded portion of the graph (dashed rectangle) shows the logistic regression fits the data without EADs (red line) better than with EADs (blue line) as expected. The bilinear regression fits the no EAD data better as well but still yields a POD corresponding to 39% hERG block (**Figure 3.4E**). The maximal curvature fitting and POD calculation is sensitive to the range of concentrations because PODs are being detected at higher concentration due to a greater curvature near the steep portion of the APD versus concentration relationship (**Figure 3.4F**). In addition, EADs are stochastic and beat-to-beat EAD genesis created abrupt APD increases, leading to oscillations in the curvature measurements (**Figure 3.4F** black line), which can increase errors in POD calculation. Overall, curve fitting and POD calculations are more reliable from a data set without the EAD region and the logistic regression method of POD calculation is the most invariant over different g_{Ks} values for full (**Figure 3.4**) or reduced data samples (**Supplemental Figure B.3**).

3.4.1.3. Minimal number of test concentrations required for POD estimation

We extended the computer modeling study to include variations in APD response to hERG block to further validate the benefits of fitting to data sets without EADs. The conductance of Na^+, Ca^{2+}, and K^+ currents were varied to have a Gaussian distribution (see *Methods*) and their respective responses to hERG block were simulated (**Figure 3.5**). At baseline, the standard deviation is approximately 30 ms (**Figure 3.5D-E**) in line with the mold-to-mold variability in the experimental data (see **Figure 3.7** below). APD variations among cells become larger with increasing drug concentration due to the presence of EADs (**Figure 3.5D-E**). In order to simulate variability of experimental data, random noise (**Supplemental Table**

B.2) was added to the APD_{90} values (**Figure 3.5F**). The fitting of logistic regression to the full simulated data (**Figure 3.5G**) was better without EAD regions as was observed in the initial modeling (up to ~0.5 end log[concentration], **Figure 3.5H**). Without noise, the mean squared error (MSE) of the logistic regression remains low until about 80% hERG block, where it starts increasing. The addition of random noise shifted the MSE higher, but the relationship in regard to increasing hERG block is similar (**Figure 3.5H**).

Each *in silico* AP concentration response curve has 100 points simulating 100 drug concentrations. However, only a few concentrations can be measured experimentally, which may hinder correct estimation of PODs. Thus, we evaluated the number of test concentrations required to calculate PODs with the least difference compared to PODs calculated from 100 concentrations. **Figure 3.5I** shows errors of logistic fitting with a varying number of concentrations, down to 3 concentrations. The MSEs are large with 3 concentrations, become smaller when the fittings include a greater number of test concentrations, and the errors become sufficiently small at ≥6 test concentrations. Similar to the comparison of logistic regression residuals, the MSE reached a minimum at about 7 concentrations for POD estimation (**Figure 3.5J**), suggesting that 6~8 test concentrations are sufficient to predict POD with greatest accuracy. This data shows that with only 4 concentrations and noise in the measurement (red data), the root mean squared error for estimating POD is about 0.1 μM for this dataset, where POD is 0.077 μM (**Figure 3.5D**), and is arguably insufficient for estimating PODs. **Figure 3.5K** plots the POD (calculated by logistic regression) probability density for the full simulated 100 concentration samples with (black) and without (red) noise and 7 concentration samples with noise (blue) which shifts the median POD by about 21% compared to full sample with noise. The results of bilinear and maximal curvature methods also support a range of 6 ~ 7 concentrations and under 81% hERG block as reasonable conditions to estimate PODs with a minimal MSE (**Supplemental Figure B.4**).

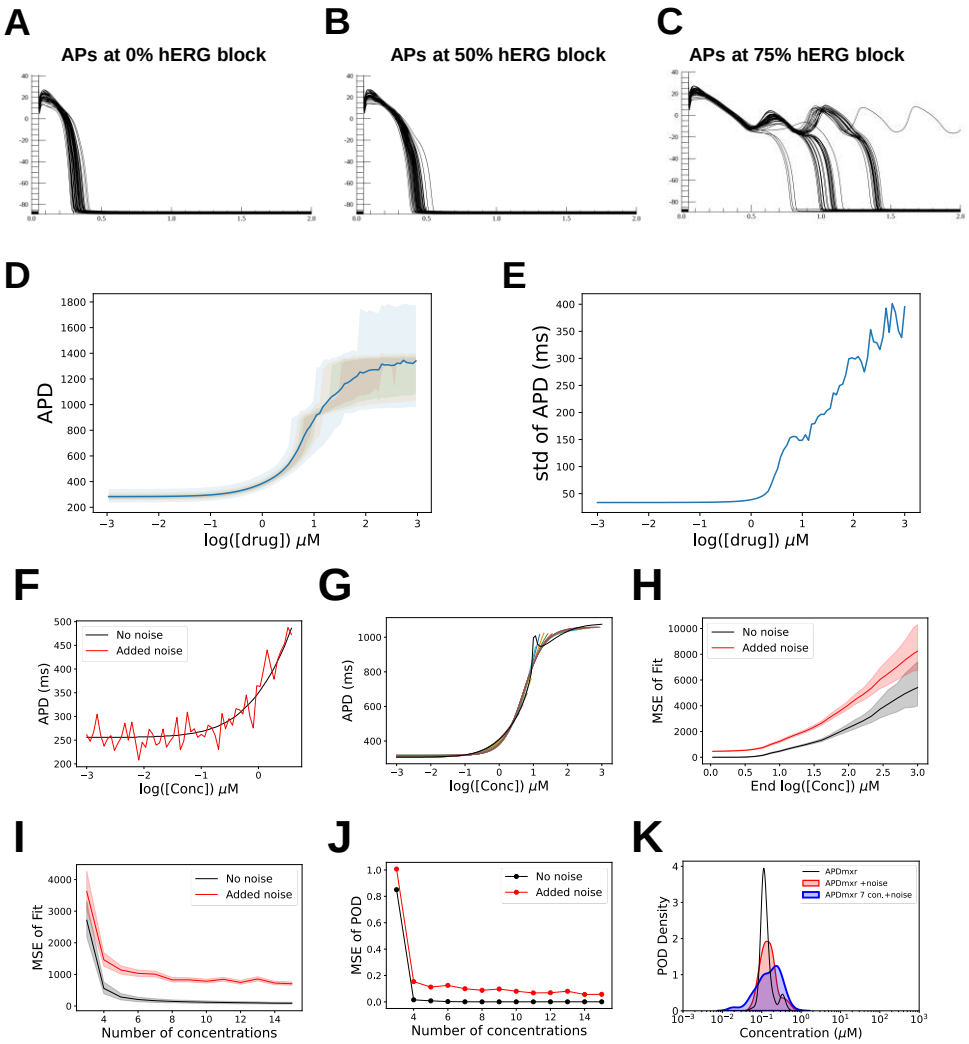

Figure 3.5. Population modeling of hERG channel block by computer simulation to compare sigmoidal regression POD calculation of full sample *in silico* data with reduced sample data. Population action potentials were modeled by randomly varying I_{Na}, I_{Ca}, I_{Kr}, and I_{Ks} conductances by 20%. **(A)** Action potential traces overlapped from 200 cell parameter sets (No I_{Kr} block). **(B)** APD prolongation after 50% of I_{Kr} is blocked. **(C)** APD prolongation and EAD genesis after blocking 75% of I_{Kr}. **(D)** Quantile plots of APD and standard deviation of APD. Drug binding to hERG was modeled using the Hill equation with IC_{50} = 1 μM and Hill coefficient h=1. **(E)** Quantile plots of normalized APD and APD standard deviation. Both raw APD and normalized APD show sigmoidal response with increasing variation at higher concentrations. Simulated data was reduced to # concentrations by resampling to model experimental conditions in which a limited number of drug concentrations are administered. **(F)** Full sample simulated data with an x range of 60 (81% block) without noise (black line) and with randomly added noise (see *Methods*, red line). **(G)** Full sample simulated data overlaid with logistic regression curves fit to curves with different x ranges. **(H)** Plot of mean squared error (MSE) of sigmoidal fit with different x ranges of simulated data without noise (black line) and with added random noise. **(I)** Plot of MSE of fit of reduced data versus number of concentrations without noise and with added noise. **(J)** Plot of MSE of POD, $\frac{1}{n}\sum_{i=1}^{n}(PODfull - PODreduced)^2$, versus number of concentrations used in resampling the reduced data (see *M*) with and without added noise. **(K)** POD probability density plot for full sample data (black, median=0.12 μM, 90% confidence interval=0.09, 0.33), full sample data with added noise (red, median=0.14 μM, 90% confidence interval=0.08, 0.38), and 7 concentration reduced concentration number data with added noise (blue, median=0.17 μM, 90% confidence interval=0.04, 0.41).

3.4.1.4. Minimal concentration range required for POD estimation

Using the simulated AP population data, we compared the three POD fit methods for full hERG block range data to reduced hERG block range data (without EADs) and reduced sample data of 7 concentrations. For both, the POD shifts to higher concentrations for the bilinear and maximal curvature fits compared to the logistic fit (**Figure 3.6**). Including the EAD region in the POD analysis (**Figure 3.6A-C**) broadens the POD distribution and results in extended tails in the distribution compared to the analysis without the EAD region (**Figure 3.6D-F**). The mean and standard deviation values reflect the effect of removing the EAD region: Logistic full = 0.2 μM ± 2.6 vs. reduced range = 0.1 μM ± 1.4; Bilinear full = 0.4 μM ± 1.5 vs. reduced range = 0.4 μM ± 1.4; Maximal curvature full = 9. 3 μM ± 9.3 vs. reduced range = 0.8 μM ± 1.2. The bilinear and maximal curvature methods exhibit greater dependence on concentration range compared to logistic regression (**Supplemental Figure B.5**). By comparing the mean POD dependency on the concentration range (endpoint log[concentration]), using the logistic regression method on the AP population simulation data produced relatively similar POD values even in the presence of EADs (ΔPOD=0.32, **Supplemental Figure B.5A**). However, the bilinear and maximal curvature methods started increasing well before the EAD region of the data and had higher ΔPOD (0.77 for Bilinear, 0.77 for softplus and 1.73 for Maximal Curvature **Supplemental Figure B.5B-D**) because these methods are greatly influenced by the rapid rise of APD near IC_{50} and later the presence of EADs (**Supplemental Figure B.5E-F**).

3.4.2. In vitro validation of POD estimation and model assessment

3.4.2.1. Characterization of baseline variance at batch-to-batch, mold-to-mold, microtissue-to-microtissue, beat-to-beat, and recording-to-recording levels

We sought to characterize the biological and technical variability of our microtissue platform at each level of experimental uncertainty: batch-to-batch, mold-to-mold, microtissue-to-microtissue, and beat-to-beat (**Figure 3.7**). Fourteen independent cardiomyocyte differentiations were used to generate at least three molds of microtissues each (**Figure 3.7A**). Action potential recordings were taken at baseline prior

to drug administration and average measurements for each batch, mold, microtissue, and individual beat were used to calculate variation at each level (**Figure 3.7B**). The average APD_{mxr} standard deviation was observed to decrease with corresponding magnitude of scale (*i.e.* between batches [91.99 ms], mold within the same batch [29.85 ± 16.12 ms], microtissue within the same mold [24.49 ± 6.98 ms], and beat-to-beat within the same microtissues [5.58 ± 7.93 ms]), reflecting the compounding effects of multiple sources of technical and biological uncertainty, particularly among different batches of differentiated CMs.

The distributions of APD_{mxr} exhibit relatively long tails, indicating the variability of mean values across batches and molds with some having substantially short or long APDs (**Figure 3.7C-F**). As a result, APD was not normally distributed among batches and molds (D'Agostino-Pearson test on normalized APD_{mxr} distributions, quantile-quantile plots in **Supplemental Figure B.6**). Moreover, APD distribution within only 57% of batches (8 of 14 batches) was normally distributed (**Supplemental Figure B.6C**). However, within the same molds, most APD distributions can be considered normal (52 out of 57 molds, 91%, **Supplemental Figure B.6D**). This degree of variation and lack of normality between batches and within batches present complexity in estimating confidence intervals for POD analysis and power analysis, requiring the use of methods that do not require a-priori distribution requirements, like the Monte Carlo method.

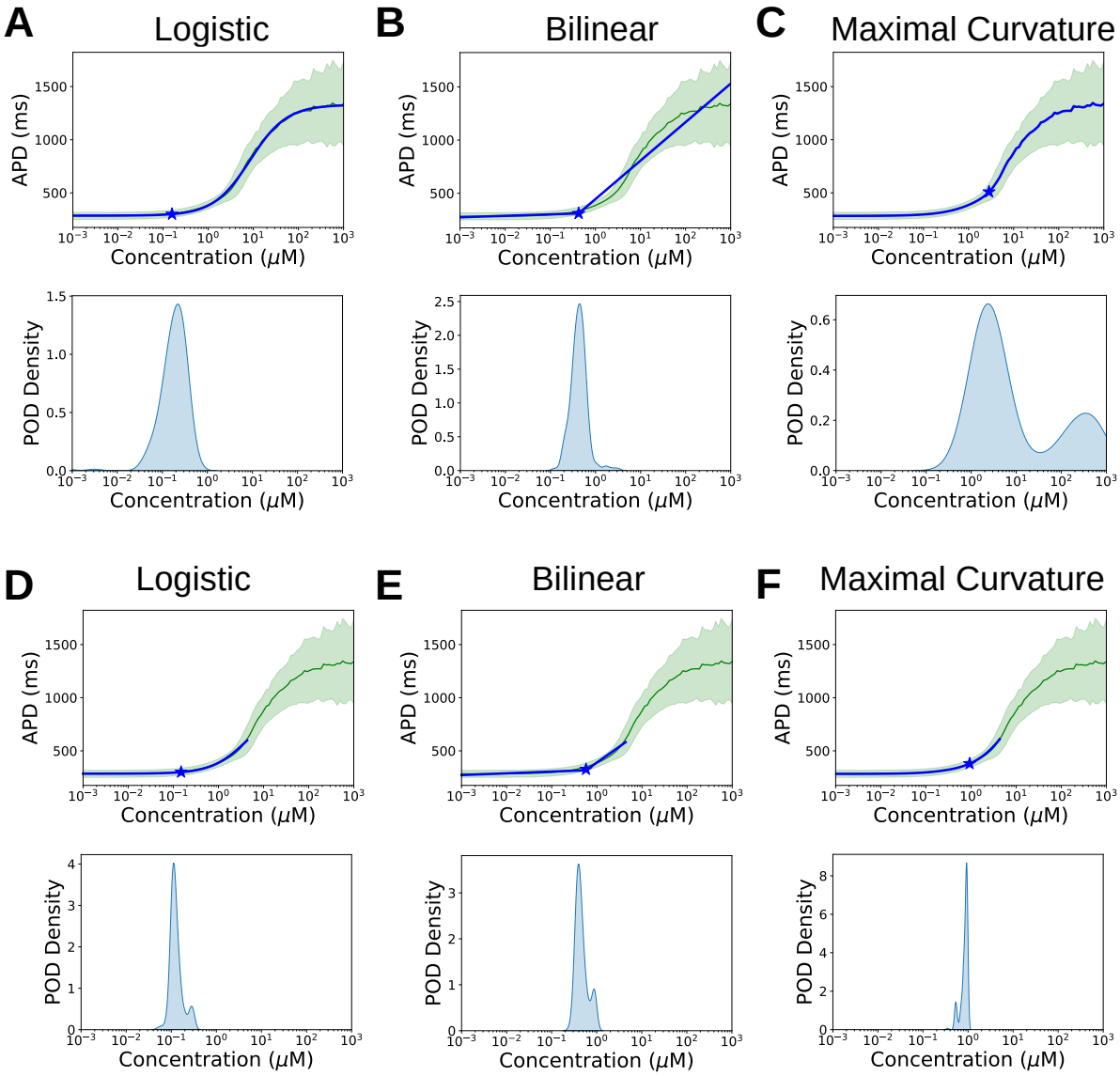

Figure 3.6. Population modeling comparison of POD values for AP data calculated with 3 different fit methods. (A-C) Mean (green line) and standard deviation (light green shading) of full concentration range of raw APD_{90} versus concentration (top) overlaid with logistic, bilinear, and cubic spline (for maximal curvature) fits (blue lines) and probability density plot of POD (bottom). Star indicates location of mean POD on the plot. **(D-F)** Mean (green line) and standard deviation (light green shading) as in (A-C) overlaid with logistic, bilinear, and cubic spline fits (blue line) of reduced concentration range data without EADs (x range = 60, 81% hERG block) for 7 concentrations (top) and corresponding probability density plot of POD (bottom). Star indicates location of mean POD on the plot.

We also analyzed the repeated variability of the experimental data with multiple scans spaced 10 minutes apart from the same microtissues under baseline condition (n = 5 batches and 9 molds) (**Supplemental Table B.2**). Recording-to-recording standard deviations for APD_{mxr} were measured to be

11.6 ms or 2.6% of mean APD_{mxr} at the microtissue level and 9.1 ms or 2.1% of mean APD_{mxr} at the mold level.

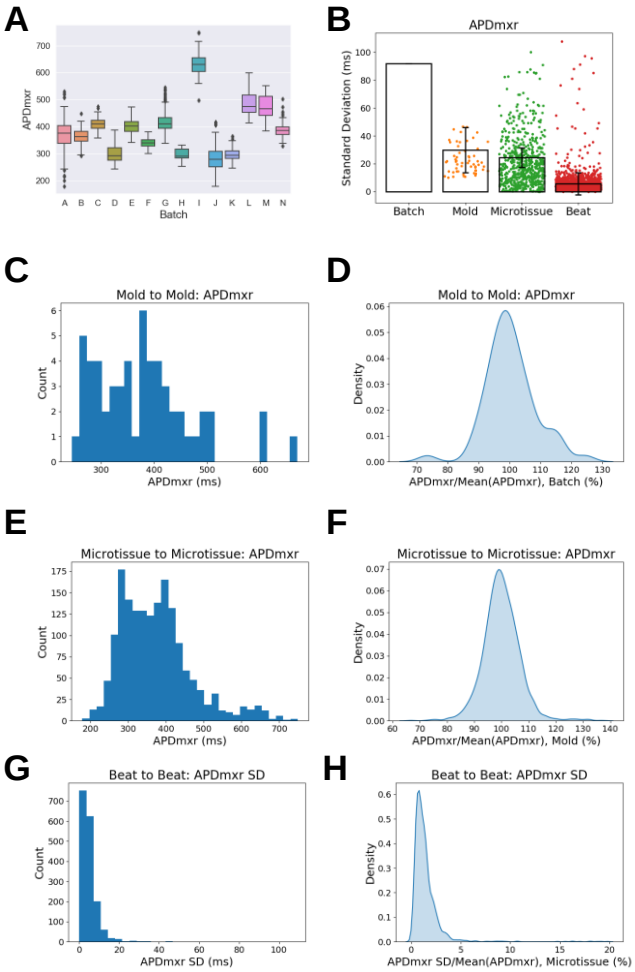

Figure 3.7. Mold-to-mold variability for a given batch is less than 10%. (A) Boxplots of mean APD_{mxr} for each batch (single recordings). (B) Mean APD_{mxr} standard deviations calculated for equal weight per batch and normalized to have same weight over different molds per batch. Data points represent standard deviations included in the mean calculation for each goup. (C) Histogram of the mean APD_{mxr} for each mold (not normalized). (D) Probability density plot of normalized mold-to-mold APD_{mxr}. Values were normalized by dividing each mold APD_{mxr} value by the mean of the batch that included those molds and expressing as percent. Standard deviation of the distribution is 8.1%. (E) Histogram of the mean APD_{mxr} for each microtissue (not normalized). (F) Probability density plot of normalized microtissue-to-microtissue APD_{mxr}. Normalization as in (D). Standard deviation of the distribution is 6.7%. (G) Histogram of APD_{mxr} standard deviations beat-to-beat per microtissue (not normalized). (H) Probability density plot of normalized beat-to-beat APD_{mxr} standard deviation. Values were normalized by dividing each beat-to-beat standard deviation by the mean APD_{mxr} of the microtissue that included those beats.

3.4.2.2. Power analysis to determine the optimal numbers of batches, molds, and microtissues

The application of POD analysis to actual *in vitro* cardiac microtissue data requires determination of the number of microtissues, molds, and batches necessary to correctly detect physiologically relevant

changes. Since the variations between batches, within batch, between molds, within mold, between microtissues, and within microtissues are all different, conventional power analysis using a single standard deviation number may cause over- or underestimates of the necessary numbers of replicates.

Instead, we used the Monte Carlo method based on the standard deviations of batch, mold, and microtissues (**Figure 3.7, Supplemental Table B.2**). We first generated two independent samples with preset APD differences of 0% (0 ms), 5% (19.5 ms), and 10% (39 ms), and performed ANOVA to examine statistical significance (**Figure 3.8**). As expected, statistical power increased with increasing numbers of simulated batches, molds, and microtissues. For independent samples, 2-3 batches of 1-2 molds per batch and >10 microtissues per mold were sufficient to detect 5% or 10% APD differences in >80% of simulated samples with reasonable Type I error rate (< 5%).

We then examined the case of repetitive measurements in which APDs were simulated from the same microtissues before and after drug treatment. As previously, two samples with preset APD differences were simulated using the Monte Carlo method. As expected, we found that repeated measures ANOVA (ANOVARM) increased statistical power, requiring many fewer microtissues and molds to identify statistically significant differences in APD (1 mold and <10 microtissues) for 5% and 10% changes in APD. However, ANOVARM substantially increased the Type I error rate when simulating molds that were not treated with APD prolonging compounds (technical variation only) (**Figure 3.8A**). Type I error occurred because variation between paired measurements among microtissues was not assumed independent within molds,but rather varied together, an assumption that was corroborated by our empirical data (**Supplemental Figure B.7).** If APD variation between repetitive measurements is random, the standard error of the mean APD of the mold between repetitive measurements is expected to be 5.8 ms (equal to the standard deviation of the microtissues between repetitive measurements times $1/\sqrt{N} = 11.6 \text{ ms} \times /\sqrt{4} \cong 5.8$ ms). However, the standard error of the mean calculated from the data is 9 ms that is slightly higher than the expected value, suggesting that the repetitive measurements in microtissues may not be

independent due to biological variations such as cardiac memory of APD from pacing [24-26]. As a result, a simple paired t-test or ANOVARM test with drug treatment may falsely reject the null hypothesis even though there is no drug effect. **Figure 3.8A** shows an example of Type I error from ANOVARM test where the difference between the mean values of APD is only ~ 4 ms. Therefore, we suggest that a threshold of ΔAPD > 5% be confirmed to indicate a physiologically meaningful change prior to using an ANOVARM test.

The bootstrapping of experimental data and paired vs. unpaired t-test also support the outcome of Type I error from the simulation. Type I errors of paired t-test rise with increasing microtissue numbers compared to independent t-test (**Figure 3.8C**). When the ΔAPD > 5% criteria was applied, Type I errors were much lower and negligible after n > 10 microtissues (blue line in **Figure 3.8D**), supporting that this simple threshold approach can avoid Type I error observed in our experimental data between repetitive measurements.

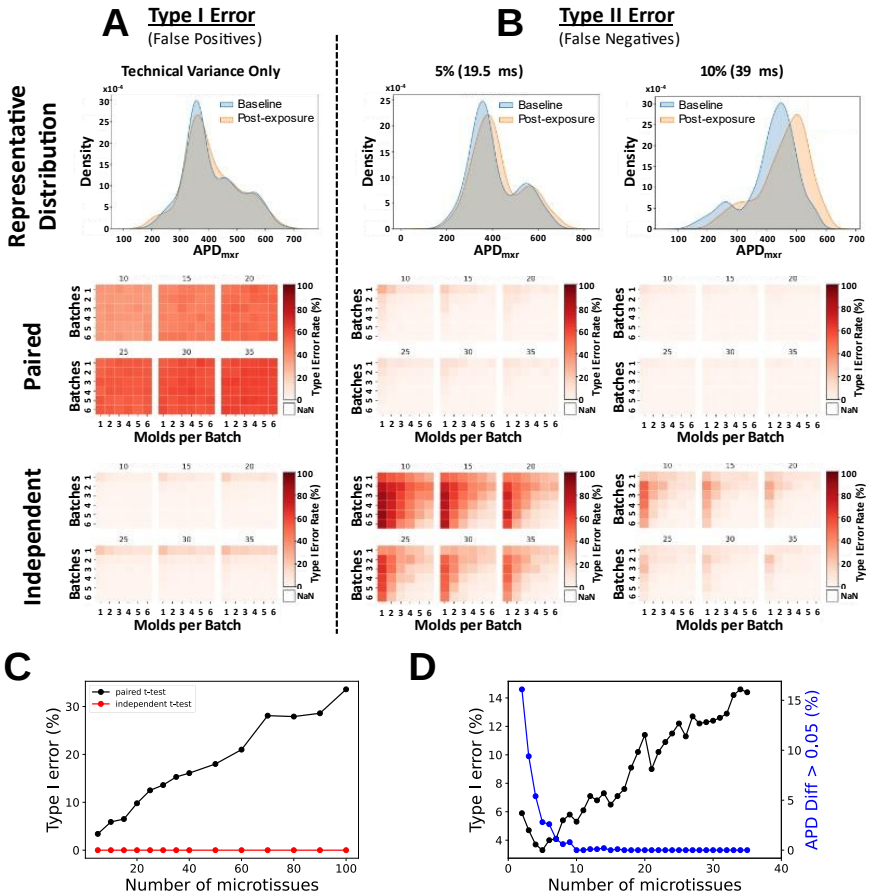

Figure 3.8. Power analysis of experimental data. Results of Monte Carlo simulations to estimate type I **(A)** and type II error **(B)** based on the mean standard deviations for batch, mold, and microtissue data (see Methods for detail). *First row:* Sample APD distribution plot of baseline (blue) and post-exposure (red). *Second row (Paired):* Type I and II error rates of paired t-test. The series of maps show Type I error rates calculated from 10 to 35 microtissues. Each map shows Type I error rates for different numbers of batches (y axis from 1 to 6 batches) and molds (x axis from 1 to 6 molds per batches). For paired t-test, Type I error rate is higher than 5% in most of the batch-mold-microtissue combinations, warning potential risks of incorrectly identifying drug effect in the absence of true APD prolongation. *Third row (Independent):* Type I and II error rates of unpaired t-test. **(C)** Plot of type I error versus microtissue number based on repeated measurements of APD_{mxr} at baseline to assess false positive rate. For each microtissue, APD_{mxr} values from the first and second recordings were resampled by bootstrapping and compared by paired or independent t-test for different numbers of microtissues (5, 10, 15, ...,40, 50, …, 90,100 microtissues) and repeated 1000x. The y-axis represents the percentage of p-values < 0.05. **(D)** Same plot of paired t-test case as in (C) with x scale to only 35 microtissues (2, 3, 4, …,34,35 microtissues) plotted with fractional mean APD difference (Recording2 – Recording1)/Recording1 > 0.05 from 1000 resamples (blue). After application of 5% threshold, Type I error rate becomes negligible with > n=10 microtissues (blue line).

3.4.2.3. Empirical POD estimation

We applied the three POD calculation methods on microtissue APD_{mxr} concentration-response data from treatment with four compounds (cisapride, ranolazine, quinidine, and verapamil). **Figure 3.9** shows examples of POD analysis applied to cisapride data. The averaged values and confidence intervals of APD

response curves from 94 microtissues were plotted (blue) and successfully fitted to logistic (panel **B**), bilinear (panel **C**), softplus (panel **D**), and maximal curvature modeling (panel **E**, red lines). The POD values estimated from the average APD response curve for each 4 models were marked with black stars. These results support that the POD methods using logistic, bilinear, and softplus, and maximal curvature can be applied to *in vitro* data.

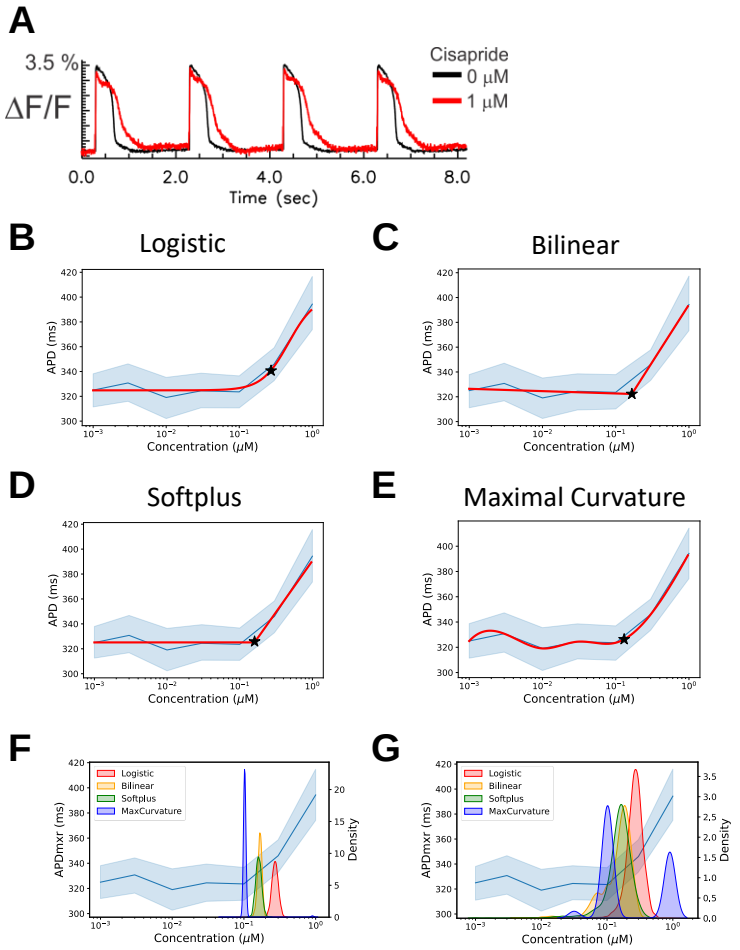

Figure 3.9. POD calculation from experimental data using 3 different curve fit methods. (A) Sample microtissue AP traces at baseline and 1 μM cisapride showing APD prolongation. **(B-E)** Cisapride concentration-APD curves (blue) and fitted curve (red) are drawn together to show the goodness of fit and POD estimations (black stars) using logistic regression (**B**, POD = 0.273 mM), bilinear (**C**, POD = 0.166 mM), softplus (**D**, POD = 0.160 mM), and maximal curvature (**E**, POD = 0.130 mM). **(F)** Probability density plots of PODs calculated from resampled data using the individual microtissue equal-weighted bootstrap method. **(G)** Probability density plots of PODs calculated from resampled data using the pooled data equal-weighted bootstrap method.

It is important to provide confidence intervals for POD estimation with an upper and lower limit of the mean value. Because normality tests failed when all the batches are combined, (**Figure 3.7,**

Supplemental Figure B.6) confidence intervals of PODs from hiPSC-derived cardiac microtissue data should not be calculated from typical standard errors. To estimate confidence intervals, we applied bootstrapping methods that generate empirical POD distributions, and the low 5% and high 95% quantiles can be used to estimate 90% confidence intervals. We examined two bootstrapping methods (see *Methods*): resampling with replacement using individual microtissues (**Figure 3.9F**) and pooled APD_{mxr} data (**Figure 3.9G**). Overall, bootstrapping microtissues shows tighter confidence intervals because this method preserves paired measurements from the same microtissues, reducing variations in estimating PODs. The maximal curvature method shows wide variation in POD distribution (**Figure 3.9F-G**, blue), as observed with computer simulation results. In addition, large variations between microtissues cause abrupt changes in curvature between concentrations, resulting in multiple peaks in the POD distribution (**Figure 3.9F-G**). The bilinear (and softplus) method shows lower values of POD estimation (in contrast to simulation results, **Figure 5**) that are at APD values within the standard deviation of baseline APDs (**Figure 3.9C-D and F-G** yellow and green, respectively) and do not meet the 5% threshold criteria to indicate physiologically meaningful adverse effects at this concentration. In contrast, the logistic method estimates POD values at APDs above the standard deviation of the baseline APD, which also pass the 5% threshold to be physiologically meaningful, aligning with simulation results and showing benefits over bilinear or maximal curvature methods. These outcomes were confirmed with dose-response data for ranolazine, quinidine, and verapamil (**Supplemental Figure B.8**) and for the APD_{tri} metric (**Supplemental Figure B.9**), which has been proposed as an important indicator of hERG channel block [15, 17].

3.5. Discussion

Drug-induced QT prolongation presents significant risks to patient safety and is under substantial regulatory review. hiPSC-based cardiac platforms provide cost-effective methods for testing physiologically relevant human-specific response metrics and reduce reliance on animal testing [2, 6]. However, justification of the analysis methods used to evaluate *in vitro* concentration-response data has

not yet been carefully evaluated in a functional model of cardiac electrophysiology. This study optimized statistical modeling for accurate POD estimation of drug-induced APD prolongation with simulated data and a finite number of batches, molds, microtissues, and test concentrations. Logistic model fitting and bootstrapping were the most reproducible and accurate methods for POD estimation, and these approaches were validated with previously published [17] experimental data from *in vitro* hiPSC-derived engineered cardiac microtissues treated with different CiPA training compounds (cisapride, ranolazine, quinidine, and verapamil).

3.5.1. Drug response experimental design informed by metric-drive POD analysis in silico

Measuring repolarization-related arrhythmia risk associated with hERG block with *in vitro* hiPSC-CM-based platforms requires validation of endpoints ensuring measured *in vitro* PODs predict a clinically determined *in vivo* adverse effect. Clinical assessments of drug induced QT prolongation typically model a linear relationship between ΔQTc and plasma drug concentration *in vivo* [8-10]. Our computer modeling supports a linear relationship at the cellular level between APD and hERG inhibition at low drug concentrations (**Figure 3.3**). However, at higher concentrations, the relationship between hERG channel block and APD becomes complex, leading to a rapid APD increase, which is further amplified by EADs, hindering POD estimation. These observations support alignment between QT prolongation *in vivo* and APD prolongation *in vitro* (prior to EAD onset). Notably, the drug concentration that elicits EADs is greater than the POD estimated from high-sensitivity action potential metrics (**Figure 3.4, Figure 3.9, and Supplemental Figure B.8**). Therefore, using the proposed POD estimate can greatly improve toxicity screening and mechanistic studies for drug development compared to detecting arrhythmic end points such as prolonged Ca^{2+} transients, EAD onset, or tachycardia like fast rhythm [27-29] .

POD estimation using the full range of simulated APD response data with and without EADs supports the conclusion that EADs shift POD estimates to higher concentrations for all three evaluated analysis methods (logistic, bilinear, and maximal curvature) (**Figure 3.4**). However, this effect was minimal with

logistic regression, which had the smallest difference between PODs estimated with and without EADs (**Figure 3.4A-C**). The robustness of logistic regression became even more apparent when the concentration-response curve had a reduced number of test concentrations with additional experimental noise (as with experimental data), with the MSE of logistic regression stabilizing at the lowest levels with six or more test concentrations without EADs (**Figure 3.5 and Supplemental Figure B.4**). When applied to dose-response data from CiPA compounds cisapride, ranolazine, quinidine, and verapamil (**Figure 3.9, Supplemental Figure B.8, Supplemental Figure B.9**), APD_{mxr} and APD_{tri} responses to hERG channel block followed a logistic response and the estimation of POD from experimental data was most robust with this approach.

3.5.2. Empirical assessment of in vitro and technical variation

When transitioning from *in silico* to *in vitro* modeling, it is imperative to consider experimental sources of variation potentially altering interpretation of *in vitro*-derived PODs. In hiPSC-CM engineered microtissue systems, variation due to hiPSC-CM batch, mold, microtissue, beat, and recording effects are all potential sources of uncertainty. In this study, we examined these sources of variation to determine the optimal experimental sample size using Monte Carlo simulation of in *vitro* microtissue data and found that collecting data from three hiPSC-CM differentiation batches with at least one mold per batch and ten or more microtissues per mold is sufficient to detect physiologically relevant delta APD of 5 or 10% relative to baseline (**Figure 3.8D**). However, simulations also suggested a high false positive rate (type I error) during paired statistical analyses due to the high number of microtissues present in relatively few molds and mold-level technical variance between repetitive measures (**Figure 3.8A-C**). While BMD analysis is not directly dependent on traditional statistical tests such as ANOVA, these findings highlight the need to quantify experimental sources of uncertainty and understand the constraints and benefits of a given platform for detecting a potentially adverse effect *in vitro*.

3.5.3. Calculating confidence intervals of PODs

The BMD approach emphasizes the estimation of lower and upper bounds (*i.e.*, a confidence interval (CI)) rather than a single mean value for a given POD estimation. This helps to assess the quality of POD estimates and allows a more stringent risk calculation using the lower estimate. Multiple sources of variation complicate CI estimation and time and cost restrict the number of measured differentiation batches and samples, limiting the appropriateness of the assumptions required for traditional CI estimation (*i.e.,* normality), especially across multiple levels of variability. The bootstrap method presents an alternative option to obtain CIs. Since bootstrapping resamples from an empirical distribution of data without underlying assumptions of the original data to generate thousands of probable data points, it has previously been used to calculate CIs for PODs [12, 14].

When examining different resampling methods (i.e., resampling from each microtissue across all concentrations and resampling of response values independently within each concentration), we found that resampling concentration-response curves from each microtissue gave the narrowest CIs in the experimental data (**Figure 3.9, Supplemental Figure B.8, Supplemental Figure B.9**). Specifically, we estimated 90% CIs for the PODs by logistic regression for cisapride (0.23-0.32 μM), ranolazine (15.6-18.5 μM), quinidine (7.66-8.92 μM), and verapamil (0.37-0.47 μM) (see **Supplemental Table B.4-7** for the results from other curve fits). The better outcome using resampling of curves from each microtissue arises from the positive correlation between ΔAPD by hERG block and baseline APD of individual microtissues, meaning that microtissues with long baseline APD will exhibit even longer APD prolongation by hERG block (correlation coefficient = 0.69 when 50% hERG block from the simulation data in **Figure 3.6**, correlation coefficient = 0.34 between baseline APD and APD at the final concentration of cisapride data), causing greater variations if resampling from the pooled data.

3.5.4. Applications of the proposed POD modeling to other metrics and platforms

The POD methods developed in this study can be applied to other metrics and other hiPSC-CM platforms, particularly in experiments with quantified variance and a sufficient number of drug

concentrations. For example, the same logistic modeling can be used to measure PODs from the AP upstroke rise time or AP amplitudes that imply Na^+ channel block in our 3D microtissue model, where resolution of AP depolarization kinetics enables millisecond time scale quantification (**Supplemental Figure B.10**). Computer modeling predicts AP upstroke rise time and AP amplitude exhibit complex multi-step responses to Na^+ channel block related to both Na^+ and Ca^{2+} channel activation to generate full amplitude action potentials. However, the initial early phase of increasing AP rise time and decreasing amplitude metrics follow logistic curves and can be used to estimate PODs.

Several studies using multi-electrode arrays (MEAs) use field potential duration (FPD) or rate-adjusted (*i.e.*, "corrected") FPD (FPDc) as a metric for assessing cardiotoxicity risk in hiPSC-CMs. While this metric is not APD, its implications for QT prolongation are derived from the action potential, and FPDc has a range of baseline variability (SD percent of mean) from 2.4 ~ 10.5% (akin to our microtissue-level variation) [30-32]. This range of variabilities overlaps with our study, and the logistic regression method would be suitable to analyze this data. Many previous MEA studies [30-34] have used 5 or 6 drug concentrations and are thus suitable for the logistic regression POD calculation method. Importantly, we present the approach to data analysis, which informs experiment design and uncovered nuances of pathophysiological parameters (like non-linear drug-response behavior and non-Gaussian data distributions). As a result, diverse datasets may be analyzed with confidence by adopting this approach.

3.5.5. Conclusions

This study provides a framework for evaluating the ability of an *in vitro* hiPSC-CM-based platform to predict risk for a specific mechanism of cardiotoxicity, namely, repolarization-related arrhythmias. A combination of computational modeling and experimental data enabled a systematic definition of physiologically relevant BMDs, concentration-response models, and experimental parameters for accurate risk assessment. This approach is highly flexible, has few *a priori* assumptions, and could be adapted for several other proarrhythmic mechanisms (*i.e.,* slow conduction, sodium channel block) and

in vitro endpoints (*i.e.,* excitability, rise time, AP amplitudes, spontaneous beating rates) in addition to those used with other systems (*e.g.,* field potential duration and calcium kinetics). Overall, incorporation of concerted, systematic evaluation of the link between *in vitro* endpoints, clinically relevant responses, and known mechanisms of toxicity will expand the potential of hiPSC-CM-based NAMs and advance the accuracy of the next-generation of *in vitro* risk assessment.

3.6. Funding

This work was supported by funding from the National Institute of Environmental Health Sciences (U01 ES028184 to Ulrike Mende, Bum-Rak Choi, Patrick McMullen, and Kareen Coulombe), COBRE pilot grant (NIH/NIGMS P20GM103652 to Bum-Rak Choi and Kareen Coulombe), and a Brown Biomedical Innovation to Impact Award (to Ulrike Mende, Bum-Rak Choi, and Kareen Coulombe).

3.7. References

1. Gintant, G., P.T. Sager, and N. Stockbridge, *Evolution of strategies to improve preclinical cardiac safety testing.* Nature Reviews Drug Discovery, 2016. **15**(7): p. 457.
2. Magdy, T., et al., *Human induced pluripotent stem cell (hiPSC)-derived cells to assess drug cardiotoxicity: opportunities and problems.* Annual review of pharmacology and toxicology, 2018. **58**: p. 83-103.
3. Burnett, S.D., et al., *Human induced pluripotent stem cell (iPSC)-derived cardiomyocytes as an in vitro model in toxicology: strengths and weaknesses for hazard identification and risk characterization.* Expert Opinion on Drug Metabolism & Toxicology, 2021: p. 1-16.
4. Chen, I.Y., E. Matsa, and J.C. Wu, *Induced pluripotent stem cells: at the heart of cardiovascular precision medicine.* Nature Reviews Cardiology, 2016. **13**(6): p. 333.
5. Daley, M.C., et al., *Beyond pharmaceuticals: Fit-for-purpose new approach methodologies for environmental cardiotoxicity testing.* ALTEX-Alternatives to animal experimentation, 2023. **40**(1): p. 103-116.

6. Yang, X., et al., *Use of human iPSC-CMs in nonclinical regulatory studies for cardiac safety assessment.* Toxicological Sciences, 2022. **190**(2): p. 117-126.

7. Zuppinger, C., *3D cardiac cell culture: a critical review of current technologies and applications.* Frontiers in cardiovascular medicine, 2019. **6**: p. 87.

8. Darpo, B., *The thorough QT/QTc study 4 years after the implementation of the ICH E14 guidance.* British journal of pharmacology, 2010. **159**(1): p. 49-57.

9. ICH, *The clinical evaluation of QT/QTc interval prolongation and proarrhythmic potential for non-antiarrhythmic drugs E14*. 2006.

10. Stockbridge, N., et al., *Practice and challenges of thorough QT studies.* Journal of Electrocardiology, 2012. **45**(6): p. 582-587.

11. Lu, J., et al., *Assessing QT/QTc interval prolongation with concentration-QT modeling for Phase I studies: impact of computational platforms, model structures and confidence interval calculation methods.* J Pharmacokinet Pharmacodyn, 2018. **45**(3): p. 469-482.

12. Travis, K.Z., I. Pate, and Z.K. Welsh, *The role of the benchmark dose in a regulatory context.* Regulatory Toxicology and Pharmacology, 2005. **43**(3): p. 280-291.

13. Sand, S., K. Victorin, and A.F. Filipsson, *The current state of knowledge on the use of the benchmark dose concept in risk assessment.* Journal of Applied Toxicology: An International Journal, 2008. **28**(4): p. 405-421.

14. Jensen, S.M., F.M. Kluxen, and C. Ritz, *A review of recent advances in benchmark dose methodology.* Risk Analysis, 2019. **39**(10): p. 2295-2315.

15. Kofron, C., et al., *A Predictive in Vitro Risk Assessment Platform for Pro-Arrhythmic Toxicity Using Human 3D Cardiac Microtissues.* Scientific Reports, 2021. **11**: p. 1-16.

16. Tomek, J., et al., *Development, calibration, and validation of a novel human ventricular myocyte model in health, disease, and drug block.* Elife, 2019. **8**: p. e48890.

17. Daley, M., et al., *In vitro to in vivo extrapolation from three-dimensional hiPSC-derived cardiac microtissues and physiologically based pharmacokinetic modeling to inform next-generation arrhythmia risk assessment.* Toxicological Sciences, 2024: p. kfae079.

18. Sager, P.T., et al., *Rechanneling the cardiac proarrhythmia safety paradigm: a meeting report from the Cardiac Safety Research Consortium.* Am Heart J, 2014. **167**(3): p. 292-300.

19. Colatsky, T., et al., *The Comprehensive in Vitro Proarrhythmia Assay (CiPA) initiative - Update on progress.* J Pharmacol Toxicol Methods, 2016. **81**: p. 15-20.

20. O'Hara, T., et al., *Simulation of the undiseased human cardiac ventricular action potential: model formulation and experimental validation.* PLoS computational biology, 2011. **7**(5): p. e1002061.

21. Soepriatna, A.H., et al., *Action potential metrics and automated data analysis pipeline for cardiotoxicity testing using optically mapped hiPSC-derived 3D cardiac microtissues.* PLoS One, 2023. **18**(2): p. e0280406.

22. Burridge, P.W., A. Holmström, and J.C. Wu, *Chemically defined culture and cardiomyocyte differentiation of human pluripotent stem cells.* Current Protocols in Human Genetics, 2015. **87**(1): p. 21.3. 1-21.3. 15.

23. Efimov, I.R., et al., *Optical mapping of repolarization and refractoriness from intact hearts.* Circulation, 1994. **90**(3): p. 1469-80.

24. Baher, A., et al., *Short-term cardiac memory and mother rotor fibrillation.* Am J Physiol Heart Circ Physiol, 2007. **292**(1): p. H180-9.

25. Jing, L., S. Chourasia, and A. Patwardhan, *Heterogeneous memory in restitution of action potential duration in pig ventricles.* J Electrocardiol, 2010. **43**(5): p. 425-32.

26. Marrus, S.B., et al., *Repolarization changes underlying long-term cardiac memory due to right ventricular pacing: noninvasive mapping with electrocardiographic imaging.* Circ Arrhythm Electrophysiol, 2012. **5**(4): p. 773-81.

27. Blinova, K., et al., *International Multisite Study of Human-Induced Pluripotent Stem Cell-Derived Cardiomyocytes for Drug Proarrhythmic Potential Assessment.* Cell Rep, 2018. **24**(13): p. 3582-3592.

28. Kitaguchi, T., et al., *CSAHi study: Evaluation of multi-electrode array in combination with human iPS cell-derived cardiomyocytes to predict drug-induced QT prolongation and arrhythmia--effects of 7 reference compounds at 10 facilities.* J Pharmacol Toxicol Methods, 2016. **78**: p. 93-102.

29. Pfeiffer, E.R., et al., *Specific prediction of clinical QT prolongation by kinetic image cytometry in human stem cell derived cardiomyocytes.* J Pharmacol Toxicol Methods, 2016. **81**: p. 263-73.

30. Hayes, H.B., et al., *Novel method for action potential measurements from intact cardiac monolayers with multiwell microelectrode array technology.* Sci Rep, 2019. **9**(1): p. 11893.

31. Nakamura, Y., et al., *Assessment of testing methods for drug-induced repolarization delay and arrhythmias in an iPS cell-derived cardiomyocyte sheet: multi-site validation study.* J Pharmacol Sci, 2014. **124**(4): p. 494-501.

32. Yamamoto, W., et al., *Electrophysiological Characteristics of Human iPSC-Derived Cardiomyocytes for the Assessment of Drug-Induced Proarrhythmic Potential.* PLoS One, 2016. **11**(12): p. e0167348.

33. Harris, K., et al., *Comparison of electrophysiological data from human-induced pluripotent stem cell-derived cardiomyocytes to functional preclinical safety assays.* Toxicol Sci, 2013. **134**(2): p. 412-26.

34. Huo, J., et al., *Evaluation of Batch Variations in Induced Pluripotent Stem Cell-Derived Human Cardiomyocytes from 2 Major Suppliers.* Toxicol Sci, 2017. **156**(1): p. 25-38.

Chapter 4 - Chronic cardiotoxicity and cardioprotection in the context of anthracycline-induced heart failure

4.1. Abstract

Despite major improvements in anticancer treatment, chemotherapy-induced cardiotoxicity continues to present an ongoing challenge to the long-term well-being of cancer survivors. Anthracyclines are one such example and remain commonly prescribed despite a significant, dose-dependent risk for developing heart failure after treatment. As a result, there is substantial interest in developing strategies for mitigating anthracycline-induced cardiotoxicity, especially through cardioprotective cotreatments. In this study, we utilized hiPSC-CMs as a preclinical screening tool for investigating three classes of potentially cardioprotective compounds (ACE inhibition, topoisomerase IIβ inhibition, and carbonic anhydrase 12 inhibition) for their ability to prevent anthracycline-induced cardiotoxicity. We successfully validated that hiPSC-CMs recapitulate concentration- and time-dependent doxorubicin toxicity for viability, function, and metabolism. We further found that neither cotreatment with the ACE inhibitor enalapril nor the topoisomerase IIβ inhibitor dexrazoxane prevented doxorubicin toxicity. Additional fatty acid-based maturation of cardiac microtissues enhanced doxorubicin-induced cardiotoxicity but did not alter the efficacy of dexrazoxane cardioprotection. Contrastingly, cotreatment with the carbonic anhydrase 12 inhibitor indisulam was observed to be cardioprotective to hiPSC-CM monolayers. However, this was not associated with previously hypothesized decreases in doxorubicin-induced glycolysis. Overall, this work validates the utility of hiPSC-CM-based models to serve as fit-for-purpose preclinical tools for chemotherapeutic design.

4.2. Introduction

In recent years, major advances in anticancer therapy have acted to simultaneously increase the survival rate of cancer patients and prolong the lives of cancer survivors [1, 2]. Despite these achievements, chemotherapy-induced cardiotoxicities, including heart failure; arrhythmia; and

cardiomyopathy, remain a major long-term challenge to patient well-being [3, 4], occurring through a variety of mechanisms across the cardiovascular system [5]. The risk of chemotherapy-induced toxicity is further exacerbated by the significant intersection between risk factors for cardiovascular disease and cancer, complicating oncological care [6]. The effects of this overlap have been increasingly recognized as an important consideration for both drug development and the management of cardiovascular health after chemotherapy, leading to the maturation of cardio-oncology as a standalone discipline [7, 8]. Despite more concerted efforts to mitigate cardiotoxicity, thousands of patients develop cardiac dysfunction as a direct result of chemotherapy, with incidences of greater than 25% of patients receiving some commonly prescribed drugs [9].

Anthracyclines, one of the most common classes of chemotherapeutics, are one such family of compounds [10]. They have been most frequently prescribed for the treatment of breast and blood cancers and, while their use has decreased in recent years, approximately 40% of adult breast cancer patients as well as 50% of childhood cancer survivors have been treated using anthracyclines [11-13]. Unfortunately, long-term cardiovascular risk is also significant in these patients and directly related to cumulative lifetime dose [14-16]. For the most frequently prescribed anthracyclines, doxorubicin, cumulative doses are typically limited to between 450 and 550 mg/m^2 to mitigate the risk of cardiovascular complications [17]. Anthracycline-induced cardiotoxicity was conventionally attributed primarily to increased reactive oxygen species (ROS) formation, but more recent work has increasingly solidified the role of inhibition of topoisomerase II, enzymes that assist the spatial rearrangement of DNA [18-20]. In proliferating cells like cancer, topoisomerase IIα is upregulated to facilitate and then repair double-stranded DNA breaks. However, a second isoform, topoisomerase IIβ, has been shown to be upregulated in quiescent cells like cardiomyocytes to assist in routine DNA and mitochondrial maintenance and is also targeted by anthracyclines [17, 19, 21]. Significant efforts have been made to circumvent anthracycline-induced cardiotoxicity, most notably with the development of liposomal formulations with better tumor

targeting [22] and next-generation anthracyclines [23]. However, while some improvements have been made they have proven cost prohibitive for most patients [24] or have been unable to sufficiently eliminate the risk of cardiotoxicity [23]. Thus, there is still a major remaining need for identifying approaches for mitigating anthracycline-induced cardiotoxicity.

Current clinical practice is to monitor heart function during and after cancer treatment, only initiating pharmacological heart failure therapies, such as angiotensin-converting enzyme (ACE) inhibitors or β-blockers, after clinically significant reductions in left ventricular ejection fraction (LVEF) [17, 25, 26]. Research in patients treated with the ACE inhibitor enalapril has shown that early intervention improves the response rate to treatment [25, 27]. As a result, clinical trials have begun to investigate the use of ACE inhibitors as co-therapies during anthracycline chemotherapy as a preventative therapy. However, overall evidence of a clinical benefit has remained mixed with only slight benefits observed in some studies [28, 29]. Still other work has focused on drugs outside the suite of traditional heart therapy medication. Dexrazoxane was originally investigated due to its properties as an iron-chelator for the prevention of ROS accumulation, but has since been identified as a competitive inhibitor of topoisomerase IIβ [30]. Promisingly, dexrazoxane was approved by the FDA for the prevention of doxorubicin-induced cardiotoxicity in 1997 [31]. However, this approval was only for metastatic breast cancer patients who had already received >300 mg/m^2 doxorubicin and it remains underutilized due to concerns about increased risk of metastasis although the risk is believed to be low.

As a result, ongoing efforts have begun to look towards other cardiac-specific mechanisms for preventing anthracycline-induced cardiotoxicity. Towards this end, human induced pluripotent stem cell-derived cardiomyocytes (hiPSC-CMs) have served as a human-specific tool for studying anthracycline-induced cardiotoxicity. hiPSC-CM-based models have been used to differentiate the cardiotoxicity risk between hiPSC donors with and without a history of doxorubicin-induced cardiotoxicity [32], increased doxorubicin sensitivity under hypoxic conditions [33], and clinically relevant toxicity to exposure profiles

mirroring *in vivo* pharmacokinetics [34]. hiPSC-CMs have more recently been leveraged as a high-throughput drug screening platform to identify novel drug targets for mitigating doxorubicin-induced cardiotoxicity, identifying carbonic anhydrase 12 (CA12) as a potential target for attenuating toxicity by preventing a doxorubicin-induced shift towards glycolysis [35]. As hiPSC-CMs are increasingly adopted by regulators and drug developers, a better understanding of their ability to predict anthracycline-induced cardiotoxicity and identify potential co-therapies will be invaluable.

Towards this end, we leveraged both two- and three-dimensional hiPSC-CM-based models to examine anthracycline-induced cardiotoxicity as well as potential cardioprotective co-therapies. We observed both concentration- and time-dependent toxicity after exposure to doxorubicin across a range of viability and functional metrics, including MTT; LIVE/DEAD; oxygen consumption rate (OCR); action potential kinetics; and contractility. Further, we found that hiPSC-CM maturation was linked to the severity of doxorubicin-induced cardiotoxicity. We further investigated the cardioprotective properties of the ACE inhibitor enalapril, the topoisomerase IIβ inhibitor dexrazoxane, and the CA12 inhibitor indisulam as cardioprotective co-therapies for the prevention of anthracycline-induced cardiotoxicity. We found that hiPSC-CMs largely reflected available data on the efficacy of cardioprotective therapies. Namely, we observed that neither enalapril nor dexrazoxane provided cardioprotection while modulation of the metabolic axis with indisulam cotreatment could reduce the severity of doxorubicin-induced cardiotoxicity. Together, these data support the use of hiPSC-CMs, especially those that have been functionally matured, as critical screening tools for identifying and minimizing drug-induced cardiotoxicity.

4.3. Materials and methods

4.3.1. Compound selection and drug exposures

Three different anthracyclines were initially used to model anthracycline-induced cardiotoxicity (doxorubicin, epirubicin, and idarubicin). However, after initial viability assessments, only doxorubicin was used for the remaining work in order to minimize experimental conditions and because it is still the most

commonly prescribed anthracycline [10]. Enalapril, dexrazoxane, and indisulam were used as cardioprotective co-therapies because of their past use in either clinical or preclinical investigations to mitigate anthracycline-induced cardiotoxicity. Enalapril is the most extensively studied of the three, with a number of small-scale clinical investigating its protective properties. Multiple mechanisms of action have been proposed, the primary of which is ACE inhibition to reduce cardiac stress, but others have suggested the ROS scavenging may also play a role [29]. Dexrazoxane, on the other hand, is FDA-approved for the prevention of doxorubicin-induced cardiotoxicity in select contexts. While ROS scavenging was once thought to be the primary mechanism, it is now broadly understood that its ability to protect the heart is related to inhibition of topoisomerase IIβ [30, 31]. Finally, indisulam is a small molecule inhibitor of CA12 that has recently been identified to have potentially cardioprotective properties outside of traditionally recognize mechanisms by maintaining long-term energy balance post-doxorubicin exposure [35]. For the majority of experiments and unless otherwise indicated, hiPSC-CMs or cardiac microtissues were treated with doxorubicin alone, cardioprotective drug alone, both, or a vehicle control for 72 hours.

4.3.2. hiPSC culture and cardiomyocyte differentiation

Ventricular hiPSC-CMs were differentiated using previously published methods [36]. Briefly, hiPSCs (WTC human male iPSCs, Gladstone Institutes) were cultured on 5 μg/mL vitronectin-coated (ThermoFisher Scientific #A14700), 100 mm-diameter culture dishes and fed daily with Essential 8 medium (Gibco #A1517001). Once 80% confluent, hiPSCS were passaged by covering in versene (0.5M EDTA: SigmaAldrich #E5134; 1.1 mM D-glucose: Gibco #15023-013) 5 minutes before mechanically lifting the cells and seeding onto 24-well plates coated with Geltrex™ (Life Technologes #A1413302) in Essential 8 medium containing 5 μM ROCK-inhibitor (Y-27632: Tocris #1254). When reaching 80% confluence again, hiPSCs were treated with 4.8 μM of the GSK3 inhibitor CHIR-99021 (Tocris #4423) for 24 ± 1 hours in cardiac differentiation media with 3 components (CDM3) consisting of RPMI 1640 basal media (Gibco #11875093) supplemented with 213 μg/mL L-ascorbic acid (Sigma Aldrich #A8960) and 500 μg/mL of

human serum albumin (Sigma Aldrich #A1653). Next, differentiating hiPSCs were given 5 µM IWP2 (Tocris #3533), a small molecule Wnt inhibitor, in a 1:1 mixture of fresh and spent CDM3 for two days. Beginning on day 5, hiPSCs were fed with regular CDM3 every other day until spontaneous beating began (days 8-10), at which point they were fed RPMI 1640 with B27 supplement (RPMI/B27; Gibco #17504044). At days 13-15, hiPSC-CMs were passaged using 0.25% trypsin (Life Technologies #27250018) in versene and replated onto a new Geltrex-coated 24-well plate (~0.5 million cell/cm^2) in RPMI/B27 containing 10% fetal bovine serum (Life Technologies #16000044), 1% penicillin-streptomycin (Sigma Aldrich #P0781), and 5 µM ROCK inhibitor. hiPSC-CMs were allowed to attach for 24 hours before being fed with regular RPMI/B27. After an additional recovery period of at least 48 hours, hiPSC-CMs were metabolically selected in a lactate media comprising of 4 mM sodium L-lactate (Sigma Aldrich #L7022) in glucose- and sodium pyruvate-free DMEM (Gibco #11966025) for four days with a single media change on the second day. After metabolic selection, hiPSC-CMs were maintained in RPMI/B27 until downstream use.

4.3.3. Cardiac fibroblast culture and storage

Primary human ventricular (Lonza #CC-2904, Lot #18TL281202) cardiac fibroblasts were cultured in DMEM/F12 (Life Technologies #11320082) supplemented with 10% fetal bovine serum, 1% penicillin-streptomycin, and 4 ng/mL basic fibroblast growth factor (Reprocell #030002). Cells were fed every other day until becoming 80 to 90% confluent, at which point they were passaged using 0.05% trypsin in versene at a density of 5,000 cells/cm^2 for subsequent viability assessment. Prior to incorporation into cardiac microtissues, fibroblasts were frozen in 10% dimethyl sulfoxide (DMSO) at -80 °C overnight before being stored in liquid nitrogen.

4.3.4. Cardiac microtissue preparation

Microtissues were created as in previously published literature [37, 38]. Agarose microtissue molds were created using sterile 2% wt/vol agarose (Invitrogen #16500500) in 1x PBS pipetted into sterile 25-microwell negative molds with 800 µM-diameter hemispherical microwells (Microtissues Inc #24-35) and

allowed to equilibrate in RPMI/B27 media with 1% penicillin streptomycin for 1 hour at 37 °C. Purified hiPSC-CMs were singularized with 0.25% trypsin in versene and combined with primary cardiac fibrblasts (passages 4-6) in a 95:5 ratio (350,000 cells per mold) in a solution of RPMI/B27 supplemented with 10% fetal bovine serum, 1% penicillin-streptomycin, and 5 µM ROCK-inhibitor. 100 µL of cell suspension was seeded into each agarose mold and allowed to settle for 30 minutes before being covered with additional media. Microtissues were cultured under electrical field stimulation with a 1 Hz, 10 V, 4 ms duration bipolar pulse train (C-Pace EP, IonOptix). After 24 hours, microtissues were fed every three days with regular RPMI/B27 and used for subsequent experiments after 6-8 days in culture.

4.3.5. Maturation media for metabolic maturation of hiPSC-CMs

For select experiments, a low-glucose, fatty acid-supplemented media was used to metabolically mature cardiomyocytes [39, 40]. This media consists of DMEM minus glucose (Gibco #11966025) supplemented with 3 mM glucose (Sigma Aldrich #G7021), 10 mM sodium lactate, 5 µg/mL vitamin B12 (Sigma Aldrich #V6629), 0.82 µM biotin (Sigma Aldrich #B4639), 5 mM creatine monohydrate (Sigma Aldrich #C3630), 2 mM taurine (Sigma Aldrich #T0625), 2 mM L-carnitine (Sigma Aldrich #C0283), 0.5 mM L-ascorbic acid, 1x non-essential amino acids (ThermoFisher #11140050), 0.5% (wt/vol) Albumax™ (Thermofisher #11021029), 1x B27 supplement, and 1% KnockOut™ serum replacement (ThermoFisher #10828028). Unless otherwise specified, standard RPMI/B27-based media compositions were used during experiments.

4.3.6. MTT viability assay

hiPSC-CMs were seeded into Geltrex-coated 96-well plates at a density of 35,000 cells/well (~110,000 cells/cm^2) in RPMI/B27 with 10% fetal bovine serum, 1% penicillin-streptomycin, and 5 µM IWP2. For standard experiments, hiPSC-CMs were treated the next day for 72 hours. For experiments with maturation media, cells were changed to either regular RPMI/B27 or maturation media and fed every 2-3 days for one week prior to drug exposure. After treatment, the MTT assay (Sigma Aldrich #TOX-1) was

performed following the manufacturers protocol. First, 3-[4,5-dimethylthiazol-2-yl]-2,5-diphenyl tetrazolium bromide was resuspended in warmed PBS at a concentration of 5 mg/mL before being added to each well (10% of media volume). After incubating for 2-4 hours at 37 °C, a solubilization solution of 0.1N hydrochloric acid and 10% triton-x 100 was added in equal volumes and mechanical trituration was used to break up cell monolayers. Absorbances at 570 nm and 690 nm were measured using a plate reader (Cytek Biosciences) and used to quantify relative viability.

4.3.7. Seahorse metabolic assay

Like the MTT viability assay, hiPSC-CMs were seeded into Geltrex-coated 96-well plates at a density of 25,000 cells/well (~75,000 cells/cm^2) in RPMI/B27 with 10% fetal bovine serum, 1% penicillin-streptomycin, and 5 µM IWP2. hiPSC-CMs were treated the next day for 72 hours before being rinsed with PBS and fed with XF basal medium (Agilent), 4 mM GlutaMax, 1 mM sodium pyruvate, and 25 mM glucose and incubated for 90 minutes at 0% CO_2 and 37 °C. OCR and extracellular acidification rate (ECAR) measurements were made with a Seahorse XFe96 Extracellular Flux Analyzer (Agilent) across time and after sequential exposures to oligomycin, FCCP, and rotenone with antimycin A.

4.3.8. MitoSOX staining and ROS generation assessment

MitoSOX™ Red (Invitrogen #M36008) is a fluorescent, live-cell stain for mitochondrial superoxide, which serves as an indicator for ROS generation. For two-dimensional monolayers, hiPSC-CMs were plated at a density of 35,000 cells/well (~110,000 cells/cm^2) in RPMI/B27 with 10% fetal bovine serum, 1% penicillin-streptomycin, and 5 µM IWP2 for 24 hours before treatment. At the end of treatment, monolayers were washed once with Hank's Buffered Saline Solution (HBSS) consisting of (in mM) 140 NaCl, 5 KCl, 1 $CaCl_2$, 0.4 $MgSO_4 \cdot 7H_2O$, 0.5 $MgCl_2 \cdot 6H_2O$, 0.3 $Na_2HPO_4 \cdot 2H_2O$, 0.4 KH_2PO_4, 6 D-glucose, and 4 $NaHCO_3$ (pH 7.2-7.4). Monolayers were next covered in a 500 nM working solution of MitoSOX™ Red and 1.5 µg/mL Hoechst 33342 (ThermoFisher Scientific #H1399) in HBSS and allowed to incubate for 37 °C and 5% CO_2 for 30 minutes. Cells were rinsed 3x times with HBSS and then imaged in HBSS using a Nikon

Eclipse Ti-E inverted fluorescent microscope. The staining protocol was kept the same for cardiac microtissues, but they were first transferred to a new 24-well plate prior to staining.

4.3.9. LIVE/DEAD staining of cardiac microtissues

After drug treatment, agarose molds of cardiac microtissues were transferred to a new 24-well plate. Excess media was removed before covering the microtissues in a staining solution containing a 1:1:8 (by volume) solution of NucBlue:Propidium Iodide:RPMI/B27 from the ReadyProbes™ Red/Blue Cell Viability Imaging Kit (Invitrogen #R37610) and allowed to incubate for 1 hour. Fluorescent imaging was performed directly in the staining solution using a Nikon Eclipse Ti-E inverted microscope. A custom CellProfiler™ [41] pipeline was used to measure the mean dead stain intensity of individual microtissues which was subsequently averaged on a per mold basis.

4.3.10. Optical mapping of cardiac action potentials

Optical mapping was performed as previously described in a temperature-controlled chamber containing (in mM) 140 NaCl, 4.0 KCl, 1.0 $MgCl_2$, 1.25 $CaCL_2$, 0.33 NaH_2PO_4, 5.0 HEPES, 5.0 sodium pyruvate, and 7.5 glucose [42]. Microtissues were stained with a 5 µM solution of di-4-ANEPPS (Invitrogen #D1199) for 2-3 minutes. Excess dye was washed away and a CMOS camera (Ultima-L, Scimedia, Japan) was used to record fluorescent images at 1,000 frames per second under 1 Hz pacing. Action potentials were reconstructed from fluorescent intensity data and semi-automated analysis using in-house, software-enabled measurement. Excitability and action potential duration to maximum rate or repolarization (APD_{mxr}) were measured for each microtissue individually and metrics were averaged across all microtissues in a single mold.

4.3.11. Contractility assessment

Microtissues were transferred within their agarose molds into 6-well plates containing polydimethylsiloxane (PDMS) holders designed to prevent motion during imaging. Brightfield videos of microtissues were acquired using a Nikon Eclipse TS100, Canon EOS 6D camera, and 10x objective at 60 fps for 15-20 seconds. A custom MATLAB script was used to crop and mask individual microtissues before

analyzing contractility using the open-source Python package MicroBundleCompute [43]. MicroBundleCompute measures frame-by-frame displacement of automatically selected fiduciary markers within videos. Maximum contraction amplitude for each microtissue was estimated by the average displacement of these pixels before averaging by mold.

4.4. Results

4.4.1. hiPSC-CMs captured concentration- and time-dependent anthracycline-induced toxicity

Anthracycline-induced cardiotoxicity is known to be proportional to cumulative exposure in patients as well as possess both acute and chronic components. We initially sought to verify that these phenomena were similarly true *in vitro* by examining concentration- and time-dependent toxicity on hiPSC-CMs. Initial concentration-dependence was examined in two-dimensional monolayers using an MTT viability assay after exposure to the anthracyclines doxorubicin, epirubicin, and idarubicin for 72 hours (**Figure 4.1A**). All three anthracyclines displayed concentration-dependent effects on hiPSC-CM viability with measured 95% confidence intervals of half-maximal effective concentrations (EC50s) of 2.0-18 μM, 2.9-8.2 μM, and 0.8-1.6 μM, respectively. For remaining experiments, only doxorubicin was used to reduce experimental burden. Concentration-dependent functional toxicity was assessed using microtissue contractility (**Figure 4.1B**). A statistically significant reduction in average pixel displacement was only observed at the highest tested doxorubicin concentration of 3 μM (0.6 ± 0.5 μm) compared to untreated controls (4.5 ± 2.3 μm). OCR, a measure of oxidative phosphorylation-based metabolism, was similarly reduced in a concentration-dependent manner (**Figure 4.1C, Supplemental Figure C.1**). For instance, basal respiration was significantly reduced even after exposure to low, 0.01 μM concentrations of doxorubicin (53.1 ± 2.1 pmol/min/10,000 cells) as well as 0.1 μM doxorubicin (42.2 ± 7.0 pmol/min/10,000 cells) compared to vehicle controls (62.4 ± 5.7 pmol/min/10,000 cells). However, OCR was nearly undetectable (2.4 ± 0.4 pmol/min/10,000 cells) after treatment with 1 μM doxorubicin and this condition was excluded from subsequent cardioprotection analysis (**Supplemental Figure C.1A**). We also observed that the baseline

ratio of OCR-to-ECAR was significantly increased for 0.01-μM-treated hiPSC-CMs (5.1 ± 0.4 pmol/mpH) compared to both control (4.6 ± 0.2 pmol/mpH), 0.1-μM-treated (4.2 ± 0.3 pmol/mpH), and 1-μM-treated (1.4 ± 0.2 pmol/mpH) hiPSC-CMs, suggesting a relative shift towards oxidative phosphorylation compared to glycolysis after 0.1-μM-doxorubicin exposure but concentration-dependent increases at higher concentrations **(Supplemental Figure C.1G**).

Time-dependent changes in viability were similarly examined after 24- and 72-hour-long exposures to 1 μM doxorubicin in two-dimensional monolayers (**Figure 4.2A**). After 72 hours, there was a significant reduction in relative viability (45.0 ± 4.7%) compared to hiPSC-CMs that had only been cultured in doxorubicin for 24 hours (86.0 ± 4.8%). This effect was also observed in functional measurements of cardiac action potentials in microtissues (**Figure 4.2B-D**). After 1- and 24-hour-long exposures to doxorubicin, there were no significant changes in microtissue excitability or APD_{mxr}. However, at 72-hours microtissues treated with 3 μM doxorubicin entirely lost excitability and 1-μM-treated microtissues had a significantly shorter APD_{mxr} (410.0 ± 44.3 ms) than vehicle-treated controls (302.2 ± 35.5 ms) (**Figure 4.2D**) as well as APD30, 50, and 80 (**Supplemental Figure C.2D-F**). Overall, we were able to observe both concentration- and time-dependent reductions in hiPSC-CM viability and function suggesting we were able to successfully recapitulate anthracycline-induced cardiotoxicity *in vitro*.

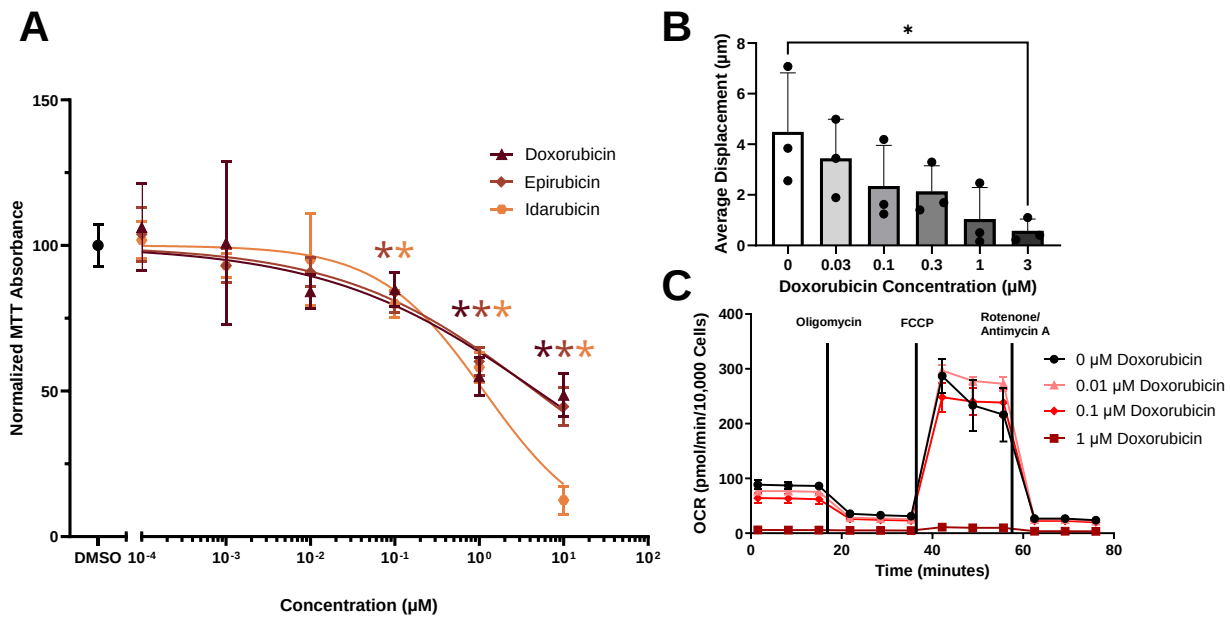

Figure 4.1. Concentration-dependent anthracycline-induced cardiotoxicity in hiPSC-CMs. (A) Relative viability of ventricular hiPSC-CMs treated with the anthracyclines doxorubicin, epirubicin, and idarubicin decreased in a concentration-dependent manner as measured by a MTT assay (N = 4 wells). Similar concentration-dependent effects were also observed in functional measures of (B) cardiac microtissue contractility (N = 3 molds; 3 microtissues per mold) and (C) oxygen consumption rate (OCR) measured by Seahorse assay (N = 8-12 wells). Data are presented as mean ± standard deviation except for (C) OCR which is presented as mean ± standard error. * indicate statistical significance ($p < 0.05$) for one-way ANOVA with a Dunnett post-hoc test compared to untreated controls.

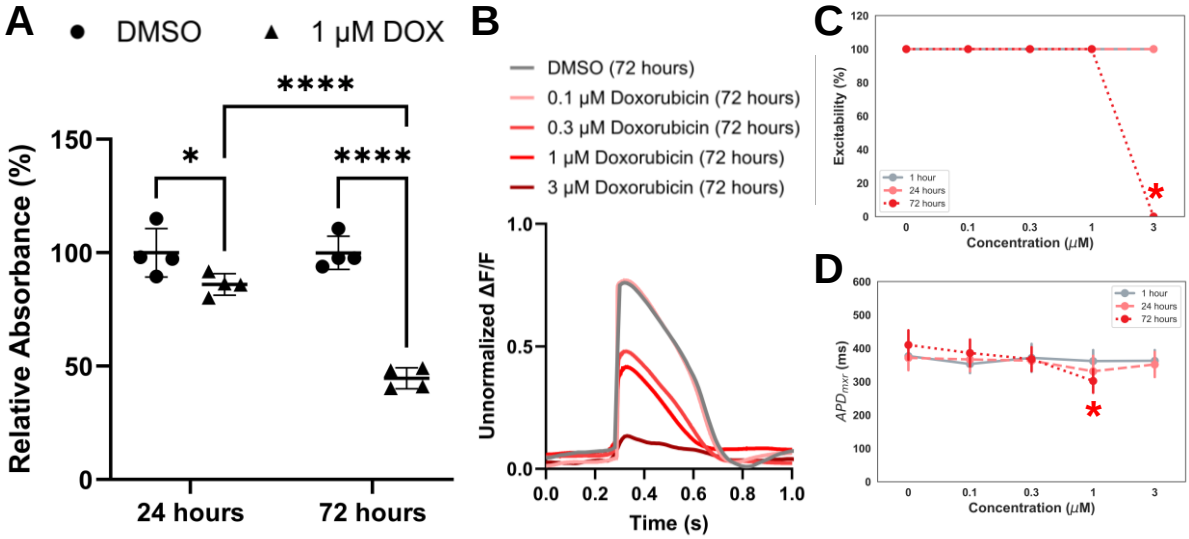

Figure 4.2. Time-dependent anthracycline-induced cardiotoxicity in hiPSC-CMs. (A) Relative viability of ventricular hiPSC-CMs treated with doxorubicin for either 24 or 72 hours demonstrate significantly different changes in relative viability as measured by an MTT assay (N = 4 wells) with time. Time- and concentration-dependent functional toxicity were also observed in (B) action potentials of cardiac microtissues, particularly (C) excitability and (D) APD_{mxr} at high doxorubicin concentrations after 72 hours (N = 3 molds; 96-104 microtissues total). * and **** indicate statistical significance ($p < 0.05$ and $p < 0.0001$, respectively) for one- or two-way ANOVA with a Dunnet or Tukey post-hoc test compared to untreated controls.

4.4.2. ACE inhibition did not prevent doxorubicin-induced cardiotoxicity

ACE inhibitor-based cardioprotection was next examined using cotreatment with enalapril, which has previously been examined clinically for its potential ability to prevent anthracycline-induced cardiotoxicity [28, 29]. As in toxicity experiments, viability was measured in cardiac microtissues using LIVE/DEAD staining after 72-hour-long exposures (**Figure 4.3A-B**). As expected, significant increases in average dead stain intensity were observed with increasing concentrations of doxorubicin (0 μM: 0.042 ± 0.022 AU; 1 μM: 0.133 ± 0.044 AU; 3 μM: 0.268 ± 0.073 AU). However, co-administration of 10 μM enalapril during treatment with 1 μM (0.115 ± 0.064 AU) or 3 μM (0.223 ± 0.105 AU) doxorubicin did not result in a significant reduction in dead stain intensity, indicating no protective effect of viability. Viability was also examined using an MTT assay (**Figure 4.3C**). As with LIVE/DEAD staining, no positive effect on viability was observed from cotreatment with enalapril concentrations up to 30 μM (66.8 ± 3.2%) compared to positive controls treated only with 3 μM doxorubicin (59.9 ± 6.2%). This was similarly true for 100 μM concentrations of enalapril (**Supplemental Figure C.3**). Contrastingly, a cardioprotective effect was observed in microtissue after cotreatment with enalapril (**Figure 4.3D**). Enalapril cotreated microtissues had significantly larger contractility (5.1 ± 1.2 μm) compared to non-cotreated microtissues (7.8 ± 0.4 μm) after 1 μM doxorubicin exposures. For 3 μM-treated microtissues, there was a similar (control: 0.4 ± 0.08 μm versus enalapril: 2.6 ± 2.3 μm), but nonsignificant, trend. Since one of the primary mechanisms of doxorubicin-induced cardiotoxicity is ROS generation [12, 17] and enalapril has been hypothesized to have ROS-scavenging properties [44], the effects of enalapril cotreatment on ROS generation was measured by MitoSOX fluorescent staining in engineered microtissues (**Figure 4.3E-F**). Enalapril cotreatment did not have a significant effect on ROS generation with enalapril-cotreated microtissues (1 μM doxorubicin: 0.084 ± 0.016 AU; 3 μM doxorubicin: 0.11 ± 0.16 AU) having similar average MitoSOX intensities to microtissues that were not treated with enalapril (1 μM doxorubicin:0.074 ± 0.015 AU; 3 μM doxorubicin: 0.10 ± 0.15 AU).

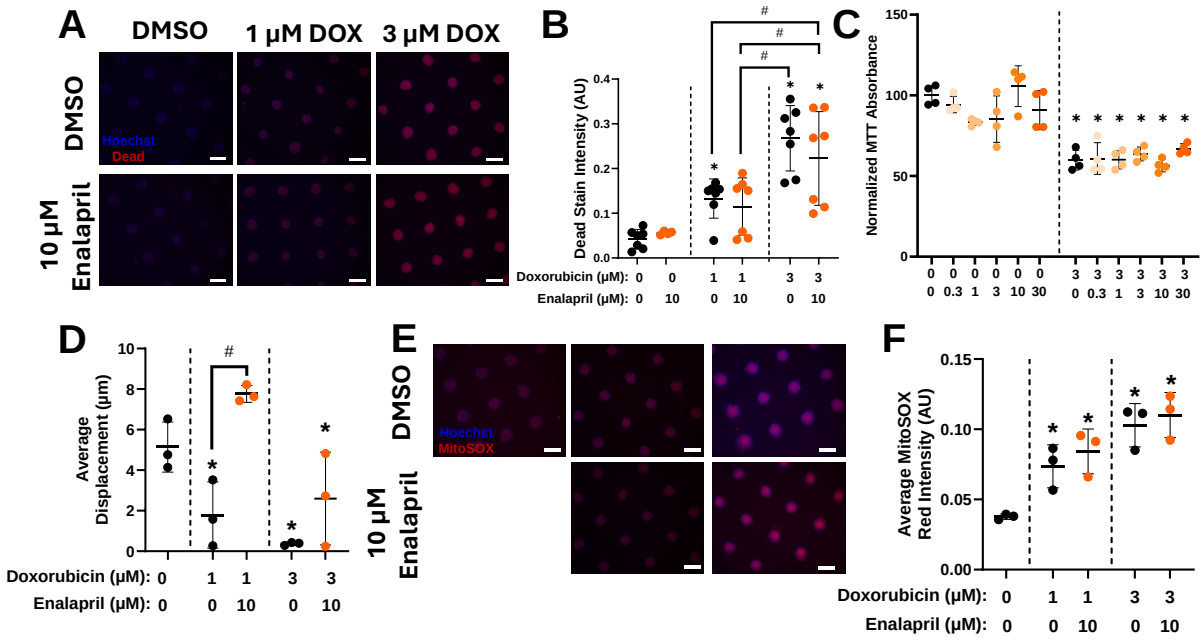

Figure 4.3. Enalapril co-treatment to prevent doxorubicin-induced cardiotoxicity. Co-treatment with the ACE inhibitor enalapril did not demonstrate cardioprotective effects on cell viability as measured by **(A-B)** LIVE/DEAD staining of cardiac microtissues (N = 7 molds) or **(C)** MTT assay of hiPSC-CM monolayer (N = 4 wells). **(D)** Functional cardioprotection was also assessed by contractility and saw significant improvements with enalapril co-treatment (N = 3 molds; 3 microtissues per mold). **(E-F)** Mechanistic assessment on ROS generation was assessed using MitoSOX fluorescent staining as an indicator of ROS generation (N = 3 molds). No significant differences due to enalapril co-treatment were observed. * indicate statistically significance ($p < 0.05$) for one- or two-way ANOVA with a Tukey post-hoc test compared to untreated controls. # indicate statistical significance compared to the bracketed group treated with the different enalapril or doxorubicin concentrations. Scale bars = 400 μm.

4.4.3. Topoisomerase IIβ inhibition did not influence doxorubicin-induced cardiotoxicity

We next examined the cardioprotective properties of the FDA-approved topoisomerase IIβ inhibitor, dexrazoxane. LIVE/DEAD staining in cardiac microtissues cotreated with 10 μM dexrazoxane and 1 μM doxorubicin had a non-significant reduction in DEAD stain intensity (0.092 ± 0.022 AU) compared to microtissues that were not cotreated with dexrazoxane (0.110 ± 0.33 AU), but both were significantly higher than untreated controls (0.056 ± 0.023 AU) (**Figure 4.4A-B**). Cotreatment with up to 30 μM dexrazoxane also did not significantly change viability measured by MTT assay for hiPSC-CMs treated with 1 μM (control: 62.3 ± 19.0% versus 30 μM dexrazoxane: 62.4 ± 12.9%) or 3 μM (control: 52.8 ± 10.2% versus 30 μM dexrazoxane: 46.4 ± 9.0%) doxorubicin. A similar lack of change in relative viability was similarly observed at higher doses of dexrazoxane up to 300 μM (**Supplemental Figure 4.3**). Finally, cotreatment with 10 μM dexrazoxane did not cause significant differences in OCR or OCR/ECAR ratio

(**Figure 4.4C and Supplemental Figure C.4**). However, there were non-significant increases between doxorubicin-treated and dexrazoxane-cotreated hiPSC-CMs in basal respiration (42.1 ± 7.0 versus 48.0 ± 3.8 pmol/min/10,000 cells, respectively) and ATP-respiration (39.1 ± 6.2 versus 42.9 ± 3.2 pmol/min/10,000 cells, respectively), which suggests some protection of hiPSC-CM metabolism. However, there were no significant differences in the relative balance of oxidative phosphorylation and glycolysis as measured by OCR/ECAR ratio (**Supplemental Figure C.5**).

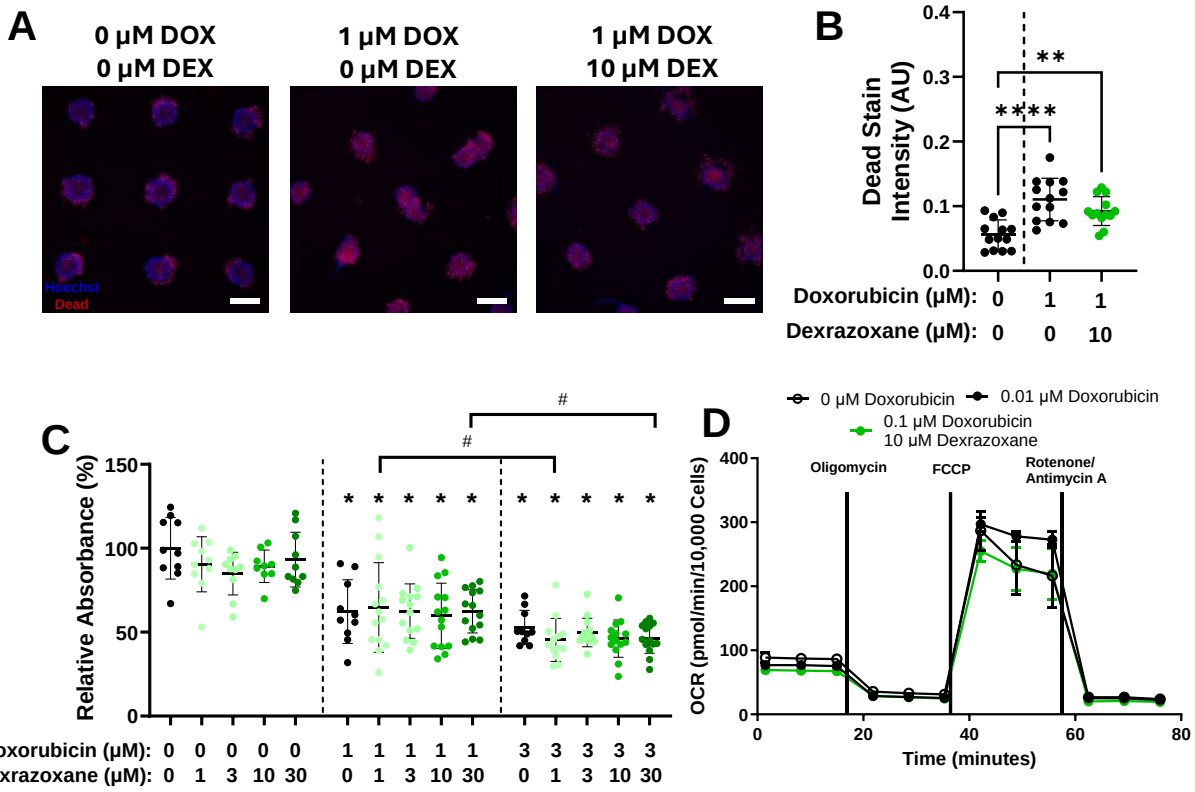

Figure 4.4. Dexrazoxane co-treatment to prevent doxorubicin-induced cardiotoxicity. Co-treatment with the topoisomerase IIβ inhibitor dexrazoxane did not demonstrate significant cardioprotective effects on cell viability as measured by **(A-B)** LIVE/DEAD staining of cardiac microtissues (N = 13 molds) or **(C)** MTT assay of hiPSC-CM monolayer (N = 10 wells). **(D)** Changes in oxygen consumption rate (OCR) were also measured to investigate the ability of dexrazoxane to prevent doxorubicin-induced metabolic changes (N = 8-12 wells). Data are displayed as mean ± standard deviation except for OCR, which is displayed as mean ± standard error. * indicate statistical significance ($p < 0.05$) for one- or two-way ANOVA with a Tukey post-hoc test compared to non-doxorubicin treated positive controls or indicated group. # indicate statistical significance compared to the bracketed group treated with different dexrazoxane concentrations. Scale bars = 400 µm.

4.4.4. hiPSC-CM maturation enhances doxorubicin-induced cardiotoxicity in cardiac microtissues

Maturation in hiPSC-CMs has been linked to shifts in topoisomerase II isoform [45]. To examine if this influenced the ability of dexrazoxane to prevent doxorubicin-induced cardiotoxicity, engineered cardiac microtissues were cultured in a low-glucose, high-fatty acid maturation media for one followed by 72-hour-long exposures to 1 μM doxorubicin with or without dexrazoxane co-treatment. Dead stain intensity was not significantly changed in control microtissues in maturation media (0.059 ± 0.018 AU) compared to standard RPMI/B27-based media (0.56 ± 0.023 AU) (**Figure 4.5A-B**). Despite similar baseline viability, microtissues cultured in maturation media and treated with doxorubicin had significantly dead stain intensities (0.233 ± 0.050 AU) compared to those in standard media (0.110 ± 0.033 AU). This also held true for dexrazoxane-cotreated microtissues, which also did not possess significantly reduced dead stain intensities compared to non-dexrazoxane-treated tissues (regular: 0.093 ± 0.022 AU versus maturation: 0.226 ± 0.100 AU). Together, these results suggest that media-based maturation significantly increases the susceptibility of microtissues to doxorubicin-induced toxicity but does not alter the ability of dexrazoxane cotreatment to prevent it. To validate these results, we similarly examined viability in two-dimensional hiPSC-CMs cultured in either maturation or standard media for one week using an MTT assay (**Figure 4.5C**). Unlike in microtissues, we did not observe a significant difference in viability between maturation media and standard culture media at a range of doxorubicin concentrations (**Figure 4.5C**).

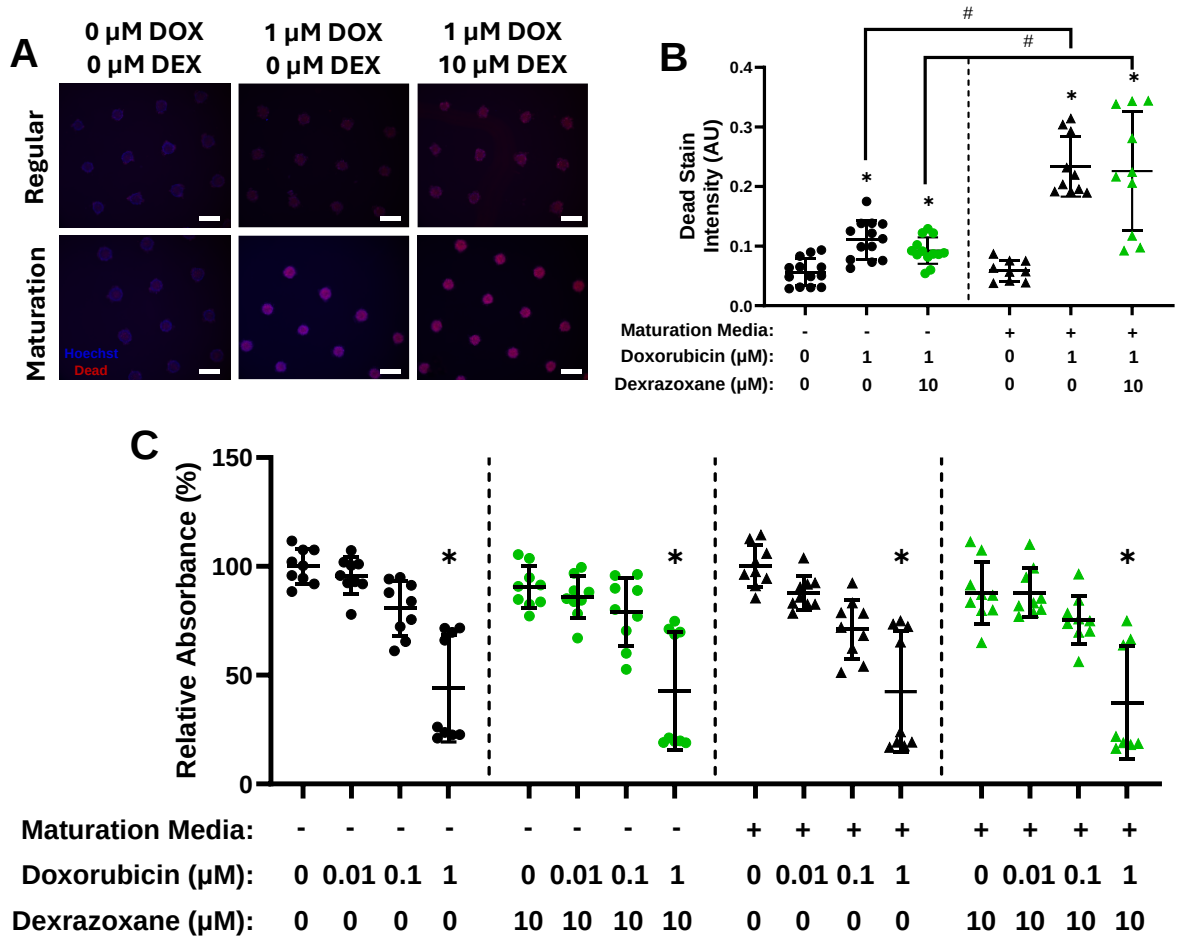

Figure 4.5. Effects of fatty acid-based maturation media on doxorubicin cardiotoxicity and dexrazoxane cardioprotection. Monolayers of hiPSC-CMs or cardiac microtissues were cultured in either standard RPMI/B27-based medias (-) or fatty acid-based maturation media (+) to shift their metabolic profile to a more adult-like phenotype. **(A-B)** LIVE/DEAD staining of cardiac microtissues (N = 13 molds) and **(C)** MTT assay of hiPSC-CM monolayer (N = 8 wells) were used to assess viability at a range of doxorubicin and dexrazoxane concentrations in regular and maturation media. * indicate statistically significance ($p < 0.05$) for one- or two-way ANOVA with a Tukey post-hoc test compared to untreated controls. # indicate statistical significance compared to the bracketed group cultured in a different media formulation. Scale bars = 400 µm.

4.4.5. Small-molecule modulation of metabolism partially rescues doxorubicin-induced cardiotoxicity in hiPSC-CM monolayers

Recent work has suggested that doxorubicin-induced glycolytic shifts in cardiomyocyte metabolism can exacerbate energy imbalances and lead to worse cardiotoxicity [46, 47]. Indisulam, a small-molecule inhibitor of CA12, has been identified as a potential therapeutic for maintaining metabolic balance and preventing anthracycline-induced cardiotoxicity [35]. We initially investigated indisulam's effect on cell viability in two-dimensional, hiPSC-CM monolayers at log-spaced doxorubicin concentrations (**Figure**

4.6A). We observed statistically significant reductions in viability from treatment with 0.01 (86.8 ± 20.6%), 0.1 (83.1 ± 15.8%), and 1 μM (43.0 ± 16.7%) doxorubicin concentrations without indisulam cotreatment compared vehicle controls (100.0 ± 17.9%). Cotreatment with 10 μM indisulam prevented significant viability loss at lower doxorubicin concentrations (0.01 μM: 85.8 ± 11.7% and 0.1 μM: 91.2 ± 6.2%) compared to vehicle controls while cotreatment significantly increased viability for hiPSC-CMs exposed to 1 μM doxorubicin (56.4 ± 12.8%). However, these same benefits were not observed with LIVE/DEAD staining of cardiac microtissues (**Figure 4.6B-C**), where dead stain intensity was not significantly different between indisulam cotreated (0.130 ± 0.024 AU) and doxorubicin-only treated microtissues (0.129 ± 0.018 AU).

Despite the significant increase in viability observed from the MTT assay, average MitoSOX intensity in two-dimensional monolayers was not significantly different with indisulam cotreatment (3.188 ± 0.505 AU/nuclei) compared to control cells (2.688 ± 0.433 AU/nuclei) (**Figure 4.6D-E**). Indisulam cotreatment did significantly decrease OCR compared to control hiPSC-CMs, causing a significant reduction in basal (42.1 ± 7.0 versus 23.4 ± 4.2 pmol/min/10,000 cells), ATP-linked (39.1 ± 6.2 versus 17.5 ± 1.9), and maximal (228.4 ± 25.5 versus 127.1 ± 18.2 pmol/min/10,000 cells) respiration as well as spare respiratory capacity (186.2 ± 19.3 versus 103.7 ± 14.3 pmol/min/10,000 cells) and non-mitochondrial oxygen consumption (20.0 ± 2.4 versus 12.1 ± 2.4 pmol/min/10,000 cells), respectively (**Figure 4.6F and Supplemental Figure C.6).** OCR/ECAR ratio also significantly decreased with indisulam cotreatment (4.3 ± 0.5 versus 2.4 ± 0.3 pmol/mpH), suggesting that indisulam shifts hiPSC-CM metabolism toward glycolysis.

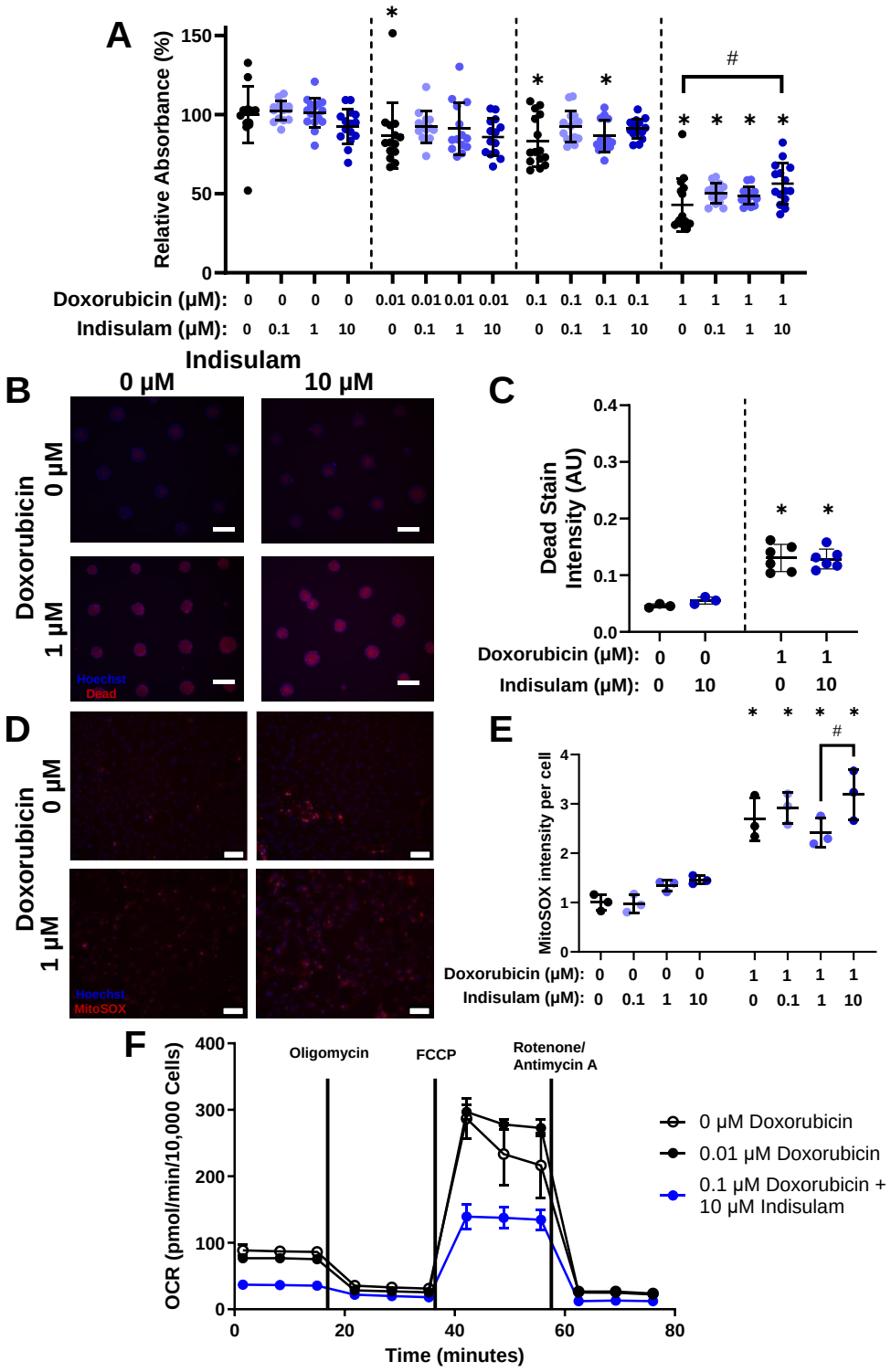

Figure 4.6. Indisulam co-treatment to prevent doxorubicin-induced cardiotoxicity. (A) Co-treatment with the carbonic anhydrase 12 inhibitor indisulam demonstrated statistically significant cardioprotection on cell viability measured in hiPSC-CM monolayers (N = 14-15 wells), but not in (**B-C**) cardiac microtissues as measured by LIVE/DEAD staining (N = 3 molds, scale bars = 400 μm). (**D-E)** ROS generation was assessed using MitoSOX fluorescent staining as an indicator of ROS generation in hiPSC-CM monolayers (N = 3 wells, scale bars = 100 μm). Data are displayed as

mean ± standard deviation except for OCR, which is provided as mean ± standard error. * indicate statistical significance ($p < 0.05$) for one- or two-way ANOVA with a Tukey post-hoc test compared to non-doxorubicin treated controls with a matched indisulam concentration. # indicate statistical significance compared to the bracketed group cultured in a different indisulam concentration.

4.5. Discussion

Chemotherapy-related cardiotoxicity, especially from anthracyclines, remains a major hurdle for preserving the long-term health of cancer survivors and presents a major clinical challenge in cardio-oncology [3-5]. While some success has been achieved with novel drug formulations and investigational molecules, cardiovascular risk remains high [22, 23]. As a result, significant effort has been expended to clarify the mechanisms of anthracycline-induced cardiotoxicity and identify potential cotherapies that can be used in conjunction with standard chemotherapy. hiPSC-CMs have increasingly become a model of choice for such preclinical screening due to their ability to recapitulate human cardiac physiology *in vitro [32, 48-50]*. In this study, we leveraged ventricular hiPSC-CMs to model doxorubicin-induced cardiotoxicity as well as screen three distinct classes of compounds (ACE inhibitors, topoisomerase IIβ inhibitors, and CA12 inhibitors) for their ability to prevent anthracycline toxicity.

Initial experiments with the anthracyclines doxorubicin, epirubicin, and idarubicin demonstrated similar concentration-dependent reductions in viability for all three compounds with a slightly larger maximum toxicity after idarubicin exposure (**Figure 4.1A**). These findings reflect previous work comparing the toxicity of these three anthracyclines on hiPSC-CMs which predicted viability EC50s within one order of magnitude of each other despite varied clinical doses [51]. Using doxorubicin as a representative anthracycline, we also observed concentration-dependent functional declines in microtissue contractility (**Figure 4.1B**), reflecting clinical declines in left ventricular ejection fraction [52]. Microtissue electrophysiology was also disrupted, with a total loss of excitability at high doxorubicin concentrations, and concentration-dependent reductions in APD_{mxr} after 72-hour-long doxorubicin exposure (**Figure 4.2B-D**). However, this loss of excitability did not occur after shorter 1- and 24-hour-long exposures. Similarly, 24-hour doxorubicin exposures caused significantly less cell death than longer exposures (**Figure 4.2A**).

hiPSC-CMs exposed to doxorubicin also had significantly reduced rates of oxidative phosphorylation (**Figure 4.1C** and **Supplemental Figure C.1**) and were more heavily reliant on glycolysis (**Supplemental Figure C.1G**). This shift towards glycolysis has been previously reported to occur *in vivo* [46, 47] as well as in hiPSC-CMs with doxorubicin treatment. Although this change was only observed at the highest tested concentration when overall mitochondrial metabolism was virtually eliminated, making it difficult to determine if this change is as robust before severe cytotoxicity. Overall, these experiments demonstrated that we successfully recapitulated concentration- and time-dependent effects of anthracycline cardiotoxicity in hiPSC-CMs on multiple metrics of viability and function.

Frontline anti-heart failure therapies, like ACE inhibitors, have had substantial interest in being repurposed as preventative treatments for anthracycline-induced cardiotoxicity [28, 29, 52]. We sought to investigate if such previously reported cardioprotective effects could be replicated in hiPSC-CMs via *in vitro* cotreatment with enalapril (**Figure 4.3**). Our data did not suggest a protective role for enalapril on cardiomyocyte viability, with non-significant differences in viability measured by both LIVE/DEAD staining (**Figure 4.3A-B**) and MTT assay (**Figure 4.3C**). Though there was a protective effect on microtissue contractility, albeit minor (**Figure 4.3D**). This lack of difference is not entirely unsurprising given that only some small-scale clinical trials have found enalapril is cardioprotective when administered during chemotherapy, with more comprehensive meta-analyses of available data suggesting little benefit mixed effects [28, 53]. Moreover, enalapril cardioprotection has traditionally been hypothesized to occur due to its primary mechanism of offloading the heart due to its effects on the vascular system more broadly, which remains a major limitation of cardiac-specific hiPSC-CM-based models [54]. Significant advances in developing microphysiological systems with integrated cardiovascular systems will ultimately be necessary to test drugs with indirect cardiac benefits beyond the capabilities of our platform. In addition to indirect cardiac benefits from traditional mechanisms, ACE inhibitors have also been hypothesized to provide secondary anthracycline cardioprotection via ROS scavenging [55, 56]. However, we did not

observe significant reductions in ROS generation from enalapril co-treatment (**Figure 4.3E-F**), suggesting enalapril does not effectively act via this mechanism. This aligns with previously published preclinical data that suggests other ACE inhibitors (*i.e.* zofenopril and captopril), are better ROS scavengers due to slight differences in their chemical structures [44, 55, 57].

We also examined direct-cardiomyocyte cardioprotection from the FDA-approved topoisomerase IIβ inhibitor, dexrazoxane, which has previously been demonstrated to protect hiPSC-CMs from doxorubicin-induced toxicity *in vitro* [45, 58]. We did not observe significant protective effects on viability (**Figure 4.4A-C**), but we did see small, non-statistically significant increases in cellular metabolism with cotreatment with dexrazoxane, suggesting minor metabolic protection (**Figure 4.4D and Supplemental Figure C.5**). Previously published work examining dexrazoxane and doxorubicin-induced cardiotoxicity suggest that hiPSC-CM immaturity may limit their ability to effectively capture dexrazoxane cardioprotection [32, 45]. In fact, at least one study found that cotreatment with dexrazoxane increased the severity of doxorubicin-induced toxicity *in vitro*, contrary to what is observed clinically [32]. Recent work has suggested that hiPSC-CM maturity similarly influences doxorubicin toxicity by promoting a transition from the α to β isoform of topoisomerase II [45]. In this study, matured hiPSC-CMs were significantly more susceptible to doxorubicin toxicity after 24 hours as measured by CCK-8 assay, TUNEL staining, and γH2AX staining. Moreover, mature hiPSC-CMs cotreated with 100 μM dexrazoxane had significantly higher relative viability than immature hiPSC-CMs, which were not significantly protected by dexrazoxane cotreatment.

It is well understood that hiPSC-CMs possess an immature phenotype relative to adult cardiomyocytes and multiple advanced culture techniques have been successfully leveraged to promote maturation [59, 60]. Building from such work, we used a previously published low-glucose, high-fatty acid media [39, 40] to promote metabolic maturation in our hiPSC-CMs and engineered microtissues. We found that maturation media did increase doxorubicin toxicity in cardiac microtissues, but not hiPSC-CM monolayers (**Figure 4.5**). However, we did not observe significant differences in dexrazoxane cardioprotection with

either assay or system. This suggests that our more mature culture system, with three-dimensional culture; electrical pacing; and maturation media, we could confirm the role of hiPSC-CM maturation to influence doxorubicin-induced toxicity *in vitro*. Several factors may account for the absence of this effect in two-dimensional culture and the efficacy of dexrazoxane even with maturation media. First, hiPSC-CMs were cultured for an additional week in maturation media compared to the additional 30 days of culture. In previous studies from our lab, we have observed significant electrophysiological maturation in microtissues cultured for an additional two-weeks without maturation media, suggesting that time may be a required pre-requisite for maturation-related changes in protein expression [61]. Further, we did not confirm the relative expression of topoisomerase II isoforms in our system with and without maturation. While generally higher expressions of topoisomerase II, regardless of isoform, may enhance toxicity, only topoisomerase IIβ is likely to increase the efficacy of dexrazoxane cardioprotection.

Beyond the relative maturity of hiPSC-CMs, we and others have documented significant shifts towards glycolytic metabolism due to doxorubicin toxicity, identifying an important role for cardiomyocyte metabolism in facilitating anthracycline-induced cardiotoxicity (**Figure 4.1C**) [46, 47]. Indisulam has recently been hypothesized to mitigate this change in hiPSC-CMs to provide a cardioprotective benefit via CA12 inhibition [35]. In this study, we observed significant improvements in cell viability from indisulam cotreatment compared (**Figure 4.6A**) in two-dimensional hiPSC-CMs, although this did not occur in microtissues (**Figure 4.6B-C**). When examining potential mechanisms for this effect, we observed that ROS generation was not improved by indisulam cotreatment (**Figure 4.6D-E**) and that, counterintuitively, hiPSC-CM respiration was reduced and there was a relative increase in glycolysis (*i.e.* reduction in OCR/ECAR ratio) (**Figure 4.6F and Supplemental Figure C.6**). This second observation runs counter to the mechanism previously proposed for indisulam cardioprotection, which suggested that CA12 inhibition prevents activation of doxorubicin-induced glycolysis [35]. However, this work only examined glycolysis with indisulam cotreatment without also measuring oxidative phosphorylation. Thus, there is a possibility

that overall energy balance is affected by indisulam, not just glycolysis, that may influence the efficacy of indisulam cotreatment.

Overall, this work supports the role of hiPSC-CMs as fit-for-purpose models of chemotherapy-induced cardiotoxicity and to specifically recapitulate key features of anthracycline-induced toxicity in both concentration- and time-dependent manners. Moreover, due to their ability to recreate multiple aspects of human cardiac physiology *in vitro*, they offer a broad platform with which to examine toxicity multiple mechanisms (*i.e.* ACE inhibition, topoisomerase IIβ inhibition, and cardiac metabolism). Critically, however, continued improvements to hiPSC-CMs function, beyond traditionally considered electrophysiology; calcium handling; and contractility, will be required to ensure their applicability to as-of-yet identified mechanisms of toxicity. Future work for this project should address the role of hiPSC-CM maturation in doxorubicin toxicity generally as well as dexrazoxane cardioprotection more specifically. Similarly, given metabolisms increasingly appreciated role in doxorubicin toxicity, additional work with indisulam or other approaches should investigate the metabolic axis as a means for protecting the heart. Ultimately, validating hiPSC-CMs as fit-for-purpose screening models will greatly advance drug discovery and focus the drug pipeline on human-relevant compounds and mechanisms for the design of better chemotherapeutics.

4.6. Acknowledgements

I would like to acknowledge the substantial contributions of the many people who supported this work, including Rojry Basnet, Ashton Szarnicki, and Dalia Heikal for their assistance in performing many of the experiments presented in this chapter. Additionally, this work was supported by Drs. Peng Zhang and Naohiro Yano from the Mitochondrial Function and *In Vivo* Imaging (MF-II) Services Core of the CardioPulmonary Vascular Biology COBRE from the Ocean State Research Institute of the Providence VA Medical Center. We are also thankful for the financial support of the Brown University Biomedical Innovations to Impact (BBII) Award (to Drs. Kareen Coulombe, Bum-Rak Choi, and Ulrike Mende).

4.7. References

1. Mariotto, A.B., et al., *Projections of the cost of cancer care in the United States: 2010–2020.* Journal of the National Cancer Institute, 2011. **103**(2): p. 117-128.
2. Parry, C., et al., *Cancer survivors: a booming population.* Cancer epidemiology, biomarkers & prevention, 2011. **20**(10): p. 1996-2005.
3. Patnaik, J.L., et al., *Cardiovascular disease competes with breast cancer as the leading cause of death for older females diagnosed with breast cancer: a retrospective cohort study.* Breast Cancer Research, 2011. **13**: p. 1-9.
4. Lenneman, C.G. and D.B. Sawyer, *Cardio-oncology: an update on cardiotoxicity of cancer-related treatment.* Circulation research, 2016. **118**(6): p. 1008-1020.
5. Lind, L., et al., *Key characteristics of cardiovascular toxicants.* Environmental health perspectives, 2021. **129**(9): p. 095001.
6. Lau, E.S., et al., *Cardiovascular risk factors are associated with future cancer.* Cardio Oncology, 2021. **3**(1): p. 48-58.
7. Ferdinandy, P., et al., *Definition of hidden drug cardiotoxicity: paradigm change in cardiac safety testing and its clinical implications.* European heart journal, 2019. **40**(22): p. 1771-1777.
8. Brown, S.-A., *Preventive cardio-oncology: the time has come.* Frontiers in Cardiovascular Medicine, 2020. **6**: p. 187.
9. Yeh, E.T. and C.L. Bickford, *Cardiovascular complications of cancer therapy: incidence, pathogenesis, diagnosis, and management.* Journal of the American College of Cardiology, 2009. **53**(24): p. 2231-2247.
10. Mross, K., *New anthracycline derivatives: what for?* European Journal of Cancer and Clinical Oncology, 1991. **27**(12): p. 1542-1544.

11. Giordano, S.H., et al., *Decline in the use of anthracyclines for breast cancer.* Journal of clinical oncology, 2012. **30**(18): p. 2232-2239.

12. Gianni, L., et al., *Anthracycline cardiotoxicity: from bench to bedside.* Journal of Clinical Oncology, 2008. **26**(22): p. 3777-3784.

13. Kremer, L., et al., *Frequency and risk factors of anthracycline-induced clinical heart failure in children: a systematic review.* Annals of Oncology, 2002. **13**(4): p. 503-512.

14. Shan, K., A.M. Lincoff, and J.B. Young, *Anthracycline-induced cardiotoxicity.* Annals of internal medicine, 1996. **125**(1): p. 47-58.

15. Von Hoff, D.D., et al., *Risk factors for doxorubicin-lnduced congestive heart failure.* Annals of internal medicine, 1979. **91**(5): p. 710-717.

16. Blanco, J.G., et al., *Anthracycline-related cardiomyopathy after childhood cancer: role of polymorphisms in carbonyl reductase genes—a report from the Children's Oncology Group.* Journal of Clinical Oncology, 2012. **30**(13): p. 1415-1421.

17. Cardinale, D., F. Iacopo, and C.M. Cipolla, *Cardiotoxicity of anthracyclines.* Frontiers in cardiovascular medicine, 2020. **7**: p. 26.

18. Saleh, Y., et al., *Anthracycline-induced cardiotoxicity: mechanisms of action, incidence, risk factors, prevention, and treatment.* Heart failure reviews, 2021. **26**: p. 1159-1173.

19. Capranico, G., et al., *Different patterns of gene expression of topoisomerase II isoforms in differentiated tissues during murine development.* Biochimica et Biophysica Acta (BBA)-Gene Structure and Expression, 1992. **1132**(1): p. 43-48.

20. Hortobagyi, G., *Anthracyclines in the treatment of cancer: an overview.* Drugs, 1997. **54**(Suppl 4): p. 1-7.

21. Vejpongsa, P. and E. Yeh, *Topoisomerase 2β: a promising molecular target for primary prevention of anthracycline-induced cardiotoxicity.* Clinical Pharmacology & Therapeutics, 2014. **95**(1): p. 45-52.

22. Batist, G., et al., *Reduced cardiotoxicity and preserved antitumor efficacy of liposome-encapsulated doxorubicin and cyclophosphamide compared with conventional doxorubicin and cyclophosphamide in a randomized, multicenter trial of metastatic breast cancer.* Journal of Clinical Oncology, 2001. **19**(5): p. 1444-1454.

23. Martins-Teixeira, M.B. and I. Carvalho, *Antitumour anthracyclines: progress and perspectives.* ChemMedChem, 2020. **15**(11): p. 933-948.

24. Raber, I. and A. Asnani, *Cardioprotection in cancer therapy: novel insights with anthracyclines.* Cardiovascular research, 2019. **115**(5): p. 915-921.

25. Cardinale, D., et al., *Early detection of anthracycline cardiotoxicity and improvement with heart failure therapy.* Circulation, 2015. **131**(22): p. 1981-1988.

26. Becker, M.M., et al., *Anthracycline cardiotoxicity: current methods of diagnosis and possible role of 18F-FDG PET/CT as a new biomarker.* Cardio-Oncology, 2023. **9**(1): p. 17.

27. Cardinale, D., et al., *Anthracycline-induced cardiomyopathy: clinical relevance and response to pharmacologic therapy.* Journal of the American College of Cardiology, 2010. **55**(3): p. 213-220.

28. Austin, D., et al., *Preventing cardiac damage in patients treated for breast cancer and lymphoma: the PROACT clinical trial.* Cardio Oncology, 2024. **6**(5): p. 684-696.

29. Zhang, Y., et al., *Protective role of enalapril in anthracycline-induced cardiotoxicity: a systematic review.* Frontiers in Pharmacology, 2020. **11**: p. 788.

30. Kollárová-Brázdová, P., et al., *Investigation of structure-activity relationships of dexrazoxane analogs reveals topoisomerase IIβ interaction as a prerequisite for effective protection against*

anthracycline cardiotoxicity. The Journal of Pharmacology and Experimental Therapeutics, 2020. **373**(3): p. 402-415.

31. Zheng, H. and H. Zhan, *Preventing Anthracycline-Associated Heart Failure: What Is the Role of Dexrazoxane?* JACC: CardioOncology, 2024. **6**(2): p. 318-321.

32. Burridge, P.W., et al., *Human induced pluripotent stem cell-derived cardiomyocytes recapitulate the predilection of breast cancer patients to doxorubicin-induced cardiotoxicity.* Nat Med, 2016. **22**(5): p. 547-56.

33. Richards, D.J., et al., *Human cardiac organoids for the modelling of myocardial infarction and drug cardiotoxicity.* Nature Biomedical Engineering, 2020. **4**(4): p. 446-462.

34. Verheijen, M., et al., *Bringing in vitro analysis closer to in vivo: Studying doxorubicin toxicity and associated mechanisms in 3D human microtissues with PBPK-based dose modelling.* Toxicology letters, 2018. **294**: p. 184-192.

35. Liu, C., et al., *CRISPRi/a screens in human iPSC-cardiomyocytes identify glycolytic activation as a druggable target for doxorubicin-induced cardiotoxicity.* Cell Stem Cell, 2024. **31**(12): p. 1760-1776. e9.

36. Burridge, P.W., A. Holmström, and J.C. Wu, *Chemically defined culture and cardiomyocyte differentiation of human pluripotent stem cells.* Current Protocols in Human Genetics, 2015. **87**(1): p. 21.3. 1-21.3. 15.

37. Kofron, C., et al., *A Predictive in Vitro Risk Assessment Platform for Pro-Arrhythmic Toxicity Using Human 3D Cardiac Microtissues.* Scientific Reports, 2021. **11**: p. 1-16.

38. Daley, M., et al., *In vitro to in vivo extrapolation from three-dimensional hiPSC-derived cardiac microtissues and physiologically based pharmacokinetic modeling to inform next-generation arrhythmia risk assessment.* Toxicological Sciences, 2024: p. kfae079.

39. Feyen, D.A., et al., *Metabolic maturation media improve physiological function of human iPSC-derived cardiomyocytes.* Cell reports, 2020. **32**(3): p. 107925.

40. Snyder, C.A., K.D. Dwyer, and K.L. Coulombe, *Advancing Human iPSC-Derived Cardiomyocyte Hypoxia Resistance for Cardiac Regenerative Therapies through a Systematic Assessment of In Vitro Conditioning.* International Journal of Molecular Sciences, 2024. **25**(17): p. 9627.

41. Stirling, D.R., et al., *CellProfiler 4: improvements in speed, utility and usability.* BMC bioinformatics, 2021. **22**(1): p. 1-11.

42. Soepriatna, A.H., et al., *Action potential metrics and automated data analysis pipeline for cardiotoxicity testing using optically mapped hiPSC-derived 3D cardiac microtissues.* Plos one, 2023. **18**(2): p. e0280406.

43. Kobeissi, H., et al., *MicroBundleCompute: Automated segmentation, tracking, and analysis of subdomain deformation in cardiac microbundles.* arXiv preprint arXiv:2308.04610, 2023.

44. Bartosz, M., J. Kedziora, and G. Bartosz, *Antioxidant and prooxidant properties of captopril and enalapril.* Free Radical Biology and Medicine, 1997. **23**(5): p. 729-735.

45. Cui, N., et al., *Doxorubicin-induced cardiotoxicity is maturation dependent due to the shift from topoisomerase IIα to IIβ in human stem cell derived cardiomyocytes.* Journal of Cellular and Molecular Medicine, 2019. **23**(7): p. 4627-4639.

46. Carvalho, R.A., et al., *Metabolic remodeling associated with subchronic doxorubicin cardiomyopathy.* Toxicology, 2010. **270**(2-3): p. 92-98.

47. Wakasugi, S., et al., *Myocardial substrate utilization and left ventricular function in adriamycin cardiomyopathy.* Journal of Nuclear Medicine, 1993. **34**(9): p. 1529-1535.

48. Chen, I.Y., E. Matsa, and J.C. Wu, *Induced pluripotent stem cells: at the heart of cardiovascular precision medicine.* Nature Reviews Cardiology, 2016. **13**(6): p. 333.

49. Gintant, G., et al., *Use of Human Induced Pluripotent Stem Cell–Derived Cardiomyocytes in Preclinical Cancer Drug Cardiotoxicity Testing: A Scientific Statement From the American Heart Association.* Circulation research, 2019. **125**(10): p. e75-e92.

50. Magdy, T., et al., *Human induced pluripotent stem cell (hiPSC)-derived cells to assess drug cardiotoxicity: opportunities and problems.* Annual review of pharmacology and toxicology, 2018. **58**: p. 83-103.

51. Bozza, W.P., et al., *Anthracycline-Induced Cardiotoxicity: Molecular Insights Obtained from Human-Induced Pluripotent Stem Cell–Derived Cardiomyocytes (hiPSC-CMs).* The AAPS journal, 2021. **23**: p. 1-12.

52. Cardinale, D., et al., *Using biomarkers to predict and to prevent cardiotoxicity of cancer therapy.* Expert review of molecular diagnostics, 2017. **17**(3): p. 245-256.

53. Zhang, C., et al., *In vitro developmental toxicology screens: a report on the progress of the methodology and future applications.* Chemical Research in Toxicology, 2016. **29**(4): p. 534-544.

54. Pointon, A., et al., *Cardiovascular microphysiological systems (CVMPS) for safety studies–a pharma perspective.* Lab on a Chip, 2021. **21**(3): p. 458-472.

55. Sacco, G., et al., *Cardioprotective effects of zofenopril, a new angiotensin-converting enzyme inhibitor, on doxorubicin-induced cardiotoxicity in the rat.* European journal of pharmacology, 2001. **414**(1): p. 71-78.

56. Sacco, G., et al., *ACE inhibition and protection from doxorubicin-induced cardiotoxicity in the rat.* Vascular pharmacology, 2009. **50**(5-6): p. 166-170.

57. Monti, M., et al., *The sulphydryl containing ACE inhibitor Zofenoprilat protects coronary endothelium from Doxorubicin-induced apoptosis.* Pharmacological research, 2013. **76**: p. 171-181.

58. Yu, X., et al., *Dexrazoxane ameliorates doxorubicin-induced cardiotoxicity by inhibiting both apoptosis and necroptosis in cardiomyocytes.* Biochemical and Biophysical Research Communications, 2020. **523**(1): p. 140-146.

59. Scuderi, G.J. and J. Butcher, *Naturally engineered maturation of cardiomyocytes.* Frontiers in cell and developmental biology, 2017. **5**: p. 50.

60. Robertson, C., D.D. Tran, and S.C. George, *Concise review: maturation phases of human pluripotent stem cell-derived cardiomyocytes.* Stem cells, 2013. **31**(5): p. 829-837.

61. Soepriatna, A.H., et al., *Human Atrial Cardiac Microtissues for Chamber-Specific Arrhythmic Risk Assessment.* Cellular and Molecular Bioengineering, 2021. **14**(5): p. 441-457.

Chapter 5 - Beyond pharmaceuticals: Fit-for-purpose new approach methodologies for environmental cardiotoxicity testing

Reproduced with permission from Daley, M.C. *et al "*Beyond pharmaceuticals: Fit-for-purpose new approach methodologies for environmental cardiotoxicity testing." *ALTEX*. 2023; 40(1):103-116. doi: 10.14573/altex.2109131. Epub 2022 Jun 1. PMID: 35648122

5.1. Abstract

Environmental factors are thought to play a substantial role in determining cardiovascular health, but data informing the risks presented by environmental toxicants is insufficient. *In vitro* new approach methodologies (NAMs) offer a promising approach with which to address the limitations of traditional *in vivo* and *in vitro* assays for assessing cardiotoxicity. Driven largely by the needs of pharmaceutical toxicity testing, considerable progress in developing NAMs for cardiotoxicity analysis has already been made. As the scientific and regulatory interest in NAMs for environmental chemicals continues to grow, a thorough understanding of the unique features of environmental cardiotoxicants and their associated cardiotoxicities is needed. Here, we review the key features of as well as important regulatory and biological considerations for fit-for-purpose NAMs for environmental cardiotoxicity. By emphasizing the challenges and opportunities presented by NAMs for environmental cardiotoxicity we hope to accelerate their development, acceptance, and application.

5.2. The need for improved cardiotoxicity evaluation of environmental chemicals

Environmental factors significantly affect global health outcomes, and cardiovascular disease (CVD), the leading cause of mortality worldwide, is no exception [1, 2]. An estimated 7-23% of CVD can be attributed to environmental factors such as air pollution, occupational hazards, agricultural run-off, and excreted chemicals [1], and a broad range of environmental chemicals are known to present cardiac-specific risk [3, 4]. Despite this, there is a shortage of knowledge regarding the cardiac-specific risks presented by environmental toxicants [5]. This gap is in large part because current cardiotoxicity testing methods have a limited ability to predict structural, electrophysiological, and contractile cardiotoxicity regardless of the underlying molecular mechanism.

5.2.1. Current cardiotoxicity testing

The major focus of recent advances in cardiotoxicity testing methods has been electrophysiological, largely due to the United States Food and Drug Administration's (FDA) adoption of International Conference on Harmonization of Technical Requirements for Registration of Pharmaceuticals for Human Use (ICH) guideline S7B in 2005 [6-8]. ICH S7B describes *in vivo* and *in vitro* models to detect delayed ventricular repolarization, a major risk factor of ventricular arrythmias [7]. Developed in response to the rapid withdrawal of prenylamine, lidoflazine, and tordiline between 1988 and 1991 due to increased incidence of torsade de pointes, a deadly ventricular arrhythmia, it rapidly set the standard for pre-clinical evaluation of cardiotoxicity.

In vivo assessment of delayed repolarization under ICH S7B relies on measuring electrophysiological features identified via electrocardiogram, primarily the QT interval, defined as time between the start of the QRS complex and end of the T wave and a metric of the duration of ventricular depolarization and repolarization [7, 9]. Prolongation of the QT interval in animal

models is considered indicative of delayed repolarization and increased arrythmia risk in humans. However, the genetic homogeny of inbred rodents and inter-species physiological differences are known to alter cardiac electrophysiology [6, 9-11], decreasing their utility for predicting human risk. For example, disparities in the expression of ion channels between human and rodent cardiomyocytes result in different heart rates and action potential kinetics, substantially altering the inter-species effect of drugs and chemicals on QT prolongation [9, 12-15]. These extrapolation challenges are especially relevant for apical endpoints that provide limited mechanistic insight [9] for *in vivo* model systems that are already expensive to implement and have limited throughput. In addition, ethical concerns surround the use of animals in toxicology, and efforts to replace, reduce, and refine *in vivo* models in biomedical research have lessened their popularity [16] and even resulted in the explicit ban of animal testing in some sectors, such as cosmetics marketed in Europe [10].

The predominant *in vitro* cardiotoxicity assay is the functional I_{Kr} assay, which is the *in vitro* portion of ICH S7B for detecting delayed repolarization [7, 9, 17]. Also known as the hERG assay, this screen examines changes in activity of the voltage-sensitive potassium channel, the primary facilitator of ventricular repolarization, whose pore-forming α subunit is encoded by the *human ether-a-go-go related gene* (hERG) [18]. Under modern nomenclature the α subunit is known as Kv11.1 and hERG as *KCNH2*. Blockade of this channel increases action potential duration and is associated with clinical QT prolongation, making the hERG assay a proxy for *in vivo* risk of ventricular fibrillation and torsade de pointes [9, 18]. Unfortunately, this approach also has a limited predictive capacity for cardiotoxicity [19]. High-throughput versions of the assay rely on immortalized cell lines modified to express voltage-sensitive potassium channels which fail to reliably reflect *in vivo* behavior [18, 20]. As a targeted, single-channel approach, this assay also cannot identify effects on other ion channels critical for proper action potential kinetics [9].

Neither the *in vivo* QT prolongation nor *in vitro* hERG assays defined in ICH S7B are designed to detect non-electrophysiological classes of cardiotoxicity (*i.e.,* structural or contractile) that can arise individually or as a result of interacting mechanisms [6, 9, 21]. Pre-clinical testing of non-electrophysiological cardiotoxicities is covered as a part of the core battery of *in vivo* assessments under the ICH S7A guidelines for general safety pharmacology. Cardiotoxicity is monitored by examining effects on blood pressure and heart rate in addition to electrocardiogram *in vivo* with optional follow-ups of other functional characteristics like cardiac output and ventricular contractility in multiple animal species [8]. *In vitro* assays that examine contractile or structural cardiotoxicity are not required, and early safety screening relies on optional target-based assays of known PoTs [22]. As a result, cardiotoxicity assessment of structural and contractile toxicities have substantial flexibility during pharmaceutical development and many approaches and study species are applied [23, 24]. However, these methods possess many of the same challenges and drawbacks as *in vivo* studies and single-target *in vitro* assays performed for electrophysiological assessment [6, 9-11, 16].

These structural, contractile, and non-hERG-related electrophysiological cardiotoxicities are increasingly appreciated as significant hazards among environmental chemicals, occurring via multiple overlapping and often incompletely understood mechanisms even for well-studied toxicants. [3, 4]. Exposure to the heavy metals (*e.g.*, arsenic, cadmium, chromium, mercury, and lead) has been associated with various non-electrophysiological cardiotoxicities such as oxidative stress, sarcomere disorganization, mitochondrial dysfunction, and calcium dysregulation in addition to increased arrhythmia risk [3, 25-27]. Polycyclic aromatic hydrocarbons (PAHs), formed as byproducts of partial combustion and constituents of crude oil, have been associated with excitation-contraction coupling dysfunction and cardiac hypertrophy [28, 29] . Polychlorinated biphenyls (PCBs), a category of industrial chemicals, have been linked to impaired left ventricular

systolic and diastolic function [30] and heart failure [31]. Mechanistic studies of PAH- and PCB-related cardiotoxicity suggest these effects arise from multiple, aryl hydrocarbon receptor-dependent and -independent pathways [32]. Bisphenol A (BPA) is also a known cardiac toxicant, and exposure has been associated with increased risk of arrhythmias, cardiac dysfunction, and heart failure [33, 34]. Organochlorine, organophosphate, and carbamate pesticides are likewise known to cause contractile dysfunction and other cardiotoxicities in addition to electrophysiological effects [35]. Consequently, neither current *in vivo* nor *in vitro* approaches are well-suited for effective assessment of the full breadth of cardiac hazards presented by environmental toxicants.

5.2.2. New approach methodologies (NAMs)

There is a growing push for new approach methodologies (NAMs) for human cardiotoxicity testing and safety assessment that address the challenges and limitations of current animal models and existing *in vitro* assays [10, 36, 37]. This new direction for toxicity assessment has largely been driven by the National Research Council report on Toxicology Testing in the 21st Century, which provided a long-term vision for developing and adopting modern approaches for toxicity testing [38, 39]. Similar initiatives have also been deployed in Europe (such as EU-ToxRisk) to promote NAM development in the European Union [10, 40]. These initiatives aim to catalyze a new, more advanced paradigm that focuses on high-throughput, mechanistic analysis of the molecular pathways of toxicity (PoTs) associated with adverse outcomes through a range of enabling technologies (*e.g.,* human stem cell culture, microfluidics, toxicogenomics, and *in silico* modeling) for specific decision-making needs [36, 41-44]. NAMs that fulfill these criteria and are designed to meet specific biological and regulatory contexts are considered to be fit-for-purpose and are consistent with this vision of the future of toxicity testing [36].

This review examines the development of fit-for-purpose NAMs for the evaluation of the cardiotoxicity of environmental chemicals (*i.e.,* assays of "environmental cardiotoxicity"). Specifically, we describe the unique elements of environmental toxicants and the features of fit-for-purpose NAMs that meet the needs of environmental safety assessment in the context of cardiac physiology. We hope to emphasize the challenges, current gaps, and need for further research and development of NAMs for environmental cardiotoxicity.

5.3. NAMs dedicated to environmental cardiotoxicity

While there is a pressing need to assess the cardiotoxic risks of an ever-increasing number of environmental chemicals [5], the majority of existing cardiotoxicity tests do not sufficiently account for the unique facets of environmental toxicants [45, 46].

5.3.1. Environmental toxicants possess more varied chemistries than pharmaceuticals

Most NAMs developed for cardiotoxicity have been optimized for pharmaceutical applications [6, 17, 21]. Potential environmental toxicants, however, represent a much broader chemical space with less well-understood mechanisms of toxicity and lower potencies (**Figure 5.1**) [45]. This pharmaceutical focus means that current *in vitro* test methods were developed using chemical libraries curated to prioritize compounds for their likelihood to be pharmaceutical leads (*e.g.,* having a low molecular weight and high water solubility) [47, 48]. As a result, prospective pharmaceuticals undergoing toxicity tests represent a substantially homogenized subset of the physicochemical space available to modern chemists (**Figure 5.1**, **Left**) [45, 47]. In contrast, environmental chemicals occupy a wider spectrum of chemistries because they represent compounds designed for more diverse applications (**Figure 5.1, Right**). This variety, in combination with the absence of selection for high-affinity biological activity, makes the needs of environmental cardiotoxicity testing substantially different from those of the pharmaceutical industry. The most useful NAMs for environmental cardiotoxicity will be able to detect

cardiotoxicity even when arising from such low potency binding and activation of unanticipated PoTs.

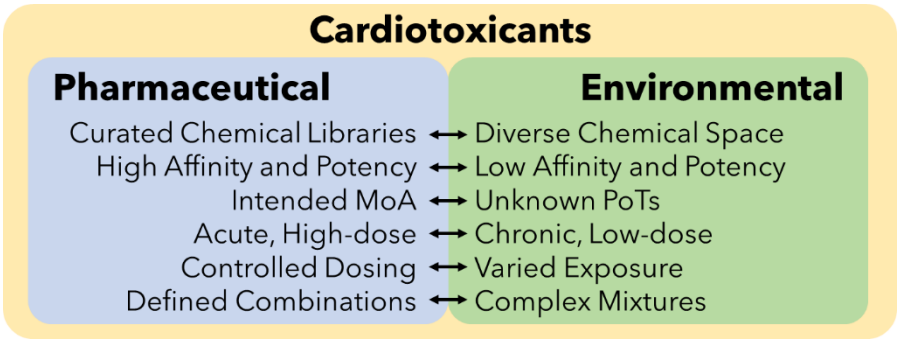

Figure 5.1. Comparison of the defining features of pharmaceutical compounds and environmental chemicals for cardiotoxicity testing. Fit-for-purpose NAMs should account for critical differences in the chemical properties and exposure profiles of pharmaceutical compounds (left) and environmental chemicals (right). Abbreviations: MoA, mechanism of action; PoTs, pathways of toxicity; NAMs, new approach methodologies.

5.3.2. Environmental toxicants have unique exposure profiles

Environmental toxicants are not only defined by their broad chemistries but also their distinct exposure profiles (**Figure 5.1**). Common "far-field" exposure scenarios can be characterized by small chronic doses in complex mixtures [39] with multiple routes of exposure such as inhalation via air pollution and ingestion via drinking water [4, 49]. These conditions differ substantially from the acutely administered single compounds of traditional cardiotoxicity testing. Moreover, the lower potencies of environmental toxicants make the ability to detect meaningful biological outcomes more difficult under chronic conditions [45]. As such, NAMs designed for the detection of environmental cardiotoxicity will require approaches that compensate for these differences. This challenge can be met in part by NAMs that have improved sensitivity in detecting environmental cardiotoxicity. Incorporation of more diverse and holistic methods, such as experimental or computational *in vitro* to *in vivo* extrapolation (IVIVE), should enable a greater quantitative understanding of complex environmental exposures such as chronic inhalation. Methods that mimic and model longer-term exposures to environmental toxicants rather than

acute biological effects will be those best suited for integration into NAMs for environmental cardiotoxicity.

5.3.3. Environmental exposures affect broad populations

Individuals exposed to environmental toxicants represent diverse populations in terms of their physiology, genetics, and cardiovascular health, each of which can compound the risk presented by otherwise sub-toxic environmental exposures, a scenario referred to as “hidden cardiotoxicity” [2, 50, 51]. NAMs for environmental cardiotoxicity will need to incorporate methods already being adopted for precision medicine to predict cardiotoxicity in individuals and populations with diverse genetic backgrounds (*e.g.,* multiple iPSC donors) and potential comorbidities (*e.g.,* myocardial infarction) [17]. Consideration of such risk factors will enhance the ability of NAMs for environmental cardiotoxicity to provide better population-representative risk assessment.

5.3.4. Environmental toxicant properties drive effective NAM design

Specific attention to the unique aspects of environmental toxicity assessment should guide continued research and design of NAMs for cardiotoxicity analysis. Due to the diverse nature of environmental toxicants and a variety of regulatory decision points, it is unlikely that a single testing paradigm will be sufficient [52]. Rather, NAMs should be designed intentionally to complement both the biological (*i.e.,* type of toxicity) and regulatory (*i.e.,* type of decision) questions asked by stakeholders [36, 53]. Reflection on their intended context of use will determine required accuracy and permittable limitations. In following sections, we will discuss the factors that determine if a NAM is fit-for-purpose for assessing environmental cardiotoxic risk in real-world contexts.

5.4. Regulatory considerations for fit-for-purpose environmental cardiotoxicity evaluation

From a regulatory standpoint, toxicity tests can be broadly categorized by the information they provide into the categories of prioritization screens, hazard screens, and risk assessment platforms [36]. Novel chemicals may require prioritization screening whereas chemicals already in the environment with suspected toxicity may need more detailed assessment. Effective NAMs for environmental cardiotoxicity will need to be cost-, time-, and resource-efficient, requiring optimization for their specific decision-making context or multiplexing to maximize the information available from a single assay. Examples of context-focused NAMs are provided below to exhibit highly tuned, fit-for-purpose platforms. The NAMs that are ultimately adopted will be those most predictive within their contexts of use, not necessarily the most technically complex or biologically complete. Thus, a thorough delineation of the intended application or applications should inform the necessary physiological features to be captured in an assay.

5.4.1. NAMs for environmental cardiotoxicity as prioritization screens

Toxicity tests that fall into the prioritization category are designed to generate an ordered list of potential toxicants that require additional evaluation. While they may not provide detailed mechanistic insight, broad assessment of relevant metrics is acceptable in early decision making prior to substantial resource commitment. Examples of this type of cardiotoxicity analysis are already being developed for both environmental toxicants [54], pharmaceutical chemicals [55, 56], and combinations of both [57]. These methods analyze cardiotoxicity data derived *in vitro* and aggregate dose-normalized metrics to calculate a safety or priority index, ranking compounds by relative risk. Even among diverse environmental toxicants, this technique can cluster chemicals by class (*i.e.,* pesticides, flame retardants, and PAHs) and hazard type [54]. This technique has also been used to identify major physicochemical properties associated with increased cardiotoxicity of related PCBs, identifying key structures and metabolites as risk factors to human health [58].

In the case of pharmaceuticals, which possess more fully characterized cardiotoxicity profiles, prioritization largely mirrors known cardiotoxicity [55, 56]. For tyrosine kinase inhibitors, a subset of anti-cancer therapeutics with wide-ranging cardiovascular side effects, prioritization further discerns between inhibitor sub-classes [56]. These insights guided subsequent experiments that provided data on a novel mechanism of TKI-induced cardiotoxicity [56]. This method is particularly powerful when leveraging data generated from high-throughput screens, allowing cardiotoxicity ranking across a broad spectrum of compounds [57]. Application of machine learning approaches to a similar high-throughput targeted hERG screen has further demonstrated that prioritization screens can enable accurate quantitative structure-activity relationship predictions for a given PoT [59]. Expansion of such techniques to datasets generated from NAMs that more broadly reproduce cardiac physiology will permit rapid prioritization of cardiotoxicity from multiple mechanisms based on chemical structure. Such high-level prioritization using next generation NAMs for environmental cardiotoxicity will ultimately enable efficient risk mitigation and biological discovery.

5.4.2. NAMs for environmental cardiotoxicity as hazard screens

While offering broad insight, prioritization screens themselves are unlikely to provide the detail needed to identify individual PoTs [36]. Hazard screens fill this niche, confirming cardiotoxicity identified during prioritization, providing additional mechanistic insight, and predicting harmful concentrations. Existing platforms are predominantly designed to examine structural [60, 61], electrophysiological [62-71], or contractile [72-79] changes separately. For example, characterization of the structural cardiotoxicity experienced by spheroids *in vitro* classified toxicants by the primary mechanism of toxicity (*i.e.,* cell viability, mitochondrial toxicity, disruption of the endoplasmic reticulum) [60]. Similarly, multi-parameter analysis of changes in the field potential shape of hiPSC-CMs using microelectrode arrays has been able to categorize

compounds by the ion channel they disrupt and their proarrhythmic potential [80]. Finally, a contractile cardiotoxicity model leveraging high-throughput imaging of cardiac spheroids effectively distinguished inotropic and non-inotropic compounds during acute exposure [76]. While increasing the complexity, expense, and length of testing, integrated systems that combine multiple hazard screens may be required to fully capture the full range of cardiac PoTs [52]. Models that examine multiple classes of cardiotoxicity concurrently could allow for identification of the predominant toxicity [81-87].

5.4.3. NAMs for environmental cardiotoxicity as risk assessment platforms

Hazard screens can ultimately be limited in their ability to inform policy makers of real environmental risk because these screens do not typically incorporate data on actual toxicant exposures (*i.e.,* concentration and duration), instead examining acute effects at relatively high doses [39]. NAMs that seek to mimic dosage, timing, and complex systems-interactions will be better suited to assess risk by linking observations to real-world exposures and outcomes via IVIVE through experimental and computational methods [36, 88, 89].

The most straightforward approach is to manually apply representative, chronic dosing regimens to existing *in vitro* cardiotoxicity models. Chronic exposure of hiPSC-CMs to physiologically relevant doses of ethanol over five days has demonstrated dose- and time-dependent effects on cardiomyocyte viability, calcium transients, and gene expression [90]. This has also been demonstrated employing physiologically based pharmacokinetic (PBPK) modeling and hiPSC-CM spheroids to examine doxorubicin cardiotoxicity *in vitro* with time-dependent concentrations that mimic *in vivo* clearance over two weeks [91]. This study observed that spheroids exposed to therapeutic regimens mirroring *in vivo* pharmacokinetics show phenotypic responses that mimic the chronic cardiotoxicity observed in cancer patients, highlighting the importance of realistic exposure profiles in chronic toxicity testing. The reverse process is also

possible. Rather than using pharmacokinetic modeling to predetermine dosing conditions, computational IVIVE models can be applied to predict the real-world exposures that result in tissue-level concentrations equivalent to those determined to be toxic within *in vitro* assays [92].

Approaches that employ more complex *in vitro* systems may further advance IVIVE by incorporating critical components of toxicant absorption, distribution, metabolism, and elimination. Microphysiological systems (MPSs) can potentially be leveraged to model pharmacokinetics and multi-organ interactions *in vitro* [46]. In emerging approaches, cardiac cells cultured in MPSs that incorporate functional liver cells demonstrate metabolite-triggered cardiotoxicities that are otherwise absent [93, 94]. While there are many advantages granted by this increase in assay complexity, incorporation of such techniques will inherently be need- and context-dependent.

5.4.4. NAMs for environmental cardiotoxicity for multiplexed decision making

Multiplexed assays that provide information about multiple decision-making contexts offer one option with which to increase efficiency. The examination of multiple, functional outcomes in combination with supplemental computational approaches has demonstrated the ability to simultaneously identify chemical hazards and provide population-level risk assessment for hundreds of chemicals [95, 96]. Such large-scale approaches can provide additional insight at multiple scales due to their ability to better characterize the variability in human cardiotoxic response while minimizing experimental burden. The scope of these assays, however, present challenges surrounding their increased experimental and analytical complexity [97] and can require numerous or carefully selected donor cell lines to maximize coverage of population effects [98]. Should such hurdles be overcome, multiplexing may provide substantial advantages in understanding and predicting environmental cardiotoxicity, and incorporation of these tools

should be considered as a method to improve the efficiency of large-scale testing of diverse environmental chemicals.

5.5. Biological considerations of fit-for-purpose environmental cardiotoxicity evaluation

From a biological standpoint, NAMs for cardiotoxicity are defined by the pathophysiological processes they attempt to mimic and measure, including the specific cell toxicities, whole organ responses, and population-level variations. To ensure a system sufficiently models this underlying physiology, effective NAMs establish a complete chain of translatability [99], alternatively known as the rule of three [100], consisting of a relevant assay system, toxicological stimulus, and system readout (**Figure 5.2**). The NAMs that most closely resemble healthy or diseased cardiac physiology, toxicant exposure, and provide information directly relevant to health outcomes are the most likely to accurately predict cardiotoxicity. To establish this chain of translatability in NAMs for environmental cardiotoxicity, the unique features of environmental toxicants must be emphasized in each individual link.

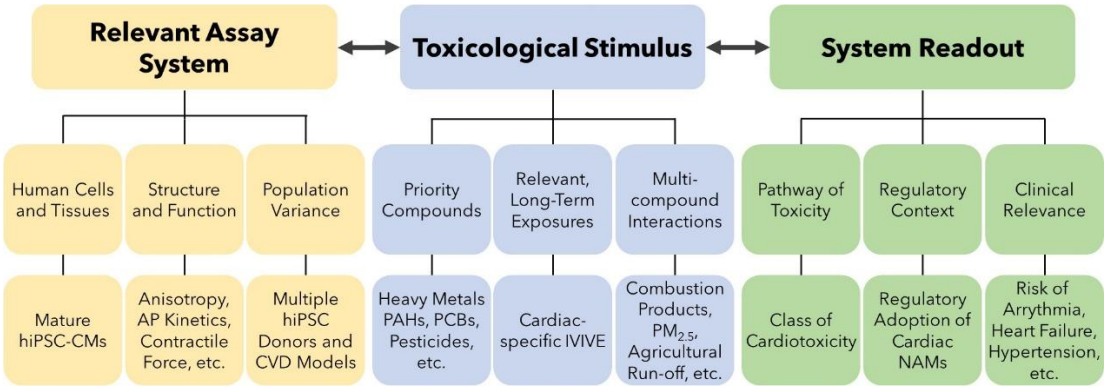

Figure 5.2. The chain of translatability for NAMs for environmental cardiotoxicity testing. Effective NAMs should include (left) a biologically relevant assay system, (center) context-appropriate stimuli, and (right) actionable system readout. Underlying general and cardiac-specific criteria for each link in the chain are listed below their respective category (top and bottom, respectively). Abbreviations: CVD, cardiovascular disease; hiPSC-CMs, human induced pluripotent stem cell-derived cardiomyocytes; IVIVE, *in vitro* to *in vivo* extrapolation; NAMs, new approach methodologies; PCBs, polychlorinated biphenyls; PAHs, polyaromatic hydrocardons; $PM_{2.5}$, fine particulate matter.

5.5.1. Fit-for-purpose NAMs recapitulate cardiac physiology

The assay system is the most prominent aspect of NAM design and has been examined extensively in the context of pharmaceutical cardiotoxicity [6, 17, 21]. As a result, significant progress has been made in developing relevant assay systems that mimic cardiac biology *in vitro* (**Figure 5.2**). A large portion of this progress has been made by applying phenotypic methods that are intended to mimic biological systems in a target-agnostic manner [99]. Target-agnosticism allows phenotypic methods to be more effective in the discovery of first-in-class small molecules compared to target-based methods [101, 102], a scenario analogous to the identification of environmental toxicity from unknown mechanisms. Contrastingly, current target-based assays are sensitive to low-dose effects for known PoTs but are unlikely to detect even severe cardiotoxicity arising from pathways and mechanisms that are not explicitly considered in their design (**Figure 5.3**). By circumventing the limitations of focused, target-centered assays, physiologically based NAMs provide a substantial opportunity for tackling the diverse chemical space and PoTs presented by environmental toxicants.

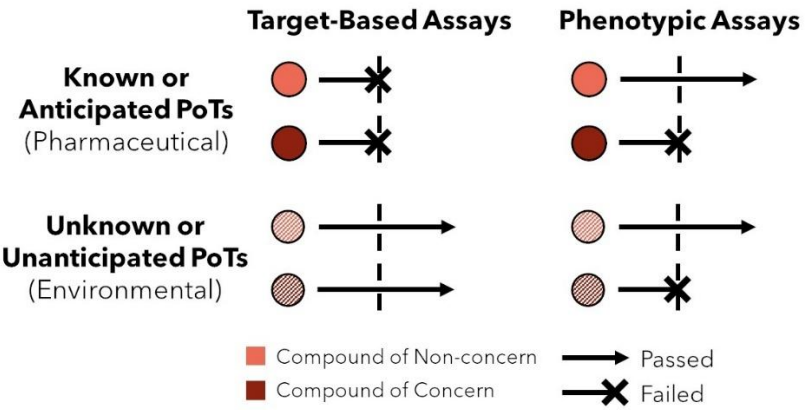

Figure 5.3. Comparison of traditional target-based and novel phenotypic *in vitro* assays in detecting known and unknown mechanisms of cardiotoxicity. (Left) Target-based assays (*e.g.,* hERG assay) isolate the effects of a single molecular target, allowing more sensitive detection of compounds with low-dose cardiotoxicity involving that PoT, but with a higher risk of false positives. (Right) Phenotypic assays (*e.g.,* spheroid or microtissue, EHT, or MPS) that better mimic human cardiac physiology can detect toxicity that results from unknown or unanticipated PoTs from environmental cardiotoxicants but can possess reduced sensitivity to specific PoTs compared to target-based assays. Abbreviations: PoT, pathway of toxicity; hERG, *human ether-a-go-go related gene*; EHT, engineered heart tissue; MPS, microphysiological system.

5.5.1.1. Distinct features of cardiac physiology are reproduced by distinct NAM designs

Current systems range from two-dimensional cardiomyocyte culture and co-culture to three-dimensional spheroids or microtissues, engineered heart tissues (EHTs), and cardiac-specific MPSs (hearts-on-a-chip), each with their respective advantages and disadvantages (**Table 5.1**) [21].

Two-dimensional monolayer systems are attractive due to their simplicity and ready integration into existing high-throughput screens including automated patch clamping, multi-electrode arrays, cellular impedance measurement, motion field imaging, and calcium imaging [103, 104]. However, two-dimensional cell culture is known to have a significant negative impact on many facets of cardiomyocyte.

Table 5.1. Advantages and disadvantages of traditional target-based and phenotypic *in vitro* assays for cardiotoxicity testing. Both traditional target-based monolayer assays (*e.g.,* the hERG assay) as well as phenotypic *in vitro* assays employing hiPSC-CMs fulfill distinct niches in cardiotoxicity assessment. Abbreviations: hERG, *human ether-a-go-go related* gene; PoT, pathway of toxicity; hiPSC-CMs, human induced pluripotent stem cell-derived cardiomyocytes.

	Model Type	Advantages	Disadvantages
Target-Based	Target-Based Monolayers (*e.g.*, hERG Assay)	Simple Sensitive Regulatory precedent	Non-human Frequent false positives Single-mechanism focus
Phenotypic	hiPSC-CM Monolayers	Human Relatively simple 2D systems	Single cell type Low sensitivity metrics
	Microtissues (spheroids)	Human Minimal cells required Self-assembled Easy-to-image High sensitivity metrics	Isotropic Indirect force measurements Pooled molecular analysis
	Engineered Heart Tissues	Human Microenvironmental control Anisotropic tissues More direct force measurement	Larger size Limited homogeneity Limited nutrient diffusion
	Microphysiological Systems (Organ-on-a-Chip)	Human Multi-organ capabilities Spatial control Fluid flow Easy-to-image	Labor intensive Specialized microfabrication

phenotype (*e.g.,* gene expression, metabolism, and contraction force) [105, 106]. Neonatal rat cardiomyocytes grown in three-dimensional aggregates display increased sensitivity to treatment with triiodothyronine (T3) and less fetal-like gene expression [107]. For hiPSC-CMs, culture in three-dimensional EHTs results in increased mitochondrial mass and oxidative phosphorylation compared to two-dimensional culture [108]. As a result, there is an increasing interest in applying these techniques in models of cardiotoxicity.

Cardiac spheroids and microtissues, self-assembling aggregates of cardiac cells, can be easily created using relatively few cells and incorporated into multi-well platforms for image-based analysis using existing testing pipelines (**.**) [109, 110]. However, they have limited utility for direct contractile force measurements because they lack the required mechanical loading and require sample pooling for some molecular analyses [109, 110]. By better modeling cardiac physiology while maintaining throughput, 3D spheroid models have demonstrated the potential for enhanced prediction of cardiotoxicity. In a comparison to hiPSC-CM monolayers, spheroids were shown to better detect the structural cardiotoxicity of 29 drugs previously approved by the FDA [60].

EHTs are created via the combination of cells and a biomaterial scaffold that is shaped by a variety of biomanufacturing methods [111, 112]. This format provides anisotropy through physical geometrical constraints, offers microenvironmental control via biomaterial selection, and permits both direct (*e.g.,* via force transducers) and indirect (*e.g.,* recording post deflection) contractile force measurements (**.**) [109, 110]. These features, along with maturation via electrical stimulation, have allowed for the development of EHT-based assays that mirror *in vivo* concentration-dependent effects of compounds with known impacts on cardiac contractility [73]. Their larger size, however, requires additional cells, limits tissue homogeneity as well as nutrient diffusion, and is generally more labor-intensive than spheroid- or microtissue-based models [109].

MPSs apply microfabrication and microfluidic techniques to create *in vitro* systems that can mimic *in vivo* spatial arrangements within and between organs [46]. These systems enable study of transport phenomena while on-chip designs permit ready integration into multi-organ models. Cardiac-only chips can provide cardiotoxicity testing platforms [72, 75] while the incorporation of other organ models, such as the liver, have been used to predict metabolite toxicity [93, 94]. However, the complexity of these systems, especially when integrating multiple organ systems, can limit throughput.

No single approach will fully capture the complexity of cardiac physiology. Already recombination of existing approaches has occurred, resulting in spheroid-based MPSs [77, 93] as well as scaffold-free EHTs made from bio-printed spheroids [113]. Further innovation of NAM designs is expected as techniques are further refined and recombined.

5.5.1.2. hiPSC-derived cardiac cells enable individual- and population-level insight

Underlying the advances described above is a reliance on hiPSC-CMs and other hiPSC-derived cardiac cells. The lineages available to researchers now include multiple sub-types of cardiomyocytes (*e.g.*, ventricular, atrial, and nodal) and non-cardiomyocytes (*e.g.,* epicardial, endocardial, and fibroblast cells) [114-116]. Human cardiac cells overcome the fundamental physiological mismatch of animal models and other cell lines in structural, electrophysiological, and contractile cardiotoxicity [6, 17, 44]. This advantage arises because hiPSC-derived cells are able to capture aspects of human cardiac physiology better than non-human approaches due to species-specific gene and protein expression patterns. This is particularly true as continued improvements are made to current differentiation techniques that accelerate their maturation and enhance their purity *in vitro* [114, 117-120]. For instance, the role of metabolic changes in driving cardiomyocyte maturity is increasingly recognized [121]. Culturing ventricular hiPSC-CMs in conditions that mimic the *in vivo* metabolic environment has been demonstrated to elicit

significant improvements in sarcomere organization, force production, and calcium handling [122]. This technique has also shown that matured hiPSC-CMs improve the fidelity of *in vitro* disease modeling by capturing phenotypes not seen with previous methods [122]. Ramped electrical stimulation of EHTs has also been shown to improve the myofibril structure, calcium handling, and electrophysiological properties of cardiomyocytes *in vitro*, leading to concentration-responses predictive of known drug effects [73, 78]. Results such as these emphasize that advances in hiPSC differentiation methods will benefit all aspects of cardiac physiology and continue to improve the sensitivity and accuracy of NAMs.

Population-level risk can also be elucidated due to the ability to readily derive hiPSCs from numerous individuals [6, 17]. Early work characterizing differences in hiPSC-CMs derived from 27 individual donors via calcium flux analysis and high-content imaging showed reproducible inter-individual variability at both baseline and in response to cardiotoxic drugs [66]. This same approach, in combination with *in silico* pharmacodynamic modeling, was able to predict corrected QT prolongation of >10 ms similarly to clinically standard thorough QT studies for arrhythmia risk [123]. This work has been expanded to include 43 donors and over 100 chemicals including environmental toxicants, food constituents, and industrial chemicals, further establishing hiPSC-CMs as suitable for population-level environmental cardiotoxicity analysis [124]. More recently, this approach has been combined with *in silico* modelling to quantify toxicodynamic variability [95]; it has also demonstrated feasibility when applied to an even broader range of over 1,000 chemicals in hiPSC-CMs from just five donors [96].

Healthy cardiac physiology, however, is not representative of a significant portion of the population due to the prevalence of CVD [2]. Current *in vivo* and *in vitro* cardiotoxicity models typically mimic non-disease states, ignoring the compounding risk of underlying CVD [51]. The use of hiPSC-CMs has enabled the study of a range of cardiac pathologies *in vitro*, particularly those

that arise from monogenic mutations (*e.g.,* long QT syndrome). This is because assay development for these conditions is more straightforward than for other, complex forms of CVD since the underlying etiology can be captured with hiPSC-CMs derived from donors with the condition or via modification of a single gene in an established hiPSC line [12, 17].

Models of more complex diseases and related changes in cardiotoxicity risk have already begun to be developed. A spheroid model of myocardial infarction that captured organotypic oxygen gradients *in vitro* has been shown to have increased sensitivity to doxorubicin toxicity compared to control spheroids [125]. hiPSC-CMs derived from breast cancer patients that experienced doxorubicin-induced toxicity have also been demonstrated to possess increased susceptibility to doxorubicin compared to hiPSC-CMs from patients that had not experienced doxorubicin-induced toxicity [83]. This work illustrates the potential of NAMs to recapitulate complex risk factors of cardiotoxicity *in vitro*. Studies such as these suggest a role of NAMs in examining patient populations that would otherwise remain unstudied in current animal models or *in vitro* assays. Expansion of such analyses will be critical in addressing the risk of hidden environmental cardiotoxicity.

5.5.2. Fit-for-purpose NAMs incorporate real-world exposure conditions as toxicological stimuli

Incorporation of exposure conditions that more adequately represent toxicological stimuli relevant for environmental cardiotoxicity is a critical goal for fit-for-purpose NAMs (**Figure 5.2**). Real-world environmental hazards involve multiple, long-term exposures, and the acute conditions commonly used in *in vitro* toxicity testing do not recapitulate these scenarios [39]. NAMs that integrate these factors will be better positioned to assess the risk of cardiotoxicity in actual populations, although challenges persist. NAMs utilizing lower exposures on the scale of weeks will need to remain viable while preserving the ability to detect subtle changes in cardiac function that reflect PoTs characteristic of environmental cardiotoxicity. Progress has already

been made in developing NAMs that meet these goals. Application of low doses of doxorubicin to *in vitro* models over two weeks has been shown to activate alternate PoTs compared to high doses that elicit acute toxicity [91], and another recent example detected acute BPA-induced arrhythmogenesis in cardiac microtissues at the physiologically relevant dose of 1 nM via high-speed optical mapping [71].

Cardiotoxicity risk assessment is further complicated by exposures to complex mixtures with potentially complementary cardiotoxicity as well as substances with unknown or variable composition, complex reaction products, and biological materials (UVCBs) [39]. The chemical composition of exposures arising from aqueous (*e.g.,* pesticide run-off or water disinfection by-products) or airborne (*e.g.,* petroleum exhaust or volatile organic chemicals) sources vary both in time and space, and individual risk of these exposures are expected to vary significantly [39, 126]. In contrast, typical co-exposure toxicity assessments make simplifying assumptions regarding mixtures by treating them as single toxicants with identical PoTs (*i.e.,* dose addition) or independent PoTs (*i.e.,* response addition) [127]. Mixtures and UVCBs, however, may invoke more complicated dynamics that may be impractical to reconstruct from information regarding individual exposures. Recent work applying NAMs to examine both individual environmental chemicals and complex mixtures directly suggests that these assumptions do not fully reflect risk [128]. Fortunately, NAMs provide a feasible approach for examining these interactions. Two-dimensional models employing hiPSC-CMs have shown concentration-dependent effects to gas oil extracts [67], simple drug mixtures [63], and the constituents of energy drinks [129]. Cardiotoxic analysis of ground soil samples has further demonstrated the ability of NAMs to correlate *in vitro* risk assessment with the spatial distribution of contaminants to identify areas of concern after site contamination [130].

While these examples are promising, extrapolation of *in vitro* data of complex mixtures and UCVBs to equivalent whole-body exposures remains an outstanding challenge. A tiered IVIVE framework would allow integration of available data on absorption, distribution, metabolism, and elimination of mixture components [131]. Where gaps in data exist, computational approaches (e.g., quantitative structure-activity relationship models) can be used to inform dosimetry models. As advances in sensitivity, throughput, and IVIVE are made, NAMs are expected to enable a more complete understanding of the environmental cardiotoxicity of complex chemical environments and long-term exposures.

5.5.3. Fit-for-purpose NAMs provide actionable system readouts

In vitro observations and *in vivo* cardiotoxicity are best connected by an evaluation platform with an easily interpretable and clinically relevant readout, the final link in the chain of translatability (**Figure 5.2**). The current standards are *in vivo* QT measurement via electrocardiogram, employed for its non-invasive collection and direct clinical applicability, and the *in vitro* hERG assay, leveraged for its simplicity and throughput, with each possessing well-established methodologies and standardized result interpretation [9]. Despite these advantages, however, both possess a disconnect between experimental readout and clinical outcomes [9, 50]. QT prolongation by itself is an imperfect surrogate for human arrhythmogenic risk due to multi-ion channel interactions that can compensate for extended repolarization times. For example, the drug ranolazine causes QT prolongation but is not proarrhythmic due to simultaneous blockade of late inward sodium currents [9, 132]. The hERG assay similarly exemplifies such a mismatch because the single-channel test fails to account for these same compensatory effects on other ion currents [9, 50]. Verapamil, a known hERG inhibitor, does not elicit QT prolongation or arrhythmogenic risk due to concurrent blockade of inward calcium currents [9, 133]. In addition,

most current methods are limited to electrophysiological readouts and do not address contractile or structural changes.

The need for broader endpoints *in vitro* that can be linked to *in vivo* manifestations of toxicity is already being addressed by NAMs that detect major classes of cardiotoxicity via simple, high-throughput readouts [6, 17]. These include methods to measure structural (ATP activity, mitochondrial integrity, cell morphology), electrophysiological (micro-electrode arrays, voltage-sensitive dyes, calcium-sensitive dyes), and contractile (displacement tracking, post deflection) cardiotoxicity that can be effectively linked to clinical effects such as cardiomyocyte viability, arrythmia generation, and reduced ejection fraction, respectively. The increased biological complexity of NAMs has also increased interest in higher content "omics-level" data [99, 126, 127]. While more difficult to interpret, omics-level data can provide holistic and detailed information regarding interacting PoTs of environmental toxicants and suggest omics-level signatures of cardiotoxicity liabilities [44]. For instance, transcriptomic analysis of hiPSC-CMs exposed to doxorubicin and other anthracyclines, chemotherapeutics with well-known cardiotoxic side effects, have suggested a common set of deregulated genes that appears prior to the onset of other cytotoxicity markers for anthracycline-induced cardiotoxicity [134]. Ultimately, the type, number, and complexity of NAM readouts will be dictated by their intended context of use.

In conjunction with the clinical relevance of a readout is the need to consider how NAMs are to be validated and adopted by the wider research and regulatory communities [36, 135]. This is especially important as NAMs have not replaced older methods and are instead utilized in parallel [39]. Moreover, validation of *in vitro* NAMs has necessarily included comparison to *in vivo* pre-clinical animal data, which do not necessarily predict known human cardiotoxicity [11, 136, 137]. Thus, regulators are shifting towards a model of integrated NAM validation that relies on empirical

evidence to demonstrate human cardiac physiology and toxicity based on intended context of use and mechanistic relevance [36, 136, 137]. It is this validation of predictive capacity in humans that will complete the biological chain of translatability for environmental cardiotoxicity testing.

5.6. Conclusion

A more complete understanding of how environmental toxicants influence human cardiovascular health and function will be essential to evaluating real-world risk. Substantial progress has been made in the past decade in developing NAMs for cardiotoxicity, but most efforts have focused on evaluating pharmaceutical, not environmental, compounds. Such advances lay a considerable foundation from which to build, with advances in hiPSC-CM-based approaches providing necessary physiological relevance for accurately capturing impacts on human cardiovascular health. To fully capitalize on this momentum and develop NAMs fit for assessing the cardiotoxicity of environmental compounds, a more deliberate consideration of their diverse chemical properties and distinct exposure conditions will be needed. Ultimately, the regulatory (*i.e.,* prioritization, hazard screening, risk assessment) and biological (*i.e.,* relevant physiology, realistic exposures, interpretable readouts) contexts of NAMs for environmental cardiotoxicity should align with their intended purpose. A robust suite of NAMs for cardiotoxicity will provide the tools necessary to realize the National Research Council's vision for 21st Century toxicity testing for environmental cardiotoxicity.

5.7. Acknowledgements

We thankfully acknowledge Dr. Mel Andersen for his insightful and thorough comments regarding the content of this manuscript as well as funding from the National Institutes of Health National Institute of Environmental Health Sciences (U01 ES028184 to Ulrike Mende, Bum-Rak Choi, Patrick McMullen, and Kareen Coulombe) and a Brown University Biomedical Innovation to Impact Award (to Ulrike Mende, Bum-Rak Choi, and Kareen Coulombe)

5.8. References

1. Prüss-Ustün, A. and C.F. Corvalán, *Preventing disease through healthy environments: towards an estimate of the environmental burden of disease*. 2006: World Health Organization.
2. Virani, S.S., et al., *Heart disease and stroke statistics—2020 update: a report from the American Heart Association.* Circulation, 2020. **141**(9): p. E139-E596.
3. Lind, L., et al., *Key characteristics of cardiovascular toxicants.* Environmental health perspectives, 2021. **129**(9): p. 095001.
4. Cosselman, K.E., A. Navas-Acien, and J.D. Kaufman, *Environmental factors in cardiovascular disease.* Nature Reviews Cardiology, 2015. **12**(11): p. 627-642.
5. Judson, R., et al., *The toxicity data landscape for environmental chemicals.* Environmental health perspectives, 2009. **117**(5): p. 685-695.
6. Magdy, T., et al., *Human induced pluripotent stem cell (hiPSC)-derived cells to assess drug cardiotoxicity: opportunities and problems.* Annual review of pharmacology and toxicology, 2018. **58**: p. 83-103.
7. ICH, *The non-clinical evaluation of the potential for delayed ventricular repolarization (Qt Interval Prolongation) by human pharmaceuticals*. 2005.
8. ICH, *Safety pharmacology studies for human pharmaceuticals S7A*. 2001. p. 36791-36792.
9. Gintant, G., P.T. Sager, and N. Stockbridge, *Evolution of strategies to improve preclinical cardiac safety testing.* Nature Reviews Drug Discovery, 2016. **15**(7): p. 457.
10. Fischer, I., C. Milton, and H. Wallace, *Toxicity testing is evolving!* Toxicology Research, 2020. **9**(2): p. 67-80.
11. Olson, H., et al., *Concordance of the toxicity of pharmaceuticals in humans and in animals.* Regulatory Toxicology and Pharmacology, 2000. **32**(1): p. 56-67.

12. Mercola, M., A. Colas, and E. Willems, *Induced pluripotent stem cells in cardiovascular drug discovery.* Circulation research, 2013. **112**(3): p. 534-548.

13. Nerbonne, J.M., et al., *Genetic manipulation of cardiac K+ channel function in mice: what have we learned, and where do we go from here?* Circulation research, 2001. **89**(11): p. 944-956.

14. Sallam, K., et al., *Finding the rhythm of sudden cardiac death: new opportunities using induced pluripotent stem cell–derived cardiomyocytes.* Circulation research, 2015. **116**(12): p. 1989-2004.

15. O'Hara, T. and Y. Rudy, *Quantitative comparison of cardiac ventricular myocyte electrophysiology and response to drugs in human and nonhuman species.* American Journal of Physiology-Heart and Circulatory Physiology, 2012. **302**(5): p. H1023-H1030.

16. Törnqvist, E., et al., *Strategic focus on 3R principles reveals major reductions in the use of animals in pharmaceutical toxicity testing.* PloS one, 2014. **9**(7): p. e101638.

17. Chen, I.Y., E. Matsa, and J.C. Wu, *Induced pluripotent stem cells: at the heart of cardiovascular precision medicine.* Nature Reviews Cardiology, 2016. **13**(6): p. 333.

18. Priest, B., I.M. Bell, and M. Garcia, *Role of hERG potassium channel assays in drug development.* Channels, 2008. **2**(2): p. 87-93.

19. Gintant, G., *An evaluation of hERG current assay performance: translating preclinical safety studies to clinical QT prolongation.* Pharmacology & therapeutics, 2011. **129**(2): p. 109-119.

20. Horvath, P., et al., *Screening out irrelevant cell-based models of disease.* Nature Reviews Drug Discovery, 2016. **15**(11): p. 751-769.

21. Gintant, G., et al., *Use of Human Induced Pluripotent Stem Cell–Derived Cardiomyocytes in Preclinical Cancer Drug Cardiotoxicity Testing: A Scientific Statement From the American Heart Association.* Circulation research, 2019. **125**(10): p. e75-e92.

22. Bowes, J., et al., *Reducing safety-related drug attrition: the use of in vitro pharmacological profiling.* Nature reviews Drug discovery, 2012. **11**(12): p. 909-922.

23. Guth, B.D., *Preclinical cardiovascular risk assessment in modern drug development.* Toxicological Sciences, 2007. **97**(1): p. 4-20.

24. Sarazan, R.D., et al., *Cardiovascular function in nonclinical drug safety assessment: Current issues and opportunities.* International Journal of Toxicology, 2011. **30**(3): p. 272-286.

25. Sevim, Ç., E. Doğan, and S. Comakli, *Cardiovascular disease and toxic metals.* Current Opinion in Toxicology, 2020. **19**: p. 88-92.

26. Balali-Mood, M., et al., *Toxic mechanisms of five heavy metals: Mercury, Lead, Chromium, Cadmium, and Arsenic.* Frontiers in pharmacology, 2021. **12**.

27. Alissa, E.M. and G.A. Ferns, *Heavy Metal Poisoning and Cardiovascular Disease.* Journal of Toxicology, 2011. **2011**: p. 870125.

28. Alhamdow, A., et al., *Early markers of cardiovascular disease are associated with occupational exposure to polycyclic aromatic hydrocarbons.* Scientific reports, 2017. **7**(1): p. 1-11.

29. Marris, C., et al., *Polyaromatic hydrocarbons in pollution: a heart-breaking matter.* The Journal of physiology, 2020. **598**(2): p. 227-247.

30. Lind, Y.S., et al., *Circulating levels of persistent organic pollutants (POPs) are associated with left ventricular systolic and diastolic dysfunction in the elderly.* Environmental research, 2013. **123**: p. 39-45.

31. Åkesson, A., et al., *Dietary exposure to polychlorinated biphenyls and risk of heart failure–a population-based prospective cohort study.* Environment international, 2019. **126**: p. 1-6.

32. Incardona, J.P., *Molecular mechanisms of crude oil developmental toxicity in fish.* Archives of environmental contamination and toxicology, 2017. **73**(1): p. 19-32.

33. Cai, S., et al., *Relationship between urinary bisphenol a levels and cardiovascular diseases in the US adult population, 2003–2014.* Ecotoxicology and Environmental Safety, 2020. **192**: p. 110300.

34. Gao, X. and H.-S. Wang, *Impact of bisphenol A on the cardiovascular system—Epidemiological and experimental evidence and molecular mechanisms.* International journal of environmental research and public health, 2014. **11**(8): p. 8399-8413.

35. Georgiadis, N., et al., *Pesticides and cardiotoxicity. Where do we stand?* Toxicology and applied pharmacology, 2018. **353**: p. 1-14.

36. Parish, S.T., et al., *An evaluation framework for new approach methodologies (NAMs) for human health safety assessment.* Regulatory Toxicology and Pharmacology, 2020. **112**: p. 104592.

37. Zink, D., J.K.C. Chuah, and J.Y. Ying, *Assessing Toxicity with Human Cell-Based In Vitro Methods.* Trends in Molecular Medicine, 2020. **26**(6): p. 570-582.

38. National Research Council, *Toxicity testing in the 21st century: a vision and a strategy*. 2007: The National Academies Press.

39. Krewski, D., et al., *Toxicity testing in the 21st century: a vision and a strategy.* Journal of Toxicology and Environmental Health, Part B, 2010. **13**(2-4): p. 51-138.

40. Daneshian, M., et al., *Highlight report: Launch of a large integrated European in vitro toxicology project: EU-ToxRisk*. 2016, Springer.

41. Kleensang, A., et al., *t4 workshop report: pathways of toxicity.* Altex, 2014. **31**(1): p. 53.

42. Ankley, G.T., et al., *Adverse outcome pathways: a conceptual framework to support ecotoxicology research and risk assessment.* Environmental Toxicology and Chemistry: An International Journal, 2010. **29**(3): p. 730-741.

43. Meek, M., et al., *New developments in the evolution and application of the WHO/IPCS framework on mode of action/species concordance analysis.* Journal of Applied Toxicology, 2014. **34**(1): p. 1-18.

44. Burnett, S.D., et al., *Human induced pluripotent stem cell (iPSC)-derived cardiomyocytes as an in vitro model in toxicology: strengths and weaknesses for hazard identification and risk characterization.* Expert Opinion on Drug Metabolism & Toxicology, 2021: p. 1-16.

45. Dix, D.J., et al., *The ToxCast program for prioritizing toxicity testing of environmental chemicals.* Toxicological sciences, 2007. **95**(1): p. 5-12.

46. Truskey, G.A., *Human microphysiological systems and organoids as in vitro models for toxicological studies.* Frontiers in public health, 2018. **6**: p. 185.

47. Hann, M.M. and T.I. Oprea, *Pursuing the leadlikeness concept in pharmaceutical research.* Current Opinion in Chemical Biology, 2004. **8**(3): p. 255-263.

48. Lipinski, C.A., et al., *Experimental and computational approaches to estimate solubility and permeability in drug discovery and development settings.* Advanced drug delivery reviews, 1997. **23**(1-3): p. 3-25.

49. Yang, F. and I.Y. Massey, *Exposure routes and health effects of heavy metals on children.* Biometals, 2019. **32**(4): p. 563-573.

50. Frommeyer, G. and L. Eckardt, *Drug-induced proarrhythmia: risk factors and electrophysiological mechanisms.* Nature Reviews Cardiology, 2016. **13**(1): p. 36-47.

51. Ferdinandy, P., et al., *Definition of hidden drug cardiotoxicity: paradigm change in cardiac safety testing and its clinical implications.* European heart journal, 2019. **40**(22): p. 1771-1777.

52. Hartung, T., et al., *Food for thought… integrated testing strategies for safety assessments.* Altex, 2013. **30**(1): p. 3.

53. Sauve-Ciencewicki, A., et al., *A simple problem formulation framework to create the right solution to the right problem.* Regulatory Toxicology and Pharmacology, 2019. **101**: p. 187-193.

54. Sirenko, O., et al., *In vitro cardiotoxicity assessment of environmental chemicals using an organotypic human induced pluripotent stem cell-derived model.* Toxicology and applied pharmacology, 2017. **322**: p. 60-74.

55. Sirenko, O., et al., *Assessment of beating parameters in human induced pluripotent stem cells enables quantitative in vitro screening for cardiotoxicity.* Toxicology and applied pharmacology, 2013. **273**(3): p. 500-507.

56. Sharma, A., et al., *High-throughput screening of tyrosine kinase inhibitor cardiotoxicity with human induced pluripotent stem cells.* Science translational medicine, 2017. **9**(377).

57. Krishna, S., B. Berridge, and N. Kleinstreuer, *High-throughput screening to identify chemical cardiotoxic potential.* Chemical Research in Toxicology, 2020. **34**(2): p. 566-583.

58. Grimm, F.A., et al., *Cardiovascular effects of polychlorinated biphenyls and their major metabolites.* Environmental health perspectives, 2020. **128**(7): p. 077008.

59. Krishna, S., et al., *High-throughput chemical screening and structure-based models to predict hERG inhibition.* Biology, 2022. **11**(2): p. 209.

60. Archer, C.R., et al., *Characterization and validation of a human 3D cardiac microtissue for the assessment of changes in cardiac pathology.* Scientific reports, 2018. **8**(1): p. 1-15.

61. Polonchuk, L., et al., *Cardiac spheroids as promising in vitro models to study the human heart microenvironment.* Scientific reports, 2017. **7**(1): p. 1-12.

62. Ando, H., et al., *A new paradigm for drug-induced torsadogenic risk assessment using human iPS cell-derived cardiomyocytes.* Journal of Pharmacological and Toxicological Methods, 2017. **84**: p. 111-127.

63. Blinova, K., et al., *Comprehensive translational assessment of human-induced pluripotent stem cell derived cardiomyocytes for evaluating drug-induced arrhythmias.* Toxicological Sciences, 2017. **155**(1): p. 234-247.

64. Blinova, K., et al., *International multisite study of human-induced pluripotent stem cell-derived cardiomyocytes for drug proarrhythmic potential assessment.* Cell reports, 2018. **24**(13): p. 3582-3592.

65. da Rocha, A.M., et al., *Detection of Drug-Induced Torsades de Pointes Arrhythmia Mechanisms Using hiPSC-CM Syncytial Monolayers in a High-Throughput Screening Voltage Sensitive Dye Assay.* Toxicological Sciences, 2020. **173**(2): p. 402-415.

66. Grimm, F.A., et al., *A human population-based organotypic in vitro model for cardiotoxicity screening.* ALTEX, 2018. **35**(4): p. 441.

67. Grimm, F.A., et al., *High-content assay multiplexing for toxicity screening in induced pluripotent stem cell-derived cardiomyocytes and hepatocytes.* Assay and drug development technologies, 2015. **13**(9): p. 529-546.

68. Guo, L., et al., *Refining the human iPSC-cardiomyocyte arrhythmic risk assessment model.* toxicological sciences, 2013. **136**(2): p. 581-594.

69. Ravenscroft, S.M., et al., *Cardiac non-myocyte cells show enhanced pharmacological function suggestive of contractile maturity in stem cell derived cardiomyocyte microtissues.* Toxicological Sciences, 2016. **152**(1): p. 99-112.

70. Pfeiffer-Kaushik, E.R., et al., *Electrophysiological characterization of drug response in hSC-derived cardiomyocytes using voltage-sensitive optical platforms.* Journal of pharmacological and toxicological methods, 2019. **99**: p. 106612.

71. Kofron, C., et al., *A Predictive in Vitro Risk Assessment Platform for Pro-Arrhythmic Toxicity Using Human 3D Cardiac Microtissues.* Scientific Reports, 2021. **11**: p. 1-16.

72. Agarwal, A., et al., *Microfluidic heart on a chip for higher throughput pharmacological studies.* Lab on a Chip, 2013. **13**(18): p. 3599-3608.

73. Feric, N.T., et al., *Engineered cardiac tissues generated in the Biowire II: a platform for human-based drug discovery.* Toxicological Sciences, 2019. **172**(1): p. 89-97.

74. Huebsch, N., et al., *Miniaturized iPS-cell-derived cardiac muscles for physiologically relevant drug response analyses.* Scientific reports, 2016. **6**: p. 24726.

75. Mathur, A., et al., *Human iPSC-based cardiac microphysiological system for drug screening applications.* Scientific reports, 2015. **5**: p. 8883.

76. Pointon, A., et al., *From the cover: high-throughput imaging of cardiac microtissues for the assessment of cardiac contraction during drug discovery.* Toxicological Sciences, 2017. **155**(2): p. 444-457.

77. Skardal, A., et al., *Multi-tissue interactions in an integrated three-tissue organ-on-a-chip platform.* Scientific reports, 2017. **7**(1): p. 1-16.

78. Nunes, S.S., et al., *Biowire: a platform for maturation of human pluripotent stem cell–derived cardiomyocytes.* Nature methods, 2013. **10**(8): p. 781-787.

79. Lee, E.K., et al., *Machine learning plus optical flow: a simple and sensitive method to detect cardioactive drugs.* Scientific reports, 2015. **5**(1): p. 1-12.

80. Clements, M. and N. Thomas, *High-throughput multi-parameter profiling of electrophysiological drug effects in human embryonic stem cell derived cardiomyocytes using multi-electrode arrays.* Toxicological Sciences, 2014. **140**(2): p. 445-461.

81. Beauchamp, P., et al., *Development and characterization of a scaffold-free 3D spheroid model of induced pluripotent stem cell-derived human cardiomyocytes.* Tissue Engineering Part C: Methods, 2015. **21**(8): p. 852-861.

82. Beauchamp, P., et al., *3D co-culture of hiPSC-derived cardiomyocytes with cardiac fibroblasts improves tissue-like features of cardiac spheroids.* Frontiers in molecular biosciences, 2020. **7**: p. 14.

83. Burridge, P.W., et al., *Human induced pluripotent stem cell–derived cardiomyocytes recapitulate the predilection of breast cancer patients to doxorubicin-induced cardiotoxicity.* Nature medicine, 2016. **22**(5): p. 547.

84. Clements, M., et al., *Bridging functional and structural cardiotoxicity assays using human embryonic stem cell-derived cardiomyocytes for a more comprehensive risk assessment.* Toxicological Sciences, 2015. **148**(1): p. 241-260.

85. Forsythe, S.D., et al., *Environmental toxin screening using human-derived 3D bioengineered liver and cardiac organoids.* Frontiers in public health, 2018. **6**: p. 103.

86. Schaaf, S., et al., *Human engineered heart tissue as a versatile tool in basic research and preclinical toxicology.* PloS one, 2011. **6**(10): p. e26397.

87. Chaudhari, U., et al., *Functional cardiotoxicity assessment of cosmetic compounds using human-induced pluripotent stem cell-derived cardiomyocytes.* Archives of toxicology, 2018. **92**(1): p. 371-381.

88. Wetmore, B.A., *Quantitative in vitro-to-in vivo extrapolation in a high-throughput environment.* Toxicology, 2015. **332**: p. 94-101.

89. Bell, S.M., et al., *In vitro to in vivo extrapolation for high throughput prioritization and decision making.* Toxicology In Vitro, 2018. **47**: p. 213-227.

90. Rampoldi, A., et al., *Cardiac toxicity from ethanol exposure in human-induced pluripotent stem cell-derived cardiomyocytes.* Toxicological Sciences, 2019. **169**(1): p. 280-292.

91. Verheijen, M., et al., *Bringing in vitro analysis closer to in vivo: Studying doxorubicin toxicity and associated mechanisms in 3D human microtissues with PBPK-based dose modelling.* Toxicology letters, 2018. **294**: p. 184-192.

92. Wetmore, B.A., et al., *Relative impact of incorporating pharmacokinetics on predicting in vivo hazard and mode of action from high-throughput in vitro toxicity assays.* toxicological sciences, 2013. **132**(2): p. 327-346.

93. Skardal, A., et al., *Drug compound screening in single and integrated multi-organoid body-on-a-chip systems.* Biofabrication, 2020. **12**(2): p. 025017.

94. Lee-Montiel, F.T., et al., *Integrated hiPSC-based liver and heart microphysiological systems predict unsafe drug-drug interaction.* bioRxiv, 2020.

95. Blanchette, A.D., et al., *A bayesian method for population-wide cardiotoxicity hazard and risk characterization using an in vitro human model.* Toxicological Sciences, 2020. **178**(2): p. 391-403.

96. Burnett, S.D., et al., *Cardiotoxicity Hazard and Risk Characterization of ToxCast Chemicals Using Human Induced Pluripotent Stem Cell-Derived Cardiomyocytes from Multiple Donors.* Chemical Research in Toxicology, 2021. **34**(9): p. 2110-2124.

97. Chiu, W.A. and I. Rusyn, *Advancing chemical risk assessment decision-making with population variability data: challenges and opportunities.* Mammalian genome, 2018. **29**(1): p. 182-189.

98. Blanchette, A.D., et al., *A tiered approach to population-based in vitro testing for cardiotoxicity: Balancing estimates of potency and variability.* Journal of Pharmacological and Toxicological Methods, 2022: p. 107154.

99. Moffat, J.G., et al., *Opportunities and challenges in phenotypic drug discovery: an industry perspective.* Nature reviews Drug discovery, 2017. **16**(8): p. 531-543.

100. Vincent, F., et al., *Developing predictive assays: the phenotypic screening "rule of 3".* Science translational medicine, 2015. **7**(293): p. 293ps15-293ps15.

101. Swinney, D., *Phenotypic vs. target-based drug discovery for first-in-class medicines.* Clinical Pharmacology & Therapeutics, 2013. **93**(4): p. 299-301.

102. Swinney, D.C. and J. Anthony, *How were new medicines discovered?* Nature reviews Drug discovery, 2011. **10**(7): p. 507-519.

103. Takasuna, K., et al., *Comprehensive in vitro cardiac safety assessment using human stem cell technology: overview of CSAHi HEART initiative.* Journal of pharmacological and toxicological methods, 2017. **83**: p. 42-54.

104. Berg, E.L., Y.-C. Hsu, and J.A. Lee, *Consideration of the cellular microenvironment: physiologically relevant co-culture systems in drug discovery.* Advanced drug delivery reviews, 2014. **69**: p. 190-204.

105. Baker, B.M. and C.S. Chen, *Deconstructing the third dimension–how 3D culture microenvironments alter cellular cues.* Journal of cell science, 2012. **125**(13): p. 3015-3024.

106. Ahmed, R.E., et al., *A Brief Review of Current Maturation Methods for Human Induced Pluripotent Stem Cells-Derived Cardiomyocytes.* Frontiers in Cell and Developmental Biology, 2020. **8**(178): p. 178.

107. Akins Jr, R.E., et al., *Three-dimensional culture alters primary cardiac cell phenotype.* Tissue Engineering Part A, 2010. **16**(2): p. 629-641.

108. Ulmer, B.M., et al., *Contractile Work Contributes to Maturation of Energy Metabolism in hiPSC-Derived Cardiomyocytes.* Stem Cell Reports, 2018. **10**(3): p. 834-847.

109. Zuppinger, C., *3D cardiac cell culture: a critical review of current technologies and applications.* Frontiers in cardiovascular medicine, 2019. **6**: p. 87.

110. Meyer, T., M. Tiburcy, and W.-H. Zimmermann, *Cardiac macrotissues-on-a-plate models for phenotypic drug screens.* Advanced Drug Delivery Reviews, 2019. **140**: p. 93-100.

111. Bajaj, P., et al., *3D biofabrication strategies for tissue engineering and regenerative medicine.* Annual review of biomedical engineering, 2014. **16**: p. 247-276.

112. Mironov, V., et al., *Biofabrication: a 21st century manufacturing paradigm.* Biofabrication, 2009. **1**(2): p. 022001.

113. Ong, C.S., et al., *Biomaterial-free three-dimensional bioprinting of cardiac tissue using human induced pluripotent stem cell derived cardiomyocytes.* Scientific reports, 2017. **7**(1): p. 1-11.

114. Protze, S.I., J.H. Lee, and G.M. Keller, *Human pluripotent stem cell-derived cardiovascular cells: from developmental biology to therapeutic applications.* Cell Stem Cell, 2019. **25**(3): p. 311-327.

115. Mikryukov, A.A., et al., *BMP10 signaling promotes the development of endocardial cells from human pluripotent stem cell-derived cardiovascular progenitors.* Cell Stem Cell, 2021. **28**(1): p. 96-111. e7.

116. Witty, A.D., et al., *Generation of the epicardial lineage from human pluripotent stem cells.* Nature biotechnology, 2014. **32**(10): p. 1026-1035.

117. Zhao, Y., et al., *Towards chamber specific heart-on-a-chip for drug testing applications.* Advanced Drug Delivery Reviews, 2020. **165-166**: p. 60-76.

118. Scuderi, G.J. and J. Butcher, *Naturally engineered maturation of cardiomyocytes.* Frontiers in cell and developmental biology, 2017. **5**: p. 50.

119. Gomez-Garcia, M.J., et al., *Maturation of human pluripotent stem cell derived cardiomyocytes in vitro and in vivo.* Seminars in Cell & Developmental Biology, 2021.

120. Schmid, C., et al., *Ion Channel Expression and Electrophysiology of Singular Human (Primary and Induced Pluripotent Stem Cell-Derived) Cardiomyocytes.* Cells, 2021. **10**(12): p. 3370.

121. Garbern, J.C. and R.T. Lee, *Mitochondria and metabolic transitions in cardiomyocytes: lessons from development for stem cell-derived cardiomyocytes.* Stem Cell Research & Therapy, 2021. **12**(1): p. 1-25.

122. Feyen, D.A., et al., *Metabolic maturation media improve physiological function of human iPSC-derived cardiomyocytes.* Cell reports, 2020. **32**(3): p. 107925.

123. Blanchette, A.D., et al., *Thorough QT/QTc in a dish: an in vitro human model that accurately predicts clinical concentration-QTc relationships.* Clinical Pharmacology & Therapeutics, 2019. **105**(5): p. 1175-1186.

124. Burnett, S.D., et al., *Population-based toxicity screening in human induced pluripotent stem cell-derived cardiomyocytes.* Toxicology and applied pharmacology, 2019. **381**: p. 114711.

125. Richards, D.J., et al., *Human cardiac organoids for the modelling of myocardial infarction and drug cardiotoxicity.* Nature Biomedical Engineering, 2020. **4**(4): p. 446-462.

126. Pauluhn, J., *Overview of inhalation exposure techniques: strengths and weaknesses.* Experimental and Toxicologic Pathology, 2005. **57**: p. 111-128.

127. Teuschler, L., et al., *Support of science-based decisions concerning the evaluation of the toxicology of mixtures: a new beginning.* Regulatory Toxicology and Pharmacology, 2002. **36**: p. 34-39.

128. Hsieh, N.-H., et al., *Risk characterization and probabilistic concentration–response modeling of complex environmental mixtures using new approach methodologies (NAMs) data from organotypic in vitro human stem cell assays.* Environmental Health Perspectives, 2021. **129**(1): p. 017004.

129. Luo, Y.-S., et al., *Relationships between constituents of energy drinks and beating parameters in human induced pluripotent stem cell (iPSC)-Derived cardiomyocytes.* Food and Chemical Toxicology, 2021. **149**: p. 111979.

130. Chen, Z., et al., *Risk Characterization of Environmental Samples Using In Vitro Bioactivity and Polycyclic Aromatic Hydrocarbon Concentrations Data.* Toxicological Sciences, 2021. **179**(1): p. 108-120.

131. Wambaugh, J.F., et al., *Toxicokinetic triage for environmental chemicals.* Toxicological Sciences, 2015. **147**(1): p. 55-67.

132. Wu, L., et al., *Reduction of repolarization reserve unmasks the proarrhythmic role of endogenous late Na+ current in the heart.* American Journal of Physiology-Heart and Circulatory Physiology, 2009. **297**(3): p. H1048-H1057.

133. Zhang, S., et al., *Mechanism of block and identification of the verapamil binding domain to HERG potassium channels.* Circulation Research, 1999. **84**(9): p. 989-998.

134. Chaudhari, U., et al., *MicroRNAs as early toxicity signatures of doxorubicin in human-induced pluripotent stem cell-derived cardiomyocytes.* Archives of toxicology, 2016. **90**(12): p. 3087-3098.

135. Marx, U., et al., *Biology-inspired microphysiological systems to advance patient benefit and animal welfare in drug development.* Alternatives to Animal Experimentation: ALTEX, 2020. **37**(3): p. 365-394.

136. ICCVAM, *A Strategic Roadmap for Establishing New Approaches to Evaluate the Safety of Chemicals and Medical Products in the United States*. 2018, National Toxicology Program, National Institute of Environmental Health ….

137. Ingber, D.E., *Is it Time for Reviewer 3 to Request Human Organ Chip Experiments Instead of Animal Validation Studies?* Advanced Science, 2020. **7**(22): p. 2002030.

Chapter 6 - A novel non-*PRKAG2* hiPSC-CM model recapitulates clinical features Wolff-Parkinson-White Syndrome *in vitro*

6.1. Abstract

Wolff-Parkinson-White Syndrome (WPW) is a form of atrial arrhythmia defined by the presence of accessory atrioventricular pathways, excess glycogen accumulation, and cardiac hypertrophy. Although only accounting for approximately 2% of WPW, researchers have traditionally relied on transgenic mice possessing point mutations in the gene encoding the γ_2-subunit (*PRKAG2*) of adenosine monophosphate-activated protein kinase (AMPK). More recently, others have also begun using human induced pluripotent stem cell-derived cardiomyocytes (hiPSC-CMs) to model monogenic forms of WPW *in vitro*. In addition to acting as a human-specific model as in those studies, they also provide a promising approach with which to leverage patient-derived cell lines to study as-of-yet unknown genetic backgrounds associated with WPW. Here, we developed one such novel, non-*PRKAG2* hiPSC line from a patient presenting with atrial fibrillation and familial WPW. We verified the ability to differentiate into ventricular and atrial hiPSC-CMs and confirmed that WPW hiPSC-CMs were larger and contained more glycogen than controls cells. We additionally examined the electrophysiological phenotype of atrial engineered microtissues generated using these cells. We found that WPW atrial microtissues beat faster and could follow higher frequency pacing in addition to possessing shorter calcium transients and longer action potential durations compared to control (WTC) atrial microtissues. Together, these results suggest we successfully recapitulated key phenotypic features of clinical WPW in hiPSC-CMs with a novel genetic disease background and for the first time in atrial hiPSC-CMs. This and similar models will be an invaluable tool in dissecting disease mechanisms and developing novel therapies for WPW.

6.2. Introduction

Atrial arrhythmias, irregular beating in the upper chambers of the heart, are the most common rhythm abnormality among adults and are associated with significantly increased mortality from stroke

and myocardial infarction [1-3]. Wolff-Parkinson-White Syndrome (WPW) is one such atrial arrhythmia, affecting approximately 0.1% to 0.3% (1-3 of 1,000) of people [4, 5]. WPW is defined clinically by the presence of an accessory atrioventricular conduction pathway that causes pre-excitation of the ventricles by bypassing the normal conduction delay that occurs through the atrioventricular node [6, 7]. This secondary pathway also significantly increases susceptibility to reentrant arrhythmias and sudden cardiac death due to the loop formed by the presence of multiple pathways between the upper and lower heart. Atrial fibrillation is also common in WPW patients, with an occurrence rate between 11% and 39%, further increasing the risk of ventricular fibrillation and sudden cardiac death [8-10]. However, radioablation of accessory pathways, the current standard of care, is often inadequate to eliminate the risk of atrial fibrillation, with the recurrence rate of WPW remaining high post-treatment [11, 12].

The most recognized genetic risk factors for WPW are mutations in the *PRKAG2* gene, which encodes an isoform of one of two regulatory subunits of the adenosine monophosphate (AMP)-activated protein kinase (AMPK). AMPK is a trimeric protein that acts as a cellular fuel gauge, working to maintain energy homeostasis in most eukaryotic cells [13]. Canonically, this is due to the γ-subunit's ability to bind AMP and ATP, which modify the conformation of the AMPK's active site and the rate of dephosphorylation of the α-subunit. When activated, AMPK upregulates catabolic, ATP-generating processes via regulation of lipid, protein, and carbohydrate metabolism [13, 14]. *PRKAG2* mutations disproportionately affect the AMP-/ATP-binding residues of the γ_2-subunit, usually reducing AMP-dependent allosteric activation but increasing basal phosphorylation. These changes have been subsequently shown to cause varying severities of ventricular pre-excitation, glycogen accumulation, and hypertrophy in multiple mouse models, mimicking clinical WPW [14-25].

Rodent models of WPW have typically relied on over-expression of mutant forms of the γ-subunit, potentially disrupting the normal isoform ratios in AMPK complexes in the heart and the ability of these models to faithfully recapitulate the manifestation of WPW in humans [14]. Human induced pluripotent

stem cell-derived cardiomyocytes (hiPSC-CMs) have risen as an alternative approach with which to model cardiac disease using patient-derived cell lines [26-29]. Unsurprisingly, this approach has begun to be applied to study WPW as well. Multiple research groups have developed hiPSC lines from patients with WPW resulting from *PRKAG2* point mutations and have observed glycogen accumulation as well as electrophysiological changes in WPW cells [30-32]. Interestingly, genetic correction of the *PRKAG2* mutation using CRISPR eliminated the disease phenotype [31].

Studies such as these provide substantial support for the utility of leveraging patient-derived hiPSC-CM-based models for the study of WPW, but have been limited in their ability to accurately model WPW *in vitro* due to their reliance on ventricular, not atrial, hiPSC-CMs. Recent advances in hiPSC-CM differentiation have enabled the differentiation of chamber-specific cardiomyocytes for the study of atrial arrhythmias [33-35]. Currently, such atrial models have not been applied to the study of WPW using hiPSC-CMs. Moreover, the generated WPW cell lines possessed a small subset of previously described *PRKAG2* mutations (R302Q and N488I) [30-32]. However, only approximately 2% of patients with WPW have mutations in the *PRKAG2* gene [36, 37] and inheritance is often complex, sporadic, or otherwise without a clear genetic component [4, 5, 38]. Thus, there is significant opportunity to leverage the chamber- and patient-specificity of hiPSC lines as well as their ability to mirror disease phenotypes, even in the absence of known genetic mutations, to study non-canonical forms of WPW.

The objective of this work was to take advantage of these advances by developing a novel atrial hiPSC-CM model of non-*PRKAG2* WPW to study the mechanistic origins of atrial arrhythmias in non-*PRKAG2* WPW. We successfully generated a novel WPW hiPSC line by reprogramming primary cells from a donor with WPW, confirming the absence of mutations in the *PRKAG2* gene. We were able to differentiate both ventricular and atrial hiPSC-CMs and observed that WPW hiPSC-CMs were significantly larger with a higher glycogen content than control hiPSC-CMs, suggesting a pro-hypertrophic phenotype similar to that observed with known *PRKAG2* mutations. We further assessed electrophysiological phenotype in

engineered atrial cardiac microtissues and found that WPW microtissues beat faster, followed higher frequency pacing, and had longer action potentials and shorter calcium transients than control tissues. Together, these characteristics suggest that non-*PRKAG2* WPW hiPSC-CMs constitute a more proarrhythmic profile with a shorter effective refractory period and higher susceptibility to triggered arrhythmias. Overall, our data support the ability of patient-derived hiPSC-CMs to recapitulate WPW *in vitro* and enable electrophysiological assessment of the mechanistic underpinnings of atrial arrhythmias arising from WPW in the absence of a known disease-causing mutation.

6.3. Materials and methods

6.3.1. Primary uroepithelial cell isolation and culture

All human procedures were approved under IRB Protocol #2944 at Brown University and performed with informed consent following applicable regulations. Samples of 50-150 mL midstream urine were collected and placed on ice for up to 1.5 hours prior to cell isolation. Urine was transferred to 50 mL conical tubes and centrifuged at 2000 rpm for 10 minutes before aspirating the supernatant, leaving 0.5-1 mL behind to avoid disturbing the cell pellet. Next, any cell pellets were combined into a new 15 mL conical tube before being diluted with at least 10 mL of 1x penicillin-streptomycin-amphotericin B in phosphate-buffed saline (PBS). The combined cells were centrifuged a second time at 2000 rpm for 10 minutes, the supernatant aspirated, and the cells resuspended in 2mL of uroepithelial media consisting of 15% premium fetal bovine serum (Avantor #1500-050), 15 mM HEPES buffer (Sigma Aldrich #H0887), 1x MEM non-essential amino acids (Fisher #11-140-050), 1x Glutamax (Fisher 35-050-061), 1x penicillin-streptomycin-amphotericin B (Zen Bio #NC0452083), 5 µg/mL insulin (Fisher #12-585-014), 500 ng/mL epinephrine (MilliporeSigma #E4250), 4 pg/mL triiodo-L-thyronine (T3: MilliporeSigma #T6397), 10 ng/mL epithelial growth factor (Lonza #CC-4107), 5 µg/mL holo-transferrin (MilliporeSigma #T0665), and 36 ng/mL hydrocortisone (Lonza #CC-4112A) in DMEM/F-12 (Gibco #11320033) supplemented with 10 µM

ROCK-inhibitor (Y-27632: Tocris #1254). Finally, the resuspended cells were seeded into a single well of a 0.1% gelatin-coated 6-well plate and incubated at 37 °C overnight.

The next day, as well as every 2-3 days afterward, the media was changed to uroepithelial media without ROCK-inhibitor. After about 3 days, small colonies of uroepithelial cells would appear. Cells typically reached 70-80% confluence around two weeks when they could be resuspended by covering in 10x TrypLE (Life Technologies #A1217702) for 5 minutes at 37 °C. Resuspended cells were spun down and frozen in CyroSTOR CS-10 (Sigma Aldrich #C2874) at -80 °C overnight or resuspended in uroepithelial media for reseeding on 0.1% gelatin-coated 6-well plates at a density of 4,000-5,000 cells/cm^2. Once frozen, uroepithelial cells were stored in liquid nitrogen until reprogramming.

6.3.2. hiPSC reprogramming and characterization

Episomal reprograming of uroepithelial cells was performed by the Emory Stem Cell and Organoids Core using a three-plasmid, seven-factor (SOX2, OCT4, KLF4, MYC, NANOG, LIN28, and SV40L T antigen) Epstein Barr nuclear antigen-based episomal system that does not integrate into the genome. Successfully reprogrammed cells were cultured in Matrigel-coated 6-well plates and fed every other day with mTeSR Plus (StemCell Technologies #100-0276). Reprogrammed cells were first characterized by Karyotype-G banding to confirm the absence of chromosomal abnormalities from reprogramming. Pluripotentency was confirmed with immunofluorescent staining for the markers SSEA4 (Cell Signaling #4755S), Oct4 (Cell Signaling #2750S), TRA-1-81 (Sigma #MAB4381), Sox2 (R&D Systems #AF2018) as well as flow cytometry of SSEA4-APC (Miltenyi Biotec #130-126-000), Oct4-APC (Miltenyi Biotec #130-117-821), TRA-1-60-PE (Miltenyi Biotec #130-122-965), Sox2-FITC (Miltenyi Biotec #130-120-790) expression. Differentiation to all germ lines was also confirmed by flow cytometry for the ectoderm (nestin-FITC: Novus Biologicals #300-266F; Pax6-PE: Biolegend #901301), mesoderm (Brachyury-APC: R&D Systems #IC2085A; NCAM-FITC: Stem Cell Technologies #60021FITC), and ectoderm (SOX17-APC: R&D Systemcs #IC1924A; CXCR4-PE: Stem Cell Technologies #60089PE) lineages. Sanger sequencing of all 16 *PRKAG2* exons was performed

from flash-frozen hiPSC samples and compared to a reference sequence to inspect for mutations in γ_2-subunit of AMPK (Azenta Life Sciences).

6.3.3. hiPSC maintenance culture

Frozen reprogrammed hiPSCs were thawed by immersion in a 37 °C water bath for 1-2 minutes before adding dropwise to 5 mL of mTeSR Plus and centrifuging at 200 g for 4 minutes. The supernatant was aspirated and the cells resuspended in 10 mL of mTeSR Plus with 10 µM ROCK-inhibitor and seeded into a 10-cm tissue culture dish. Cells were fed the next day with unmodified mTeSR Plus and every other day thereafter. Once 70-80% confluent, hiPSCs were passaged by covering with 3 mL of ReLeSR (StemCell Technologies #100-0483) for 30 seconds before aspirating. After an additional 4 minutes, cells were resuspended in 5 mL of mTeSR Plus and centrifuged at 200 g for 4 minutes. The supernatant was aspirated before resuspension in mTeSR Plus with 5 µM ROCK-inhibitor and at a seeding ratio of 1:10 onto another Geltrex-coated 10-cm tissue culture dish.

Long-term, all hiPSC culture was converted to our standard hiPSC culture protocol in Essential 8 medium (Gibco #A1517001). Cells are fed Essential 8 medium daily until 70-80% confluent when they are passaged by covering with versene (0.5M EDTA: SigmaAldrich #E5134; 1.1 mM D-glucose: Gibco #15023-013) for 5 minutes prior to centrifugation at 200 g for 4 minutes. Cells are resuspended in Essential 8 medium with 5 µM ROCK-inhibitor at a ratio of 1:10 onto either Geltrex-coated or vitronectin (ThermoFisher Scientific #A14700) for the newly reprogrammed and our control cell line (GCaMP6f-expressing WTC-11 human male iPSCs, Gladstone Institutes), respectively. To acclimate reprogrammed cells to Essential 8 medium, a single passage was performed using a 1:1 ratio of Essential 8 and mTeSR Plus.

6.3.4. hiPSC-cardiomyocyte differentiation

Ventricular and atrial hiPSC-CMs were differentiated following previously published methods [33, 39]. For ventricular hiPSC-CMs, 80% confluent hiPSCs were passaged with versene as for standard hiPSC

maintenance culture prior to seeding onto 24-well plates coated with Geltrex in Essential 8 medium containing 5 µM ROCK-inhibitor. The next day, cardiac differentiation was initiated by treating the hiPSCs with 3.5 to 4.8 µM of a GSK3-inhibitor (CHIR99021: Tocris #4423) in cardiac differentiation medium with three components (CDM3) consisting of RPMI1640 basal medium (Gibco #11875093) supplemented with 213 µg/mL L-ascorbic acid (Sigma Aldrich #A8960) and 500 µg/mL human serum albumin (Sigma Aldrich #A1653). After 24 ± 1 hours in GSK-3 inhibitor, the cells were fed with unmodified CDM3 for two days. At 72 ± 2 hours after the initiation of differentiation, hiPSCs were exposed to 5 µM IWP2 (Tocris #3533) in a 1:1 mixture of spent and new CDM3 for an additional two days. Starting on day 5 post-initiation, cells were fed with CDM3 every other day until the initiation of beating between days 8 and 10, after which they were fed with RPMI1640 supplemented with B27 (Gibco #17504044). Atrial hiPSC-CMs were differentiated identically to ventricular hiPSC-CMs with the additional supplementation of culture medium with 1 µM retinoic acid (Sigma Aldrich #R2625) on days 3 to 6. On days that cells are not fed; retinoic acid is added directly to wells.

Between days 11 and 15, hiPSC-CMs were passaged with 0.25% trypsin (Life Technologies #27250018) in versene and replated at a 1:1 ratio onto a second Geltrex-coated 24-well plate in RPMI/B27 supplemented with 10% fetal bovine serum (Life Technologies #16000044) and 1% penicillin-streptomycin (Sigma Aldrich #P0781) and 5 µM ROCK-inhibitor. After attaching overnight, hiPSC-CMs were allowed to recover for an additional 48 hours in RPMI/B27 before four days of metabolic selection in glucose- and pyruvate-free DMEM (Gibco #11966025) supplemented with 4 mM sodium L-lactate (Sigma Aldrich #L7022) with a media change after the first two days. hiPSC-CMs were then maintained in RPMI/B27 with media changes every 2-3 days until downstream use.

6.3.5. Measurement of hiPSC-CM size with immunocytochemistry

hiPSC-CMs were passaged normally and seeded at a density of 7500 cells per cm^2 onto Geltrex-coated 8-well chamber slides (Fisher #12-565-8) to achieve a density at which single cells would be more easily

identified. After 24 hours, the media was aspirated and the cells fixed in 4% paraformaldehyde (Sigma Aldrich #P6148) for 10-15 minutes at room temperature followed by 3x 5-minute rinses in PBS. Next, cells were permeabilized in 0.25% Triton-X 100 in PBS for 6 minutes followed by 2x rinses in PBS and coated in a blocking buffer of 1% bovine serum albumin (Sigma Aldrich #A8806) in PBS for 1 hour at room temperature. The blocking buffer was then replaced with a primary antibody solution containing mouse anti-cardiac troponin T (cTnT; 1:250; Invitrogen #MA5-12960) in blocking buffer. After overnight incubation at 4 °C, the cells were washed for 3x 5-minutes with PBS and then coated with a fluorescently labeled secondary antibody solution containing AlexaFluor 594 goat anti-mouse IgG (1:250; Invitrogen #A-11005) for 1 hour at room temperature. Finally, the cells were counterstained with 1.5 μg/mL Hoecsht (Sigma Aldrich #B2261) in PBS and washed twice. Coverslips were mounted using several drops of ProLong Glass Antifade Mountant (Life Technologies #P36980) and allowed to cure in the dark for 24 hours at 4 °C. Fluorescent images were acquired at 20x magnification using a Nikon Ti2-E Widefield Fluorescent Microscope. A custom MATLAB script was used to identify overlapping objects containing both a nucleus (DAPI channel) and cTnT (TRITC channel) to measure two-dimensional cell area.

6.3.6. Measurement of hiPSC-CM purity and size with flow cytometry

A sample of 0.5-1 million hiPSC-CMs was collected during normal passaging and was fixed in a 4% paraformaldehyde solution for 10-15 minutes. Fixed cells were centrifuged at 300 g for 5 minutes, the paraformaldehyde removed and stored in 5% FBS in PBS until staining. Cells were permeabilized with 0.75% saponin (Acros #41923) in PBS with 5% FBS before staining with a 1:100 dilution of mouse anti-cTnT (Invitrogen #MA5-12960) overnight at 4 °C before rinsing with PBS and a 1-hour-long stain with a 1:250 dilution of PE-conjugated goat anti-mouse IgG (Jackson #115-116-072) in 0.75% saponin at room temperature. Samples were analyzed with a Cytek Aurora Cell Sorter and FlowJo with gates set based on isotype antibody controls. The mean forward scatter area of $cTnT^+$ cells was used as a proxy for average cardiomyocyte size for a given differentiation.

6.3.7. Assessing hiPSC-CM glycogen content

Samples of 1 million hiPSC-CMs from independent differentiations were flash-frozen in liquid nitrogen and stored at -80 °C until use. For analysis, frozen samples were thawed on ice and cells were lysed in 200 µL of sterile ultrapure water before being boiled for 10 minutes. Insoluble components were removed by centrifugation at 18,000 g for 10 minutes and collecting the supernatant. Protein concentrations was first measured using a Pierce™ BCA Protein Assay (ThermoFisher #23227) and samples were diluted to identical protein concentrations prior to measuring protein-normalized glycogen content using a Abcam™ Glycogen Assay Kit (Abcam #ab65620).

6.3.8. Cardiac fibroblast culture and storage

Primary human ventricular (Lonza #CC-2904, Lot #18TL281202) or atrial (Lonza #CC-2903, Lot #18TL312486) cardiac fibroblasts were cultured in DMEM/F12 supplemented with 10% fetal bovine serum, 1% penicillin-streptomycin, and 4 ng/mL basic fibroblast growth factor (Reprocell #030002). Cells were fed every other day until becoming 80 to 90% confluent, at which point they were passaged using 0.05% trypsin in versene at a density of 5,000 cells/cm^2 for subsequent viability assessment. Prior to incorporation into cardiac microtissues, fibroblasts were frozen in 10% dimethyl sulfoxide (DMSO) at -80 °C overnight before being stored in liquid nitrogen.

6.3.9. Cardiac microtissue preparation

Microtissues were created as previously described [40, 41]. Briefly, agarose microtissue molds were created with sterile 2% (wt/vol) agarose (Invitrogen #16500500) in 1x PBS pipetted into sterile 35-microwell negative molds with 800-µm-diameter hemispherical microwells (Microtissues Inc #24-35). After formation, agarose molds were equilibrated in RPMI/B27 media with 1% penicillin-streptomycin for at least 1 hour at 37 °C. Metabolically purified hiPSC-CMs were singularized with 0.25% trypsin in versene and combined with 5% chamber-matched cardiac fibroblasts (passage 4-6). A total of 350,000 cells per mold (10,000 cells per microtissue) were seeded into each agarose mold in a total volume of 100 µL of RPMI/B27 supplemented with 10% fetal bovine serum, 1% penicillin-streptomycin, and 5 µM ROCK-

inhibitor. The cell suspension was allowed to settle for 30 minutes before being covered with media. Microtissues were cultured under electrical field stimulation with a 1 Hz, 10 V, 4 ms duration bipolar pulse train (C-Pace EP, IonOptix) for the remainder of culture. After 24 hours, the media was exchanged for media without ROCK-inhibitor and refreshed every three days. Microtissues were fully compacted, beating on pace, and ready for optical mapping after one week.

6.3.10. Optical mapping of cardiac action potentials and calcium transients

Optical mapping was performed as previously described [42]. Cardiac microtissues were transferred to a temperature-controlled chamber containing (in mM) 140 NaCl, 4.0 KCl, 1.0 $MgCl_2$, 1.25 $CaCL_2$, 0.33 NaH_2PO_4, 5.0 HEPES, 5.0 sodium pyruvate, and 7.5 glucose. Additional solution was gently perfused through the chamber. Microtissues were stained with either a 5 µM solution of a voltage-sensitive dye (di-4-ANEPPS: Invitrogen #D1199) or 0.5 mg/mL fluorescent calcium indicator (Rhod-2: Invitrogen #R1244) for 2-3 minutes or 10 minutes, respectively, before washing to remove excess. A CMOS camera (Ultima-L, Scimedia, Japan) was used to record fluorescent images at 1,000 frames per second under spontaneous or paced conditions. Action potential and calcium transient traces were reconstructed from fluorescence intensity data averaged across microtissue area and semi-automated analysis using in-house software-enabled measurement of both metrics measuring action potential and calcium transient shape as previously described [42]. For action potential measurements, this included excitability; cycle length; stimulation delay; rise time; and action potential duration to 30% (APD30), 50% (APD50), 80% (APD80), or maximum rate of repolarization (APD_{mxr}); and action potential triangulation (APD_{tri}: $APD_{mxr} – APD_{50}$). For calcium transients, this included cycle length, stimulation delay, rise time, rise time tau, maximum amplitude, amplitude of the initial rise phase, total calcium duration, and relaxation tau.

6.4. Results

6.4.1. Generation of a novel WPW hiPSC line with no *PRKAG2* mutation

Uroepithelial cells isolated from a donor with WPW (45-year-old Caucasian male) were reprogrammed using a seven-factor Epstein Barr nuclear antigen-based episomal system to induce the

expression of pluripotency genes (Emory Stem Cell and Organoids Core). Three clones that were initially isolated post-reprogramming were karyotyped, confirming the absence of chromosomal abnormalities (**Figure 6.1A**). Flow cytometry confirmed high purity (> 85%) of hiPSCs expressed the pluripotency markers SSEA4, SOX2, TRA-1-60, and Oct4 (**Figure 6.1B-C**). Pluripotency of hiPSC colonies was further confirmed by positive immunofluorescent staining against SSEA4, SOX2, TRA-1-81, and Oct 4 (**Figure 6.1D-E**). Having confirmed successful reprogramming, the ability of the novel hiPSC line to differentiate to all three major germ lines was confirmed by flow cytometry against endodermal (CXCR4 and SOX17), mesodermal (NCAM and Brachyury), and ectodermal (Pax6 and Nestin) markers (**Figure 6.2**). Since the majority of identified genetic mutations linked to WPW involve mutations in the *PRKAG2* gene, Sanger sequencing was used to examine the genomic sequence of the *PRKAG2* gene in both the novel WPW hiPSC line and our control hiPSCs (**Supplemental Figure D.1**). Neither the WPW or control hiPSC lines possessed *PRKAG2* mutations, suggesting that our WPW hiPSCs possess a novel genetic background linked to WPW.

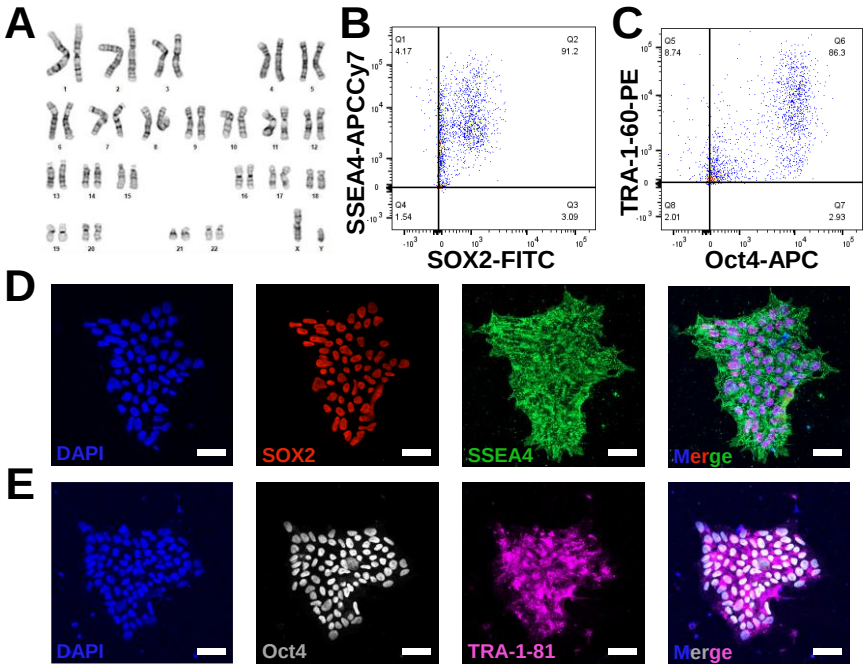

Figure 6.1. Pluripotency characterization of novel WPW hiPSC line. (A) WPW hiPSCs from the donor possessed a normal karyotype without chromosomal abnormalities from reprogramming. **(B-C)** Flow cytometry confirmed high percentages of pluripotent cells (> 85%) for four different markers of pluripotency, including **(B)** SOX2, SSEA4, **(C)** Oct4, and TRA-1-60. **(D-E)** Pluripotency was further confirmed by positive immunofluorescent staining of the markers **(D)** SOX2, SSEA4, **(E)** Oct4, TRA-1-81 in individual hiPSC colonies. Scalebars are 50 µm.

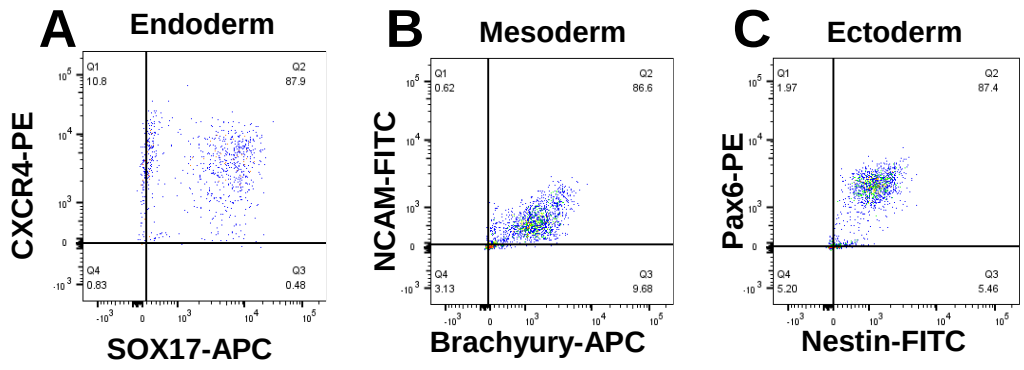

Figure 6.2. Flow Cytometry of Differentiation Markers for All Germ Lines. Reprogrammed cells from the WPW donor were more than 80% positive for the **(A)** endodermal (CXCR4, SOX17), **(B)** mesodermal (NCAM, Brachyury), and **(C)** ectodermal (Pax6, Nestin) markers after initiation of differentiation.

6.4.2. WPW hiPSC-CMs possess a hypertrophic phenotype and enhanced glycogen storage

Having developed a novel WPW hiPSC line, we confirmed the ability of these cells to differentiate into cardiomyocytes using standard biphasic Wnt activation and inhibition with small molecules. Both control and WPW lines were successfully differentiated to atrial and ventricular hiPSC-CMs as confirmed by immunofluorescent staining (**Figure 6.3A-B**) and flow cytometry (**Figure 6.3C**) against the cardiomyocyte marker cTnT. While beating cardiomyocytes were generated for both sub-types, ventricular differentiations resulted in higher purities (WTC: 79.9 ± 12.3% versus WPW: 89.1 ± 8.6%) than atrial differentiations (WTC: 57.3 ± 11.6% versus WPW: 63.9 ± 26.3%) although there were no significant differences between cell line or chamber type. The size of hiPSC-CMs was quantified from $cTnT^+$ cells to circumvent variations in differentiation purities using both two-dimensional area from immunofluorescent images and average forward scatter peak area from flow cytometry. WPW atrial hiPSC-CMs possessed a significantly larger two-dimensional area (2,280 ± 2,110 μm^2) compared to all other hiPSC-CMs, including control atrial (1,210 ± 860 μm^2) and ventricular (1,480 ± 1,400 μm^2) as well as WPW ventricular (1,650 ± 1,240 μm^2) cardiomyocytes (**Figure 6.3D**). WPW ventricular cells were the second largest condition, but were only significantly larger than control atrial hiPSC-CMs. Average differentiation hiPSC-CM size was not significantly different when measured using flow cytometry (**Figure 6.3E**). However, the data follow a similar trend to that measured in hiPSC-CM monolayers, with both atrial

and ventricular WPW hiPSC-CMs possessing larger forward scatter peak areas than WTC hiPSC-CMs. Finally, we characterized cellular glycogen content to determine if cell type influenced glycogen accumulation (**Figure 6.3F**). We observed that ventricular WPW hiPSC-CMs had significantly higher glycogen content (2.53 ± 1.34 µg/µg) compared to WTC ventricular (0.55 ± 0.20 µg/µg), WTC atrial (1.14 ± 0.45 µg/µg), or WPW atrial hiPSC-CMs (0.74 ± 0.93 µg/µg), which all had similar glycogen content.

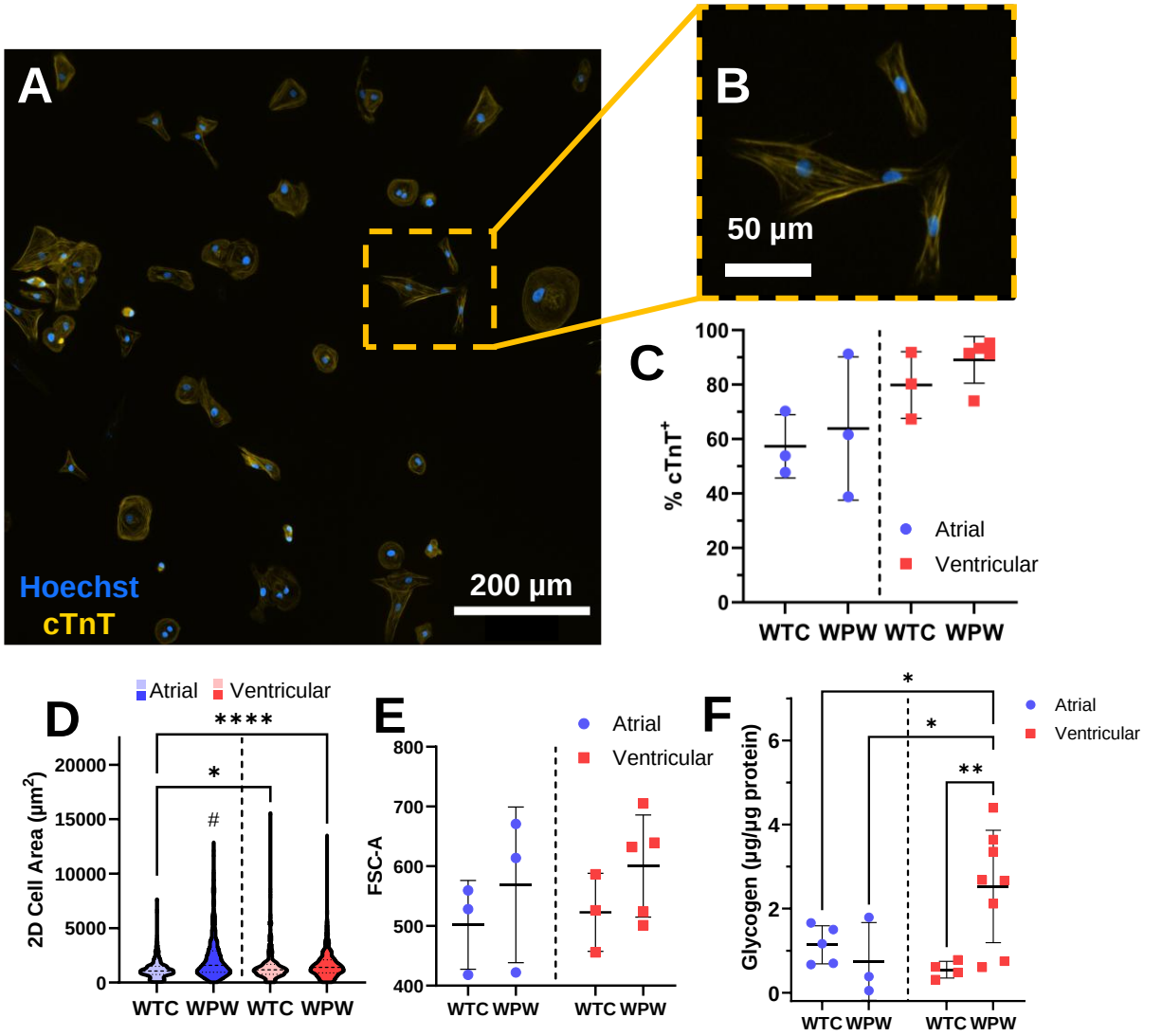

Figure 6.3. Differentiation and characterization of cardiomyocytes from novel WPW hiPSCs. (A-B) Immunofluorescent staining of nuclei (blue) and cardiac troponin T (cTnT; red) of atrial hiPSC-CMs differentiated using the novel WPW cell line. **(C)** Flow cytometry was used to measure the purity (% $cTnT^+$) of atrial and ventricular differentiations from both WPW and control lines (N = 3-5 differentiations). Cell size was further characterized in $cTnT^+$ cells using both **(D)** distribution of two-dimensional cell area from fluorescent images from a single differentiation (N = 326-935 cells per condition) as well as **(E)** average forward scatter peak area (FSC-A) for individual differentiations (N = 3-5 differentiations). **(F)** Protein-normalized glycogen content was measured to characterize glycogen accumulation in cardiomyocytes from control and WPW lines (N = 3-8 differentiations). Data are displayed

as mean ± standard deviation except for **(D)** cell area, which is a probability density of the data. *, **, and *** indicate statistical significance ($p < 0.05$; $p < 0.01$; and $p < 0.0001$, respectively) for two-way ANOVA and Tukey post-hoc test between bracketed groups. # indicates statistical significance ($p < 0.05$) compared to all other groups.

6.4.3. Electrophysiological characterization of WPW hiPSC-CMs

To understand potentially proarrhythmic electrophysiological differences in WPW hiPSC-CMs, cardiac action potentials were measured in atrial microtissues from high purity differentiations (>70% $cTnT^+$) under both spontaneous and paced conditions. Under spontaneous conditions, WPW atrial microtissues possessed a significantly shorter cycle length (846 ± 28 ms) compared to control atrial microtissues (1,054 ± 108 ms) (**Figure 6.4A-B**). In addition to faster spontaneous beating, WPW microtissues also maintained excitability in response to high-frequency challenge pacing (**Figure 6.4C-D**). Both WPW and control microtissues maintained excitability up to 3 Hz. At 4 Hz, control microtissues lost the ability to keep pace with stimulation (65.1 ± 11.3%) whereas the majority of WPW microtissues maintained excitability (96.8 ± 5.5%). This combination of higher frequency spontaneous beating and the ability to follow high-frequency pacing suggests that WPW hiPSC-CMs have a more proarrhythmic electrophysiological profile than non-WPW hiPSC-CMs.

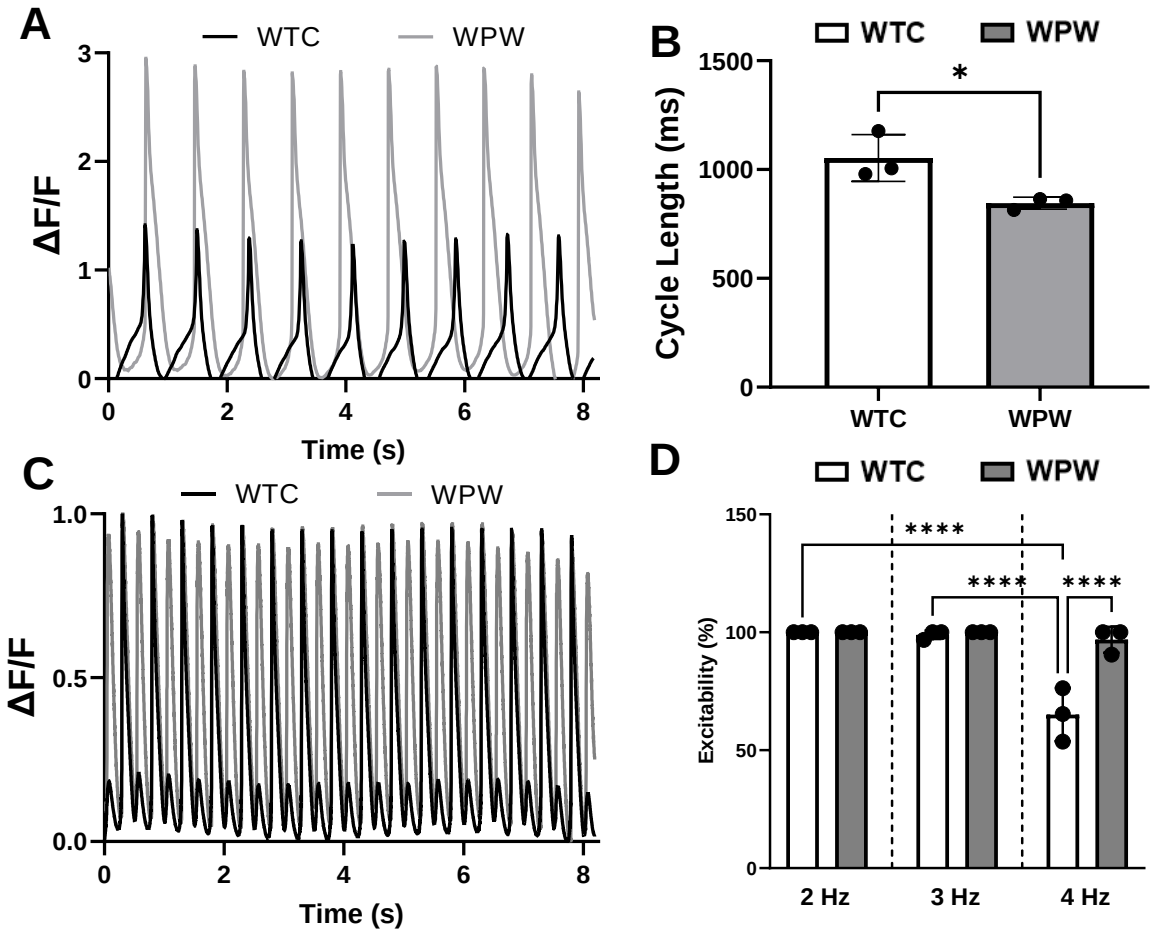

Figure 6.4. Atrial WPW hiPSC-CMs form a more proarrhythmic substrate than control cardiomyocytes. (A) Representative action potential traces from spontaneously beating WTC control and WPW microtissues. **(B)** Mold-averaged cycle length of atrial microtissues showed that WPW microtissues beat more rapidly than control microtissues. **(C)** Representative action potential traces at 4 Hz pacing from WTC control and WPW microtissues. **(D)** Mold-averaged excitability across multiple pacing frequencies for both WTC control and WPW microtissues showed that WPW hiPSC-CMs could follow higher beat rates. Data are displayed as mean ± standard deviation. * and **** indicate statistical significance ($p < 0.05$ and $p < 0.0001$, respectively) for two-way ANOVA and Tukey post-hoc test or unpaired Student's t test as appropriate (n = 3 molds).

Underlying differences in action potential kinetics were examined in detail under 2 Hz pacing in order to understand specific electrophysiological differences that may contribute to differences in spontaneous beat rate and excitability (**Figure 6.5**). WPW atrial microtissues possessed statistically significantly longer APD30 (83.1 ± 9.5 ms), APD50 (121.0 ± 6.5), APD80 (189.0 ± 13.0), APD_{mxr} (259.5 ± 29.7), and APD_{tri} (138.0 ± 23.6 ms) compared to WTC microtissues (APD30: 50.6 ± 5.9 ms; APD50: 72.9 ± 8.8 ms; APD80: 127.7 ± 13.0 ms; APD_{mxr}: 121.8 ± 36.7 ms; and APD_{tri}: 78.6 ± 30.9 ms). Both the depolarization-focused metrics stimulation delay (WTC: 2.7 ± 0.6 ms versus WPW: 2.2 ± 1.3 ms) and rise time (WTC: 11.1 ± 2.7 ms versus

WPW: 6.5 ± 3.3 ms) were not significantly different between the two hiPSC lines under 2 Hz pacing. Contrastingly, spontaneous rise time was shorter in WPW microtissues (8.5 ± 4.0 ms) compared to WTC microtissues (20.2 ± 5.4 ms), suggesting potential differences in depolarizing sodium currents during spontaneous beating (**Supplemental Figure D.2B**). Relative differences in action potential duration were similarly maintained under spontaneous conditions (**Supplemental Figure D.2B**).

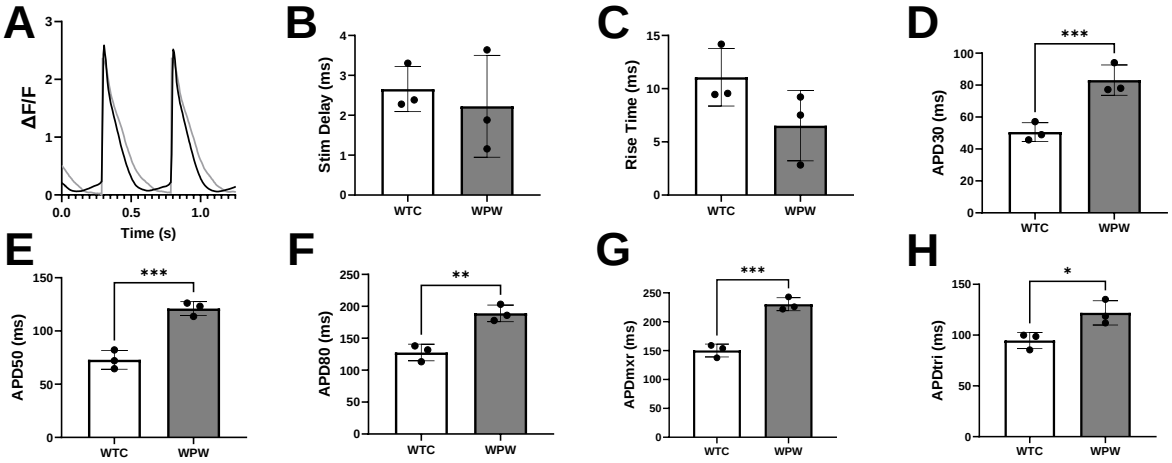

Figure 6.5. Quantification of action potentials from 2 Hz-paced microtissues. (A) Representative action potential trace from 2 Hz-paced WTC control and WPW microtissues enabled measurement of mold-averaged **(B)** stimulation (stim) delay, **(C)** rise time, **(D)** APD30, **(E)** APD50, **(F)** APD80, **(G)** APD_{mxr}, **(H)** APD_{tri}**.** Data are displayed as mean ± standard deviation. *, **, ***, and **** indicate statistical significance ($p < 0.05$, $p < 0.01$, $p < 0.001$, and $p < 0.0001$, respectively) from and unpaired Student's t-test (n = 3 molds).

6.4.4. Calcium transient properties of WPW hiPSC-CMs

Calcium transients were quantified to provide additional insight into the electrophysiological phenotype of WPW cardiomyocytes under both spontaneous (**Supplemental Figure D.3**) and 2 Hz-paced conditions (**Figure 6.6**). In contrast to action potential duration, calcium transients were significantly shorter in WPW atrial microtissues (308.2 ± 8.5 ms) compared to controls (374.2 ± 12.5 ms) (**Figure 6.6G**). Calcium transient rise time was also significantly shorter in WPW microtissues (66.2 ± 9.1 ms) versus control microtissues (87.9 ± 5.8 ms) (**Figure 6.6C**). No other metrics were significantly different in paced microtissues, but both rise time (WTC: 35.8 ± 4.0 ms versus WPW: 23.8 ± 3.8 ms) and relaxation time (WTC: 374.0 ± 24.3 ms versus WPW: 289.0 ± 34.0 ms) constants were significantly smaller during spontaneous beating of WPW atrial microtissues as well (**Supplemental Figure D.3C and H**). This trend

was similar in paced microtissues, but the difference was not significant (**Figure 6.6D and H**) and suggests that the shorter calcium duration in WPW microtissues is due to a combination of faster calcium release and reuptake compared to control microtissues.

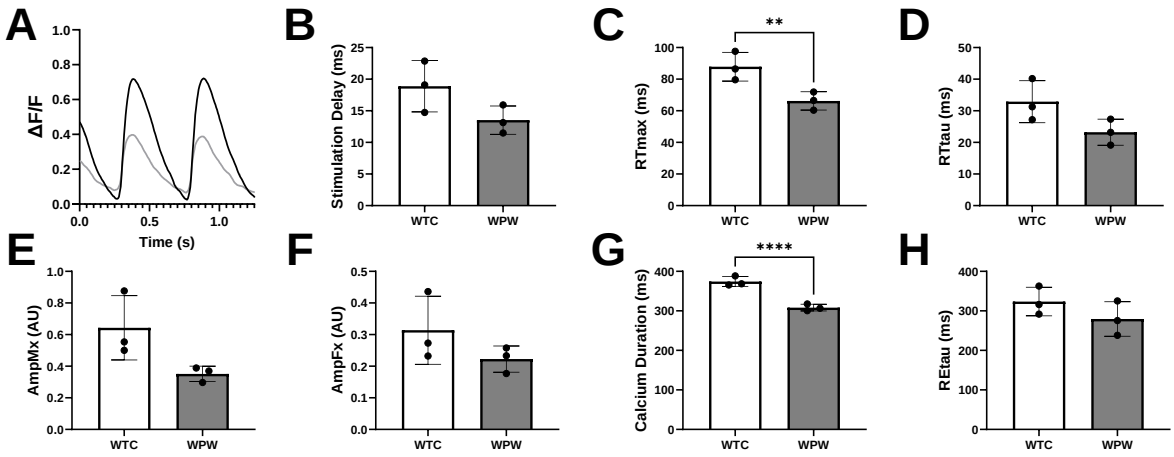

Figure 6.6. Quantification of calcium transients from 2 Hz-paced microtissues. (A) Representative calcium traces from 2 Hz-paced WTC control and WPW microtissues enabled measurement of mold-averaged **(B)** stimulation delay, **(C)** rise time (RTmax), **(D)** rise time tau (RTtau), **(E)** maximum amplitude (AmpMx), **(F)** amplitude of the initial rise phase (AmpFx), **(G)** total calcium transient duration, and **(H)** relaxation tau (REtau)**.** Data are displayed as mean ± standard deviation. ** and **** indicate statistical significance ($p < 0.01$ and $p < 0.0001$, respectively) from an unpaired Student's t-test (n = 3 molds).

6.5. Discussion

WPW remains a poorly understood form of atrial arrhythmia arising from the formation of accessory atrioventricular conduction pathways in addition to an elevated risk of atrial fibrillation [11]. Typically, studies examining WPW have relied on rodent models with mutations in the *PRKAG2* gene, but species-to-species differences and reliance on known mutations limit the broad relevance to WPW etiology across genetic backgrounds in humans. *In vitro* approaches leveraging hiPSC-CMs offer a promising technique for studying the electrophysiological triggers of disease using patient-derived cell lines for recapitulating cellular phenotypes *in vitro* [26-29], and recent work has begun to leverage known *PRKAG2* mutations in hiPSC-CM models of WPW [30-32]. In this study, we expanded on hiPSC-CM-based models of WPW by generating a novel, non-*PRKAG2* hiPSC line from a patient who presents clinically with atrial fibrillation to examine human-relevant phenotypes from an as-of-yet studied genetic background. We leveraged chamber-specific differentiation protocols and engineered cardiac microtissues [33] to examine atrial

electrophysiology in contrast to previous hiPSC-CM-based studies that relied on traditional ventricular differentiation protocols [30-32], expanding the clinical relevance of tissue-engineered models of WPW and furthering our basic understanding of disease mechanisms.

We successfully differentiated both atrial and ventricular cardiomyocytes from our non-*PRKAG2* WPW hiPSC line as confirmed by the expression of cTnT (**Figure 6.3A-B**). Acting as a proxy for cardiac hypertrophy, we found that atrial WPW hiPSC-CMs were significantly larger in two-dimensional area than control cells (**Figure 6.3D**) and that the volume of WPW hiPSC-CMs was also larger, but not significantly, than control cardiomyocytes (**Figure 6.3E**). These observations mirror observations of enlarged hearts in mouse models [5, 22, 43-47] and enlarged cardiomyocytes in hiPSC-based models of WPW [30-32]. Cardiac hypertrophy, as well as the formation of accessory pathways in WPW, are thought to arise due to excess accumulation of glycogen in cardiomyocytes prior to the formation of the annulus fibrosis, and elevated glycogen content is observed in human patients as well as animal and hiPSC-CM models with *PRKAG2* mutations [6, 14]. We similarly observed elevated glycogen concentrations in ventricular, but not atrial, WPW hiPSC-CMs compared to controls (**Figure 6.3F**), suggesting that glycogen accumulation may be conserved in WPW even in the absence of mutations in *PRKAG2*. Together, these data suggest that we successfully replicated cellular phenotypes associated with WPW.

In examining the electrophysiological characteristics of atrial microtissues generated from our novel hiPSC line, we identified potential contributors to the proarrhythmic phenotype associated with WPW. We observed that atrial WPW microtissues beat more rapidly and were more excitable under high-frequency pacing than control atrial cardiomyocytes (**Figure 6.4**). These data suggest that WPW cells form a more proarrhythmic atrial substrate due to a higher probability of triggered arrhythmias combined with a higher susceptibility to reentrant arrhythmias due to a lower effective refractory period [10, 12]. Additionally, we found that WPW microtissues possessed longer action potential durations (**Figure 6.5**) but shorter calcium transients (**Figure 6.6**). While cell-level data are not typically available from published

mouse studies, previous data in three ventricular hiPSC-CMs with R302Q mutations in *PRKAG2* partially mirror our observations [30-32]. Like in our hiPSC line, action or field potential duration was significantly increased in one of three lines with non-significant increases in the other two [30, 31] . Constitutive activation of AMPK by modulation of the α-subunit has been shown to prolong cardiac action potentials in rat ventricular cardiomyocytes [48], although glycogen content was not examined in these cells to account for the effects of metabolism in these cells. Calcium duration was only measured in two of the three hiPSC lines [30], but unlike in our study, calcium transient duration was increased. Two of the three cell lines also possessed a slower spontaneous beat rate while the third was similar to control cells [30, 31]. For the R302Q mutation, this matches how patients typically present clinically as sinus bradycardia is associated with this genotype [31]. Unfortunately, the only other hiPSC-CM study of WPW did not perform electrophysiological assessment of their cells, so the effects of other *PRKAG2* mutations, and specifically N488I, in hiPSC-CMs cannot be compared [32]. The differences between our and these previous studies may also be a result of known differences between atrial and ventricular electrophysiology [33, 49], highlighting the importance of our novel use of atrial hiPSC-CMs to examine atrial arrhythmias.

The variation in electrophysiological phenotypes between and within these hiPSC-CM studies also reflects the high degree of variability in how WPW manifests clinically and points to a significant role for genes beyond *PRKAG2* to cause WPW. For instance, multiple studies examining familial WPW resulting from the same R302Q mutation in humans have linked the presence of the mutation to glycogen accumulation, hypertrophy, and preexcitation [15, 16, 18]. However, at least one four-member family with the R302Q mutation has been identified that had no hypertrophy or preexcitation despite presenting with other conduction defects such as a short PR interval [17]. This diversity is also unsurprisingly apparent across the full spectrum of identified *PRKAG2* mutations [14]. In *in vitro* and mouse studies examining the effect of *PRKAG2* mutations on AMPK activity, there is an approximately even split between those that

measured increased AMPK activity [5, 24, 44, 46, 50, 51] and those that observed reduced activity [21, 22, 43, 45, 47, 52].

Despite differences in measured AMPK activity, increased cardiac glycogen was observed in all but one of the published rodent models [5], although others with the same mutation report glycogen accumulation [16, 46, 50]. It has been suggested that glycogen accumulation is the primary event leading to the development of WPW and that observed reductions in AMPK activity are the result of suppression by glycogen or other metabolites at later time points [14, 16, 24, 45]. Previous work in a cardiac-specific N488I *PRKAG2* mutant mouse model found that stopping excess glycogen storage by inhibition of glucose-6-phosphate-stimulated glycogen synthesis prevented the development of ventricular preexcitation, but surprisingly not cardiac hypertrophy due to early hyperactivity of Akt and cardiomyocyte proliferation followed by post-natal hypertrophy [53]. This suggests separate, glycogen-dependent and -independent mechanisms for pre-excitation and cardiac hypertrophy in WPW, respectively, and highlights the complexity of identifying individual mechanistic causes for the clinical features of WPW. Clinical data also suggests that electrophysiological changes can occur independently of cardiac hypertrophy for at least one mutation (*i.e.* R531G) [23]. Our results provide indirect evidence towards this hypothesis since we observed cardiomyocyte hypertrophy and glycogen accumulation in the absence of a *PRKAG2* mutation that could influence AMPK activity in the heart. However, AMPK may be modulated by changes in other regulatory proteins or mutations in other AMPK subunits.

Our work provides a foundation from which to leverage human atrial models of WPW to investigate proarrhythmic phenotypes in WPW, particularly from as-of-yet described mutations. Building from these findings, future work will need to examine specific ion channel expression and ion currents to identify an electrophysiological mechanism for the proarrhythmic effects observed in our novel WPW hiPSC-CMs and relating these changes to glycogen accumulation or AMPK activity. The development of additional cell lines from related family members with and without WPW would also enhance the ability of this model

to identify subtle electrophysiological and molecular changes resulting from WPW by providing a more specific non-WPW control. Overall, hiPSC-CM models, especially those leveraging newly available chamber-specific protocols, will provide an invaluable tool for dissecting human-specific disease mechanisms and identifying novel treatments for WPW.

6.6. Acknowledgements

We would like to acknowledge the contributions of Samuel Lorenzo for his assistance in performing portions of the experimental work in support of this chapter in addition to funding from a National Science Foundation CAREER Award (to KLKC) under award number 2047583. This research project was also supported in part by the Emory University Integrated Stem Cell and Organoids Core, which is subsidized by the Emory University School of Medicine. Additional support was provided by the National Center for Georgia Clinical and Translational Science Alliance of the National Institutes of Health under award number UL1TR002378. The content is solely the responsibility of the authors and does not necessarily reflect the official views of the National Institute of Health. Finally, we would also like to acknowledge the contribution of study participants without whom this work would not be possible.

6.7. References

1. Martin, S.S., et al., *2024 heart disease and stroke statistics: a report of US and global data from the American Heart Association.* Circulation, 2024. **149**(8): p. e347-e913.
2. Stewart, S., et al., *A population-based study of the long-term risks associated with atrial fibrillation: 20-year follow-up of the Renfrew/Paisley study.* The American journal of medicine, 2002. **113**(5): p. 359-364.
3. Go, A.S., et al., *Prevalence of diagnosed atrial fibrillation in adults: national implications for rhythm management and stroke prevention: the AnTicoagulation and Risk Factors in Atrial Fibrillation (ATRIA) Study.* Jama, 2001. **285**(18): p. 2370-2375.

4. Coban-Akdemir, Z.H., et al., *Wolff–Parkinson–White syndrome: De novo variants and evidence for mutational burden in genes associated with atrial fibrillation.* American Journal of Medical Genetics Part A, 2020. **182**(6): p. 1387-1399.

5. Yang, X., et al., *Physiological expression of AMPKγ2RG mutation causes Wolff-Parkinson-White syndrome and induces kidney injury in mice.* Journal of Biological Chemistry, 2016. **291**(45): p. 23428-23439.

6. Miyamoto, L., *Molecular Pathogenesis of Familial Wolff-Parkinson-White Syndrome.~ Molecular Mechanisms of Cardiac Glycogen Regulation by AMPK~.* The Journal of Medical Investigation, 2018. **65**(1.2): p. 1-8.

7. Al-Khatib, S.M. and E.L. Pritchett, *Clinical features of wolff-parkinson-white syndrome.* American heart journal, 1999. **138**(3): p. 403-413.

8. Gallagher, J.J., et al., *Wolff-Parkinson-White syndrome. The problem, evaluation, and surgical correction.* Circulation, 1975. **51**(5): p. 767-785.

9. Gallagher, J.J., et al., *The preexcitation syndromes.* Progress in cardiovascular diseases, 1978. **20**(4): p. 285-327.

10. Centurion, O.A., *Atrial fibrillation in the Wolff-Parkinson-White syndrome.* Journal of atrial fibrillation, 2011. **4**(1): p. 287.

11. Bunch, T.J., et al., *Long-term natural history of adult Wolff–Parkinson–White syndrome patients treated with and without catheter ablation.* Circulation: Arrhythmia and Electrophysiology, 2015. **8**(6): p. 1465-1471.

12. Fengler, B.T., W.J. Brady, and C.U. Plautz, *Atrial fibrillation in the Wolff-Parkinson-White syndrome: ECG recognition and treatment in the ED.* The American journal of emergency medicine, 2007. **25**(5): p. 576-583.

13. Carling, D., *AMPK signalling in health and disease.* Current opinion in cell biology, 2017. **45**: p. 31-37.

14. Salt, I.P. and D.G. Hardie, *AMP-activated protein kinase: an ubiquitous signaling pathway with key roles in the cardiovascular system.* Circulation research, 2017. **120**(11): p. 1825-1841.

15. Gollob, M.H., et al., *Identification of a gene responsible for familial Wolff–Parkinson–White syndrome.* New England Journal of Medicine, 2001. **344**(24): p. 1823-1831.

16. Arad, M., et al., *Constitutively active AMP kinase mutations cause glycogen storage disease mimicking hypertrophic cardiomyopathy.* The Journal of clinical investigation, 2002. **109**(3): p. 357-362.

17. Charron, P., et al., *A familial form of conduction defect related to a mutation in the PRKAG2 gene.* Europace, 2007. **9**(8): p. 597-600.

18. Thevenon, J., et al., *High prevalence of arrhythmic and myocardial complications in patients with cardiac glycogenosis due to PRKAG2 mutations.* Europace, 2017. **19**(4): p. 651-659.

19. Blair, E., et al., *Mutations in the γ2 subunit of AMP-activated protein kinase cause familial hypertrophic cardiomyopathy: evidence for the central role of energy compromise in disease pathogenesis.* Human molecular genetics, 2001. **10**(11): p. 1215-1220.

20. Akman, H.O., et al., *Fatal infantile cardiac glycogenosis with phosphorylase kinase deficiency and a mutation in the γ2-subunit of AMP-activated protein kinase.* Pediatric research, 2007. **62**(4): p. 499-504.

21. Bayrak, F., et al., *Ventricular pre-excitation and cardiac hypertrophy mimicking hypertrophic cardiomyopathy in a Turkish family with a novel PRKAG2 mutation.* European journal of heart failure, 2006. **8**(7): p. 712-715.

22. Xie, C., et al., *Genome editing with CRISPR/Cas9 in postnatal mice corrects PRKAG2 cardiac syndrome.* Cell research, 2016. **26**(10): p. 1099-1111.

23. Gollob, M.H., et al., *Novel PRKAG2 mutation responsible for the genetic syndrome of ventricular preexcitation and conduction system disease with childhood onset and absence of cardiac hypertrophy.* Circulation, 2001. **104**(25): p. 3030-3033.

24. Burwinkel, B., et al., *Fatal congenital heart glycogenosis caused by a recurrent activating R531Q mutation in the γ2-subunit of AMP-activated protein kinase (PRKAG2), not by phosphorylase kinase deficiency.* The American Journal of Human Genetics, 2005. **76**(6): p. 1034-1049.

25. Laforêt, P., et al., *A new mutation in PRKAG2 gene causing hypertrophic cardiomyopathy with conduction system disease and muscular glycogenosis.* Neuromuscular Disorders, 2006. **16**(3): p. 178-182.

26. Chen, I.Y., E. Matsa, and J.C. Wu, *Induced pluripotent stem cells: at the heart of cardiovascular precision medicine.* Nature Reviews Cardiology, 2016. **13**(6): p. 333.

27. Avior, Y., I. Sagi, and N. Benvenisty, *Pluripotent stem cells in disease modelling and drug discovery.* Nature reviews Molecular cell biology, 2016. **17**(3): p. 170.

28. Lippi, M., et al., *Human cell modeling for cardiovascular diseases.* International Journal of Molecular Sciences, 2020. **21**(17): p. 6388.

29. Savoji, H., et al., *Cardiovascular disease models: a game changing paradigm in drug discovery and screening.* Biomaterials, 2019. **198**: p. 3-26.

30. Zhan, Y., et al., *Establishment of a PRKAG2 cardiac syndrome disease model and mechanism study using human induced pluripotent stem cells.* Journal of molecular and cellular cardiology, 2018. **117**: p. 49-61.

31. Ben Jehuda, R., et al., *CRISPR correction of the PRKAG2 gene mutation in the patient's iPSC-derived cardiomyocytes eliminates the electrophysiological and structural abnormalities.* Heart Rhythm, 2018. **15**(2): p. 267-276.

32. Hinson, J.T., et al., *Integrative analysis of PRKAG2 cardiomyopathy iPS and microtissue models identifies AMPK as a regulator of metabolism, survival, and fibrosis.* Cell reports, 2016. **17**(12): p. 3292-3304.

33. Soepriatna, A.H., et al., *Human Atrial Cardiac Microtissues for Chamber-Specific Arrhythmic Risk Assessment.* Cellular and Molecular Bioengineering, 2021. **14**(5): p. 441-457.

34. Zhao, Y., et al., *A platform for generation of chamber-specific cardiac tissues and disease modeling.* Cell, 2019. **176**(4): p. 913-927. e18.

35. Zhao, Y., et al., *Towards chamber specific heart-on-a-chip for drug testing applications.* Advanced Drug Delivery Reviews, 2020. **165-166**: p. 60-76.

36. Gruner, C., et al., *Sarcomere protein gene mutations in patients with apical hypertrophic cardiomyopathy.* Circulation: Cardiovascular Genetics, 2011. **4**(3): p. 288-295.

37. Murphy, R.T., et al., *Adenosine monophosphate-activated protein kinase disease mimicks hypertrophic cardiomyopathy and Wolff-Parkinson-White syndrome: natural history.* Journal of the American College of Cardiology, 2005. **45**(6): p. 922-930.

38. Ehtisham, J. and H. Watkins, *Is Wolff-Parkinson-White syndrome a genetic disease?* Journal of cardiovascular electrophysiology, 2005. **16**(11): p. 1258-1262.

39. Burridge, P.W., A. Holmström, and J.C. Wu, *Chemically defined culture and cardiomyocyte differentiation of human pluripotent stem cells.* Current Protocols in Human Genetics, 2015. **87**(1): p. 21.3. 1-21.3. 15.

40. Kofron, C., et al., *A Predictive in Vitro Risk Assessment Platform for Pro-Arrhythmic Toxicity Using Human 3D Cardiac Microtissues.* Scientific Reports, 2021. **11**: p. 1-16.

41. Daley, M., et al., *In vitro to in vivo extrapolation from three-dimensional hiPSC-derived cardiac microtissues and physiologically based pharmacokinetic modeling to inform next-generation arrhythmia risk assessment.* Toxicological Sciences, 2024: p. kfae079.

42. Soepriatna, A.H., et al., *Action potential metrics and automated data analysis pipeline for cardiotoxicity testing using optically mapped hiPSC-derived 3D cardiac microtissues.* Plos one, 2023. **18**(2): p. e0280406.

43. Sidhu, J.S., et al., *Transgenic mouse model of ventricular preexcitation and atrioventricular reentrant tachycardia induced by an AMP-activated protein kinase loss-of-function mutation responsible for Wolff-Parkinson-White syndrome.* Circulation, 2005. **111**(1): p. 21-29.

44. Arad, M., et al., *Transgenic mice overexpressing mutant PRKAG2 define the cause of Wolff-Parkinson-White syndrome in glycogen storage cardiomyopathy.* Circulation, 2003. **107**(22): p. 2850-2856.

45. Davies, J.K., et al., *Characterization of the role of γ2 R531G mutation in AMP-activated protein kinase in cardiac hypertrophy and Wolff-Parkinson-White syndrome.* American Journal of Physiology-Heart and Circulatory Physiology, 2006. **290**(5): p. H1942-H1951.

46. Wolf, C.M., et al., *Reversibility of PRKAG2 glycogen-storage cardiomyopathy and electrophysiological manifestations.* Circulation, 2008. **117**(2): p. 144-154.

47. Thorn, S.L., et al., *Chronic AMPK activity dysregulation produces myocardial insulin resistance in the human Arg302Gln-PRKAG2 glycogen storage disease mouse model.* EJNMMI research, 2013. **3**: p. 1-9.

48. Light, P.E., C.H. Wallace, and J.R. Dyck, *Constitutively Active Adenosine Monophosphate–Activated Protein Kinase Regulates Voltage-Gated Sodium Channels in Ventricular Myocytes.* Circulation, 2003. **107**(15): p. 1962-1965.

49. Schram, G., et al., *Differential distribution of cardiac ion channel expression as a basis for regional specialization in electrical function.* Circulation research, 2002. **90**(9): p. 939-950.

50. Zou, L., et al., *N488I mutation of the γ2-subunit results in bidirectional changes in AMP-activated protein kinase activity.* Circulation research, 2005. **97**(4): p. 323-328.

51. Yavari, A., et al., *Mammalian γ2 AMPK regulates intrinsic heart rate.* Nature communications, 2017. **8**(1): p. 1258.

52. Zhang, B.-l., et al., *Identification and functional analysis of a novel PRKAG2 mutation responsible for Chinese PRKAG2 cardiac syndrome reveal an important role of non-CBS domains in regulating the AMPK pathway.* Journal of Cardiology, 2013. **62**(4): p. 241-248.

53. Kim, M., et al., *Mutation in the γ2-subunit of AMP-activated protein kinase stimulates cardiomyocyte proliferation and hypertrophy independent of glycogen storage.* Circulation research, 2014. **114**(6): p. 966-975.

Chapter 7 - Discussion

Limitations in the ability to accurately assess the safety and efficacy of novel compounds continue to present substantial hurdles to efficient drug discovery and design. This body of work sought to broaden the applicability and impact of fit-for-purpose human induced pluripotent stem cell-derived cardiomyocyte (hiPSC-CM) models across a broad spectrum of preclinical contexts. Each Aim was designed to examine a single facet of drug discovery; including risk assessment (Aim 1), drug screening (Aim 2), and target identification (Aim 3); such they validated the use of hiPSC-CMs for improving the efficiency and predictiveness of preclinical testing overall. Here, the major outcomes of each aim, as well as their broader impacts and future directions, are discussed.

7.1. Major outcomes

In Aim 1, we were able to leverage a combination of high-fidelity *in vitro* and *in silico* modeling to accurately predict human-specific proarrhythmic risk. Building from our existing engineered cardiac microtissue model [1], we tested concentration-responses across multiple orders of magnitude in individual microtissues (**Chapter 2**). This approach was further complemented with a robust suite of computational approaches including a detailed analysis of experimental requirements for robust point of departure analysis for accurately predicting potentially adverse concentrations in humans (**Chapter 3**). Additional *in silico* physiologically based pharmacokinetic modeling finalized the connection between *in vitro* effects and *in vivo* toxicity and enabled accurate prediction of human proarrhythmic risk from a range of hERG-inhibiting compounds [2] (**Chapter 2**). As well as confirming the ability of this model to perform accurate risk assessment, we also identified action potential triangulation (APD_{tri}) as a more sensitive metric for repolarization-related proarrhythmic risk compared to action potential duration, which to-date is more widely used. Together, this work illustrates the ability of hiPSC-CMs to form a central component for proarrhythmia assessment within the existing regulatory environment.

Building from our validated risk assessment model, Aim 2 demonstrated the ability of hiPSC-CMs to act as a screening platform for drug design and development by assessing toxicity and cardioprotection across a range of functional metrics (**Chapter 4**). We developed and leveraged a range of different assays, including those measuring viability; metabolism; reactive oxygen species generation; electrophysiology; and contractility and demonstrated the ability for hiPSC-CMs to capture diverse physiological endpoints. Moreover, the flexibility of hiPSC-CMs enabled us to investigate the cardioprotective effects of drugs with varied mechanisms of action in a target-agnostic manner from several classes of drugs that have been previously proposed to prevent anthracycline-induced cardiotoxicity (angiotensin-converting enzyme inhibitors, topoisomerase IIβ inhibitors, and carbonic anhydrase 12 inhibitors). We revealed a key role for hiPSC-CM maturation in enhancing doxorubicin induced toxicity in three-dimensional microtissues, which has also been shown to affect the cardioprotective capacity of the topoisomerase IIβ inhibitor dexrazoxane [3], further supporting the need for advanced culture techniques to maximize the relevance of hiPSC-CMs in model systems. Using this approach, we were able to partially confirm the hypothesized cardioprotective effects of indisulam [4], although treatment promoted rather than inhibited doxorubicin-induced glycolysis. In addition to pharmaceutical drug development, the ability of hiPSC-CMs to serve as phenotypic assays also makes them particularly well-suited for screening environmental chemicals due to their ability to simultaneously capture unrelated modes of toxicity (**Chapter 5**).

Finally, in Aim 3 we expanded into the realm of cardiac disease modeling by developing a novel patient-derived hiPSC line for precision model of the atrial arrhythmia Wolff-Parkinson-White Syndrome (WPW) (**Chapter 6**). Unlike previous models [5-8], we could examine WPW that is not caused by a mutation in *PRKAG2*, an approach that is only possible with patient-derived cell lines. Additionally, we utilized chamber-specific differentiation protocols to generate atrial cardiomyocytes, a critical aspect of modeling atrial arrhythmias like WPW but one that has not been performed in previous hiPSC-CM studies of WPW [5-7]. We were able to recapitulate key facets of WPW cardiac phenotypes in our hiPSC-CMs

including glycogen accumulation and cardiomyocyte hypertrophy and identified potentially proarrhythmic electrophysiological changes (*i.e.* increased spontaneity, longer action potentials, and shorter calcium durations) in atrial hiPSC-CMs that may be linked to the initiation of atrial fibrillation in WPW patients.

By highlighting the potential benefits of hiPSC-CM-based models across this diverse array of applications, we demonstrated their suitability as multi-purpose tools throughout drug development and their ability to play a critical role in the future of drug discovery.

7.2. Broader impacts

7.2.1. Context of use determines fit-for-purpose requirements

While we successfully leveraged hiPSC-CMs across multiple stages of drug development, the differences in requirements for each context of use emphasized the need for tailoring specific models to be fit-for-purpose [9-11]. For instance, high-fidelity risk assessment of lead compounds late in the drug development pipeline versus early hazard screening of thousands of chemicals have significantly different needs regarding physiological relevance, throughput, and cost [12]. Two-dimensional monolayers are readily compatible with a broad range of existing commercial assays and automated analysis systems, significantly increasing their simplicity and cost-effectiveness for screening applications [13, 14]. In contrast, three-dimensional engineered cardiac tissues better capture *in vivo* cardiac physiology while increasing complexity and reducing throughput [15, 16]. In risk assessment applications with high cost-benefit ratios, particularly when screening relatively few compounds, such models are more likely to be needed. These differences in requirements underpinned our diverging approaches between screening potentially cardioprotective compounds and proarrhythmic risk assessment, particularly because our three-dimensional microtissues were cultured for an additional week under electrical stimulation, which has been shown to improve tissue maturation [17-20].

Increasing the relative maturity of hiPSC-CMs is also critically important when mechanisms and endpoints of interest are absent in less mature cardiomyocytes. In the context of this work, topoisomerase II expression and dexrazoxane cardioprotection have been previously shown to be dependent on the relative maturity of hiPSC-CMs [3] and we demonstrated that doxorubicin-induced toxicity increased with metabolic maturation of cardiac microtissues. Similarly, validating that hiPSC-CMs capture disease-specific phenotypes, like glycogen accumulation and cardiac hypertrophy in the patient-specific WPW model, is imperative for ensuring that subsequently discovered mechanisms or therapeutics are truly reflective of what is observed *in vivo*. This is especially true for atrial arrhythmia like WPW, which are reliant on previously unavailable differentiation protocols to generate chamber-specific cardiomyocytes. Thus, our work provides additional support to the growing evidence and demand for context-specific, validated hiPSC-CM platforms for modeling cardiac toxicity and disease [11, 12].

7.2.2. Reproducibility in hiPSC-CM analysis

Even in validated systems, variation arising from either biological or technical sources can obscure the detection of physiologically relevant changes in endpoints. Previous work with hiPSC-CM-based platforms has focused on line-to-line variability due to donor-specific differences [21-23]. However, there is an increasing appreciation for the effects of other sources of variation, such as plate-to-plate variability, for influencing the ability of a study to detect changes in a parameter of interest [24]. Yet, sources of variation are typically only considered in isolation, limiting the utility of these analyses. We extended this work by developing a framework by which to leverage *in silico* modeling and *in vitro* data to examine the effects of multiple levels of technical and biological variation simultaneously in order to define experimental requirements (*e.g.* sample size and number of test concentrations) for risk assessment using hiPSC-CMs in engineered microtissues. Such techniques are of particular interest within a regulatory context for endpoints like delayed repolarization for which the relative magnitude of potentially adverse effects is well-defined [25-28]. Moreover, this approach is flexible for well-characterized systems and can be

adapted for other endpoints, applications, and sources of variability such that it can be adopted broadly across multiple contexts of use. Ultimately, confidence in alternative new approach methodologies that utilize hiPSC-CMs will be based on accounting for or minimizing such variability.

7.3. Future directions

Adoption of hiPSC-CM-based systems throughout preclinical drug development has already begun and is likely to grow as the challenges facing regulatory acceptance are addressed [29]. To assist in accelerating this process beyond the substantial work presented here, we have outlined immediate and long-term questions that follow directly from this dissertation.

7.3.1. Proarrhythmic risk assessment

Due to significant regulatory scrutiny, our model and other hiPSC-CM models of proarrhythmic risk focus on detecting delayed repolarization, particularly from inhibition of the hERG channel in ventricular cardiomyocytes [2, 30-33]. Moreover, most of the validation of these models occurs with a relatively small subset of compounds from the Comprehensive *in vitro* Proarrhtyhmia (CiPA) Initiative that are all known to inhibit hERG [34]. However, a number of other proarrhythmic mechanisms related to other forms of cardiac arrhythmias could benefit significantly from the use of hiPSC-CM-based models. For instance, the inhibition of voltage-gated sodium channels is known to significantly impair cardiac conduction and contribute to the formation of arrhythmias but are underexamined in cardiac preclinical assays [35]. Endpoints already available in our engineered microtissue model such as excitability, rise time, and stimulation delay are sensitive to sodium channel block and can be readily applied to this challenge. Additionally, specific assessments of drug-induced atrial arrhythmias like atrial fibrillation and supraventricular tachycardia, which are associated with exposure to a number of compounds [36, 37], are generally excluded from *in vitro* preclinical screening. Atrial engineered tissues [38-40], including our microtissue system [41], have demonstrated chamber specificity and offer an as-of-yet underexplored opportunity for preventing atrial toxicity.

7.3.2. Chemotherapy-induced cardiotoxicity

Anthracycline-induced cardiotoxicity has remained a major challenge in managing the long-term well-being of cancer patients [42]. We and others have successfully used hiPSC-CMs to model doxorubicin cardiotoxicity as well as screen cardioprotective therapies for its prevention [3, 4, 21, 43-45]. However, growing evidence that modulation of the metabolic axis and energy balance in cardiomyocytes offers an alternative to topoisomerase IIβ inhibition [4] which is associated with concerns of reducing the efficacy chemotherapy and increasing the risk of metastasis [46]. To effectively model doxorubicin-induced cardiotoxicity and cardiac metabolism more generally, maturation of hiPSC-CMs with novel media formulations or other approaches appears to be required and should be pursued rigorously to advance this work. Another important consideration is the effect of exposure parameters on the sensitivity of hiPSC-CMs to potentially cardioprotective effects [45]. While peak plasma concentrations of doxorubicin reach concentrations above 1 μM during chemotherapy, this only last for several hours and longer-term exposures are significantly lower [47-49]. Thus, models of chronic cardioprotection may need to rely on doxorubicin exposures that occur over even longer time periods to accurately mimic the effects of chronic, rather than acute, cardiotoxicity. Chemotherapy-induced cardiotoxicity is also not unique to anthracyclines [50, 51], and similar screening for preventative therapies should be investigated for a variety of other compounds as well.

7.3.3. Modeling non-*PRKAG2* WPW

Line-to-line variability between hiPSC-CMs has been known to contribute significantly to differences in baseline characteristics generally [23] and to WPW phenotype in close relatives with identical *PRKAG2* mutations [5]. While we have established an initial non-*PRKAG2* line and confirmed WPW phenotype *in vitro*, robust confirmation will require generation of additional control and WPW lines from the same family with non-*PRKAG2* WPW to minimize variability due to genetic differences not related to the primary disease mechanism. Identification of the underlying genetic mechanism for WPW in these patients would also substantially advance our understanding of the pathophysiology of WPW but would likely require less

targeted approaches such as whole genome or exome sequencing to identify variants of unknown significance, polygenic risk score, or other genes of interest. In addition to genetic approaches, molecular analysis of the activity and expression of AMPK and cardiac ion channels can be used to detect if non-*PRKAG2* WPW affects similar signaling pathways and identify the mechanisms for altered electrophysiology. Lastly, the initiation of atrial fibrillation in WPW is still poorly understood, but engineered cardiac models using patient-derived hiPSC-CMs provide ideal model systems for examining the roles of external factors such as biochemical and mechanical stress in inducing fibrillation.

7.3.4. Long-term directions

Tissue-engineered cardiac models must ultimately link underlying biology and stimulus to a relevant readout [9, 10]. This will occur across multiple fronts, most notably with continued efforts to mature hiPSC-CMs cultured *in vitro* such that they can replicate *in vivo* physiology as accurately as possible [19, 20, 52]. These innovations are already occurring throughout the field of cardiac tissue engineering, with common markers of cardiomyocyte maturation (*e.g.* sarcomere length, contractile stress, and conduction velocity) improving across published literature [53]. However, adult-like phenotypes remain elusive. Fortunately, complete maturity may not be necessary for many applications if context-specific endpoints and mechanisms are validated for a given model. Additional advances in the specificity of differentiation protocols, enabling precise differentiation of not only ventricular and atrial, but also pacemaker cells, left- and right-chamber specific cardiomyocytes, and other non-cardiomyocytes will enable modeling of an increasingly broad range of diseases [54-56]. Final fit-for-purpose requirements for hiPSC-CM applications will take shape as we move towards an equilibrium between academic research, industrial applications, and regulatory requirements.

7.4. Conclusions

This dissertation has advanced the development of fit-for-purpose hiPSC-CM-based models, particularly in engineered microtissues, with each aim illustrating a distinct context of preclinical drug

development and demonstrating the efficacy of hiPSC-CMs for proarrhythmic risk assessment, anthracycline-induced cardiotoxicity screening, and *in vitro* modeling of WPW. As these techniques are more widely adopted across academia, industry, and regulatory agencies, they will serve to provide efficient, *in vivo*-free and human-specific methods to continue to reduce reliance on animal models. Ultimately, tissue engineered models like these will enable accurate, precise, and human-centered development of next-generation medicines to improve human health.

7.5. References

1. Kofron, C., et al., *A Predictive in Vitro Risk Assessment Platform for Pro-Arrhythmic Toxicity Using Human 3D Cardiac Microtissues.* Scientific Reports, 2021. **11**: p. 1-16.
2. Daley, M., et al., *In vitro to in vivo extrapolation from three-dimensional hiPSC-derived cardiac microtissues and physiologically based pharmacokinetic modeling to inform next-generation arrhythmia risk assessment.* Toxicological Sciences, 2024: p. kfae079.
3. Cui, N., et al., *Doxorubicin-induced cardiotoxicity is maturation dependent due to the shift from topoisomerase IIα to IIβ in human stem cell derived cardiomyocytes.* Journal of Cellular and Molecular Medicine, 2019. **23**(7): p. 4627-4639.
4. Liu, C., et al., *CRISPRi/a screens in human iPSC-cardiomyocytes identify glycolytic activation as a druggable target for doxorubicin-induced cardiotoxicity.* Cell Stem Cell, 2024. **31**(12): p. 1760-1776. e9.
5. Zhan, Y., et al., *Establishment of a PRKAG2 cardiac syndrome disease model and mechanism study using human induced pluripotent stem cells.* Journal of molecular and cellular cardiology, 2018. **117**: p. 49-61.
6. Ben Jehuda, R., et al., *CRISPR correction of the PRKAG2 gene mutation in the patient's iPSC-derived cardiomyocytes eliminates the electrophysiological and structural abnormalities.* Heart Rhythm, 2018. **15**(2): p. 267-276.

7. Hinson, J.T., et al., *Integrative analysis of PRKAG2 cardiomyopathy iPS and microtissue models identifies AMPK as a regulator of metabolism, survival, and fibrosis.* Cell reports, 2016. **17**(12): p. 3292-3304.

8. Salt, I.P. and D.G. Hardie, *AMP-activated protein kinase: an ubiquitous signaling pathway with key roles in the cardiovascular system.* Circulation research, 2017. **120**(11): p. 1825-1841.

9. Moffat, J.G., et al., *Opportunities and challenges in phenotypic drug discovery: an industry perspective.* Nature reviews Drug discovery, 2017. **16**(8): p. 531-543.

10. Vincent, F., et al., *Developing predictive assays: the phenotypic screening "rule of 3".* Science translational medicine, 2015. **7**(293): p. 293ps15-293ps15.

11. Fischer, I., C. Milton, and H. Wallace, *Toxicity testing is evolving!* Toxicology Research, 2020. **9**(2): p. 67-80.

12. Daley, M.C., et al., *Beyond pharmaceuticals: Fit-for-purpose new approach methodologies for environmental cardiotoxicity testing.* ALTEX-Alternatives to animal experimentation, 2023. **40**(1): p. 103-116.

13. Takasuna, K., et al., *Comprehensive in vitro cardiac safety assessment using human stem cell technology: overview of CSAHi HEART initiative.* Journal of pharmacological and toxicological methods, 2017. **83**: p. 42-54.

14. Berg, E.L., Y.-C. Hsu, and J.A. Lee, *Consideration of the cellular microenvironment: physiologically relevant co-culture systems in drug discovery.* Advanced drug delivery reviews, 2014. **69**: p. 190-204.

15. Baker, B.M. and C.S. Chen, *Deconstructing the third dimension–how 3D culture microenvironments alter cellular cues.* Journal of cell science, 2012. **125**(13): p. 3015-3024.

16. Ahmed, R.E., et al., *A Brief Review of Current Maturation Methods for Human Induced Pluripotent Stem Cells-Derived Cardiomyocytes.* Frontiers in Cell and Developmental Biology, 2020. **8**(178): p. 178.

17. Feric, N.T., et al., *Engineered cardiac tissues generated in the Biowire II: a platform for human-based drug discovery.* Toxicological Sciences, 2019. **172**(1): p. 89-97.

18. Nunes, S.S., et al., *Biowire: a platform for maturation of human pluripotent stem cell–derived cardiomyocytes.* Nature methods, 2013. **10**(8): p. 781-787.

19. Scuderi, G.J. and J. Butcher, *Naturally engineered maturation of cardiomyocytes.* Frontiers in cell and developmental biology, 2017. **5**: p. 50.

20. Lu, Y., et al., *Advancements in techniques for human iPSC-derived cardiomyocytes maturation: mechanical and electrical stimulation approaches.* Biophysical Reviews, 2025: p. 1-15.

21. Burridge, P.W., et al., *Human induced pluripotent stem cell-derived cardiomyocytes recapitulate the predilection of breast cancer patients to doxorubicin-induced cardiotoxicity.* Nat Med, 2016. **22**(5): p. 547-56.

22. Blanchette, A.D., et al., *A tiered approach to population-based in vitro testing for cardiotoxicity: Balancing estimates of potency and variability.* Journal of Pharmacological and Toxicological Methods, 2022: p. 107154.

23. Mannhardt, I., et al., *Comparison of 10 control hPSC lines for drug screening in an engineered heart tissue format.* Stem cell reports, 2020. **15**(4): p. 983-998.

24. Gintant, G., et al., *Repolarization studies using human stem cell-derived cardiomyocytes: Validation studies and best practice recommendations.* Regulatory toxicology and pharmacology, 2020. **117**: p. 104756.

25. Darpo, B., *The thorough QT/QTc study 4 years after the implementation of the ICH E14 guidance.* British journal of pharmacology, 2010. **159**(1): p. 49-57.

26. ICH, *The clinical evaluation of QT/QTc interval prolongation and proarrhythmic potential for non-antiarrhythmic drugs E14*. 2006.

27. Stockbridge, N., et al., *Practice and challenges of thorough QT studies.* Journal of Electrocardiology, 2012. **45**(6): p. 582-587.

28. Lu, J., et al., *Assessing QT/QTc interval prolongation with concentration-QT modeling for Phase I studies: impact of computational platforms, model structures and confidence interval calculation methods.* J Pharmacokinet Pharmacodyn, 2018. **45**(3): p. 469-482.

29. Yang, X., et al., *Use of human iPSC-CMs in nonclinical regulatory studies for cardiac safety assessment.* Toxicological Sciences, 2022. **190**(2): p. 117-126.

30. Blinova, K., et al., *International multisite study of human-induced pluripotent stem cell-derived cardiomyocytes for drug proarrhythmic potential assessment.* Cell reports, 2018. **24**(13): p. 3582-3592.

31. Ando, H., et al., *A new paradigm for drug-induced torsadogenic risk assessment using human iPS cell-derived cardiomyocytes.* Journal of Pharmacological and Toxicological Methods, 2017. **84**: p. 111-127.

32. Blinova, K., et al., *Comprehensive translational assessment of human-induced pluripotent stem cell derived cardiomyocytes for evaluating drug-induced arrhythmias.* Toxicological Sciences, 2017. **155**(1): p. 234-247.

33. da Rocha, A.M., et al., *Detection of Drug-Induced Torsades de Pointes Arrhythmia Mechanisms Using hiPSC-CM Syncytial Monolayers in a High-Throughput Screening Voltage Sensitive Dye Assay.* Toxicological Sciences, 2020. **173**(2): p. 402-415.

34. Colatsky, T., et al., *The Comprehensive in Vitro Proarrhythmia Assay (CiPA) initiative - Update on progress.* J Pharmacol Toxicol Methods, 2016. **81**: p. 15-20.

35. Chaudhary, K.W., et al., *An overview of drug-induced sodium channel blockade and changes in cardiac conduction: Implications for drug safety.* Clinical and Translational Science, 2024. **17**(12): p. e70098.

36. Kaakeh, Y., et al., *Drug-induced atrial fibrillation.* Drugs, 2012. **72**: p. 1617-1630.

37. Chen, W., et al., *Drugs associated with a risk of supraventricular tachycardia: analysis using the OpenVigil database.* Journal of International Medical Research, 2024. **52**(3): p. 03000605241238993.

38. Devalla, H.D., et al., *Atrial-like cardiomyocytes from human pluripotent stem cells are a robust preclinical model for assessing atrial-selective pharmacology.* EMBO molecular medicine, 2015. **7**(4): p. 394-410.

39. Zhao, Y., et al., *A platform for generation of chamber-specific cardiac tissues and disease modeling.* Cell, 2019. **176**(4): p. 913-927. e18.

40. Zhao, Y., et al., *Towards chamber specific heart-on-a-chip for drug testing applications.* Advanced Drug Delivery Reviews, 2020. **165-166**: p. 60-76.

41. Soepriatna, A.H., et al., *Human Atrial Cardiac Microtissues for Chamber-Specific Arrhythmic Risk Assessment.* Cellular and Molecular Bioengineering, 2021. **14**(5): p. 441-457.

42. Mross, K., *New anthracycline derivatives: what for?* European Journal of Cancer and Clinical Oncology, 1991. **27**(12): p. 1542-1544.

43. Karhu, S.T., et al., *GATA4-targeted compound exhibits cardioprotective actions against doxorubicin-induced toxicity in vitro and in vivo: establishment of a chronic cardiotoxicity model using human iPSC-derived cardiomyocytes.* Archives of toxicology, 2020. **94**(6): p. 2113-2130.

44. Richards, D.J., et al., *Human cardiac organoids for the modelling of myocardial infarction and drug cardiotoxicity.* Nature Biomedical Engineering, 2020. **4**(4): p. 446-462.

45. Verheijen, M., et al., *Bringing in vitro analysis closer to in vivo: Studying doxorubicin toxicity and associated mechanisms in 3D human microtissues with PBPK-based dose modelling.* Toxicology letters, 2018. **294**: p. 184-192.

46. Zheng, H. and H. Zhan, *Preventing Anthracycline-Associated Heart Failure: What Is the Role of Dexrazoxane?* JACC: CardioOncology, 2024. **6**(2): p. 318-321.

47. Mross, K., et al., *Pharmacokinetics and metabolism of epidoxorubicin and doxorubicin in humans.* Journal of Clinical Oncology, 1988. **6**(3): p. 517-526.

48. Gustafson, D.L., et al., *Doxorubicin pharmacokinetics: Macromolecule binding, metabolism, and excretion in the context of a physiologic model.* Journal of pharmaceutical sciences, 2002. **91**(6): p. 1488-1501.

49. Lai, C., et al., *Doxorubicin pharmacokinetics and toxicity in patients with aggressive lymphoma and hepatic impairment.* Blood Advances, 2023. **7**(4): p. 529-532.

50. Patnaik, J.L., et al., *Cardiovascular disease competes with breast cancer as the leading cause of death for older females diagnosed with breast cancer: a retrospective cohort study.* Breast Cancer Research, 2011. **13**: p. 1-9.

51. Lenneman, C.G. and D.B. Sawyer, *Cardio-oncology: an update on cardiotoxicity of cancer-related treatment.* Circulation research, 2016. **118**(6): p. 1008-1020.

52. Robertson, C., D.D. Tran, and S.C. George, *Concise review: maturation phases of human pluripotent stem cell-derived cardiomyocytes.* Stem cells, 2013. **31**(5): p. 829-837.

53. Ewoldt, J.K., et al., *Induced pluripotent stem cell-derived cardiomyocyte in vitro models: benchmarking progress and ongoing challenges.* Nature Methods, 2025. **22**(1): p. 24-40.

54. Torre, E., et al., *State-of-the-Art Differentiation Protocols for Patient-Derived Cardiac Pacemaker Cells.* International Journal of Molecular Sciences, 2024. **25**(6): p. 3387.

55. Lyra-Leite, D.M., et al., *A review of protocols for human iPSC culture, cardiac differentiation, subtype-specification, maturation, and direct reprogramming.* STAR protocols, 2022. **3**(3): p. 101560.

56. Zhang, H., et al., *Retinoic acid modulation guides human-induced pluripotent stem cell differentiation towards left or right ventricle-like cardiomyocytes.* Stem Cell Research & Therapy, 2024. **15**(1): p. 184.

A. Appendix A – Supplemental Material for Chapter 2

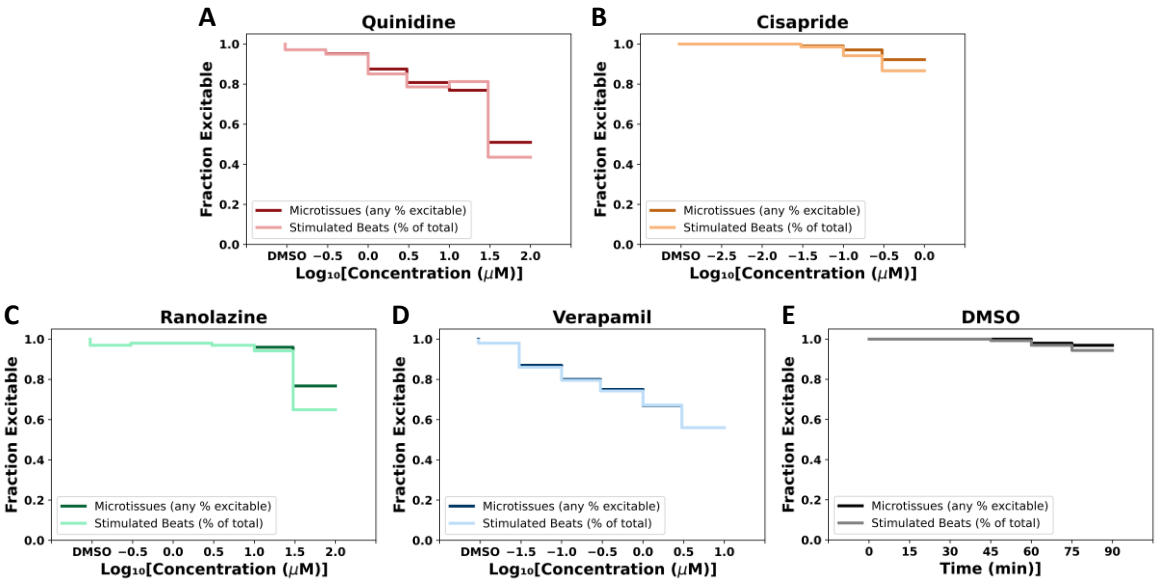

Supplemental Figure A.1 Survival curve of engineered human cardiac microtissues excitability across time and concentration. Microtissue excitability was recorded after sequential exposure to (A) quinidine, (B) cisapride, (C) ranolazine, (D) verapamil for 15 minutes at the indicated concentrations during optical mapping. (E) Time-matched vehicle controls (0.1% DMSO) were also obtained to separate the effects of exposure time and drug treatment. Darker lines indicate excitability as the fraction of microtissues with at least one detected beat. Lighter lines indicate the fraction of detected beats of the total stimulated (4 per microtissue per recording). Data represent n = 97-104 microtissues across 3 molds and 2-3 differentiations per compound.

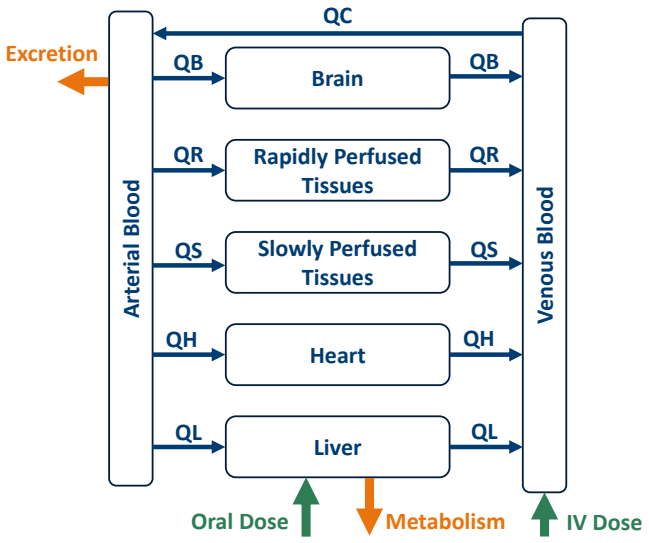

Supplemental Figure A.2. Structure of the generic physiologically based pharmacokinetic (PBPK) model. QL, QH, QS, QR, QB refer to blood flow to each tissue compartment. QC refers to the cardiac output. All tissues are described as flow limited.

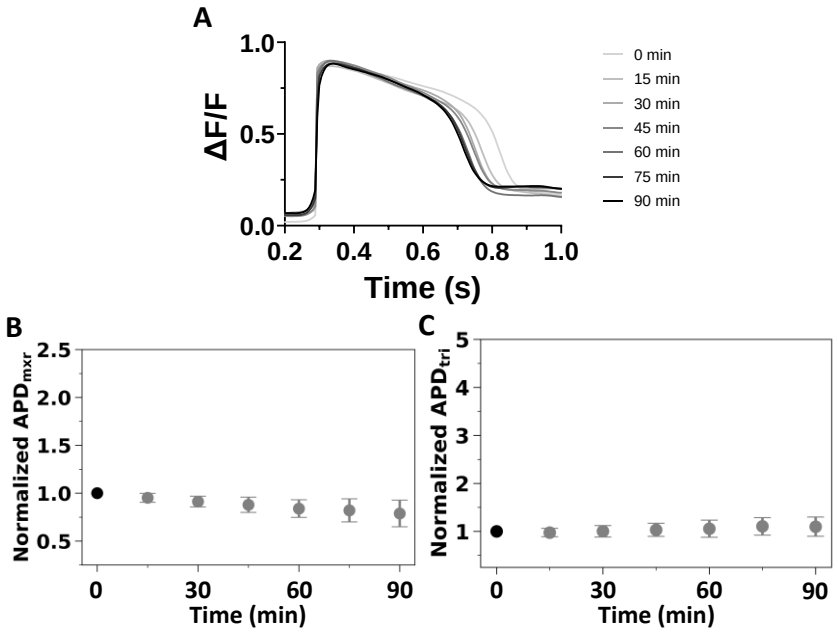

Supplemental Figure A.3. Time-dependent action potential responses of engineered human cardiac microtissues. (A) Representative action potential traces of microtissues exposed to 0.1% DMSO recorded at 15-minute intervals. (B) Action potential duration to maximum rate of repolarization (APD_{mxr}) and (C) action potential triangulation (APD_{tri}) were quantified for each microtissue and normalized to their respective baseline control prior to DMSO exposure. The left-most point (black) indicates the pre-treatment control with a normalized value of one. Data are represented as mean ± standard deviation for n = 94 microtissues across 3 molds and 3 differentiations.

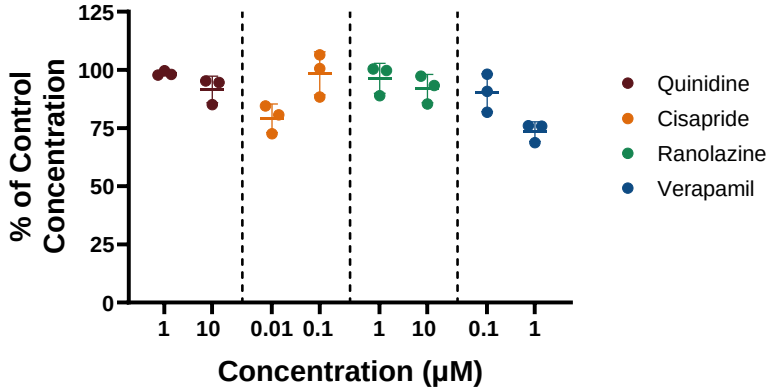

Supplemental Figure A.4. *In vitro* kinetics. The relative free concentration of each test compound was measured with high-performance liquid chromatography tandem mass spectrometry (Alera Labs, LLC) after perfusion through the optical mapping setup containing microtissue-free agarose molds. Data are represented as mean ± standard deviation with individual datapoints marked by circles (n = 3 per concentration). The average relative free concentrations across both tested concentrations was used to adjust the point of departure subsequent risk assessment.

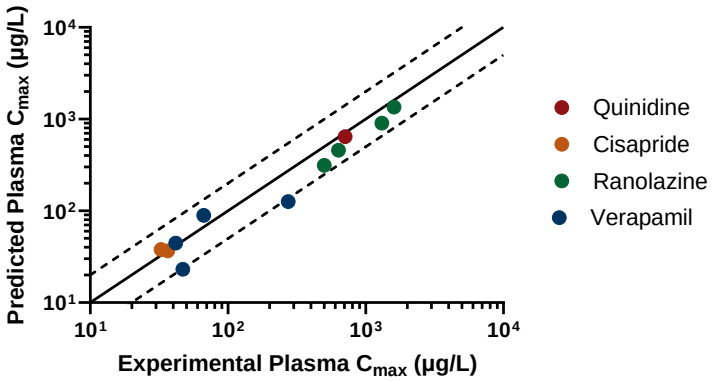

Supplemental Figure A.5. Validation of PBPK model performance versus previously published *in* vivo pharmacokinetic data. Mean PBPK model predictions of peak plasma concentration (C_{max}) are shown against experimentally measured counterpart for each *in vivo* study examined (Supplementary Table 3). Predictions are shown to be in good agreement with empirical data, falling within a two-fold difference (dashed lines). The additional solid line represents the ideal case where predicted values equal experimental observations.

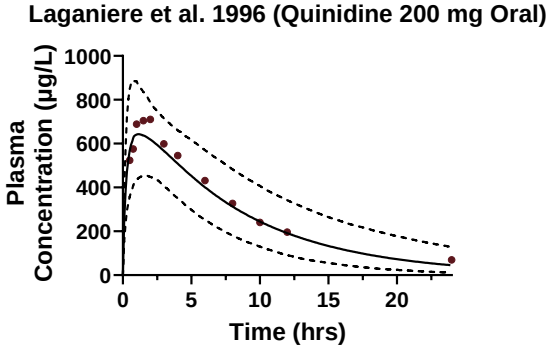

Supplemental Figure A.6. Model simulated versus observed quinidine plasma concentration profiles in human adults receiving a single bolus oral dose. Symbols represent the compound concentration measured in individuals, whereas lines represent model simulations of compounds plasma concentrations. The solid line represents mean plasma concentration-time profiles, whereas the dashed lines represent the 5th and 95th percentiles for the predicted values.

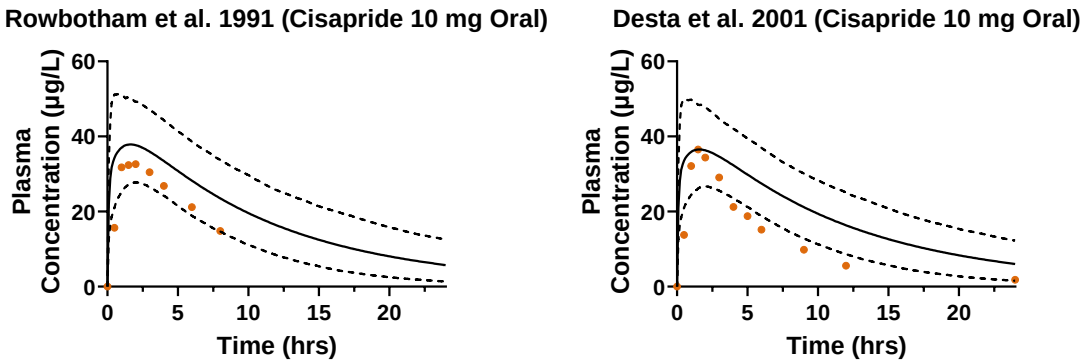

Supplemental Figure A.7. Model simulated versus observed cisapride plasma concentration profiles in human adults receiving a single bolus oral dose. Symbols represent the compound concentration measured in individuals, whereas lines represent model simulations of compounds plasma concentrations. The solid line represents mean plasma concentration-time profiles, whereas the dashed lines represent the 5th and 95th percentiles for the predicted values.

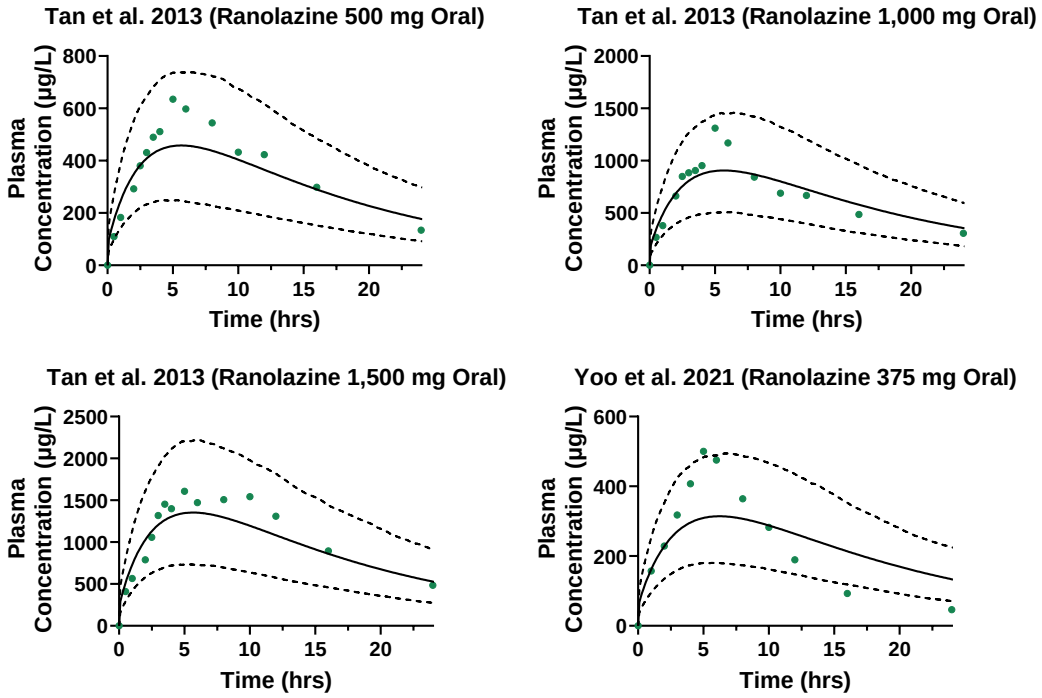

Supplemental Figure A.8. Model simulated versus observed ranolazine plasma concentration profiles in human adults receiving an IV dose or a single bolus oral dose. Symbols represent the compound concentration measured in individuals, whereas lines represent model simulations of compounds plasma concentrations. The solid line represents mean plasma concentration-time profiles, whereas the dashed lines represent the 5th and 95th percentiles for the predicted values.

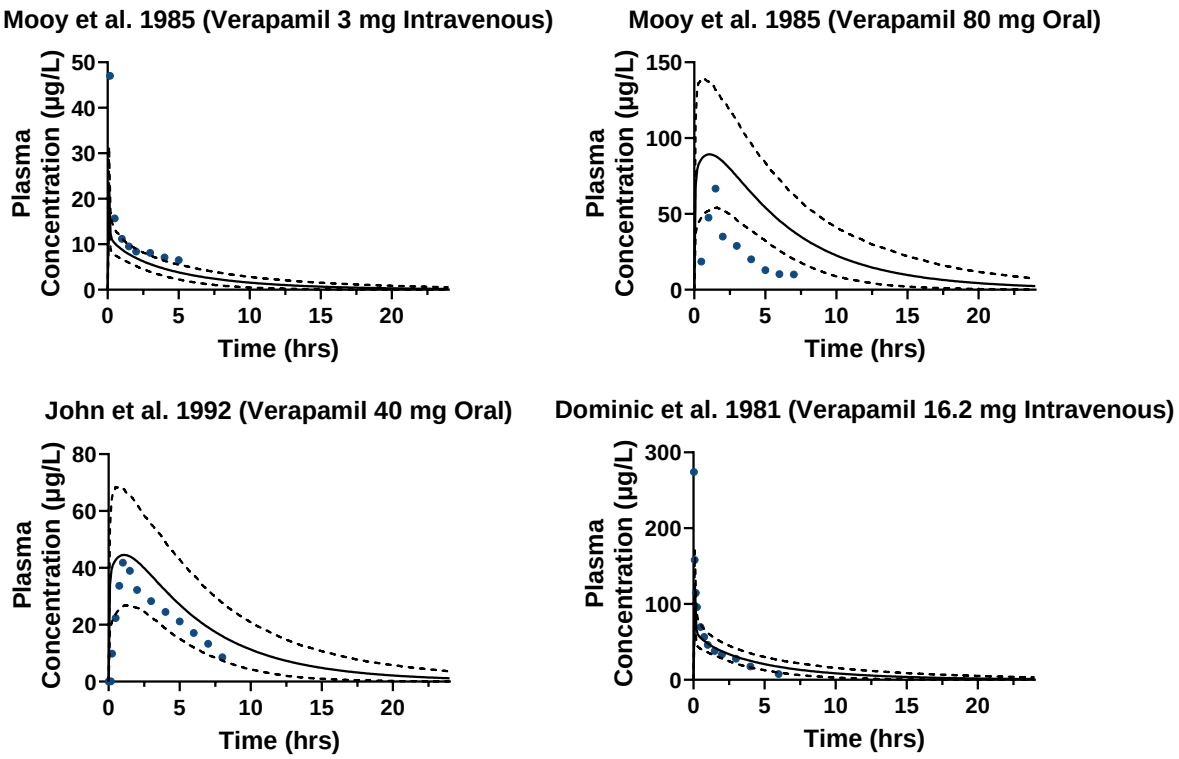

Supplemental Figure A.9. Model simulated versus observed verapamil plasma concentration profiles in human adults receiving an IV dose or a single bolus oral dose. Symbols represent the compound concentration measured in individuals, whereas lines represent model simulations of compounds plasma concentrations. The solid line represents mean plasma concentration-time profiles, whereas the dashed lines represent the 5th and 95th percentiles for the predicted values.

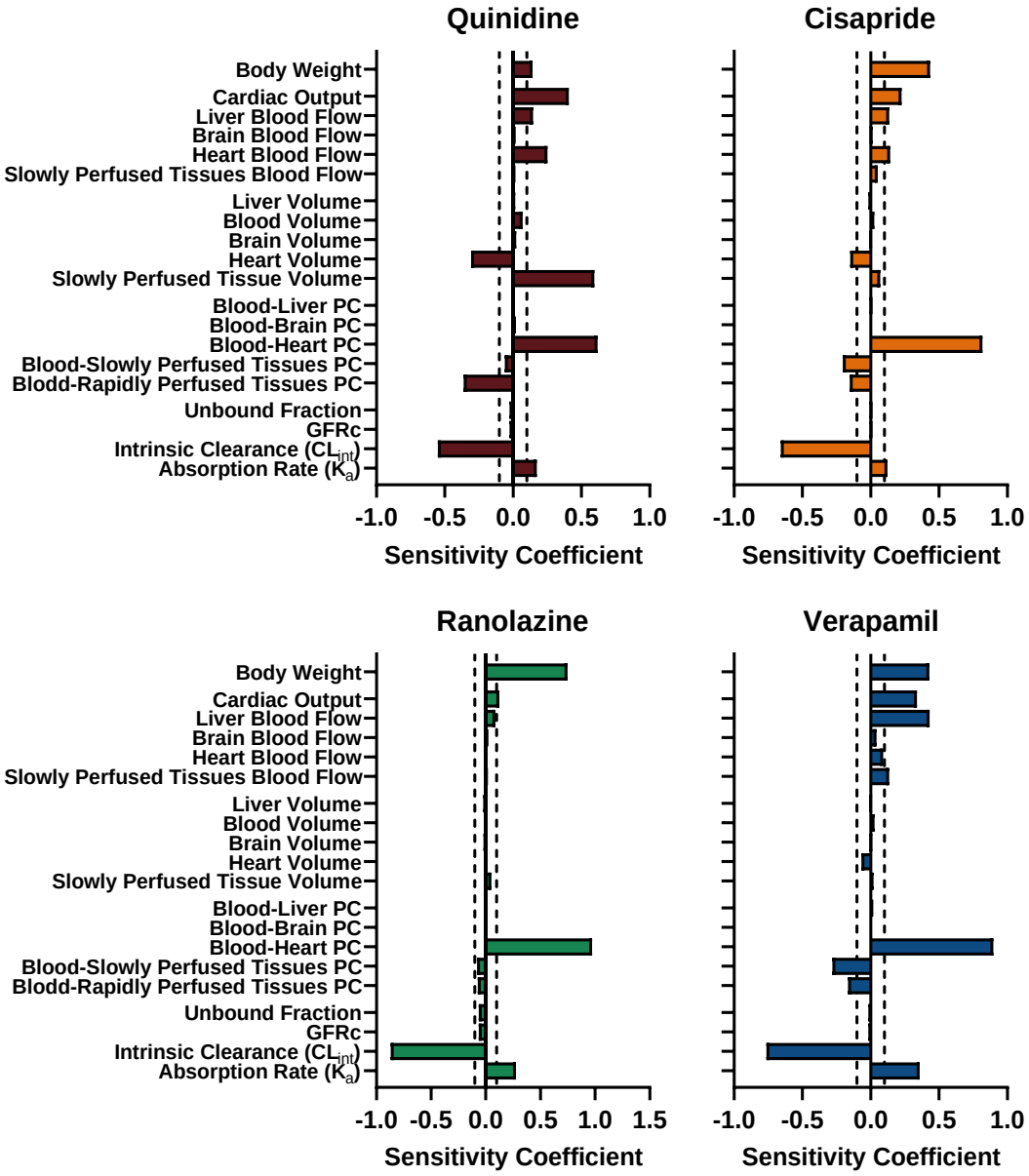

Supplemental Figure A.10. Sensitivity analysis. Model parameters (y-axis) and their associated absolute sensitivity coefficient (SC) (x-axis) are given grouped by parameter category (body weight, blood flows, volumes, partition coefficients (PCs), and metabolism) from top to bottom. The larger the absolute value of the SC, the more important the parameter. A normalized SC of 1 represents that a 1% change in the parameter results in a 1% change in the internal dose metric of choice. A negative SC indicates the given parameter influences the dose metric in an inverse direction. Models were considered sensitive to a parameter if the magnitude of the SC was greater than 0.1 (dashed lines).

Supplemental Table A.1. Physiological parameters used for the human generic physiologically based pharmacokinetic (PBPK) model.

Parameters Name	Parameters Description	Human values	Units	Source
BW[a]	Body Weight	81.2	kg	Study specific
QC	Cardiac Output	423.37	L/h	[1]
QLc	Blood flow to the liver	0.215	Fraction of cardiac output	[1]
QBc	Blood flow to the brain	0.1155	Fraction of cardiac output	[1]
QHc	Blood flow to the heart	0.04	Fraction of cardiac output	[1]
QSc	Blood flow to the slowly perfused tissues	0.4065	Fraction of cardiac output	[1]
VLc	Liver volume	0.0197	Fraction of body weight	[1]
VVc	Blood volume	0.0569	Fraction of body weight	[1]
VBc	Brain volume	0.017	Fraction of body weight	[1]
VHc	Heart volume	0.05	Fraction of body weight	[1]
VSc	Slowly perfused tissues volume	0.4531	Fraction of body weight	[1]
VolUc	Volume of urine	22	ml/kg/day	[2]
GFRc	Glomerular filtration rate	1.8	ml/min/kg body weight	[3]

[a]The body weights varied depending on the in vivo studies used to parametrize and validate the model. A body weight of 81.2 kg was used for any other simulations.

[b]A total fractional volume of 0.85 based on the assumption of 85% perfused volume [4]. The rest of the body (15%) is assumed to be non-perfused tissues (bone, hair, etc.).

[*]All the fraction of tissues weight to blood volume and fraction of total plasma flow to tissues are used in the code to calculate tissues volumes and blood flows that are finally used in the main code.

Supplemental Table A.2. Physicochemical parameters used for the generic human physiologically based pharmacokinetic (PBPK) model.

Parameters Name	Parameters Description	Quinidine	Cisapride	Ranolazine	Verapamil	Units	Source
MW	Molecular weight	324.424	465.95	427.54	454.61	g/mol	PubChem
Log P	Partition coefficient	3.44	3.3	2.07	3.79	-	PubChem
pKa	Dissociation constant	8.56	8.24	2.2	8.92	-	PubChem
RBP	Ratio blood/plasma	0.88	0.64	0.64	0.85	-	DrugBank
Fup	Unbound fraction in plasma	0.2	0.04	0.38	0.1		EPA dashboard
PL	Liver-blood partition coefficient	5.67	4.78	2.76	5.4	-	QSAR model[a]
PB	Brain-blood partition coefficient	2.73	1.7[b]	0.3[c]	0.15[d]	-	QSAR model[a]
PH	Heart-blood partition coefficient	11.1	6[b]	3[c]	2.11[d]	-	QSAR model[a]
PS	Slowly perfused tissues-blood partition coefficient	0.6	2.95	1.8	3.31	-	QSAR model[a]
PR	Rapidly perfused tissues-blood partition coefficient	5.67	4.78	2.76	5.4	-	Same as liver
CL_{int}	Intrinsic clearance	32.76[g]	31.38[e]	72.87[h]	144.17[f]	L/h	Based on *in vivo* data
Ka	Oral absorption rate	0.6	0.8	0.065	0.7	/h	Fitted

[a]Partition coefficients were predicted using the algorithm from Poulin and Theil (2012).
[b]Fitted to [5]
[c][6]
[d][7]
[e]CL_{int} was derived from the total clearance from FDA (23.62 L/h).
[f]An average of the total clearance from [8] (41.1 L/h), [9] (63.6 L/h), and the CL_{int} in vitro (12.7 µL/min/10^6 hepatocytes) from the EPA dashboard was calculated and used in the PBPK model.
[g]An average of the total clearance from [10] (18.85 L/h), [11] (28.86 L/h), [12] (29.025 L/h), [13] (36.94 L/h), and the CL_{int} *in vitro* from the EPA dashboard was calculated and used in the PBPK model.
[h]CL_{int} was derived from the total clearance from [14] (43.6 L/h).

Supplemental Table A.3. *In vivo* studies used to parameterize and validate the physiologically based pharmacokinetic (PBPK) model.

Compound	Dose (mg)	Body Weight (Kg)	Dose (mg/kg)	Dose Type	Dose Timing	Reference
Quinidine	200	75	2.667	Oral	Bolus dose	[12]
Cisapride	10	81.21	0.123	Oral	Bolus dose	[15]
Cisapride	10	76.6	0.131	Oral	Bolus dose	[16]
Ranolazine	500	61.3	8.157	Oral	Bolus dose	[14]
Ranolazine	1000	61.3	16.313	Oral	Bolus dose	[14]
Ranolazine	1500	61.3	24.470	Oral	Bolus dose	[14]
Ranolazine	375	73.45	5.106	Oral	Bolus dose	[17]
Verapamil	40	81.21	0.493	Oral	Bolus dose	[18]
Verapamil	80	81.21	0.985	Oral	Bolus dose	[8]
Verapamil	3	81.21	0.037	IV	5-minute infusion	[8]
Verapamil	-	81.21	0.2	IV	5-minute infusion	[9]

Supplemental Table A.4. Supplementary Table 4. Comparison of maximal plasma and heart concentrations (C_{max}) predicted by the *in silico* physiologically based pharmacokinetic model. Plasma and heart C_{max} were measured after the model reached steady state from a daily oral bolus dose at either the lowest or highest therapeutic dose for each compound.

Compound	Dose (mg; low-high)	Plasma C_{max} after oral exposure to therapeutic dose (μM; low-high)	Heart C_{max} after oral exposure to therapeutic dose (μM; low-high)
Quinidine	100-325	0.90-2.94	7.22-23.48
Cisapride	5-20	0.029-0.11	0.15-0.60
Ranolazine	375-1000	0.63-1.69	1.88-5.01
Verapamil	40-360	0.08-0.73	0.16-1.46

Supplemental Table A.5. Comparison of literature and *in vitro* point of departure (POD) plasma concentrations. *In vitro* binding-adjusted PODs for each compound and metric were converted to a total plasma concentration based on the plasma-to-heart concentration ratio at steady state (**Table 2.2**, **Supplemental Table A.4**). Previously reported total plasma concentrations that resulted in 20 ms increases in QTc in human patients were used as a comparison because they are akin to the 5% threshold used in this study when assuming a 400 ms QTc at baseline. If significant changes in QTc were not observed, the highest plasma concentration is reported instead.

Compound	Metric	Predicted Plasma Concentration at PoD (μM)	Literature Plasma Concentration (μM)	Reference(s)
Quinidine	APD_{mxr}	2.43-2.84	2.0[a] 1.2[a] 0.56-2.3[b] 1.35-1.70[a] 0.85-1.54[a] 0.29[a] 0.48[a]	[19] [20, 21] [22, 23] [11] [13] [24] [10]
	APD_{tri}	0.77-0.97		
Cisapride	APD_{mxr}	0.035-0.048	0.084-0.28[a] 0.185[a]	[25] [26]
	APD_{tri}	0.0064-0.014		
Ranolazine	APD_{mxr}	7.55-8.55	8.58[a] 19.4[a] 18.0[a]	[20, 21] [27] [28]
	APD_{tri}	0.92-2.27		
Verapamil	APD_{mxr}	0.025-0.05	>0.44[c] >0.35[c]	[20, 21] [29]
	APD_{tri}	0.25-0.40		

[a]Estimated as the plasma concentration that would result in a 20 ms (~5%) increase in QTc in human patients.
[b]Directly reported concentration for 10-20% increase in QTc.
[c]No significant change in QTc. Highest examined *in vivo* plasma concentration given.

References

1. Brown, R.P., et al., *Physiological parameter values for physiologically based pharmacokinetic models.* Toxicology and industrial health, 1997. **13**(4): p. 407-484.
2. Valentin, J., *Basic anatomical and physiological data for use in radiological protection: reference values: ICRP Publication 89.* Annals of the ICRP, 2002. **32**(3-4): p. 1-277.
3. Lin, J.H., *Applications and limitations of interspecies scaling and in vitro extrapolation in pharmacokinetics.* Drug metabolism and disposition, 1998. **26**(12): p. 1202-1212.
4. Clewell, H.J., et al., *Evaluation of the potential impact of age-and gender-specific pharmacokinetic differences on tissue dosimetry.* Toxicological Sciences, 2004. **79**(2): p. 381-393.
5. Michiels, M., et al., *Pharmacokinetics and tissue distribution of the new gastrokinetic agent cisapride in rat, rabbit and dog.* Arzneimittel-forschung, 1987. **37**(10): p. 1159-1167.
6. Liu, X., et al., *Gender difference in ranolazine pharmacokinetics in rats.* European journal of drug metabolism and pharmacokinetics, 2003. **28**: p. 119-123.
7. Todd, E.L. and D.R. Abernethy, *Physiological pharmacokinetics and pharmacodynamics of (±)-verapamil in female rats.* Biopharmaceutics & drug disposition, 1987. **8**(3): p. 285-297.
8. Mooy, J., et al., *Pharmacokinetics of verapamil in patients with renal failure.* European journal of clinical pharmacology, 1985. **28**: p. 405-410.
9. Dominic, J.A., et al., *The pharmacology of verapamil. III. Pharmacokinetics in normal subjects after intravenous drug administration.* Journal of cardiovascular pharmacology, 1981. **3**(1): p. 25-38.
10. Shin, J.G., et al., *Possible interethnic differences in quinidine-induced QT prolongation between healthy Caucasian and Korean subjects.* British journal of clinical pharmacology, 2007. **63**(2): p. 206-215.
11. El-Eraky, H. and S.H. Thomas, *Effects of sex on the pharmacokinetic and pharmacodynamic properties of quinidine.* British journal of clinical pharmacology, 2003. **56**(2): p. 198-204.

12. Laganière, S., et al., *Pharmacokinetic and pharmacodynamic interactions between diltiazem and quinidine.* Clinical Pharmacology & Therapeutics, 1996. **60**(3): p. 255-264.

13. Wooding-Scott, R., et al., *The pharmacokinetics and pharmacodynamics of quinidine and 3-hydroxyquinidine.* British journal of clinical pharmacology, 1988. **26**(4): p. 415-421.

14. Tan, Q.-Y., et al., *Tolerability and pharmacokinetics of ranolazine following single and multiple sustained-release doses in Chinese healthy adult volunteers: a randomized, open-label, Latin square design, phase I study.* American Journal of Cardiovascular Drugs, 2013. **13**: p. 17-25.

15. Desta, Z., et al., *Stereoselective pharmacokinetics of cisapride in healthy volunteers and the effect of repeated administration of grapefruit juice.* British journal of clinical pharmacology, 2001. **52**(4): p. 399-407.

16. Rowbotham, D., K. Milligan, and P. McHugh, *Effect of single doses of cisapride and ranitidine administered simultaneously on plasma concentrations of cisapride and ranitidine.* BJA: British Journal of Anaesthesia, 1991. **67**(3): p. 302-305.

17. Yoo, H., et al., *Pharmacokinetics and Safety of Extended-release Ranolazine in Korean and White Healthy Subjects.* Clinical Therapeutics, 2021. **43**(3): p. 526-534. e4.

18. John, D.N., et al., *Pharmacokinetics and pharmacodynamics of verapamil following sublingual and oral administration to healthy volunteers.* British journal of clinical pharmacology, 1992. **33**(6): p. 623-627.

19. Holford, N., et al., *The effect of quinidine and its metabolites on the electrocardiogram and systolic time intervals: concentration-effect relationships.* British journal of clinical pharmacology, 1981. **11**(2): p. 187-195.

20. Johannesen, L., et al., *Differentiating drug-induced multichannel block on the electrocardiogram: randomized study of dofetilide, quinidine, ranolazine, and verapamil.* Clinical Pharmacology & Therapeutics, 2014. **96**(5): p. 549-558.

21. Vicente, J., et al., *Comprehensive T wave morphology assessment in a randomized clinical study of dofetilide, quinidine, ranolazine, and verapamil.* Journal of the American Heart Association, 2015. **4**(4): p. e001615.

22. Redfern, W.S., et al., *Relationships between preclinical cardiac electrophysiology, clinical QT interval prolongation and torsade de pointes for a broad range of drugs: evidence for a provisional safety margin in drug development.* Cardiovascular Research, 2003. **58**(1): p. 32-45.

23. Darbar, D., et al., *Sympathetic activation enhances QT prolongation by quinidine.* Journal of Cardiovascular Electrophysiology, 2001. **12**(1): p. 9-14.

24. Karbwang, J., et al., *A comparison of the pharmacokinetic and pharmacodynamic properties of quinine and quinidine in healthy Thai males.* British journal of clinical pharmacology, 1993. **35**(3): p. 265.

25. Cools, F., et al., *A comparison of the pharmacokinetics of two dosing regimens of cisapride and their effects on corrected QT interval in premature infants.* European journal of clinical pharmacology, 2003. **59**: p. 17-22.

26. van Haarst, A.D., et al., *The influence of cisapride and clarithromycin on QT intervals in healthy volunteers.* Clinical Pharmacology & Therapeutics, 1998. **64**(5): p. 542-546.

27. Chaitman, B.R., *Efficacy and safety of a metabolic modulator drug in chronic stable angina: review of evidence from clinical trials.* Journal of cardiovascular pharmacology and therapeutics, 2004. **9**(1_suppl): p. S47-S64.

28. NLM, *DailyMed*. 2005, U.S. National Library of Medicine: Bethesda, MD.

29. Holtzman, J.L., et al., *The pharmacodynamic and pharmacokinetic interaction between single doses of flecainide acetate and verapamil: effects on cardiac function and drug clearance.* Clinical Pharmacology & Therapeutics, 1989. **46**(1): p. 26-32.

B. Appendix B Supplemental Material for Chapter 3

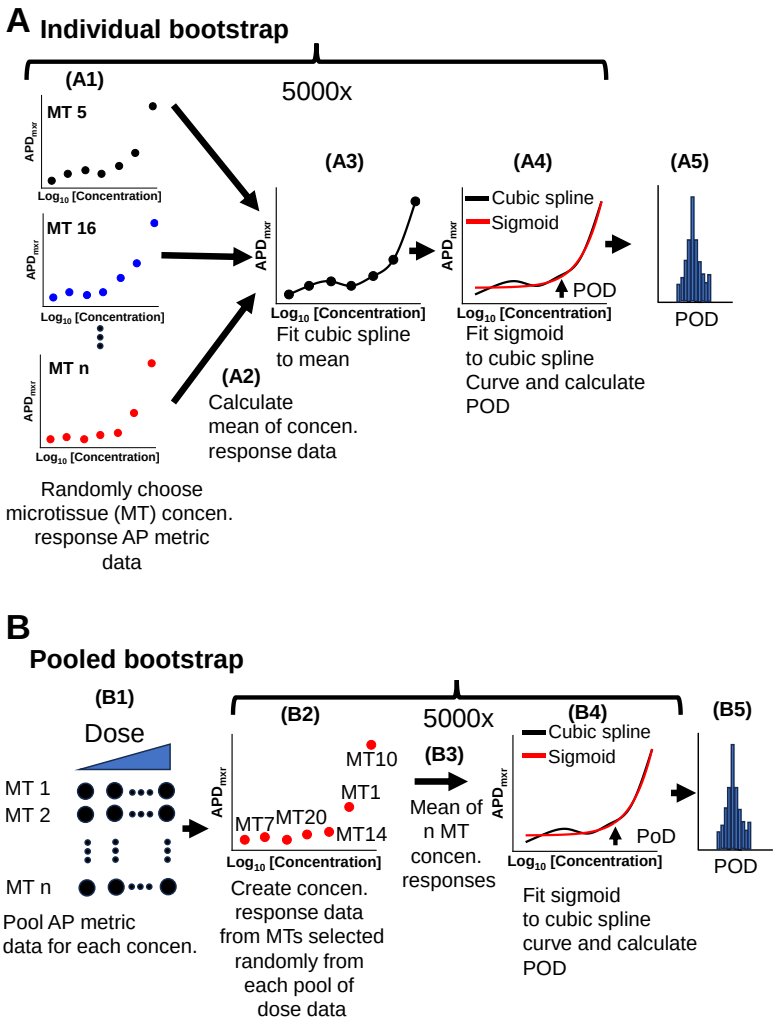

Supplemental Figure B.1. Sample procedure using bootstrapping to calculate confidence intervals for PODs from APD_{mxr} using logistic regression. (A) Individual microtissue bootstrap resampling with replacement: randomly selects the complete AP metric data (APD_{mxr} or APD_{tri}) from each microtissue (**A1**, all concentrations) and then calculates a mean concentration response curve from the randomly chosen microtissues (**A2**). For logistic regression and maximum curvature methods, a cubic spline is fit to this mean response curve (**A3**) and then the fit data are used to apply the respective POD calculation method (**A4**). The bilinear regression is fit to the concentration data directly. The POD distributions (**A5**) were created from the resampled data set (N=5000 repeats) and the 5^{th} and 95^{th} percentiles of this distribution represent the boundaries of the two-tailed 90% confidence interval for the estimated mean POD. **(B)** Pooled bootstrap resampling with replacement: the AP metric data are pooled for each compound concentration (**B1**) and from these pools, a concentration response curve is created by random selection of microtissue data (**B2**) (each curve contains different microtissues at each concentration) and then the mean concentration response curve (**B3**) is fit as in the individual bootstrapping (**B4-B5**).

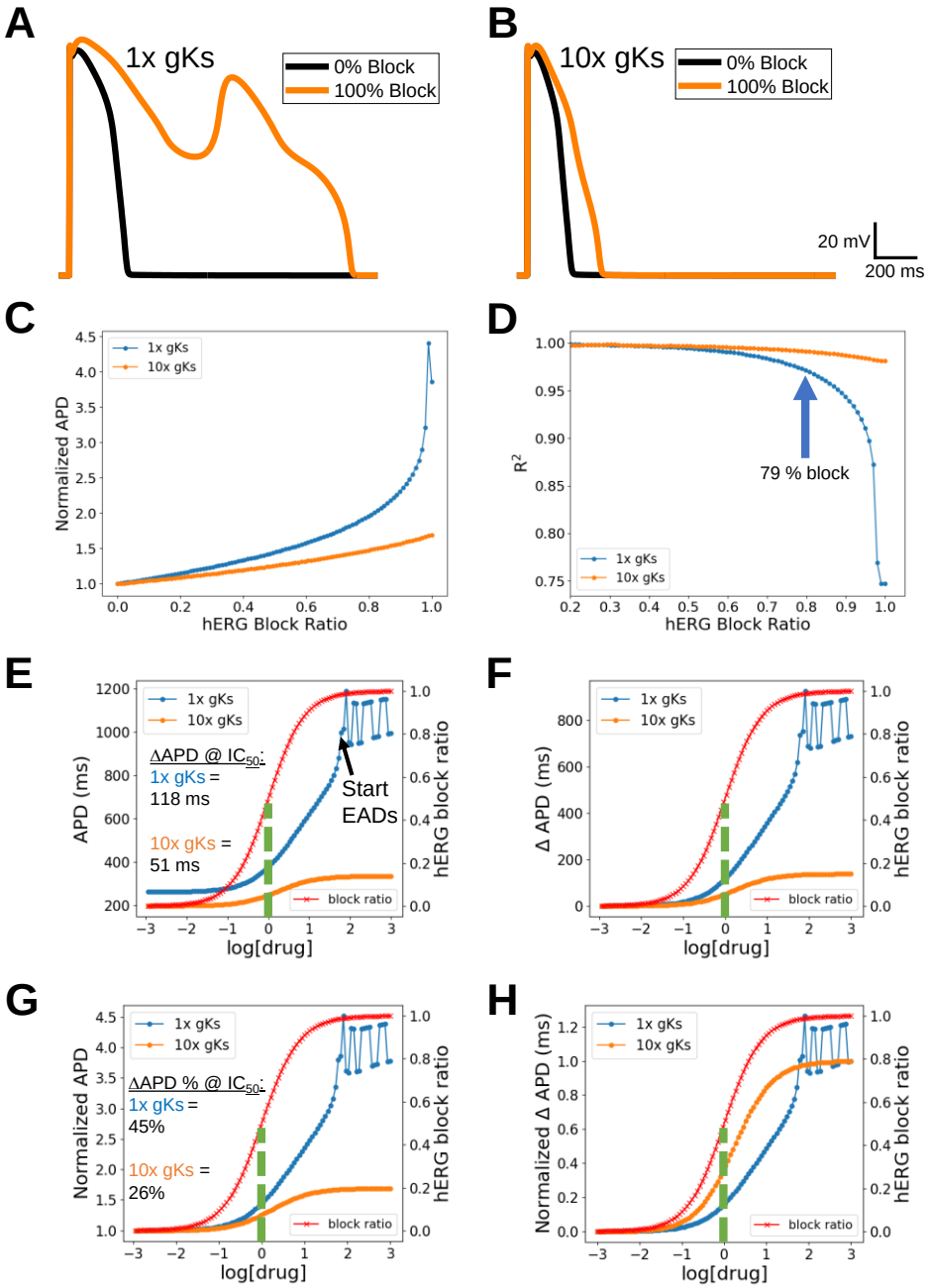

Supplemental Figure B.2. APD prolongation due to hERG block only in original O'Hara Rudy human action potential model is linear to 100% block with no EADs. (A) Sample simulation traces from the O'Hara et al. human action potential model [1] at different percentages of hERG block with a gKs of 0.00476 mS/µF (1x) which triggered early after depolarizations (EADs) with 90 – 100% block of hERG. (B) Sample simulation traces as in (A) with 10x gKs (0.0476 mS/µF) for no EADs. (C) Plot of normalized APD vs. linear hERG block ratio showing non-linear behavior of APD above 50% hERG block. (D) Plot of R^2 vs. linear hERG block ratio. R^2 drops below 0.95 after 79% block for data with EADs (1x gKs). (E) Plot of absolute APD values vs. log drug concentration (IC_{50} of 1 µM, dashed green line) and right y-axis hERG block ratio vs. log drug concentration. (F – G) Same plots as (E) for ΔAPD, Normalized APD, and Normalized ΔAPD.

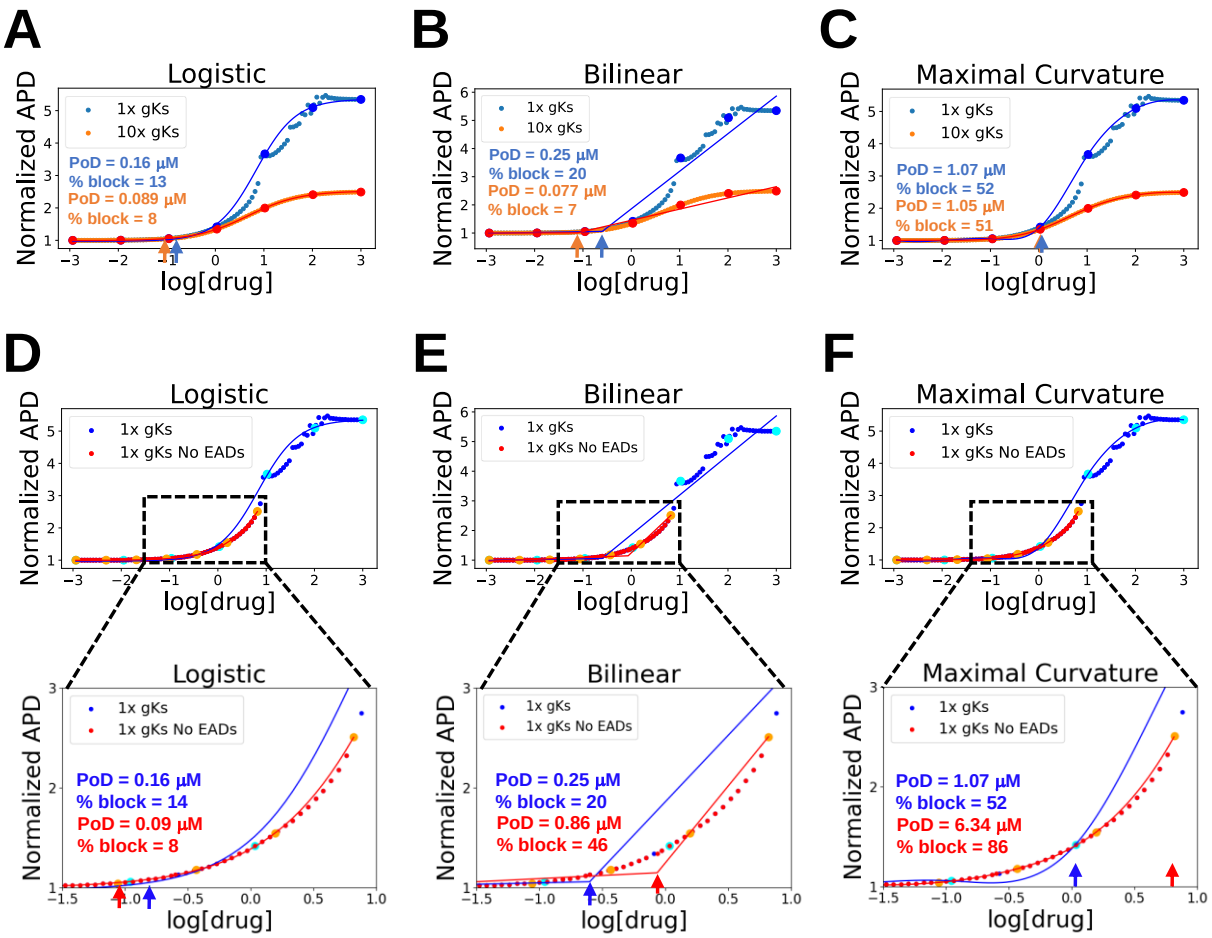

Supplemental Figure B.3. POD calculations from reduced sample simulation data. (A) POD values for reduced sample data sets (7 sample) from the computer simulation with and without EADs calculating POD using logistic regression with threshold set to a 5% change in APD from baseline (0% block). Blue (1x gKs) and orange (10x gKs) arrows indicate the position of POD on graph. (B) POD values from bilinear regression of reduced sample data (C) POD values from maximum curvature POD calculation method. (D – F) Plots and fitting as in A – C comparing POD calculation methods for full 1x gKs APD data (blue symbols) to 1x gKs APD data with EAD region removed (red symbols). Expanded plots show details of curve fitting and that removing EADs improves fitting for logistic regression.

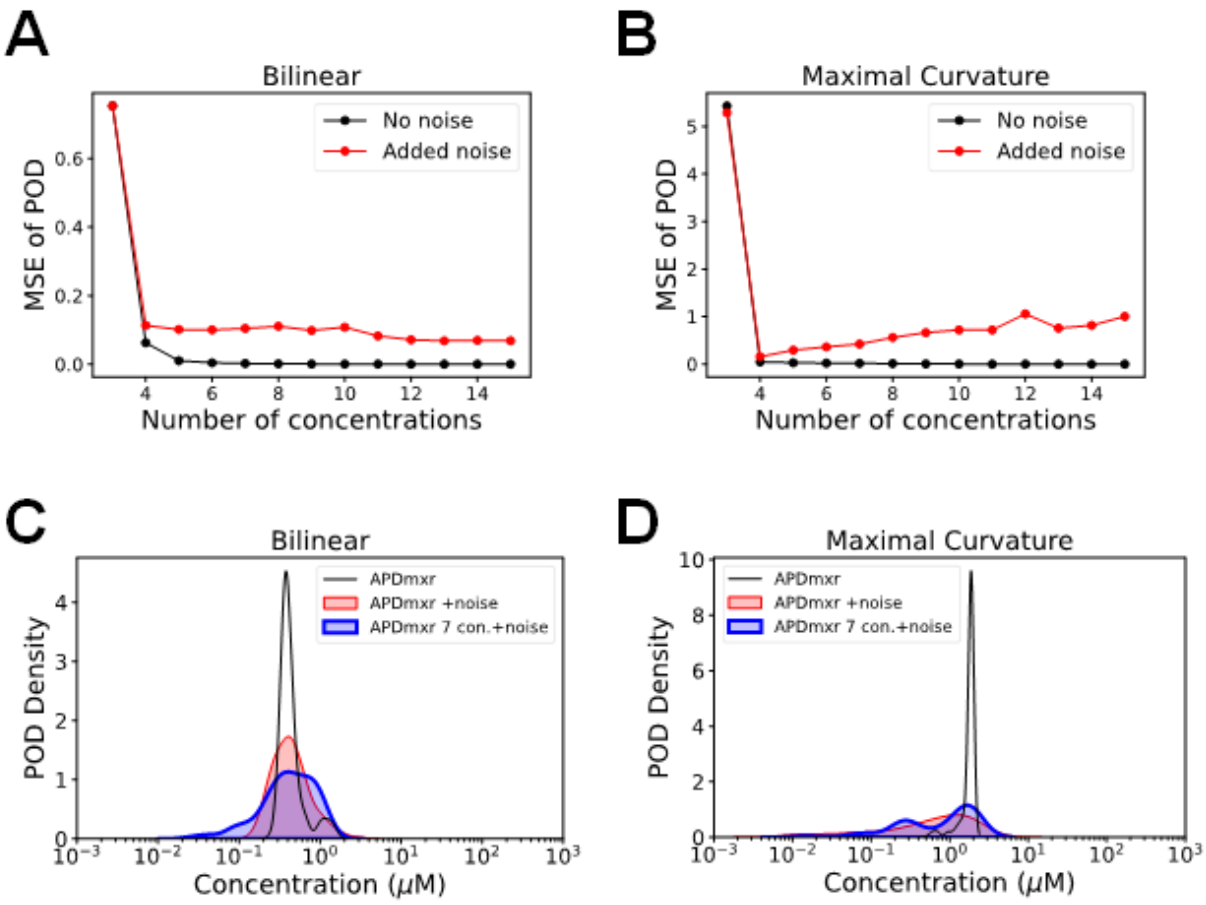

Supplemental Figure B.4. Mean squared error of POD. (A) Plot of MSE of POD, $\frac{1}{n}\sum_{i=1}^{n}(PoDfull - PoDreduced)^2$, from bilinear fit vs. number of doses used in resampling the reduced data (see methods) with and without added noise. **(B)** Plot of MSE of POD, $\frac{1}{n}\sum_{i=1}^{n}(PoDfull - PoDreduced)^2$, from maximum curvature vs. number of doses used in resampling the reduced data (see methods) with and without added noise. **(C)** Bilinear fit calculated POD kernel density plot for full sample data (black, median=0.38 µM, 90% confidence interval=0.33, 1.14), full sample data with added noise (red, median=0.42 µM, 90% confidence interval=0.20, 1.14), and 7 concentration reduced sample data with added noise (blue, median=0.43 µM, 90% confidence interval=0.09, 1.03). **(D)** Maximum curvature calculated POD kernel density plot for full sample data (black, median=1.87 µM, 90% confidence interval=1.07, 1.87), full sample data with added noise (red, median=0.71 µM, 90% confidence interval=0.02, 2.17), and 7 concentration reduced sample data with added noise (blue, median=1.07 µM, 90% confidence interval=0.08, 1.87).

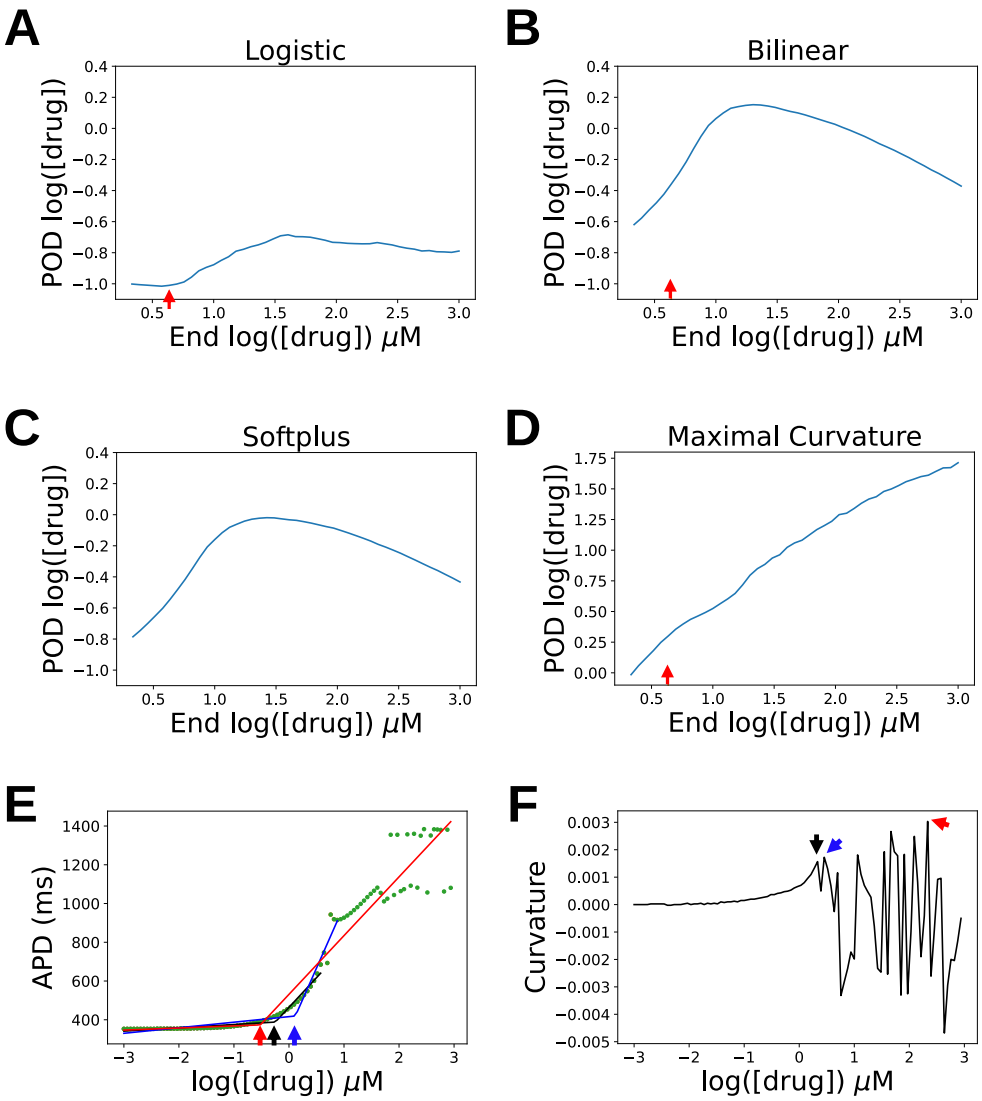

Supplemental Figure B.5. POD dependence on presence or absence of EADs for APD population modeling calculated by 3 fitting methods. (A) Plot of mean POD (log[concentration]) vs. End log[concentration] (maximum x value in concentration-response curve) for PODs calculated with logistic method. Note stable POD values beyond the last point without effect of EADs (red arrow). Maximum ΔPOD = 0.32. **(B)** Plot as in (A) for bilinear fit method. Note the mean POD changes even before the effect of EADs (red arrow). Maximum ΔPOD = 0.77. **(C)** Plot as in (A) for softplus method. Maximum ΔPOD = 0.77. **(D)** Plot as in (A) for maximum curvature method of POD calculation. As in case of the bilinear fit, the mean POD is increasing even without EADs and continues to increase for the full extent of the data. Maximum ΔPOD = 1.73. **(E)** Plot of single set of APD data from population simulation for 3 different end log([drug]) ranges fit with bilinear regression (black = -3.0:0.63, blue = -3.0:0.93, red = -3.0:3.0) lines to demonstrate why the mean POD follows a biphasic relationship as seen in (B, C). **(F)** Plot of curvature calculated from the same set of simulated APD data as in (E) for 3 different end log([drug]) ranges. The maximal curvature for each range is indicated by arrows (black = -3.0:0.63, blue = -3.0:1.0, red = -3.0:3.0) showing the general increase of maximum curvature with increasing end log([drug]) range.

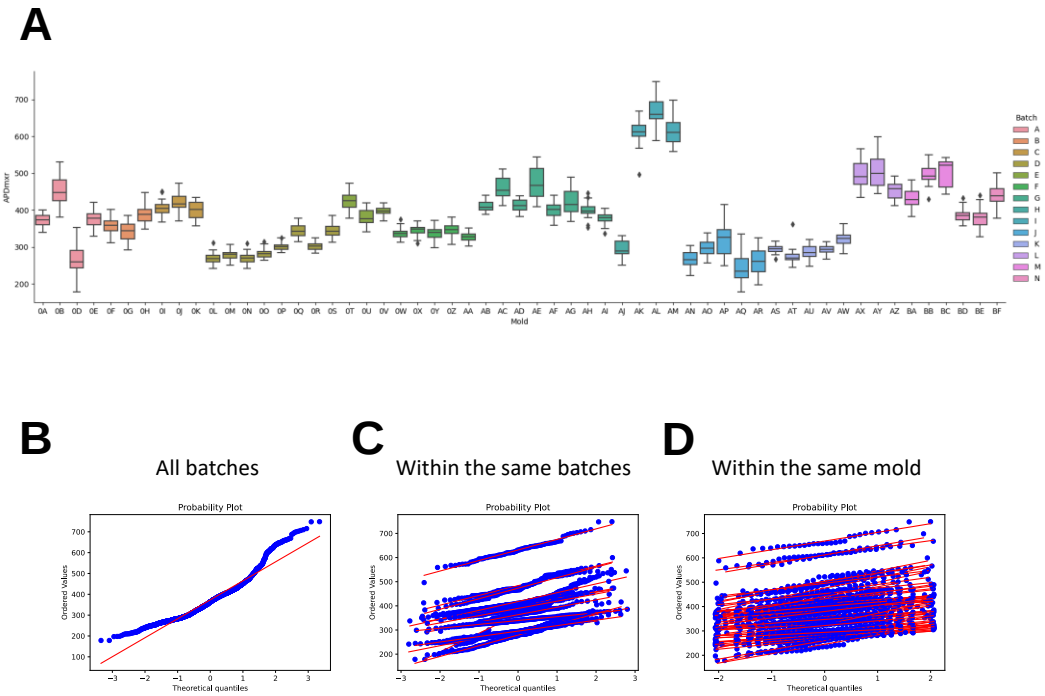

Supplemental Figure B.6. Experimental data APD distribution. (A) Box plot of APD_{mxr} from N=14 batches, 3~4 molds per batch. **(B)** Probability plot (ordered values vs. theoretical quantiles) for all batches showing the deviation from a normal distribution. Red line represents a normal distribution. APD was not normally distributed (D'Agostino-Pearson test). **(C)** Probability plot as in B within same batches. 8 of 15 batches were found to be normally distributed (57% of batches, D'Agostino-Pearson test). **(D)** Probability plot as in B within the same mold showing a better fit to normal distribution (52 out of 57 molds, 91%, D'Agostino-Pearson test).

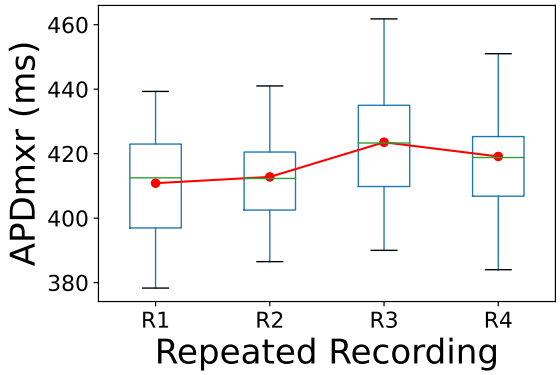

Supplemental Figure B.7. Mold level technical variance of microtissue APDs. Boxplot of APD_{mxr} for repeated recordings from a single mold showing the microtissue APDs vary together rather than randomly. Red symbols represent mean APD_{mxr} (31 microtissues) for each recording (R1, R2…).

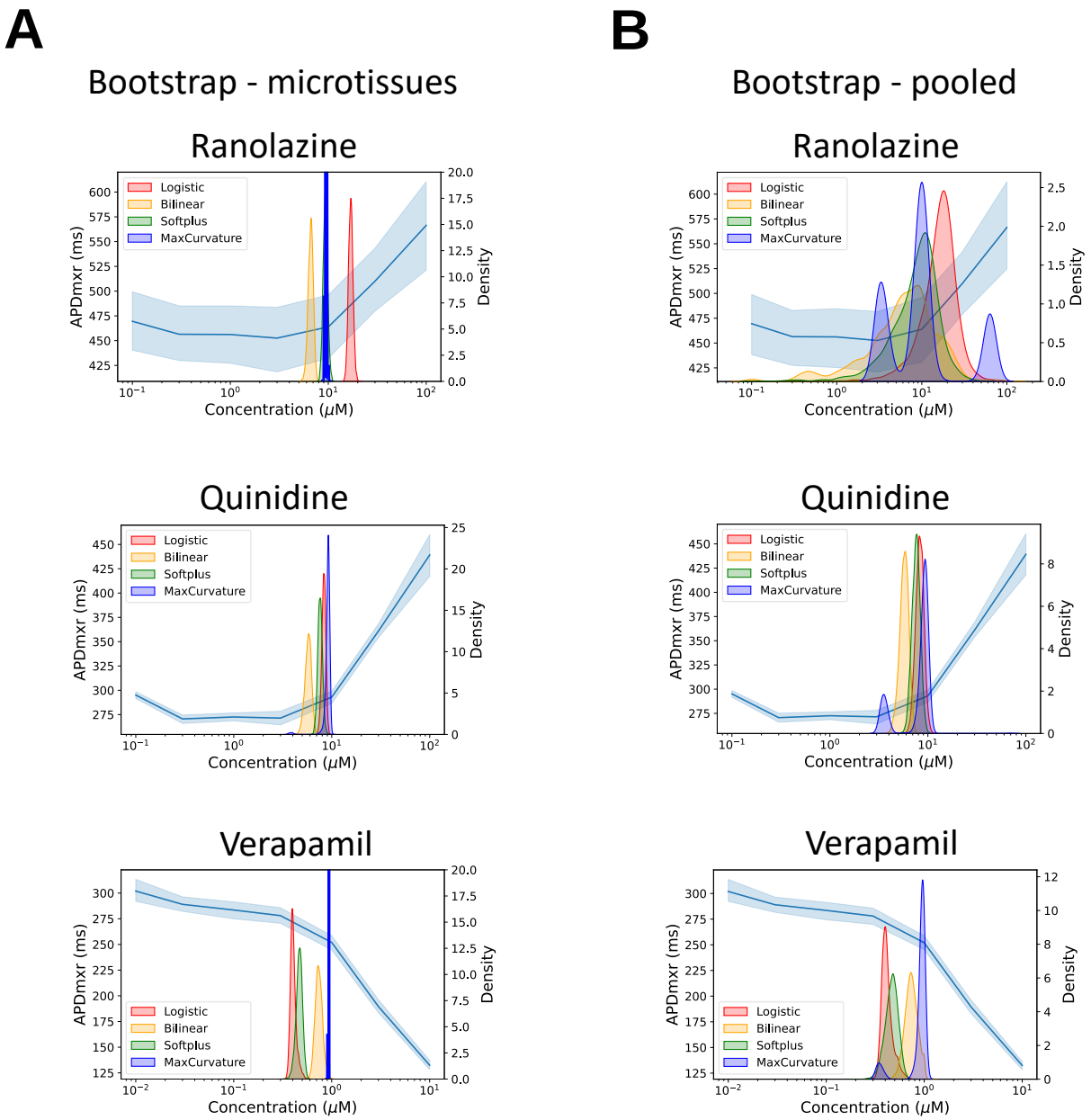

Supplemental Figure B.8. Comparison of POD distributions calculated from raw APD_{mxr} data using 4 different curve fit methods for ranolazine, quinidine, and verapamil. (A) Kernel density plots of PODs calculated with 4 different methods from resampled data (5000x) using the individual microtissue bootstrap method overlaid on concentration vs. APD_{mxr} curves (blue) for ranolazine, quinidine, and verapamil. **(B)** Kernel density plots of PODs calculated from resampled data (5000x) using the pooled data bootstrap method overlaid on concentration vs. APD_{mxr} curves (blue) as in (A).

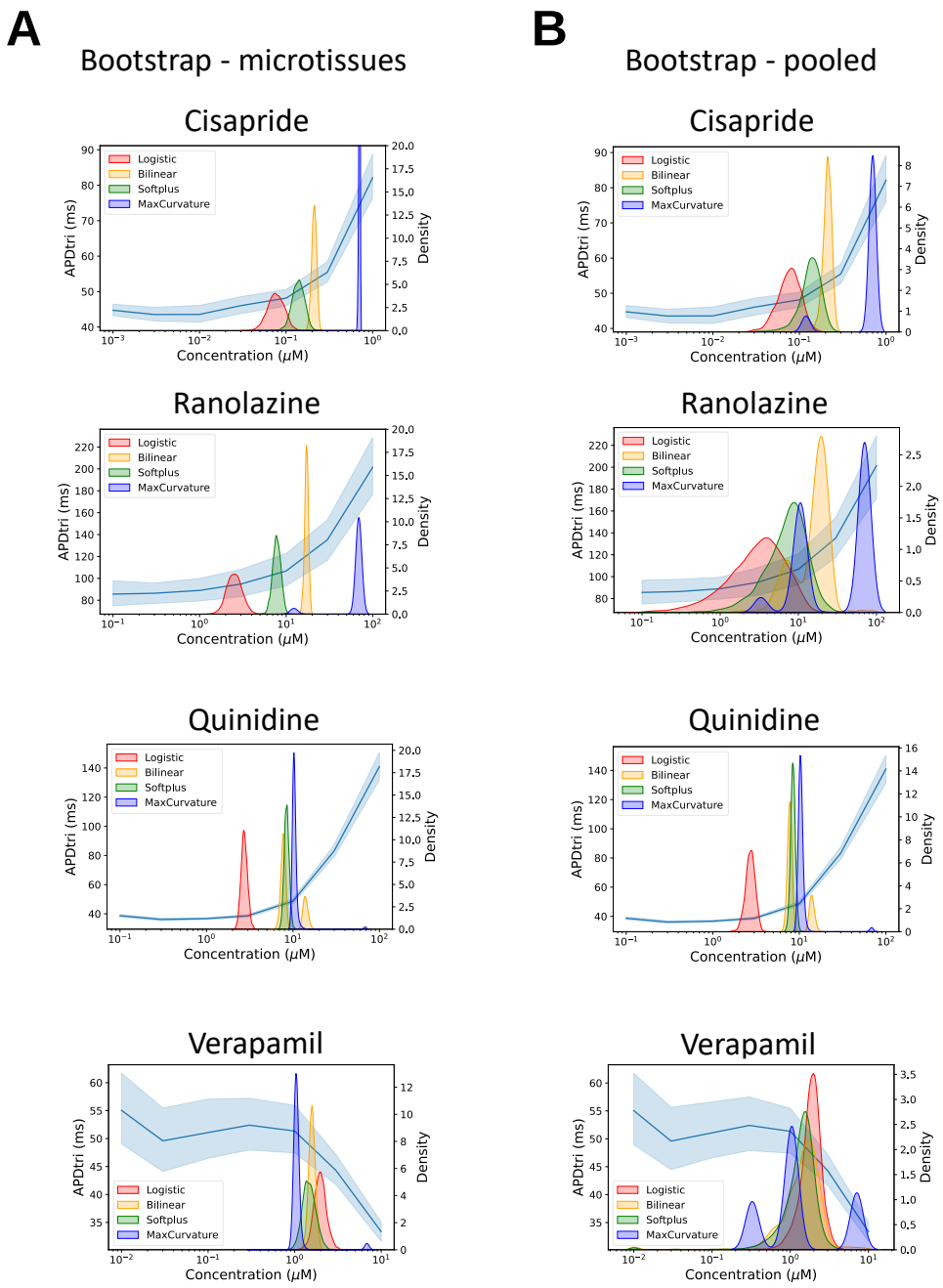

Supplemental Figure B.9. Comparison of POD distributions calculated from raw APD triangulation data (APD_{tri}) using 3 different curve fit methods. (A) Kernel density plots of PODs calculated with different fit methods from resampled data (5000x) using the individual microtissue bootstrap method overlaid on concentration vs. APD_{mxr} curves (blue) for cisapride, ranolazine, quinidine, and verapamil experimental data. **(B)** Kernel density plots of PODs calculated from resampled data (5000x) using the pooled data bootstrap method overlaid on concentration vs. APD_{mxr} curves (blue) as in (A).

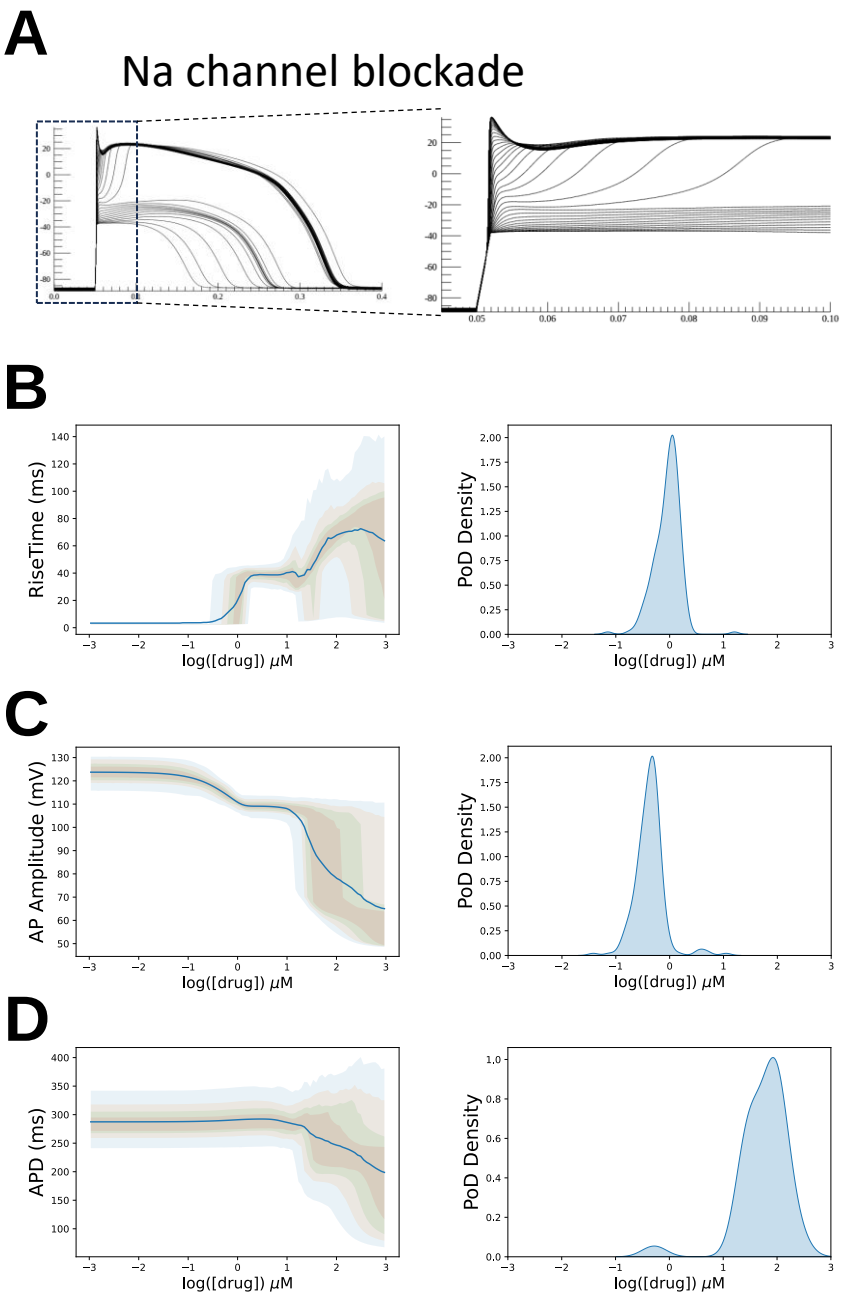

Supplemental Figure B.10. POD analysis of Na channel block only using rise time AP metric. (A) AP traces of computer simulation under Na channel block. Right panel shows zoomed region within dashed rectangle. **(B)** Plot of normalized rise time vs. Na channel block ratio (left panel) for the same gCa as in (A). Kernel density plot of POD calculated from AP rise time by logistic regression method. The AP is mainly Ca^{2+} based beyond 70% Na channel block and the rise time changes linearly with the block ratio after about 20% block. Increasing gCa to 2x shifts the rise time relation to higher percentage block. **(C)** Plot of AP amplitude vs. Na channel block ratio (left panel) and kernel density plot of POD calculated from AP amplitude by logistic regression method (right panel). **(D)** Plot of APD vs. Na channel block ratio (left panel) and kernel density plot of POD calculated from APD by logistic regression method (right panel).

Supplemental Table B.1. Methods of calculating point of departure (POD).

Method	Description	Advantages	Limitations	References
No/Low Observed Adverse Effect Level (NOAEL, LOAEL)	Standard statistical test determines the highest tested concentration without a significant effect (NOAEL) or the lowest tested concentration with a significant effect (LOAEL).	• Simple • Historical standard • Few required samples	• Heavily dependent on study design (concentrations, number of groups, sample numbers)	[2-4]
Bilinear Breakpoint	Two lines are fit to the data, one horizontal and one sloped, with the POD defined as the intersection of those two points.	• Simple	• Assumption of threshold response and no response sub-threshold. • Assumption of linear response post-threshold. • More test concentrations needed (5-6)	[5-7]
Benchmark Dose	A mathematical model (*e.g.,* sigmoidal curve) is fit to the data to estimate a POD based on a pre-defined threshold (*e.g.*, % change)	• Biologically relevant • Multiple models • Modern Standard	• More complex • Pre-determined response shape. • High dose responses needed for saturated response • More test concentrations needed (5-6)	[8, 9]
Maximum Curvature	An interpolated-spline model is fit to the concentration-response data. The curvature is calculated along the spline and the POD is defined concentration with the maximum curvature.	• Semi-parametric	• Irregular curve • More test concentrations needed (5-6)	[10]

Supplemental Table B.2. Standard deviation of APD_{mxr} and APD_{tri} values measured from baseline, repeated measure, and 7 dose cisapride application. MT = microtissue; BL = baseline; B/M = batch/mold.

	Baseline				Repeated Measure		Cisapride	
AP Metric	Batch	Mold	Microtissue	Beat	Mold	Microtissue	ΔMetric Batch/Mold, within mold	ΔMetric Ratio Batch/Mold, within mold
APD_{mxr}:								
Mean (ms)	390.2	378.7	373. 7		439.3	441.3	82.2, 78.2	1.2, 1.2
Mean SD (ms)	92.0	29.9	24.5	5.6	9.1	11.6	38.6, 41.2	0.07, 0.12
SD of SD (ms)		16.1	7.0	7.9	7.8	9.7		
% of mean	23.6	7.9	6.6		2.1	2.6	47.0, 52.6	5.6, 10.2
APD_{tri}:								
Mean (ms)	60.0	57.0	54.5		57.7	54.9	39.1	1.9
Mean SD (ms)	29.9	11.8	19.0	26.5	2.0	3.7	16.0	0.4
SD of SD (ms)		9.6	13.6	26.4	0.7	3.3		
% of mean	49.8	20.7	34.8		3.5	6.7	40.9	20.1

Supplemental Table B.3. Mean standard deviation and 95% confidence intervals for batch-to-batch, mold-to-mold, microtissue-to-microtissue, and beat-to-beat variation. SD calculated for equal weight per batch and normalized to have same weight over different molds per batch.

AP Metric	Batch-to-Batch	Mold-to-Mold	Microtissue-to-Microtissue	Beat-to-Beat
Excitability SD	0.758	0.716	0.92	0
Excitability CI	± 1.486	± 1.403	± 1.804	0
Stim Delay SD	5.427	5.304	5.391	0.388
Stim Delay CI	± 10.636	± 10.395	± 10.566	± 0.76
Rise Time SD	7.65	3.315	3.123	0.861
Rise Time CI	± 14.994	± 6.497	±6.122	± 1.687
APD_{30} SD	56.458	27.09	35.682	10.204
APD_{30} CI	± 110.658	± 53.097	± 69.936	± 20
APD_{50} SD	74.654	27.422	29.97	6.277
APD_{50} CI	± 146.321	± 53.747	± 58.742	± 12.302
APD_{80} SD	90.694	31.823	34.298	11.352
APD_{80} CI	± 177.759	± 62.372	± 67.224	± 22.25
APD_{mxr} SD	91.986	29.846	24.485	5.579
APD_{mxr} CI	± 180.293	± 58.498	± 47.991	± 10.935
APD_{tri} SD	29.89	11.787	18.968	26.498
APD_{tri} CI	± 58.584	± 23.102	± 37.177	± 51.936

Supplemental Table B.4. POD confidence interval values for cisapride based on POD distributions. APD_{mxr} and APD_{tri} experimental data for the two different bootstrap methods (Individual microtissues or pooled concentrations).

AP Metric	Fit type	Bootstrap Method	5% (μM)	Median (μM)	95% (μM)	Mean (μM)	Min. (μM)	Max. (μM)
APD_{mxr}	Logistic	Individual	0.229	0.272	0.322	0.273	0.185	0.385
		Pooled	0.163	0.268	0.403	0.273	0.004	0.641
	Bilinear	Individual	0.147	0.167	0.186	0.167	0.08	0.203
		Pooled	0.057	0.167	0.255	0.162	0.005	0.974
	Softplus	Individual	0.137	0.16	0.187	0.161	0.115	0.237
		Pooled	0.065	0.16	0.27	0.164	0.001	0.438
	Curvature	Individual	0.102	0.102	0.106	0.11	0.05	0.966
		Pooled	0.099	0.102	0.902	0.384	0.032	0.902
APD_{tri}	Logistic	Individual	0.053	0.076	0.108	0.078	0.034	0.168
		Pooled	0.045	0.078	0.122	0.080	0.023	0.237
	Bilinear	Individual	0.188	0.212	0.234	0.211	0.150	0.264
		Pooled	0.171	0.212	0.250	0.211	0.063	0.738
	Softplus	Individual	0.105	0.139	0.180	0.140	0.071	0.241
		Pooled	0.078	0.138	0.199	0.139	0.015	0.319
	Curvature	Individual	0.684	0.708	0.708	0.704	0.043	0.708
		Pooled	0.117	0.708	0.708	0.645	0.033	0.708

Supplemental Table B.5. POD confidence interval values for ranolazine based on POD distributions. APD_{mxr} and APD_{tri} experimental data for the two different bootstrap methods (Individual microtissues or pooled concentrations).

AP Metric	Fit type	Bootstrap Method	5% (μM)	Median (μM)	95% (μM)	Mean (μM)	Min. (μM)	Max. (μM)
APD_{mxr}	Logistic	Individual	15.574	16.956	18.507	16.982	14.332	21.613
		Pooled	6.157	16.854	30.066	17.385	0.127	75.537
	Bilinear	Individual	5.972	6.635	7.270	6.626	5.066	8.106
		Pooled	0.891	6.680	21.763	8.556	0.100	97.731
	Softplus	Individual	8.586	9.332	10.204	9.355	7.725	11.392
		Pooled	2.518	9.381	19.117	9.842	0.107	51.287
	Curvature	Individual	9.226	9.550	9.886	9.457	8.610	10.965
		Pooled	3.162	9.886	63.826	17.256	3.162	70.795
APD_{tri}	Logistic	Individual	1.833	2.519	3.531	2.576	1.289	5.373
		Pooled	0.580	3.218	9.450	3.846	0.102	25.309
	Bilinear	Individual	15.767	17.248	18.688	17.248	13.802	20.316
		Pooled	5.412	17.376	26.417	16.779	0.900	99.836
	Softplus	Individual	6.501	7.792	9.296	7.845	5.1	11.815
		Pooled	2.149	7.674	16.363	8.219	0.130	35.095
	Curvature	Individual	13.032	68.391	70.795	65.196	10.965	70.795
		Pooled	3.890	68.391	70.795	43.602	3.162	73.282

Supplemental Table B.6. POD confidence interval values for quinidine based on POD distributions. APD_{mxr} and APD_{tri} experimental data for the two different bootstrap methods (Individual microtissues or pooled concentrations).

AP Metric	Fit type	Bootstrap Method	5% (μM)	Median (μM)	95% (μM)	Mean (μM)	Min. (μM)	Max. (μM)
APD_{mxr}	Logistic	Individual	7.656	8.310	8.922	8.304	7.026	9.95
		Pooled	7.027	8.278	9.622	8.297	5.542	11.554
	Bilinear	Individual	5.015	5.774	6.447	5.756	4.124	7.359
		Pooled	4.757	5.763	6.750	5.758	3.777	8.322
	Softplus	Individual	6.958	7.598	8.307	7.612	6.279	9.269
		Pooled	6.414	7.599	8.845	7.613	5.184	10.328
	Curvature	Individual	8.318	9.226	9.550	9.062	3.508	10.233
		Pooled	3.388	9.226	9.886	8.184	3.162	70.795
APD_{tri}	Logistic	Individual	2.389	2.731	3.159	2.747	2.115	3.729
		Pooled	2.166	2.725	3.317	2.732	1.646	4.106
	Bilinear	Individual	7.198	7.908	14.626	9.429	6.174	16.822
		Pooled	7.238	7.894	14.620	9.271	6.419	17.010
	Softplus	Individual	7.601	8.450	9.430	8.473	6.737	10.640
		Pooled	7.602	8.439	9.372	8.457	6.603	11.015
	Curvature	Individual	9.886	10.233	11.350	10.918	9.886	68.391
		Pooled	9.886	10.233	11.350	11.524	9.886	70.795

Supplemental Table B.7. POD confidence interval values for verapamil based on POD distributions. APD_{mxr} and APD_{tri} experimental data for the two different bootstrap methods (Individual microtissues or pooled concentrations).

AP Metric	Fit type	Bootstrap Method	5% (μM)	Median (μM)	95% (μM)	Mean (μM)	Min. (μM)	Max. (μM)
APD_{mxr}	Logistic	Individual	0.369	0.402	0.467	0.407	0.334	0.593
		Pooled	0.353	0.407	0.540	0.420	0.296	0.746
	Bilinear	Individual	0.649	0.738	0.848	0.742	0.541	0.990
		Pooled	0.580	0.737	0.948	0.747	0.451	1.226
	Softplus	Individual	0.410	0.469	0.523	0.468	0.311	0.595
		Pooled	0.352	0.470	0.585	0.470	0.162	0.793
	Curvature	Individual	0.923	0.923	0.955	0.932	0.861	0.955
		Pooled	0.376	0.923	0.989	0.869	0.316	1.096
APD_{tri}	Logistic	Individual	1.511	1.965	2.598	1.994	0.923	3.477
		Pooled	1.027	1.865	2.864	1.901	0.080	4.421
	Bilinear	Individual	1.373	1.587	1.837	1.593	1.093	2.284
		Pooled	0.538	1.560	2.704	1.631	0.01	9.927
	Softplus	Individual	1.114	1.462	1.991	1.496	0.817	3.350
		Pooled	0.586	1.444	2.317	1.446	0.01	4.770
	Curvature	Individual	1.023	1.023	1.175	1.228	0.339	7.079
		Pooled	0.316	1.059	6.607	2.198	0.316	6.839

References

1. O'Hara, T., et al., *Simulation of the undiseased human cardiac ventricular action potential: model formulation and experimental validation.* PLoS Comput Biol, 2011. **7**(5): p. e1002061.
2. Crump, D., et al., *Urine fractions that release flehmen in black-tailed deer,Odocoileus hemionus columbianus.* J Chem Ecol, 1984. **10**(2): p. 203-15.
3. Slob, W., et al., *A statistical evaluation of toxicity study designs for the estimation of the benchmark dose in continuous endpoints.* Toxicol Sci, 2005. **84**(1): p. 167-85.
4. Travis, K.Z., I. Pate, and Z.K. Welsh, *The role of the benchmark dose in a regulatory context.* Regul Toxicol Pharmacol, 2005. **43**(3): p. 280-91.
5. Gollapudi, B.B., et al., *Quantitative approaches for assessing dose-response relationships in genetic toxicology studies.* Environ Mol Mutagen, 2013. **54**(1): p. 8-18.
6. Lutz, W.K. and R.W. Lutz, *Statistical model to estimate a threshold dose and its confidence limits for the analysis of sublinear dose-response relationships, exemplified for mutagenicity data.* Mutat Res, 2009. **678**(2): p. 118-22.
7. Pottenger, L.H. and B.B. Gollapudi, *Genotoxicity testing: moving beyond qualitative "screen and bin" approach towards characterization of dose-response and thresholds.* Environ Mol Mutagen, 2010. **51**(8-9): p. 792-9.
8. Sand, S., K. Victorin, and A.F. Filipsson, *The current state of knowledge on the use of the benchmark dose concept in risk assessment.* J Appl Toxicol, 2008. **28**(4): p. 405-21.
9. EPA, *Benchmark Dose Technical Guidance*. 2012, U.S. EPA.
10. To, K. and L. Burgoon, *GRAVEE: Good Risk Assessment Values for Environmental Exposures.* 2021.

C. Appendix C – Supplemental Material for Chapter 4

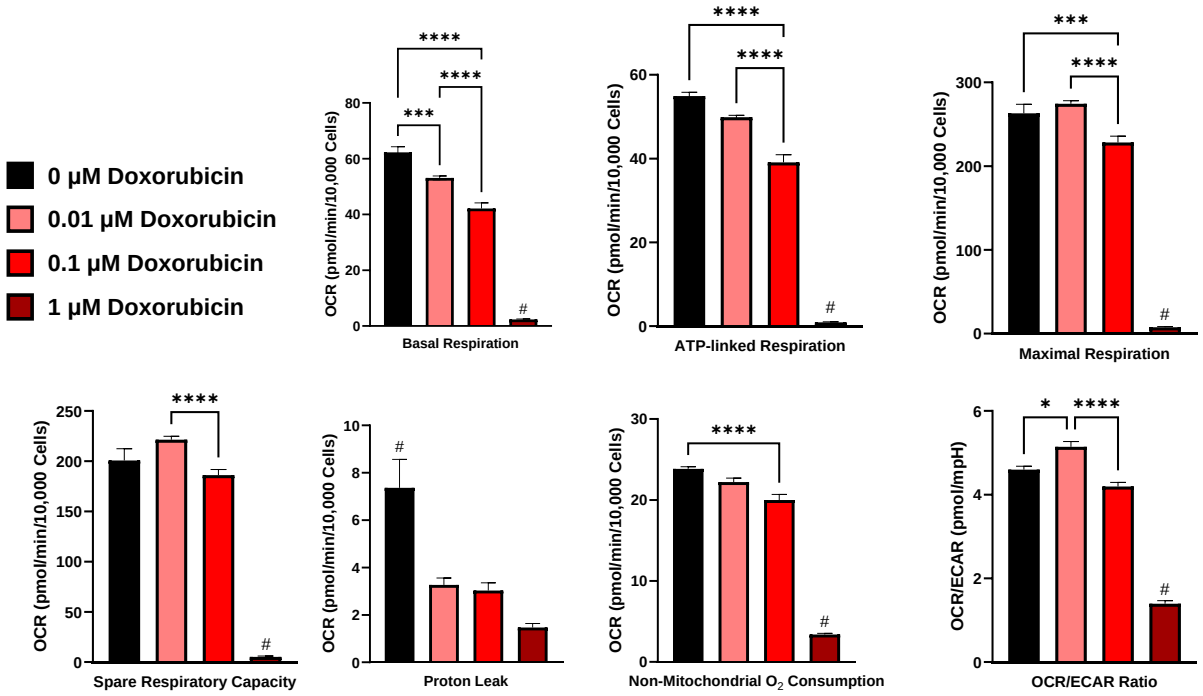

Supplemental Figure C.1. Effects of doxorubicin exposure on hiPSC-CM metabolism. The oxygen consumption rate (OCR) of hiPSC-CMs was quantified after 72-hour-long exposures to either 0, 0.01, 0.1, or 1 µM doxorubicin to calculate **(A)** basal respiration, **(B)** ATP-linked respiration, **(C)** maximal respiration, **(D)** spare respiratory capacity, **(E)** proton leak, and **(F)** non-mitochondrial oxygen consumption. **(G)** Additionally, extracellular acidification rate (ECAR) was quantified at baseline to examine the balance of oxidative phosphorylation and glycolysis with doxorubicin exposure (OCR/ECAR). Data are presented as mean ± standard error (N = 8-12 wells). *, **, ***, and **** indicate statistical significance ($p < 0.05$; $p < 0.01$; $p < 0.001$; $p < 0.0001$, respectively) for a one-way ANOVA with a Tukey post-hoc test. # indicate statistical significance ($p < 0.05$) compared to all other groups.

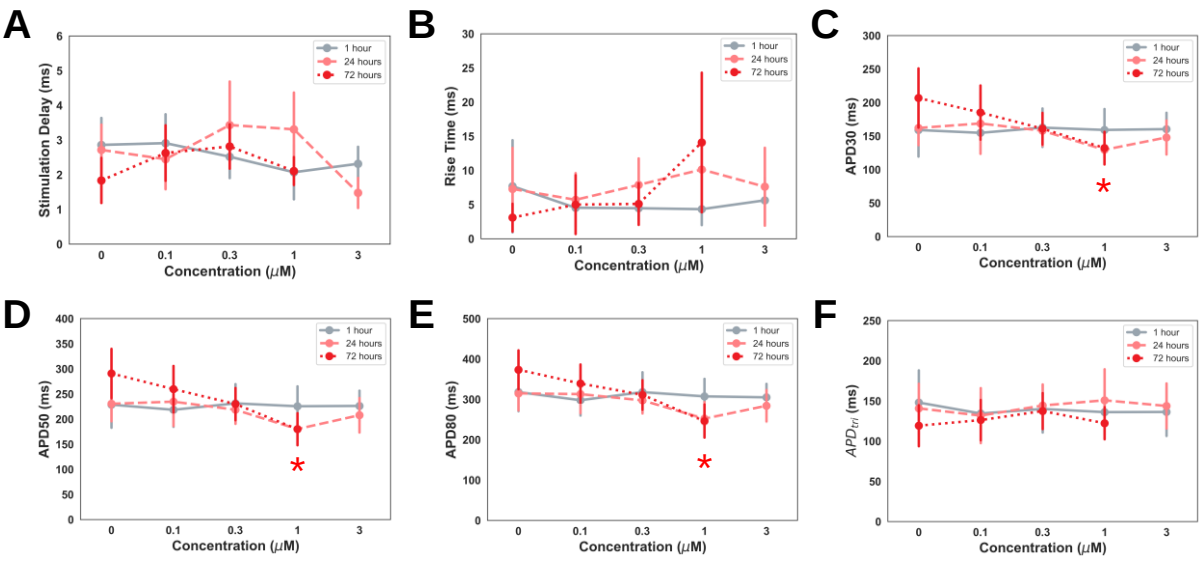

Supplemental Figure C.2. Additional action potential metrics after doxorubicin exposure. Time- and concentration-dependent functional toxicity was measured in cardiac microtissue action potentials using **(A)** stimulation delay, **(B)** rise time, **(C)** APD30, **(D)** APD50, **(E)** APD80, and **(F)** APD_{tri} after 1-hour, 24-hour, and 72-hour doxorubicin exposures (N = 3 molds; 96-104 microtissues total). * indicate statistical significance ($p < 0.05$ and $p < 0.0001$, respectively) for one- or two-way ANOVA with a Dunnet post-hoc test compared to untreated controls.

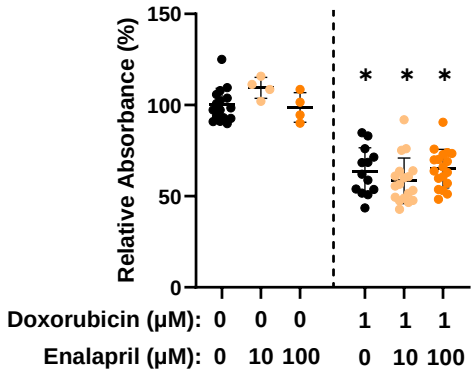

Supplemental Figure C.3. High concentration enalapril co-treatment. hiPSC-CM viability was also examined at high concentrations of enalapril using an MTT assay. No statistically significant effects of enalapril were observed (N = 4-18 wells; up to 3 experiments). * indicate statistically significance ($p < 0.05$) as determined by a two-way ANOVA with a Tukey post-hoc test compared to untreated controls.

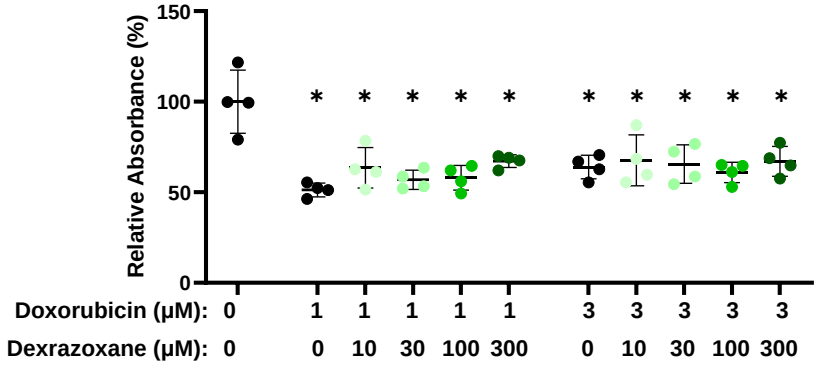

Supplemental Figure C.4. High concentration dexrazoxane co-treatment. hiPSC-CM viability was also examined at high concentrations of dexrazoxane using an MTT assay. No statistically significant effects of dexrazoxane were observed (N = 4 wells). * indicate statistically significance ($p < 0.05$) as determined by a one-way ANOVA with a Tukey post-hoc test compared to untreated controls.

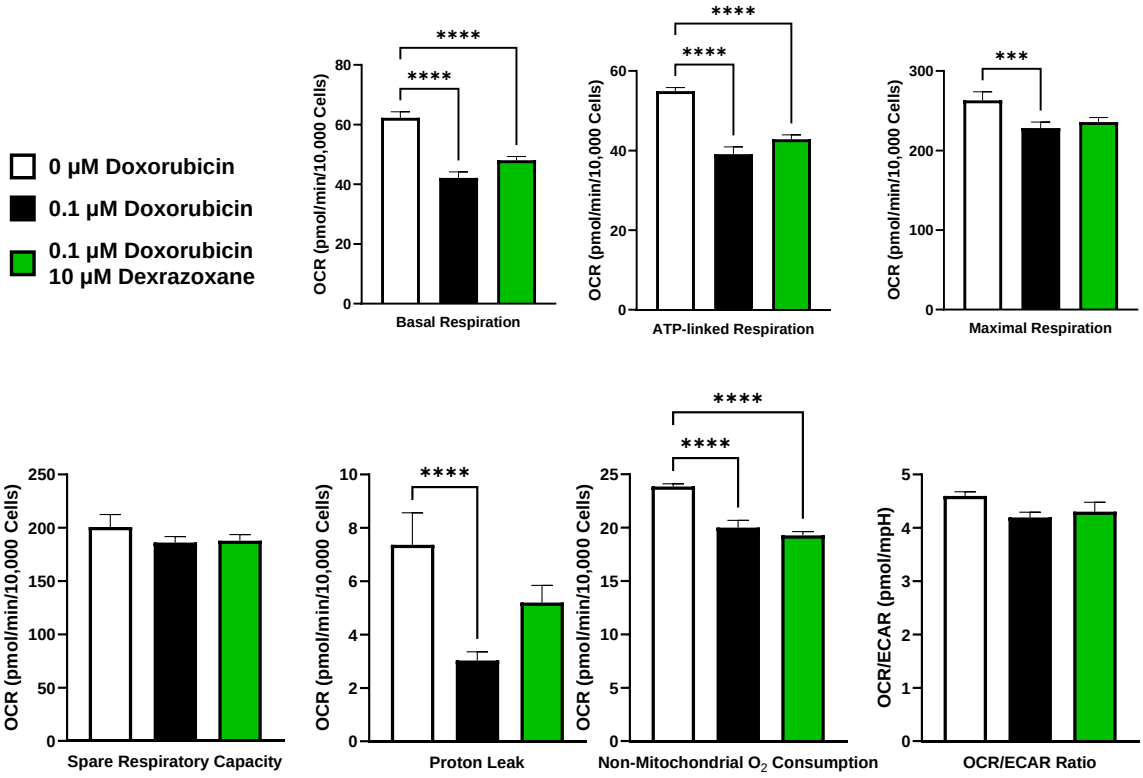

Supplemental Figure C.5. Effects of dexrazoxane exposure on hiPSC-CM metabolism post-doxorubicin exposure. The oxygen consumption rate (OCR) of hiPSC-CMs was quantified after 72-hour-long exposures to either 0, 0.01, 0.1, or 1 μM doxorubicin to calculate **(A)** basal respiration, **(B)** ATP-linked respiration, **(C)** maximal respiration, **(D)** spare respiratory capacity, **(E)** proton leak, and **(F)** non-mitochondrial oxygen consumption. **(G)** Additionally, extracellular acidification rate (ECAR) was quantified at baseline to examine the balance of oxidative phosphorylation and glycolysis with doxorubicin exposure (OCR/ECAR). Data are presented as mean ± standard error (N = 8-12 wells). *, **, ***, and **** indicate statistical significance ($p < 0.05$; $p < 0.01$; $p < 0.001$; $p < 0.0001$, respectively) for a one-way ANOVA with a Tukey post-hoc test.

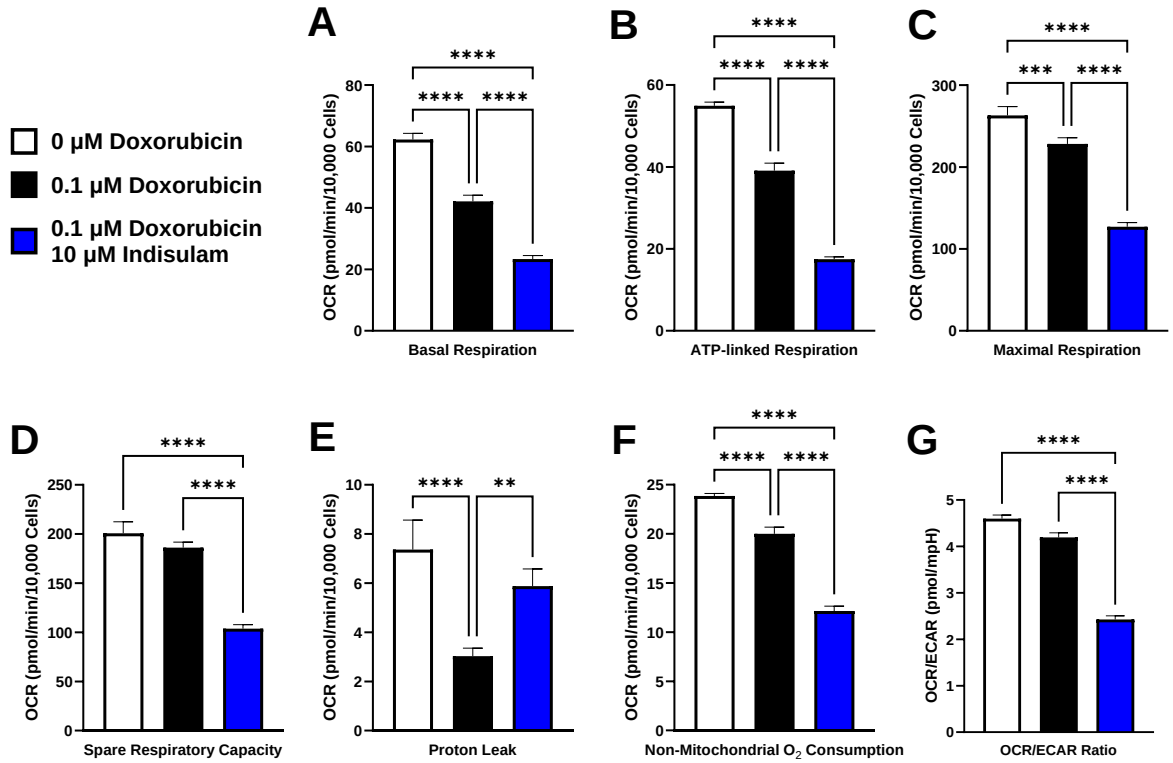

Supplemental Figure C.6. Effects of indisulam cotreatment on hiPSC-CM metabolism post-doxorubicin exposure. The oxygen consumption rate (OCR) of hiPSC-CMs was quantified after 72-hour-long exposures to either 0, 0.01, 0.1, or 1 µM doxorubicin to calculate **(A)** basal respiration, **(B)** ATP-linked respiration, **(C)** maximal respiration, **(D)** spare respiratory capacity, **(E)** proton leak, and **(F)** non-mitochondrial oxygen consumption. **(G)** Additionally, extracellular acidification rate (ECAR) was quantified at baseline to examine the balance of oxidative phosphorylation and glycolysis with doxorubicin exposure (OCR/ECAR). Data are presented as mean ± standard error (N = 8-12 wells). *, **, ***, and **** indicate statistical significance ($p < 0.05$; $p < 0.01$; $p < 0.001$; $p < 0.0001$, respectively) for a one-way ANOVA with a Tukey post-hoc test.

D. Appendix D – Supplemental Material for Chapter 6

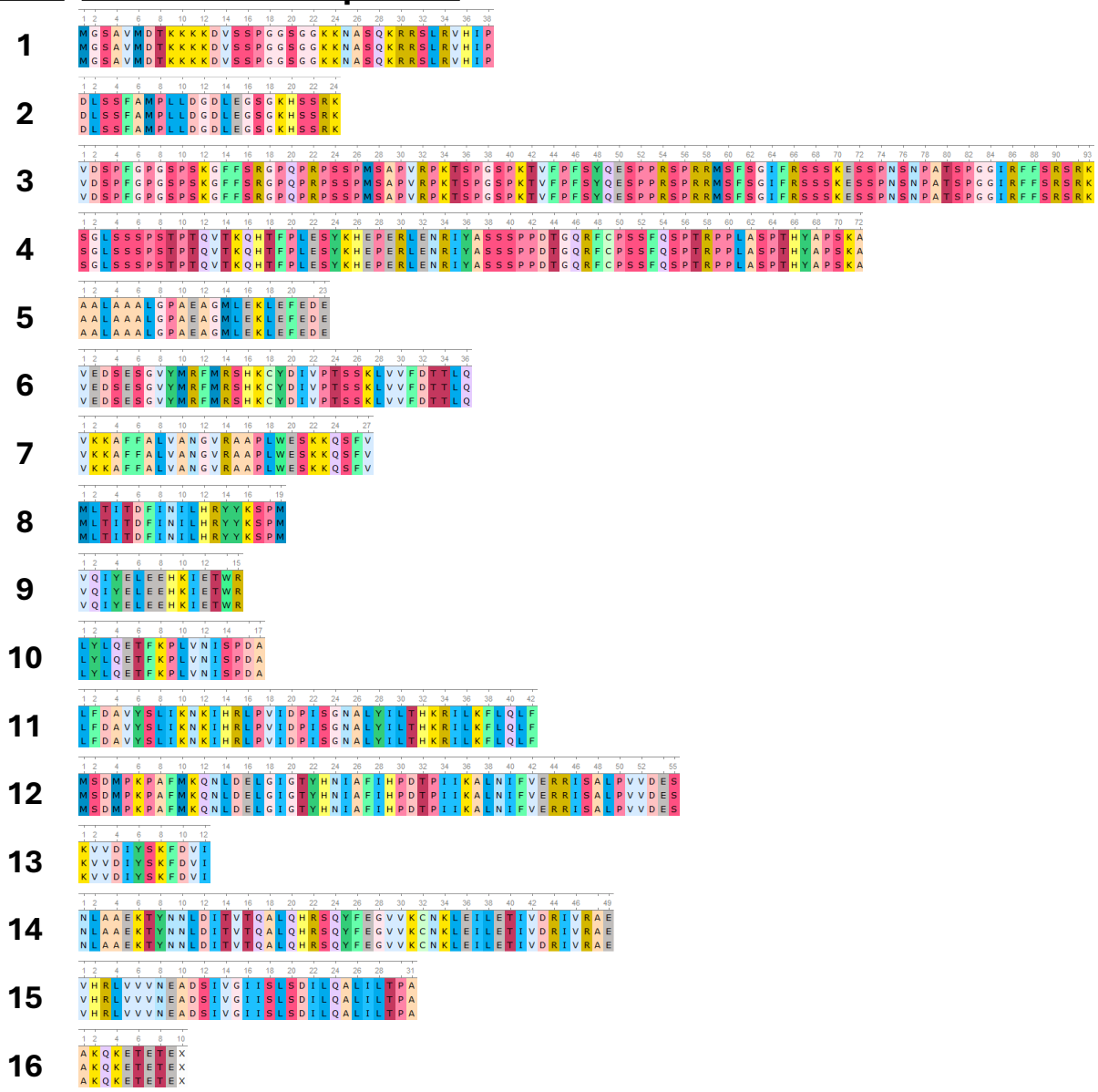

Supplemental Figure D.1. Amino acid sequence of γ_2-subunit of AMPK based on Sanger sequencing of *PRKAG2* exons from genomic DNA. (top rows) Consensus sequence was compared to (middle rows) WTC control hiPSCs and (bottom row) novel WPW hiPSCs as single-letter amino acid codes. Amino acids encoded across splice junctions were excluded for visualization.

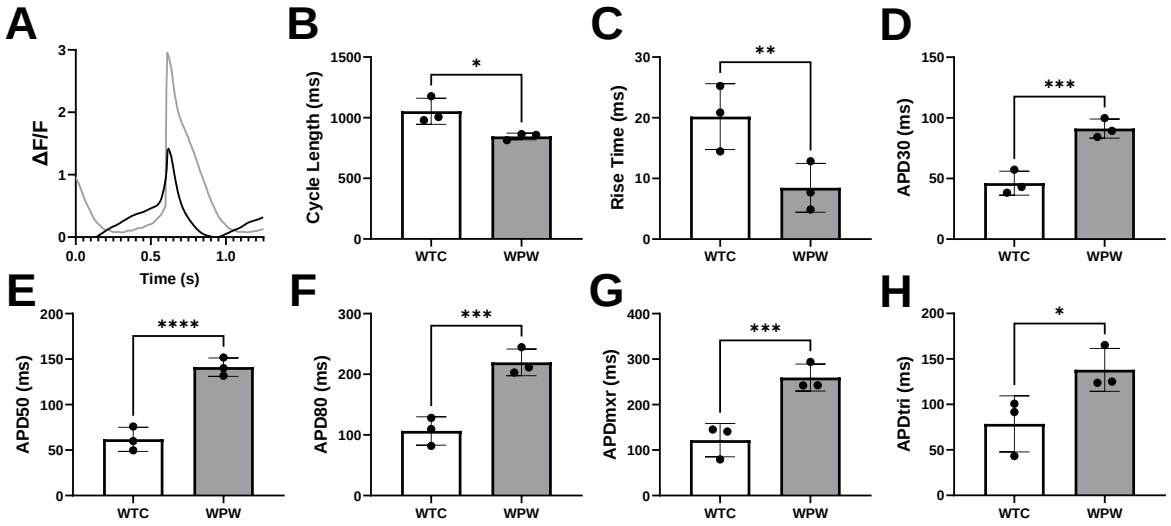

Supplemental Figure D.2. Quantification of action potentials from spontaneously beating microtissues. (A) Representative action potential trace from spontaneously beating WTC control and WPW microtissues enabled measurement of mold-averaged (B) cycle length, (C) rise time, (D) APD30, (E) APD50, (F) APD80, (G) APD_{mxr}, (H) APD_{tri}. Data are displayed as mean ± standard deviation. *, **, ***, and **** indicate statistical significance ($p < 0.05$, $p < 0.01$, $p < 0.001$, and $p < 0.0001$, respectively) from and unpaired Student's t-test (N = 3 molds).

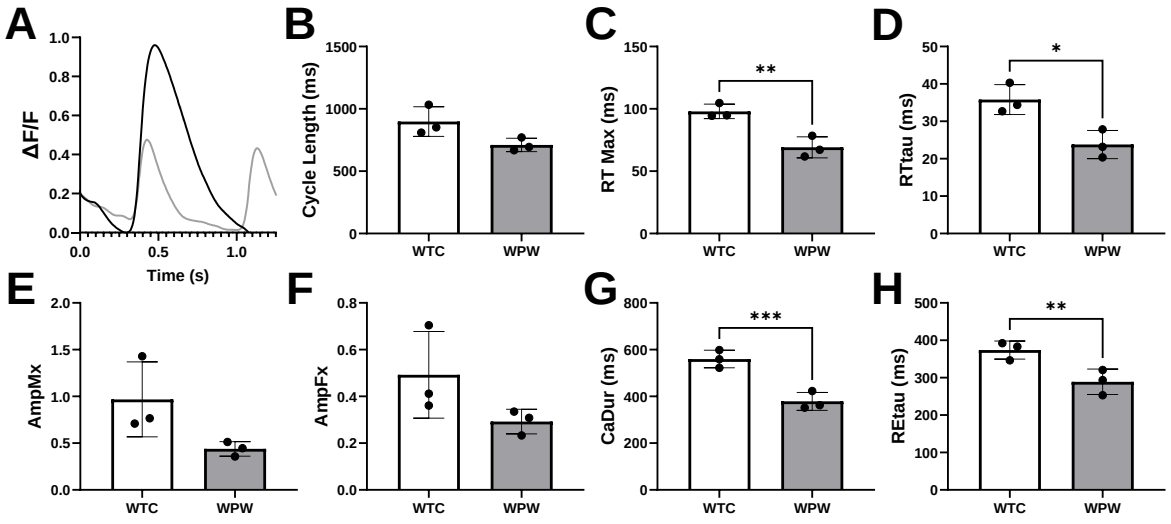

Supplemental Figure D.3. Quantification of calcium transients from spontaneously beating microtissues. (A) Representative calcium traces from spontaneously beating WTC control and WPW microtissues enabled measurement of mold-averaged **(B)** cycle length, **(C)** rise time (RTmax), **(D)** rise time tau (RTtau), **(E)** maximum amplitude (AmpMx), **(F)** amplitude of the initial rise phase (AmpFx), **(G)** total calcium transient duration, and **(H)** relaxation tau (REtau)**.** Data are displayed as mean ± standard deviation. *, ** and *** indicate statistical significance ($p < 0.05$, $p < 0.01$ and $p < 0.001$, respectively) from an unpaired Student's t-test (N = 3 molds).